Development of Nanomedicine for the Treatment of Breast Cancer Metastases

by

Neha Kaushal

A dissertation submitted in partial fulfillment
of the requirements for the degree of
Doctor of Philosophy
(Biomedical Engineering)
in the University of Michigan
2017

Doctoral Committee:

Assistant Professor Ariella Shikanov, Chair
Professor Sofia D. Merajver
Professor David Samuel Sept
Professor Lonnie David Shea

Neha Kaushal

nkaus@umich.edu

ORCID iD: 0000-0003-0982-6194

To caffeine and friends, my companions through many a long night in lab

Acknowledgements

I would like to thank my Ph.D. advisor, Dr. Mohamed E.H. ElSayed, for believing in me and giving me the opportunity to work on an extremely interesting and impactful thesis project. His gumption, support, and note-worthy work ethic inspired as well as helped me see my project to fruition. I would like to extend a special thanks to Dr. Ariella Shikanov for all the guidance, support, and mentorship she offered me in my final year of graduate school. I would like to thank my parents for being great role models and providing me an unabated platform to explore my curiosity and passion for seeking out the unknown. A special thanks to my brother for his constant encouragement and support throughout my time in graduate school. I'd also like to thank Dr. Sofia D. Merajver and her lab for the valuable advice and experimental support they provided me during our research collaboration. I would like to acknowledge the contributions of Dr. Yasemin Yuksel Durmaz and Dr. Gopinath Tiruchinapally for their unyielding efforts toward the synthesis of the nanopolymers used in my research. A special thanks to all my labmates and friends who made my time in graduate school a truly enjoyable and memorable experience. And finally the BME department and Dr. Lonnie Shea for helping me out through tough times and providing me with ample resources to complete my research project.

Table of Contents

List of Figures

Abstract

Development of Nanomedicine for the Treatment of Breast Cancer Metastases

by

Neha Kaushal

Chair: Ariella Shikanov

RhoC-GTPase, a member of the Ras-superfamily of small guanosine triphosphatases (GTPases), is over-expressed in advanced breast cancer and has been implicated in highly motile and invasive cancer phenotypes. The overexpression of RhoC mRNA in advanced breast cancers suggests that it plays a role as a transformative oncogene for human mammary epithelial cells and as a potential marker to screen breast cancer patients with highly aggressive tumors and provide therapeutic interventions prior to the development of metastases. Short interfering RNA (siRNA) inhibits RhoC protein expression resulting in the suppression of breast cancer metastasis by inhibiting cancer cell invasion and migration. Transforming anti-RhoC siRNA into a clinically-viable therapy requires the development of biocompatible delivery systems that incorporate a large dose of siRNA and shuttle the therapeutic payload into the cytoplasm of aggressive breast cancer cells. This dissertation describes the development of peptide targeted, degradable, pH-sensitive, membrane-destabilizing β-cyclodextrin (β-CD) polymers that proved effective in condensing anti-RhoC siRNA to form "smart" nanoparticles. The peptide targeted "smart" nanoparticles facilitated selective homing into target breast cancer cells through receptor-mediated endocytosis and achieved functional delivery of anti-RhoC siRNA past the endosome into the cytoplasm of breast cancer cells resulting in the efficient knockdown of RhoC mRNA and protein levels. Specifically, we utilized the varying reactivity of the primary and secondary hydroxyl groups of the β-CD core to develop asymmetric "smart" polymers. The secondary hydroxyl groups were modified with amphiphilic copolymers comprising of pH-sensitive dimethyl aminoethyl methacrylate (DMAEMA) and hydrophobic hexyl methacrylate (HMA) monomers incorporated at a 50/50 molar feed ratio and grafted via acid-labile hydrazone linkages to form β-CD-P(HMA-*co*-DMAEMA) polymers. The β-CD-P(HMA-*co*-DMAEMA) polymers were stable at physiological pH, but rapidly degraded into membrane-active fragments at the acidic pH of the endosome. The siRNA molecules were complexed to the P(HMA-co-DMAEMA) grafts following the partial conversion of DMAEMA monomers into cationic TMAEMA monomers. The β-CD-P(HMA-*co*-DMAEMA-*co*-TMAEMA) polymers delivered anti-RhoC siRNA into the cytoplasm of SUM149 and MDA-MB-231 cells resulting in a 80-90% and 90-100% reduction in RhoC mRNA and protein levels, respectively. The incorporation of peptide targeted moieties to the free ends of polyethylene glycol (PEG) brushes on the primary face of the β-CD core resulted in selective accumulation of “smart” nanoparticles in breast cancer cells overexpressing underglycosylated Mucin 1 (uMUC1) surface receptors both *in vitro* and *in vivo*. Further, combining the peptide ligands and anti-RhoC siRNA molecules on the same asymmetric nanoparticle demonstrated a synergistic reduction in breast cancer cell invasion and migration *in vitro*. These results collectively confirm the successful development of a targeted, degradable “smart” nanoparticles that can enhance the functional delivery of anti-RhoC siRNA into the cytoplasm of aggressive breast cancer cell both *in vitro* and *in vivo.*

Chapter 1

Introduction

1.1 Breast cancer: incidence, epidemiology and risk factors

Breast cancer is a major global public health problem in women. It is the most common cancer among women with an estimated 1.15 million incident cases diagnosed in 2002, constituting nearly one fifth of the estimated 5.0 million cancer cases diagnosed each year in the world. Among the reported incident cases and deaths from the disease - developed countries account for 641,600 cases and 190,900 deaths while less developed countries account for 509,700 cases and 219,600 deaths[1, 2]. If the current trends in incidence rates hold constant, there will be approximately 2.7 million new cases in the world in 2030, with more than 60% of the cases (1.72 million) occurring in less developed regions of the world. Thereby, suggesting a steady growth in the incidence and mortality rates of the disease with considerable variation by world region **(Figure 1.1 and 1.2)**. For instance, the estimated age-standardized rates varied from 18.7 per 100,000 women in China to 99.4 per 100,000 women in North America **(Figure 1.1 and 1.2)**[3]**.** In general, the incidence is high (greater than 80 per 100,000) in developed regions of the world and low (less than 30 per 100,000) in developing regions; the range of mortality rates is much less (approximately 6 – 23 per 100,000) because of the more favorable survival of breast cancer in (high-incidence) developed regions. The highest incidence rates of breast cancer are observed in northern and western Europe, North America, Australia, New Zealand, and in southern countries of South America, notably Uruguay and Argentina[1] **(Figure 1.1).** In general, the high rates of breast cancer in developed countries are the consequence of a higher prevalence of the known risk factors for the disease. The risk factors include early age at menarche, nulliparity, late age at first birth, late age at any birth, low parity, exposure to exogenous hormones (e.g., oral contraceptives and menopausal hormone therapy), obesity, and late menopause – relate to the hormonal (largely estrogen) milieu to which the breast is exposed from menarche to the cessation of ovulation at menopause. The depletion of circulating estrogen after menopause attributes to the age-specific incidence of breast cancer - a rapid increase in incidence rate before menopause (up to age 50 years) while the rate of incidence decreases thereafter. While incidence rates are less than 40 per 100,000 women in most less developed countries, breast cancer is still the most common cancer among women in the majority of less developed countries. This increase is widely attributed to the ‘‘westernization’’ of lifestyles, an ill-defined surrogate for changes in factors such as childbearing, anthropometric attributes, and lifestyle characteristics.

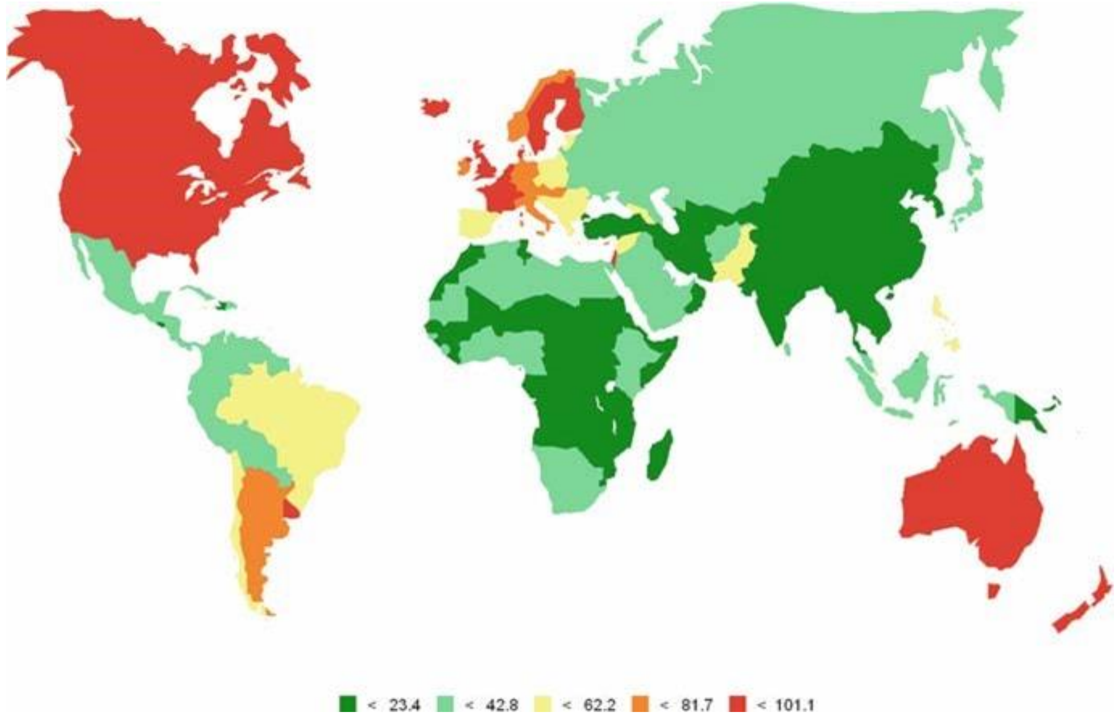

Figure 1.1: The global burden of breast cancer in 2002; age-standardized incidence rates per 100,000

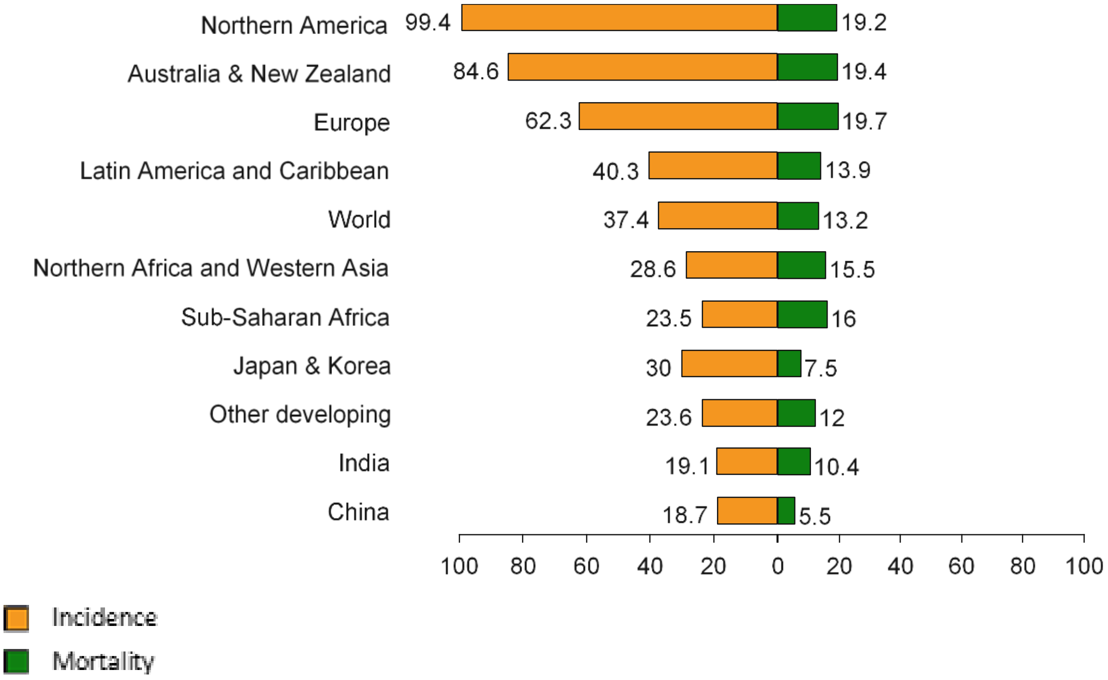

Figure 1.2: Breast cancer incidence and mortality in 2002: rates per 100,000 by region

1.2 Trends in North America

An observed increase in the incidence rate of the disease appeared in the US between 1980 and 1987 due to the widespread increase in mammographic screening during that period. The overall rate of increase has slowed to 0.6% per year since the late 1980s. According to the US SEER cancer registries, the period between 2002 and 2003 showed a statistically significant decline in female breast cancer incidence rates[4]. On further analyses by tumor size and stage, the study suggested that the incidence rates decreased for small tumors (2 cm) by 4.1% per year from 2000 through 2003 and for localized disease by 3.1% per year from 1999 through 2003[4]. No decrease in incidence was observed for larger tumors or advanced-stage disease during the same periods. The decreasing rate of mortality in many high-risk countries can be attributed to a combination of the introduction of mammographic screening, and improved awareness and intensified early clinical diagnosis resulting in the diagnosis of more small, early stage tumors; and advances in both primary and adjuvant treatments for breast cancer[2].

1.3 Breast cancer: staging and treatment

Until fairly recently, breast cancer was viewed as a single deadly disease that warranted the use of extreme treatment measures[5]. For instance, records dating back to 1600 B.C. indicate the use of cauterization techniques by Egyptian physicians to treat breast cancer, while extensive surgeries involving removal of the breast and all the surrounding muscle and bone were adopted during the Renaissance period[6]. Halsted adapted a less extreme but still extensive surgery that became the standard of care in the late 19th century[6].

By the first half of the 20th century, clinicians began to subscribe to the “one-size doesn’t fit all” concept implying that not all breast cancers shared the same prognosis or required the same treatment. Therefore, attempts were made to define characteristics that could reliably delineate between tumors that required aggressive treatment from those that did not. In 1987, the International Union against Cancer (UICC) and the American Joint Committee on Cancer (AJCC) adapted the tumor-node-metastasis (TNM) staging convention as the international standard for reliable diagnosis and treatment of the disease[6]. The TNM system originally developed by Pierre Denoix (1942) represented an attempt to classify cancer based on the major morphological attributes of malignant tumors that were thought to influence disease prognosis: size of the primary tumor (T), presence and extent of regional lymph node involvement (N), and presence of distant metastases (M).

Breast cancer staging is useful because of its ability to estimate prognosis. **Figure 1.3** shows the relationship between cancer stage and 10-year relative survival in breast cancer patients (adapted from a report by Bland and colleagues that used data from 1.3 million cases (1985 to 1996) in the National Cancer Data Base (NCDB))[5]. The data suggests that there are significant differences among stages: only 5% to 12% of Stage I/II patients die in the first 10 years after diagnosis, compared with over 60% of Stage III patients and over 90% of Stage IV patients. Breast cancer staging also provides valuable information about appropriate treatment options for each cancer stage. For instance, AJCC/UICC staging is commonly used to select patients and to report outcomes in clinical trials; therefore, clinicians can make a reasoned judgment about whether treatment strategies reported in the literature will be appropriate for their patients.

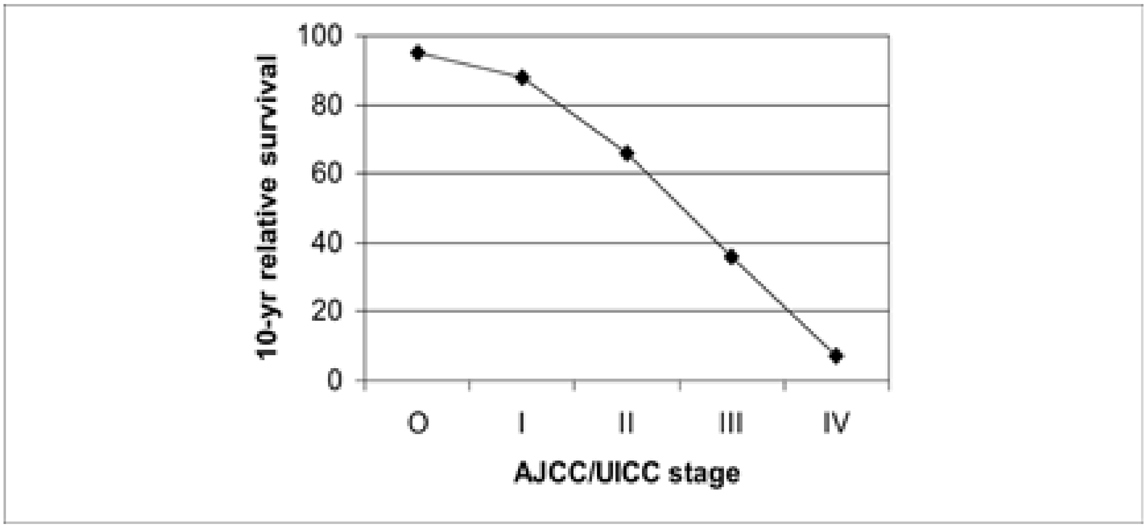

Figure 1.3: Ten-year Relative Survival Associated with AJCC/UICC (TNM) Breast Cancer Stage

The objective of treating patients diagnosed with early-stage breast cancer is to cure them of the disease – local surgical interventions supplemented with adjuvant therapies are frequently explored to eradicate microscopic tumor cells that may have spread systemically at the time of diagnosis using chemotherapy, endocrine therapy, and biological therapy[3]. However, in metastatic breast cancer (stage IV), cure is very uncommon and the goals are symptom palliation and prolongation of survival. Therefore, maximizing quality of life (Qol) during therapy assumes the greatest importance. The median survival of metastatic breast cancer (MBC) is 2–4 years; this estimate has been relatively stable over decades. The median survival of MBC patients, however, varies based on prognostic characteristics exhibited by the patient: those with ER-positive or PR-positive disease presenting with metastases only to the bones have a longer median survival, whereas patients with ER-negative/ PR-negative disease involving liver, lung, or brain have a shorter median survival[7].

The current standard of treatment for metastatic breast cancer involves palliative interventions like chemotherapy or endocrine therapy. Chemotherapy is the initial therapy for ER-negative/PR-negative metastatic breast cancer, of metastatic breast cancer with widespread, symptomatic visceral disease, and for ER-positive or PR-positive breast cancer that is endocrine therapy-refractory[7]. Multiple chemotherapy agents have activity in metastatic breast cancer, with higher response rates in first (30–60%) than in subsequent (10–40%) lines of treatment. Given the palliative nature of chemotherapy for metastatic disease, a favorable side effect profile is desirable. However, drug-related toxicities such as low blood counts and fatigue often occur with prolonged chemotherapy duration, prompting consideration of a hiatus in treatment according to patient tolerance. The use of Trastuzumab, a monoclonal antibody (mAb) against HER-2/neu, in combination with taxane-based chemotherapy for metastatic disease is the current standard of treatment for HER-2/neu-positive metastatic breast cancer due to improved patient survival[8]. Other mAb-based treatments like Bevacizumab (a mAb directed against vascular endothelial growth factor) is believed to work by inhibiting new blood vessel formation in tumors[9]. Bevacizumab delays the time to disease progression when combined with paclitaxel in first-line metastatic therapy, but without a significant impact on survival or time to progression. For women with metastatic breast cancer involving bone, bisphosphonates are an additional component of their systemic therapy. The bisphosphonates inhibit osteoclast function, thus inhibiting bone loss at sites of metastasis and reducing the risks of pathologic fracture, pain, and functional impairment. A side effect of bisphosphonates is osteonecrosis of the jaw, a failure of bone healing sometimes associated with dental work which may cause recurrent infections and pain. In summary, it is evident that alternative treatment options that can tackle the metastatic spread at the source, while improving patient Qol, overall survival rate, and tumor-targeted delivery of therapeutic agents to overcome systemic treatment associated toxicities, are needed.

1.4 Metastatic breast cancer

Metastasis is of great significance to the clinical management of breast cancer since cancer associated mortality stems primarily from the disseminated disease rather than the primary tumor. Recent evidence suggests that the onset of metastasis can be an early event and potentially 60% - 70% of patients have initiated the metastatic process at the time of diagnosis[10]. Metastasis is the process, whereby cancer cells spread throughout the body, establishing new colonies in organs at a distance from the one where the primary tumor originated. To successfully colonize a secondary site - a cancer cell must complete a sequential series of steps before it becomes a clinically detectable lesion. These steps typically include separation from the primary tumor, invasion through surrounding tissues and basement membranes, entry and survival in circulation, lymphatics or peritoneal space, and colonization of a distant target organ[10]. These are usually, but not always, followed by extravasation into the surrounding tissue, survival in the foreign microenvironment, proliferation, and induction of angiogenesis, all the while evading apoptotic death. To successfully complete the sequence of metastatic events, the cells of the primary tumor must have the ability to a) interact with the local microenvironment, b) migrate, c) invade the surrounding tissue, d) resist apoptosis, and e) induce angiogenesis[11]. The onset of these metastatic phenotypes observed in primary cancer cells have been shown to be due to the overexpression of RHO-family GTPase proteins that regulate and control cell morphology and motility in metastatic cancer **(Figure 1.4)**[12]. The aggressive migratory and metastatic phenotypes expressed by these transformed cells are a result of combined, but distinct, effect of Rho-regulated kinases, ROCK1 and ROCK2[13]. Modulation of RHO-protein activity has shown to modulate the metastasis of tumor cells by disrupting epithelial-sheet organization, increasing cell motility, and promoting the degradation of the ECM[13]. These studies have led to further investigation of the role and mechanism of action of Rho-family proteins in regulating cytoskeletal dynamics that affect multiple cellular functions including cell motility and invasiveness observed during metastasis.

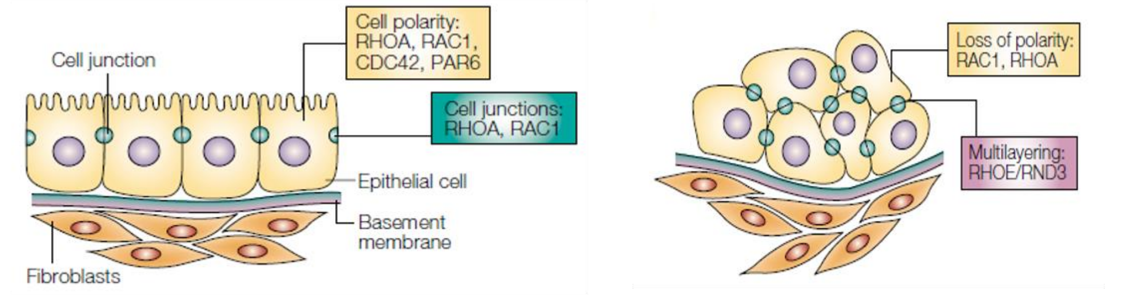

(A) Normal Epithelial Cells

(B) Benign Tumors: loss of polarity and multi-layering

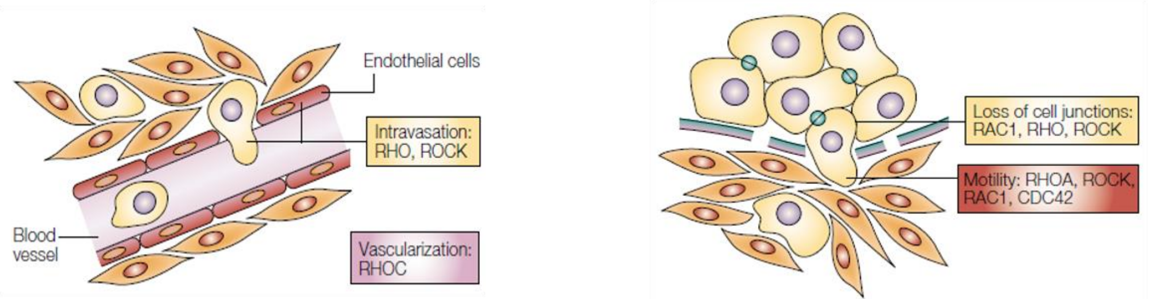

(D) Metastasis to a distant site:
intravasation & extravasation

(C) Locally Invasive Tumors: loss boundaries and
increased motility

Figure 1.4: Involvement of RHO proteins at different stages of tumor progression. A) Maintenance of normal epithelial polarity. **B)** Benign tumors: loss of polarity and multilayering. **C)** Locally invasive tumors: loss of tissue boundaries and increased motility. RHOA and RAC1 regulate proteases that facilitate motility by degrading the BM. **D)** Metastasis to a distant site: intravasation and extravasation. RHOC promotes expression of angiogenic factors, leading to an increase in vascularization of the tumor.

1.5 Role of RhoC-GTPase proteins in breast cancer metastasis

RhoC, a member of the Ras superfamily of low molecular weight guanine nucleotide (GTP)-binding proteins[14], have been implicated in the signal transduction process of integrins and growth factor receptors to the cytoplasm through a tightly regulated and highly complex signaling pathway[15]. By cycling between an inactive GDP-bound and active GTP-bound state, RhoC acts as a molecular on/off switch[16] that is involved in all aspects of cellular motility and invasion including maintaining cell polarity, cytoskeletal organization, and external signal transduction[17, 18, 19]. The Rho-GTPase cycle is tightly regulated by three groups of proteins **(Figure 1.5)**[15]. Guanine nucleotide exchange factors (GEF's) facilitate the exchange of inactive GDP for active GTP molecules, GTPase-activating proteins (GAP's) negatively regulate the switch by enhancing its intrinsic GTPase activity[20], and guanine nucleotide dissociation inhibitors (GDI's) are thought to block the GTPase cycle by sequestering and solubilizing the GDP-bound form of the protein. RhoC-GTPase activity in migrating cells is associated with focal adhesion assembly formation and cell contractility. An important downstream Rho target involved in facilitating actin:myosin filament assembly and subsequent contractility is the Ser/Thr kinase p160ROCK[13]. In its active state, p160ROCK, phosphorylates and activates LIMK, which in turn phosphorylates and inactivates cofilin leading to stabilization of actin filaments within the actin:myosin filament bundle. p160ROCK interacts with and phosphorylates the myosin binding subunit (MBS) of myosin light chain (MLC) phosphatase and thereby inactivates it. This leads to increased levels of myosin phosphorylation, which then results in their cross-linking with actin filaments and generates contractile forces. This promotes movement of the cell body and facilitates detachment of the rear end of the cells[13] **(Figure 1.5)**.

Another important Rho-downstream target is mDia, the mammalian ortholog of Drosophila Diaphanous **(Figure 1.5)**. mDia belongs to the formin-homology containing family of proteins, which have been linked to actin filament assembly in both Drosophila and yeast[13]. The binding of Rho-GTP to mDia opens up and activates this scaffold protein. This activated complex in combination with p160ROCK facilitates the assembly of actin:myosin filaments. Therefore, the involvement of activated RhoC proteins in cell migration and invasion of metastasizing cancer cells led to the evaluation of their possible use as a therapeutic target for the treatment of metastatic cancer.

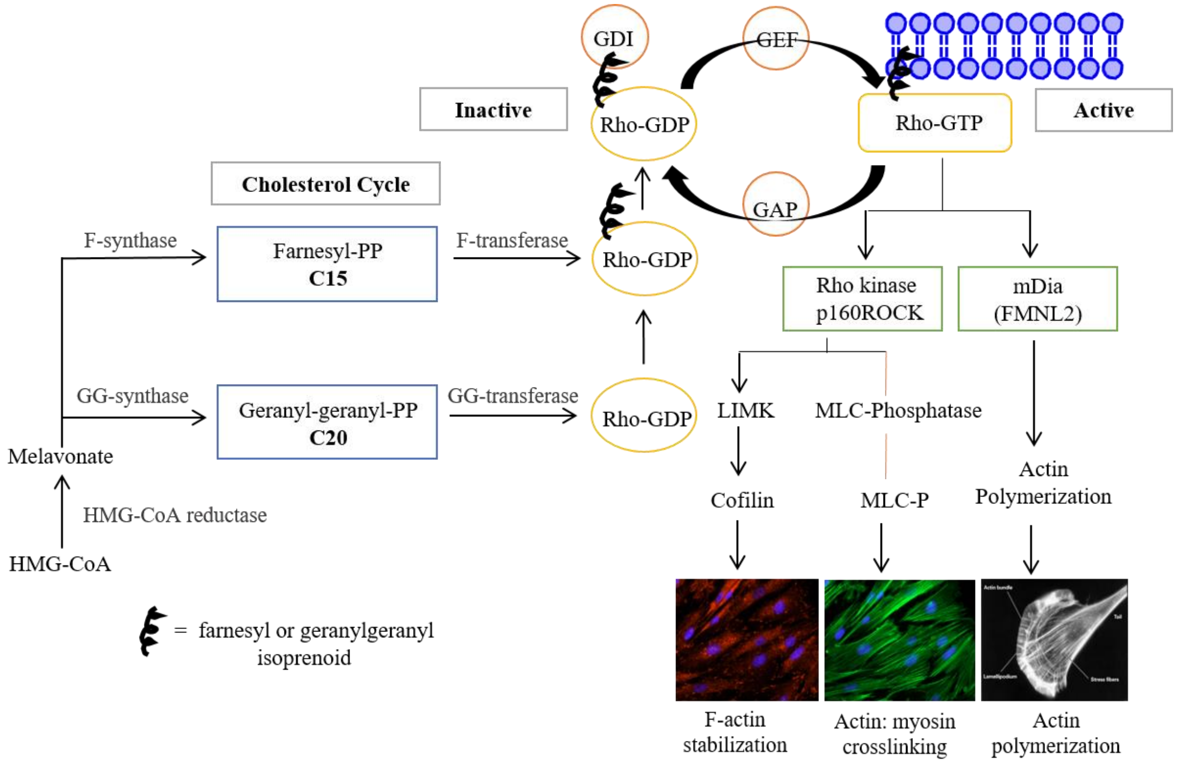

Figure 1.5: Model of RHO-protein regulation. RHO proteins can bind either GTP or GDP. When bound to GDP, they can be sequestered in the cytoplasm by RHO–GDP dissociation inhibitors (RHO–GDIs). The exchange of GDP for GTP is promoted by RHO guanine nucleotide exchange factors (RHO–GEFs), and is often associated with translocation of RHO proteins to cell membranes. GTP-bound RHO proteins interact with a range of effector proteins and modulate their ability to regulate cell behaviour. Most RHO proteins have an intrinsic ability to hydrolyse GTP to GDP and inorganic phosphate (P), which can be promoted by RHO–GTPase-activating proteins (RHO–GAPs).

1.6 RhoC: a therapeutic target for suppressing breast cancer metastases

Our collaborator, Professor Merajver, and others have previously shown that the overexpression of RhoC in breast cancer cells is strongly associated with aggressive cancer phenotypes with poor clinical outcomes[16, 17, 21, 22]. Further, Merajver et. al. showed that RhoC-transfected human mammary epithelial (HME) cells grew under anchorage-independent conditions became motile and invasive through enhanced formation of actin stress fibers and focal adhesion contacts, produced angiogenic factors, and were tumorigenic and metastatic when orthotopically implanted in nude mice[23, 22, 24]. These findings clearly indicate that RhoC protein plays a critical role in promoting the proliferation, migration, and invasion of cancer cells and warrants its consideration as a therapeutic target for suppressing breast cancer metastases. Earlier research showed that the use of anti-RhoC silencing RNA (siRNA) (5'-GACCUGCCUCCUCAUCGUCTT-3') to knock down RhoC expression at the mRNA level and subsequent protein levels – inhibited breast cancer cell proliferation, migration, and invasion *in vitro*[25] and tumor growth and angiogenesis *in vivo*[19]. The goal of our study was to transform this promising anti-RhoC siRNA into an effective and clinically-viable therapy to suppress the metastatic spread of breast cancer cells.

1.7 Introduction to small interfering RNA therapy

Gene therapy involving the use of plasmid DNA (pDNA), antisense oligonucleotide (ASODN), and small interfering RNA (siRNA) to regulate specific gene expression has been harnessed for the treatment of diseases ranging from viral infections[26, 27], hereditary disorders, and cancers[28, 29]. Specifically, siRNA molecules have been extensively studied following Fire and Mello's work that demonstrated the use of double-stranded RNA (dsRNA) via the endogenous RNA interference (RNAi) pathway to suppress gene expression in *Caenorhabditis elegans*[30]. Since the discovery of RNAi in 1998, several proof-of-principle experiments pertaining to the therapeutic potential of siRNA have been demonstrated both *in vitro* and *in vivo*[31, 32]. In recent years, RNAi has gained momentum in gene silencing and drug development because of its ability to silence the expression of virtually any gene with high efficiency and specificity, including targets traditionally considered to be 'undruggable'. Owing to its great potential in biological research and drug development, large amounts of effort and capital have been invested in bringing siRNA therapeutics to the market. At least 22 RNAi-based drugs have entered clinical trials, which include treatments for age-related macular degeneration (AMD), respiratory syncytial virus infection, and solid tumors. Among these clinical trials, most siRNAs are administered by local delivery, typically via the intravitreal or intranasal routes. However, local delivery may not be appropriate for all diseases. Under some circumstances, systemic drug administration by intravenous (i.v.) injection is needed. Therefore, numerous studies have focused on the design and development of carriers that can encapsulate siRNA molecules into stable particles to achieve efficient targeted delivery of the siRNA payload *in vivo*.

1.8 Basic concept and mechanism of small interfering RNA (siRNA)

RNAi is natural endogenous pathway specific to eukaryotic cells by which sequence-specific dsRNA is able to target and cleave complementary mRNA[31]. RNAi is triggered by the presence of long pieces of dsRNA (> 30 bp) in the cell cytoplasm, which are cleaved into the fragments known as siRNA (21–23 bp) by the enzyme Dicer[33]. In practice, siRNA can be synthetically produced and then directly introduced into the cell, thus circumventing Dicer mechanics **(Figure 1.6)**. The siRNA, is then incorporated into a protein complex called the RNA-induced silencing complex (RISC)[34]. Argonaute 2 (AGO2), a multifunctional protein contained within RISC, unwinds the double-stranded siRNA, after which the sense strand (or passenger strand) of the siRNA is cleaved[35]. The activated RISC, which contains the antisense strand (or guide strand) of the siRNA, selectively seeks out and degrades mRNA that is complementary to the antisense strand[36] **(Figure 1.6).** The degradation of target mRNA molecules results in the subsequent suppression of the associated protein expression. The activated RISC complex can then move on to destroy additional mRNA targets, which further propagates gene silencing[37]. This extra potency ensures a therapeutic effect for 3–7 days in rapidly dividing cells, and for several weeks in non-dividing cells[38]. Eventually, siRNAs are diluted below a certain therapeutic threshold or degraded within the cell, and so repeated administration is necessary to achieve a persistent effect. There are three strategies for RNAi: short hairpin RNA (shRNA), endogenous microRNA (miRNA) and small interfering RNA (siRNA). Among them, siRNA is more suitable for drug use because it does not require genome integration and can be easily synthesized.

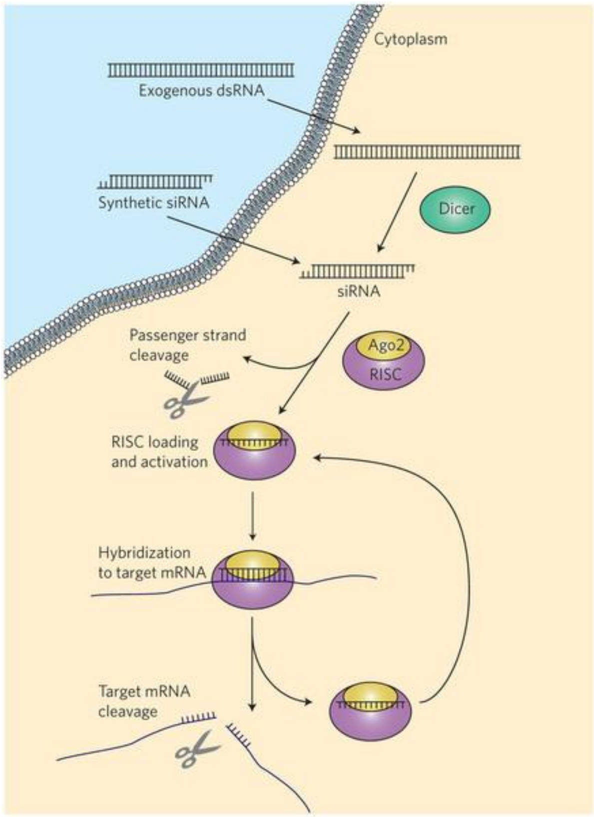

Figure 1.6: RNAi mechanism. Briefly, the long dsRNA is cleaved into siRNA in the cytoplasm by Dicer enzymes. The double-stranded siRNA molecules are then unwound into passenger and guide strands in the RISC-AGO2 complex. The activated RISC-siRNA complex seek out, bind and degrade complimentary mRNA molecules. The degradation of target mRNA molecules results in the suppression of target proteins.

1.9 Barriers to systemic siRNA delivery *in vivo*

The clinical use of siRNA-based drugs in cancer therapy is limited by the ability to efficiently deliver naked siRNA molecules to the cytoplasm of target cells. The siRNA molecules face several physiological barriers upon administration into the bloodstream, owing to their low stability, non-specific tissue penetration, and poor cellular uptake.

1.9.1 Serum nuclease instability

Naked siRNA molecules are extremely susceptible to serum nuclease degradation and can stimulate the innate immune system through the Toll-like receptor 7 (TLR7) pathway[39, 40, 41]. The reported half-life for unprotected siRNA in serum ranges from several minutes to 1 h[39]. A common strategy to address both these challenges entails the chemical modification of the siRNA backbone. The incorporation of 2'-*O*-methyl modifications into the sugar structure of selected nucleotides within both the sense and antisense strands has been shown to evade the immune response **(Figure 1.7).** 2'-*O*-methyl modifications have also been shown to confer resistance to endonuclease activity and to abrogate off-target effects when incorporated into the seed region, on the antisense strand. Other common modification approaches include the introduction of phosphorothioate backbone linkages at the 3'-end of the RNA strands to reduce susceptibility to exonucleases. It is also possible to incorporate alternative 2' sugar modifications (for example, a fluorine substitution) to increase resistance to endonucleases. However, an increase in siRNA stability did not necessarily translate into enhanced gene silencing activity in mice. In addition, the degradation of modified siRNA molecules may produce unsafe products in the body.

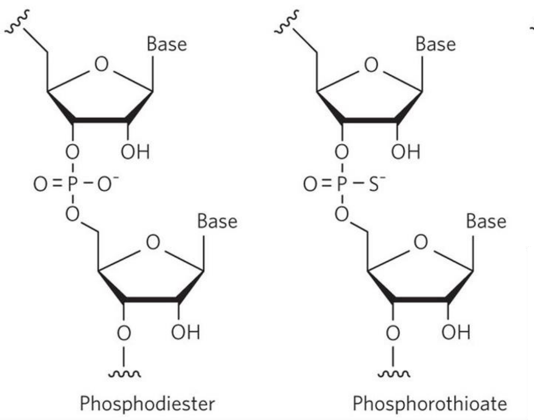

Figure 1.7: Chemical modifications of siRNA molecules

1.9.2 Non-specific tissue distribution

In addition to nuclease degradation and renal clearance – other major barriers to *in vivo* delivery of siRNA includes their non-specific uptake by the reticuloendothelial system (RES). The RES comprises of phagocytic cells, including circulating monocytes and tissue macrophages, the physiological function of which is to clear the system of foreign pathogens, cellular debris, and apoptotic cells[42]. Organs like the liver and spleen that are highly perfused and exhibit a fenestrated vasculature harbor an abundance of tissue macrophages. Therefore, these organs accumulate high concentrations of siRNA following systemic administration. siRNA uptake after standard i.v. tail vein injection or intraperitoneal (i.p.) injection has been noted in the liver, spleen, kidney and bone marrow at 4 h, but the overall signal was weak[43]. The non-specific tissue distribution results in a significantly reduced therapeutic effect at the target site.

1.9.3 Poor cellular uptake and internalization

The hydrophilicity and negative charge of naked siRNA molecules prevents them from readily crossing biological membrane into the cytoplasm of target cells and induce effective gene inhibition[44]. Previous studies showed that siRNAs can access the cytoplasm by hydrodynamic injection, where large amount of siRNA molecules were rapidly injected into the body that resulted in the transient damage of cell membranes in highly vascularized organs[32]. However, this method is highly dangerous and not applicable for human use. Thus far, there is no evidence showing the efficient internalization of siRNA molecules into cells after conventional IV injections.

1.10 Synthetic materials for siRNA delivery

In order to develop siRNA-based molecules for cancer therapy, we need to develop effective delivery systems that can overcome the *in vivo* barriers encountered by naked siRNA. Therefore, the delivery systems must be engineered to (i) provide serum stability, (ii) allow immune evasion, (iii) mitigate interactions with serum proteins and non-cancer cells, (iv) resist non-specific accumulation in the RES, (v) preferentially extravasate and accumulate at the target site, (vi) permit cell entry and endosomal escape to avail the RNAi machinery in the cytoplasm of the target cells[45], and (vii) have low toxicity[46]. The design rational for siRNA delivery systems stems from viral vectors that were previously used to deliver therapeutic payload into target cells. Viral vectors, such as retrovirus[47] and adenovirus[48], have displayed high efficiency in transferring nucleic acid into various mammalian cells. However, their safety profile, immunogenicity, and high cost limit their clinical application[49, 50]. This led to the need for non-viral delivery vehicles that can facilitate both uptake into the target tissue of interest and protect siRNA payloads and inhibit nonspecific delivery.

1.10.1 Lipid-based vectors

Prior to their use with siRNA, liposomes were used as delivery vectors for DNA-based drugs, owing to their ability to protect oligonucleotides from nuclease degradation and renal clearance, and to promote cellular uptake and endosomal escape[51]. Several lipid nanoparticles have emerged over time to effectively deliver siRNA drugs. Cationic lipids like *N*-[1-(2,3-dioleyloxy)propyl]-*N*,*N*,*N*-trimethlylammonium chloride (DOTMA) **(Figure 1.8)** to deliver both DNA and RNA into mouse, rat, and human cell lines are commonly used transfection reagents[52]. Cationic lipids have a cationic hydrophilic head group which is attached to a lipid hydrophobic moiety through a linker. The transfection mechanism of liposomes involves electrostatic interactions between negatively charged nucleic acids and positively charged lipids. When mixed together, they spontaneously form lipoplexes. Cationic lipids like dioleoyl-phosphatidylethanol-amine and 1,2-dioleoyl-3-trimethylammonium-propane (DOTAP) **(Figure 1.8)** have been shown to exhibit efficient delivery of siTNF-α and low toxicity profiles in mouse models – making them the most widely used lipid vectors[53]. Cationic lipoplexes composed of DOTAP and cholesterol have exhibited enhanced transfection efficiency and reduced degradation compared to conventional lipoplexes[54]. In addition, the use of liver-targeted DOTAP/cholesterol to deliver siRNA against hepatitis B virus (HBV) through i.v. administration proved to show specific accumulation in the liver and functional suppression in viral protein expression *in vivo*[54]. To improve the pharmacokinetic profile of cationic lipids - liposomes were coated with lipid-anchored PEG. But using PEG has been shown to have some limitations, as the steric and charge effect of the PEG molecule blocks the interaction between the liposome and the endosomal membrane and subsequent endosomal escape. Moreover, although liposomes are among the most popular nucleic acid delivery agents, some concerns regarding their safety for therapeutic use remain. Toxicity of certain cationic lipid particles has been reported both *in vitro* and *in vivo*[55], and certain synthetic agents have been found to induce a gene signature of their own that might increase the off-target effects of siRNA[56, 57]

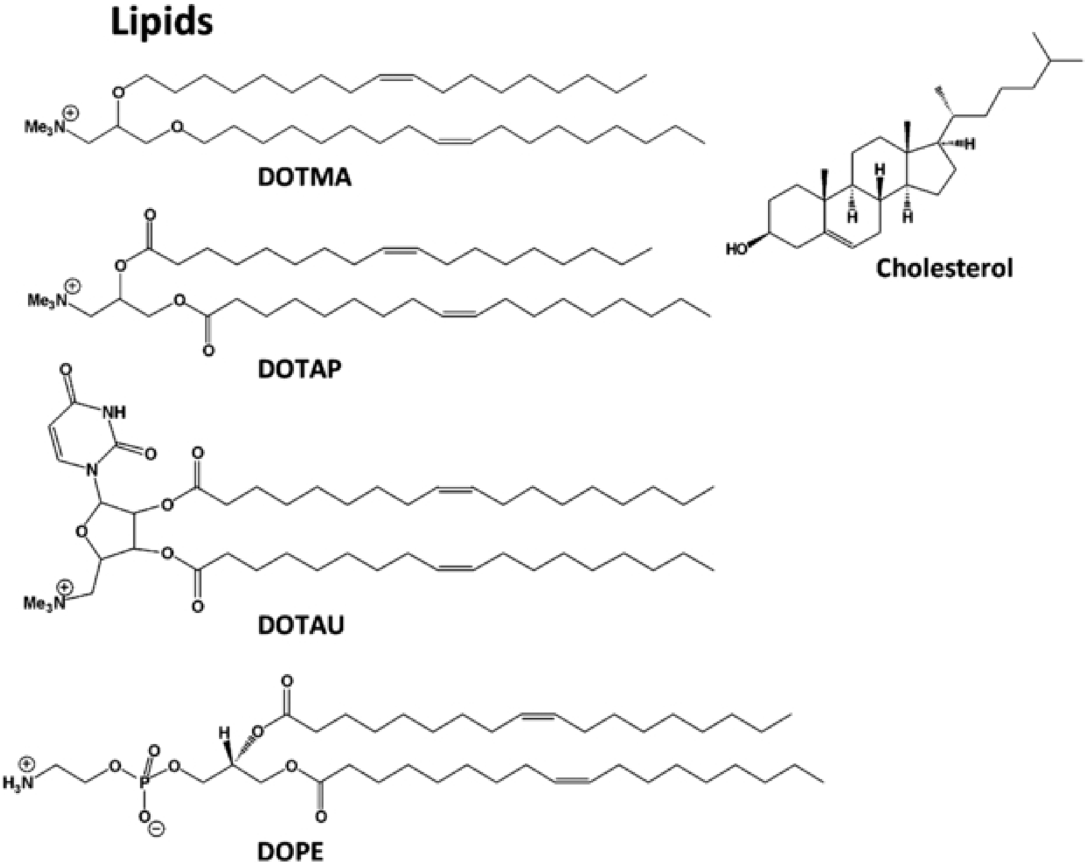

Figure 1.8: Chemical structure of common liposome reagents

1.10.2 Polymer-based vectors

Cationic linear and branched polymers make efficient transfection agents because of their ability to condense large nucleic acids into stabilized nanoparticles[58, 59]. The positively charged polymers, through electrostatic interactions, form polyplexes with the negatively charged phosphates of DNA, siRNA, and other oligonucleotides. These polyplexes have also shown to stimulate nonspecific endocytosis as well as endosomal escape[56]. The proposed escape mechanism is the 'proton-sponge' effect[58], whereby buffering of the endosome leads to an accumulation of ions within this compartment and an osmotic pressure that eventually bursts the endosome[60] .

PEI is a broadly investigated delivery carrier for the administration of a wide range of nucleotide-based therapies, including DNA, siRNA and oligonucleotides **(Figure 1.9)**[61, 62] . The intraperitoneal administration of complexed siRNA led to the delivery of the intact siRNA into the tumors and a marked reduction of tumor growth through siRNA-mediated downregulation of human epidermal growth factor 2 (HER2; also known as ERBB2)[63].There has been significant concern regarding the toxicity of PEI at higher molecular masses and high doses[64, 65-]. Poly (L-lysine) (PLL) **(Figure 1.9)** is a cationic biodegradable polymer that has been used as a non-viral gene delivery system for many years due to their excellent condensing ability with anionic agents[66, 67]. A variety of PLL derivatives have been synthesized to improve stability, decrease toxicity, and increase half-life *in vivo*[66, 67, 68]. For example, previous studies proved that grafting hydrophilic PEG molecules to PLL significantly increase the circulation time of the encapsulated siRNA molecules and the accumulation in tumor tissues[68]. However, PLL-based polyplexes were limited in their ability to escape the endosomal/lysosomal trafficking pathway[69] and subsequently release siRNA release into the cytoplasm of target cells, resulting in low transfection efficiency and deemed inadequate for clinical applications[70].

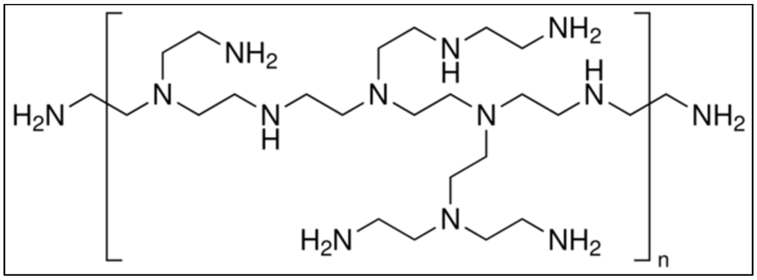

PEI

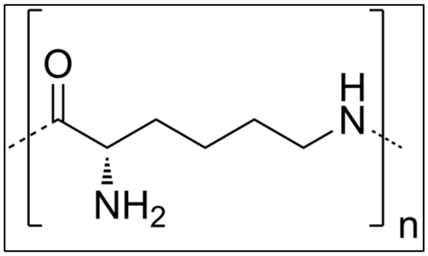

PLL

Figure 1.9: Chemical structure of commonly used cationic polymers

Polymer–siRNA conjugates have also shown potential for applications in systemic siRNA delivery. Specifically, a polymer-conjugated delivery system called Dynamic PolyConjugates (DPC) have demonstrated efficient delivery of siRNA to hepatocytes **(Figure 1.10)**[71]. Key features of the DPC technology include a membrane-active cationic polymer, the ability to reversibly mask the activity of this polymer until it reaches the acidic environment of the endosome, and the ability to target this modified polymer and its siRNA cargo specifically to hepatocytes after intravenous injection. DPCs were capable of inducing knockdown of two mouse liver genes. Analyses of serum liver enzyme and cytokine levels in treated mice indicated that siRNA complexes formed with this synthetic polymer were well tolerated[71].

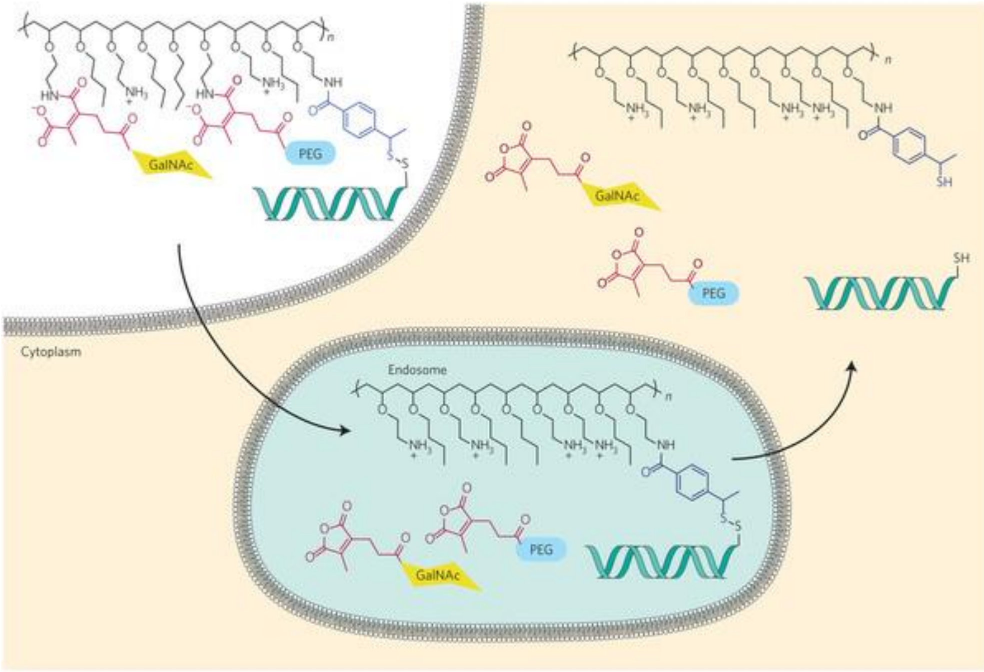

Figure 1.10: DPC materials are designed to respond to the acidic environment of the endosome and the reducing environment of the cytoplasm. In circulation, the membrane-disrupting PBAVE polymer (black) is shielded by PEG. After cell uptake, the PEG chains are shed as the pH of the endosome lowers, exposing the polymer and causing endosomal release. In the cytoplasm, the disulphide bond linking the siRNA to the polymer is reduced, freeing siRNA to trigger RNAi. GalNAc is included in the formulation as a targeting ligand to aid uptake by hepatocytes.

1.11 Challenges and proposed solutions for systemic administration

1.11.1 siRNA packaging

Among the numerous requirements to be addressed in the development of safe and effective siRNA delivery systems, the first criteria involves the stable packaging of siRNA molecules. The system should have the ability to (i) prevent charge repulsion between negatively charged siRNA duplexes and cell membrane, (ii) shield the siRNA molecules from serum and nuclease degradation, and (iii) condense the siRNA molecules into nano-sized particles and facilitate their internalization into target cells[72]. Due to the anionic nature of siRNA molecules, cationic lipids and polymers can easily complex siRNAs into stable particles through electrostatic interactions. These particles usually carry a positive surface charge, which allows them to be taken up by cells through absorptive endocytosis. This complexation also limits the access of nuclease enzymes to siRNA and prevents degradation[73].

1.11.2 Stability of siRNA carriers

Although the cationic surface charge of siRNA-based carriers improve cellular uptake, it suffers from poor pharmacokinetic properties when administered systemically. For instance, the positively charged particles can non-specifically interact with blood components to form large aggregates, which activate the complement system and eventually lead to rapid removal of particles from circulation through the RES system[70, 72, 74]. The incorporation of hydrophilic polymers like PEG in non-viral carriers have been shown to mask the cationic surface charge, reduce their non-specific binding with serum proteins, and therefore prolong their circulation time[75]. The modifications of carriers with PEG, however, affect their complexation with siRNA molecules, internalization into cells, and the transfection efficiency[76]. To improve the transfection efficiency of PEGylated nanoparticles, including rationally designed PEG length and density or incorporation of pH-sensitive bonds linkers between the PEG molecule and the carriers. Therefore, the molecular weight and density of PEG molecules incorporated into siRNA-based carrier systems must be carefully selected[77].

1.11.3 Diffusion across the endothelial barrier

The non-viral carriers encapsulating the desired dose of therapeutic siRNA molecules need to extravasate through the vascular endothelium to reach the target tissue. One of the unique features of tumor microvessels is their leakiness due to endothelial discontinuity. The pore size of tumor microvessels ranges from 100 to 780 nm in diameter. In comparison, microvessels in most normal tissues are less leaky; the tight junctions between endothelial cells are usually <2 nm and the pore size in post-capillary venules is <6 nm, whereas fenestrated endothelium of the renal glomeruli and the sinusoidal endothelium of the liver and spleen show larger pore sizes of 40–60 and 150 nm, respectively[78]. Due to vessel leakiness, the major pathway of drug transport across tumor microvascular wall is by extravasation *via* diffusion and/or convection through the discontinuous endothelial junctions, while transcytosis plays a relatively minor role. Using the leakiness of tumor vessels, siRNA carriers (up to 500nm in size) can accumulate in the interstitial tumor space via the enhanced retention and permeability (EPR) effect **(Figure 1.11)**[79,] . This unique feature of the tumor vasculature facilitates successful delivery of non-viral complexes to the tumor tissue without the incorporation of targeting ligands[79, 80].

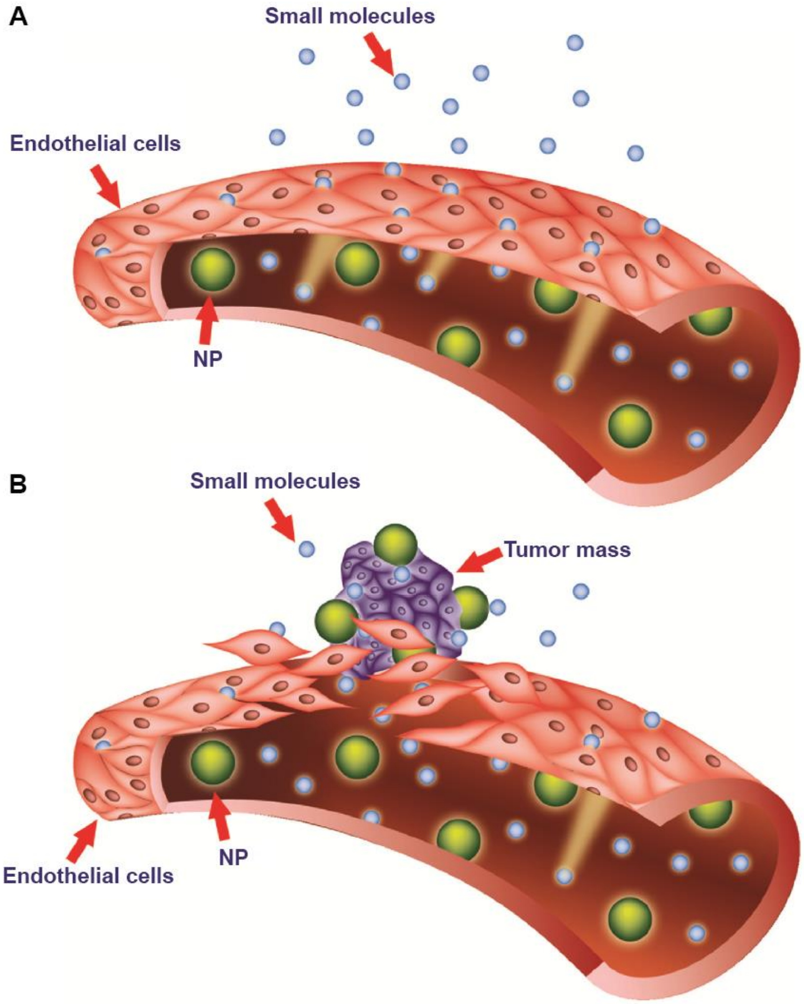

Figure 1.11: Schematic drawing showing the accumulation of nanoparticles (NP) by the EPR effect. Differences between normal **(A)** and tumor **(B)** vessels are depicted. The large fenestrations between the endothelial cells in the tumor vessels allows NP's to reach the matrix of the tumor cells by the EPR effect. Conversely, normal tissue contains tightly joined endothelial cells that prevents the diffusion of NP's outside the blood vessels.

1.11.4 Cellular entry

On reaching the interstitial space of the tumor tissue, the non-viral siRNA carriers must traverse the cellular membrane of the target cell. The cellular membrane is composed of a lipid bilayer with embedded proteins that is selectively permeable to ions and small hydrophobic molecules through passive diffusion[81]. However, for large, charged particles, such as lipoplexes and polyplexes, previous studies have shown that most of them pass the cell membrane through endocytic pathways, including clathrin-mediated endocytosis (absorptive or receptor mediated)[82], lipid-raft mediated endocytosis (calveolae mediated or not)[83], phagocytosis (occurs in specialized cells), and macropinocytosis[84, 85].

1.11.5 Non-specific uptake

The most common route of entry for cationic lipoplexes and polyplexes into cells is through non-specific absorptive endocytosis by the clathrin-coated pit mechanism. This is due to the electrostatic interaction between positively charged particles and the cellular membrane, containing negatively charged glycoprotein, proteoglycans, and glycerophosphates[86]. The uptake of these cationic molecules into cells can be enhanced by increasing their surface charge, which results in a higher affinity to the plasm membrane[87], but this strategy is not practical since it also increases particle-associated toxicity and renal clearance. Previous work by Rejman et. al. showed that DOTAP/DNA lipoplexes were taken up into cells only through clathrin-mediated endocytosis, while PEI/DNA polyplexes were internalized by both clathrin and caveolae-mediated endocytosis mechanisms[88]. However, the exact route of cationic particles to be taken up by cells varies largely between different cell types and vectors used. The contribution of each pathway in the cellular uptake of siRNA complexing nanoparticles is still poorly understood[89].

1.11.6 Targeted uptake

In order to selectively deliver therapeutic siRNA molecules to target cells, the non-viral siRNA carriers can be coated with targeted ligands and specific antibodies, which are recognized by specific cell surface receptors[90, 91]. For example, asialoglycoprotein receptors that specifically bind asialoglycoproteins is abundantly expressed in hepatocytes[92]. Incorporation of sugar moieties like asialoglycoprotein or galactose into the vector proved to effectively target liver cancer cells both *in vitro* and *in vivo*[93]. Transferrin and folic acid are commonly use targeting ligands – as they can be easily conjugated to the surface of non-viral vectors and the receptors that bind specifically to these ligands are overexpressed in tumor cells[94, 95]. The use of exogenous ligands has also been examined as a means of targeting distribution and improving efficacy *in vivo*. Exogenous ligands are generally attached to the distal end of PEG groups anchored to the delivery system.

1.11.7 Endo-lysosomal escape mechanism

After internalization into cells via endocytosis, the non-viral vectors are entrapped in the endosome, where the pH drops from physiological (7.4) to around 5-6 due to the ATPase proton pumps[96]. The endocytic vesicles sequentially fuse with early endosomes which mature into late endosomes before fusing with lysosomes **(Figure 1.12)**. The fate of the internalized molecules inside the vesicle depends on the specific type of receptors and includes the following: recycled to the cell surface, degraded inside lysosomes, or released to other intracellular compartments including the cytosol[97]. The endosomal entrapment and lysosomal degradation of siRNA–carrier contributes to the low transfection efficiency and is a major impediment for non-viral carriers. In order to escape from enzymatic degradation, the non-viral siRNA vectors should be able to release siRNA molecules to the cytoplasm at an early stage of the endo-lysosomal trafficking to preserve their therapeutic functions. Various approaches have been proposed to improve endosomal escape of non-viral siRNA based vectors based on two main hypotheses, “proton sponge” effect and membrane destabilizing effect. Detail mechanisms will be explained in Chapter 2.

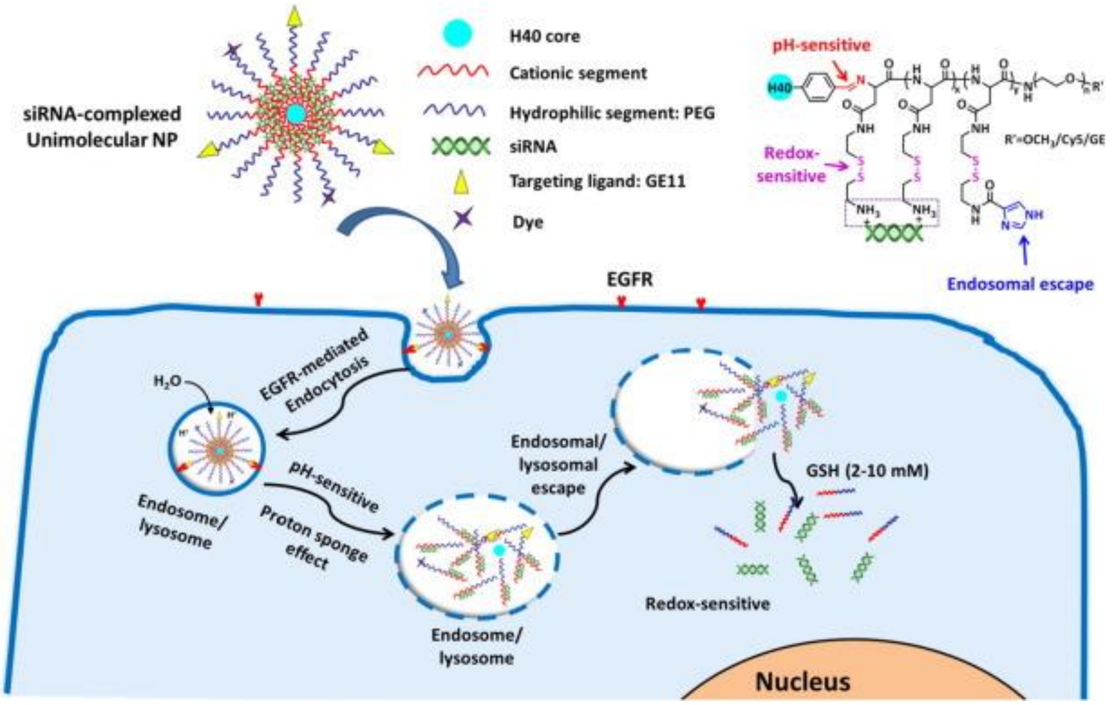

Figure 1.12: pH/redox dual-sensitive unimolecular NPs with excellent endosomal/lysosomal escape capabilities for efficient targeted delivery of siRNA. A schematic diagram of the cellular uptake of siRNA-complexed NPs and the subcellular release of siRNA into the cytosol.

1.11.8 Nucleic acid/vector dissociation

On escaping the endosomal compartment, the non-viral siRNA vectors need to rapidly decomplex siRNA molecules and release them into the cytoplasm. Poor decomplexation of the loaded DNA/RNA molecules have been reported to result in low transfection efficiency[98]. The disassembly of the nucleic acids from the vectors can be regulated by the use of carriers exhibiting lower cationic charge or the use of degradable vectors. For example, ester and hydrazone bonds are incorporated as linkers between cationic grafts and the polymer backbone – resulting in vector fragmentation and cargo dissociation upon hydrolysis of the linkers[99]. It is, therefore, important to develop a vector which forms stable, compact particles with siRNA molecules, but rapidly release the therapeutic cargo into the cytoplasm upon endosomal escape.

1.11.9 Effective RNA interference (RNAi)

Unlike plasmid DNA, which can be replicated or incorporated into the host chromosome, siRNA molecules elicit only a transient suppression in gene expression (i.e., 3 – 7 days in fast dividing cells, and up to a month in slow dividing cells) in proliferating cells[78]. The persistence of silencing in different cell types depends on factors such as proliferation rate and transcriptional activity[100]. In addition, siRNA-induced gene silencing usually only suppress target gene expression, but does not completely inhibit their translation. The RNAi mechanism is deemed effective when the target protein expression is suppressed under a specific threshold to induce the desired change in biological effect. And this requires the efficacious cytoplasmic delivery of the desired dose of therapeutic siRNA molecules as well as avoiding off-target effects.

References

1. Boyle P, Ferlay J. Cancer incidence and mortality in Europe, 2004. *Ann Oncol*. 2005;16(3):481-488. http://dx.doi.org/10.1093/annonc/mdi098.
2. Jemal A, Bray F, Center MM, Ferlay J, Ward E, Forman D. Global cancer statistics. *CA Cancer J Clin*. 2011;61(2):69-90. doi:10.3322/caac.20107.
3. Ferlay J, Héry C, Autier P, Sankaranarayanan R. Global burden of breast cancer. In: *Breast Cancer Epidemiology*. ; 2010:1-19. doi:10.1007/978-1-4419-0685-4_1.
4. National Cancer Institute SSB. Cancer Incidence – Surveillance, Epidemiology, and End Results (SEER) Registries Research Data. Surveillance, Epidemiology, and End Results (SEER) Program (http://www.seer.cancer.gov). http://seer.cancer.gov/data/metadata.html. Published 2007.
5. Egner JR. AJCC Cancer Staging Manual. *JAMA J Am Med Assoc*. 2010;304:1726. doi:10.1001/jama.2010.1525.
6. American Cancer Society. Breast Cancer Staging 7th Edition. *Am Jt Comm Cancer*. 2010:1-2. cancerstaging.org.
7. Zeichner SB, Terawaki H, Gogineni K. A review of systemic treatment in metastatic triple-negative breast cancer. *Breast Cancer Basic Clin Res*. 2016;10:25-36. doi:10.4137/BCBCr.s32783.
8. Slamon DJ, Leyland-Jones B, Shak S, et al. Use of chemotherapy plus a monoclonal antibody against HER2 for metastatic breast cancer that overexpresses HER2. *N Engl J Med*. 2001;344(11):783-792. doi:10.1056/NEJM200103153441101.
9. Genentech I. AVASTIN® (bevacizumab). *Cell*. 2009;44(0):1-25. doi:10.3174/ajnr.A1987.
10. Hunter KW, Crawford NPS, Alsarraj J. Mechanisms of metastasis. *Breast Cancer Res*. 2008;10(1):S2. doi:10.1186/bcr1988.
11. Bacac M, Stamenkovic I. Metastatic cancer cell. *Annu Rev Pathol*. 2008;3:221-247. doi:10.1146/annurev.pathmechdis.3.121806.151523.
12. Ridley AJ. Rho Proteins and Cancer. *Breast Cancer Res Treat*. 2004;84(1):13-19. doi:10.1023/B:BREA.0000018423.47497.c6.
13. Vega FM, Fruhwirth G, Ng T, Ridley AJ. RhoA and RhoC have distinct roles in migration and invasion by acting through different targets. *J Cell Biol*. 2011;193(4):655-665. doi:10.1083/jcb.201011038.
14. Etienne-Manneville S, Hall A. Rho GTPases in cell biology. *Nature*. 2002;420(6916):629-635. doi:10.1038/nature01148.
15. Sahai E, Marshall CJ. Rho–Gtpases and Cancer. *Nat Rev Cancer*. 2002;2(2):133-142. doi:10.1038/nrc725.
16. Clark E a, Golub TR, Lander ES, Hynes RO. Genomic Analysis of metastasis reveals an essential role for RhoC. *Nature*. 2000;406(6793):277-279. doi:10.1038/35018520.
17. Van den Eynden GG, Van der Auwera I, Van Laere S, et al. Validation of a tissue microarray to study differential protein expression in inflammatory and non-inflammatory breast cancer. *Breast Cancer Res Treat*. 2004;85(1):13-22. doi:10.1023/B:BREA.0000021028.33926.a8.
18. Fritz G, Just I, Kaina B. Rho GTPases are over-expressed in human tumors. *Int J Cancer*. 1999;81(5):682-687. doi:10.1002/(SICI)1097-0215(19990531)81:5<682::AID-IJC2>3.0.CO;2-B.
19. van Golen KL, Wu ZF, Qiao XT, Bao LW, Merajver SD. RhoC GTPase, a novel

transforming oncogene for human mammary epithelial cells that partially recapitulates the inflammatory breast cancer phenotype. *Cancer Res*. 2000;60(20):5832-5838.

20. Raftopoulou M, Hall A. Cell migration: Rho GTPases lead the way. *Dev Biol*. 2004;265(1):23-32. doi:10.1016/j.ydbio.2003.06.003.
21. Wu M, Wu Z-F, Rosenthal DT, Rhee EM, Merajver SD. Characterization of the roles of RHOC and RHOA GTPases in invasion, motility, and matrix adhesion in inflammatory and aggressive breast cancers. *Cancer*. 2010;116(11 Suppl):2768-2782. doi:10.1002/cncr.25181.
22. Rosenthal DT, Zhang J, Bao L, et al. RhoC Impacts the Metastatic Potential and Abundance of Breast Cancer Stem Cells. *PLoS One*. 2012;7(7):e40979. doi:10.1371/journal.pone.0040979.
23. Li DQ, Hou YF, Wu J, et al. Gene expression profile analysis of an isogenic tumour metastasis model reveals a functional role for oncogene AF1Q in breast cancer metastasis. *Eur J Cancer*. 2006;42(18):3274-3286. doi:10.1016/j.ejca.2006.07.008.
24. Van Golen KL, Wu ZF, Xiao Tan Qiao, Li Wei Bao, Merajver SD. RhoC GTPase, a novel transforming oncogene for human mammary epithelial cells that partially recapitulates the inflammatory breast cancer phenotype. *Cancer Res*. 2000;60(20):5832-5838.
25. Pillé JY, Denoyelle C, Varet J, et al. Anti-RhoA and Anti-RhoC siRNAs inhibit the proliferation and invasiveness of MDA-MB-231 breast cancer cells in vitro and in vivo. *Mol Ther*. 2005;11(2):267-274. doi:10.1016/j.ymthe.2004.08.029.
26. Morrissey D V, Lockridge JA, Shaw L, et al. Potent and persistent in vivo anti-HBV activity of chemically modified siRNAs. *Nat Biotech*. 2005;23(8):1002-1007. http://dx.doi.org/10.1038/nbt1122.
27. Okumura A, Pitha PM, Harty RN. ISG15 inhibits Ebola VP40 VLP budding in an L-domain-dependent manner by blocking Nedd4 ligase activity. *Proc Natl Acad Sci* . 2008;105(10):3974-3979. doi:10.1073/pnas.0710629105.
28. Shen H, Sun T, Ferrari M. Nanovector delivery of siRNA for cancer therapy. *Cancer Gene Ther*. 2012;19(6):367-373. http://dx.doi.org/10.1038/cgt.2012.22.
29. Davis ME, Zuckerman JE, Choi CHJ, et al. Evidence of RNAi in humans from systemically administered siRNA via targeted nanoparticles. *Nature*. 2010;464(7291):1067-1070. http://dx.doi.org/10.1038/nature08956.
30. Fire A, Xu S, Montgomery MK, Kostas SA, Driver SE, Mello CC. Potent and specific genetic interference by double-stranded RNA in Caenorhabditis elegans. *Nature*. 1998;391(6669):806-811. http://dx.doi.org/10.1038/35888.
31. Elbashir SM, Harborth J, Lendeckel W, Yalcin A, Weber K, Tuschl T. Duplexes of 21-nucleotide RNAs mediate RNA interference in cultured mammalian cells. *Nature*. 2001;411(6836):494-498. http://dx.doi.org/10.1038/35078107.
32. McCaffrey AP, Meuse L, Pham T-TT, Conklin DS, Hannon GJ, Kay MA. Gene expression: RNA interference in adult mice. *Nature*. 2002;418(6893):38-39. http://dx.doi.org/10.1038/418038a.
33. Bernstein E, Caudy AA, Hammond SM, Hannon GJ. Role for a bidentate ribonuclease in the initiation step of RNA interference . *Nature*. 2001;409(6818):363-366. http://dx.doi.org/10.1038/35053110.
34. Rand TA, Ginalski K, Grishin N V, Wang X. Biochemical identification of Argonaute 2 as the sole protein required for RNA-induced silencing complex activity. *Proc Natl Acad Sci United States Am* . 2004;101(40):14385-14389. doi:10.1073/pnas.0405913101.

35. Matranga C, Tomari Y, Shin C, Bartel DP, Zamore PD. Passenger-Strand Cleavage Facilitates Assembly of siRNA into Ago2-Containing RNAi Enzyme Complexes. *Cell*. 2005;123(4):607-620. doi:http://dx.doi.org/10.1016/j.cell.2005.08.044.
36. Ameres SL, Martinez J, Schroeder R. Molecular Basis for Target RNA Recognition and Cleavage by Human RISC. *Cell*. 2007;130(1):101-112. doi:http://dx.doi.org/10.1016/j.cell.2007.04.037.
37. Hutvágner G, Zamore PD. A microRNA in a Multiple-Turnover RNAi Enzyme Complex. *Science (80-)*. 2002;297(5589):2056 LP-2060. http://science.sciencemag.org/content/297/5589/2056.abstract.
38. Bartlett DW, Davis ME. Insights into the kinetics of siRNA-mediated gene silencing from live-cell and live-animal bioluminescent imaging. *Nucleic Acids Res*. 2006;34(1):322-333. doi:10.1093/nar/gkj439.
39. LAYZER JM, MCCAFFREY AP, TANNER AK, HUANG ZAN, KAY MA, SULLENGER BA. In vivo activity of nuclease-resistant siRNAs. *RNA*. 2004;10(5):766-771. doi:10.1261/rna.5239604.
40. Jackson AL, Linsley PS. Recognizing and avoiding siRNA off-target effects for target identification and therapeutic application. *Nat Rev Drug Discov*. 2010;9(1):57-67. http://dx.doi.org/10.1038/nrd3010.
41. Nguyen DN, Mahon KP, Chikh G, et al. Lipid-derived nanoparticles for immunostimulatory RNA adjuvant delivery. *Proc Natl Acad Sci* . 2012;109(14):E797-E803. doi:10.1073/pnas.1121423109.
42. Mosser DM, Edwards JP. Exploring the full spectrum of macrophage activation. *Nat Rev Immunol*. 2008;8(12):958-969. http://dx.doi.org/10.1038/nri2448.
43. Larson SD, Jackson LN, Chen LA, Rychahou PG, Evers BM. Effectiveness of siRNA uptake in target tissues by various delivery methods. *Surgery*. 2007;142(2):262-269. doi:http://dx.doi.org/10.1016/j.surg.2007.03.011.
44. Aagaard L, Rossi JJ. RNAi therapeutics: Principles, prospects and challenges. *Adv Drug Deliv Rev*. 2007;59(2–3):75-86. doi:http://dx.doi.org/10.1016/j.addr.2007.03.005.
45. Alexis F, Pridgen E, Molnar LK, Farokhzad OC. Factors affecting the clearance and biodistribution of polymeric nanoparticles. In: *Molecular Pharmaceutics*. Vol 5. ; 2008:505-515. doi:10.1021/mp800051m.
46. Xu C, Wang J. Delivery systems for siRNA drug development in cancer therapy. *Asian J Pharm Sci*. 2015;10(1):1-12. doi:http://dx.doi.org/10.1016/j.ajps.2014.08.011.
47. Barton GM, Medzhitov R. Retroviral delivery of small interfering RNA into primary cells. *Proc Natl Acad Sci*. 2002;99(23):14943-14945. doi:10.1073/pnas.242594499.
48. Shen C, Buck AK, Liu X, Winkler M, Reske SN. Gene silencing by adenovirus-delivered siRNA. In: *FEBS Letters*. Vol 539. ; 2003:111-114. doi:10.1016/S0014-5793(03)00209-6.
49. Favre D, Provost N, Blouin V, et al. Immediate and long-term safety of recombinant adeno-associated virus injection into the nonhuman primate muscle. *Mol Ther*. 2001;4(6):559-566. doi:10.1006/mthe.2001.0494.
50. Kay MA, Glorioso JC, Naldini L. Viral vectors for gene therapy: the art of turning infectious agents into vehicles of therapeutics. *Nat Med*. 2001;7(1):33-40. doi:10.1038/83324.
51. Xu Y, Szoka FC. Mechanism of DNA Release from Cationic Liposome/DNA Complexes Used in Cell Transfection,. *Biochemistry*. 1996;35(18):5616-5623. doi:10.1021/bi9602019.

52. Felgner PL, Gadek TR, Holm M, et al. Lipofection: a highly efficient, lipid-mediated DNA-transfection procedure. *Proc Natl Acad Sci U S A*. 1987;84(21):7413-7417. doi:10.1073/pnas.84.21.7413.
53. Wu SY, McMillan NAJ. Lipidic systems for in vivo siRNA delivery. *AAPS J*. 2009;11(4):639-652. doi:10.1208/s12248-009-9140-1.
54. Torrecilla J, Rodríguez-Gascón A, Solinís MÁ, Del Pozo-Rodríguez A. Lipid nanoparticles as carriers for RNAi against viral infections: Current status and future perspectives. *Biomed Res Int*. 2014;2014. doi:10.1155/2014/161794.
55. Lv H, Zhang S, Wang B, Cui S, Yan J. Toxicity of cationic lipids and cationic polymers in gene delivery. *J Control Release*. 2006;114(1):100-109. doi:http://dx.doi.org/10.1016/j.jconrel.2006.04.014.
56. Akhtar S, Benter IF. Nonviral delivery of synthetic siRNAs in vivo. *J Clin Invest*. 2007;117(12):3623-3632. doi:10.1172/JCI33494.
57. Hollins AJ, Omidi Y, Benter IF, Akhtar S. Toxicogenomics of drug delivery systems: Exploiting delivery system-induced changes in target gene expression to enhance siRNA activity. *J Drug Target*. 2007;15(1):83-88. doi:10.1080/10611860601151860.
58. Boussif O, Lezoualc'h F, Zanta MA, et al. A versatile vector for gene and oligonucleotide transfer into cells in culture and in vivo: polyethylenimine. *Proc Natl Acad Sci U S A*. 1995;92(16):7297-7301. http://www.ncbi.nlm.nih.gov/pmc/articles/PMC41326/.
59. Putnam D. Polymers for gene delivery across length scales. *Nat Mater*. 2006;5(6):439-451. http://dx.doi.org/10.1038/nmat1645.
60. Akinc A, Thomas M, Klibanov AM, Langer R. Exploring polyethylenimine-mediated DNA transfection and the proton sponge hypothesis. *J Gene Med*. 2005;7(5):657-663. doi:10.1002/jgm.696.
61. Lungwitz U, Breunig M, Blunk T, Göpferich A. Polyethylenimine-based non-viral gene delivery systems. In: *European Journal of Pharmaceutics and Biopharmaceutics*. Vol 60. ; 2005:247-266. doi:10.1016/j.ejpb.2004.11.011.
62. Zintchenko A, Philipp A, Dehshahri A, Wagner E. Simple Modifications of Branched PEI Lead to Highly Efficient siRNA Carriers with Low Toxicity. *Bioconjug Chem*. 2008;19(7):1448-1455. doi:10.1021/bc800065f.
63. Urban-Klein B, Werth S, Abuharbeid S, Czubayko F, Aigner A. RNAi-mediated gene-targeting through systemic application of polyethylenimine (PEI)-complexed siRNA in vivo. *Gene Ther*. 2004;12(5):461-466. http://dx.doi.org/10.1038/sj.gt.3302425.
64. Kichler A. Gene transfer with modified polyethylenimines. *J Gene Med*. 2004;6(SUPPL. 1). doi:10.1002/jgm.507.
65. Kircheis R, Wightman L, Wagner E. Design and gene delivery activity of modified polyethylenimines. *Adv Drug Deliv Rev*. 2001;53(3):341-358. doi:http://dx.doi.org/10.1016/S0169-409X(01)00202-2.
66. Inoue Y, Kurihara R, Tsuchida A, et al. Efficient delivery of siRNA using dendritic poly(l-lysine) for loss-of-function analysis. *J Control Release*. 2008;126(1):59-66. doi:10.1016/j.jconrel.2007.10.022.
67. Watanabe K, Harada-Shiba M, Suzuki A, et al. In vivo siRNA delivery with dendritic poly(L-lysine) for the treatment of hypercholesterolemia. *Mol Biosyst*. 2009;5:1306-1310. doi:10.1039/b900880b.
68. Kano A, Moriyama K, Yamano T, Nakamura I, Shimada N, Maruyama A. Grafting of poly(ethylene glycol) to poly-lysine augments its lifetime in blood circulation and

accumulation in tumors without loss of the ability to associate with siRNA. *J Control Release*. 2011;149(1):2-7. doi:10.1016/j.jconrel.2009.12.007.

69. Akinc A, Langer R. Measuring the pH environment of DNA delivered using nonviral vectors: Implications for lysosomal trafficking. *Biotechnol Bioeng*. 2002;78(5):503-508. doi:10.1002/bit.20215.
70. Guo J, Bourre L, Soden DM, O'Sullivan GC, O'Driscoll C. Can non-viral technologies knockdown the barriers to siRNA delivery and achieve the next generation of cancer therapeutics? *Biotechnol Adv*. 2011;29(4):402-417. doi:10.1016/j.biotechadv.2011.03.003.
71. Rozema DB, Lewis DL, Wakefield DH, et al. Dynamic PolyConjugates for targeted in vivo delivery of siRNA to hepatocytes. *Proc Natl Acad Sci U S A*. 2007;104(32):12982-12987. doi:0703778104 [pii]\r10.1073/pnas.0703778104 [doi].
72. Wong SY, Pelet JM, Putnam D. Polymer systems for gene delivery—Past, present, and future. *Prog Polym Sci*. 2007;32(8–9):799-837. doi:http://dx.doi.org/10.1016/j.progpolymsci.2007.05.007.
73. Mintzer MA, Simanek EE. Nonviral vectors for gene delivery. *Chem Rev*. 2009;109(2):259-302. doi:10.1021/cr800409e.
74. Merdan T, Kopeček J, Kissel T. Prospects for cationic polymers in gene and oligonucleotide therapy against cancer. *Adv Drug Deliv Rev*. 2002;54(5):715-758. doi:10.1016/S0169-409X(02)00046-7.
75. Klibanov AL, Maruyama K, Torchilin VP, Huang L. Amphipathic polyethyleneglycols effectively prolong the circulation time of liposomes. *FEBS Lett*. 1990;268(1):235-237. doi:10.1016/0014-5793(90)81016-H.
76. Erbacher P, Bettinger T, Belguise-Valladier P, et al. Transfection and physical properties of various saccharide, poly(ethylene glycol), and antibody-derivatized polyethylenimines (PEI). *J Gene Med*. 1999;1(3):210-222. doi:10.1002/(SICI)1521-2254(199905/06)1:3<210::AID-JGM30>3.0.CO;2-U.
77. Petersen H, Fechner PM, Martin AL, et al. Polyethylenimine-graft-poly(ethylene glycol) copolymers: Influence of copolymer block structure on DNA complexation and biological activities as gene delivery system. *Bioconjug Chem*. 2002;13(4):845-854. doi:10.1021/bc025529v.
78. Wang J, Lu Z, Wientjes MG, Au JL-S. Delivery of siRNA therapeutics: barriers and carriers. *AAPS J*. 2010;12(4):492-503. doi:10.1208/s12248-010-9210-4.
79. Jang SH, Wientjes MG, Lu D, Au JLS. Drug delivery and transport to solid tumors. *Pharm Res*. 2003;20(9):1337-1350. doi:10.1023/A:1025785505977.
80. Jain RK, Stylianopoulos T. Delivering nanomedicine to solid tumors. *Nat Rev Clin Oncol*. 2010;7(11):653-664. doi:10.1038/nrclinonc.2010.139.
81. Conner SD, Schmid SL. Regulated portals of entry into the cell. *Nature*. 2003;422(6927):37-44. doi:10.1038/nature01451.
82. Harush-Frenkel O, Debotton N, Benita S, Altschuler Y. Targeting of nanoparticles to the clathrin-mediated endocytic pathway. *Biochem Biophys Res Commun*. 2007;353(1):26-32. doi:10.1016/j.bbrc.2006.11.135.
83. Beddoes CM, Case CP, Briscoe WH. Understanding nanoparticle cellular entry: A physicochemical perspective. *Adv Colloid Interface Sci*. 2015;218:48-68. doi:10.1016/j.cis.2015.01.007.
84. Zhang J, Zhang X, Liu G, et al. Intracellular trafficking network of protein nanocapsules: Endocytosis, exocytosis and autophagy. *Theranostics*. 2016;6(12):2099-2113.

doi:10.7150/thno.16587.

85. Mercer J, Helenius A. Virus entry by macropinocytosis. *Nat Cell Biol*. 2009;11(5):510-520. doi:10.1038/ncb0509-510.

86. Mislick K a, Baldeschwieler JD. Evidence for the role of proteoglycans in cation-mediated gene transfer. *Proc Natl Acad Sci U S A*. 1996;93(22):12349-12354. doi:10.1073/pnas.93.22.12349.

87. Blau S, Jubeh TT, Haupt SM, Rubinstein A. Drug targeting by surface cationization. *Crit Rev Ther Drug Carrier Syst*. 2000;17(5):425-465. doi:10.1615/CritRevTherDrugCarrierSyst.v17.i5.10.

88. Rejman J, Bragonzi A, Conese M. Role of clathrin- and caveolae-mediated endocytosis in gene transfer mediated by lipo- and polyplexes. *Mol Ther*. 2005;12(3):468-474. doi:10.1016/j.ymthe.2005.03.038.

89. Ruponen M, Honkakoski P, Tammi M, Urtti A. Cell-surface glycosaminoglycans inhibit cation-mediated gene transfer. *J Gene Med*. 2004;6(4):405-414. doi:10.1002/jgm.522.

90. Kudgus RA, Walden CA, McGovern RM, Reid JM, Robertson JD, Mukherjee P. Tuning Pharmacokinetics and Biodistribution of a Targeted Drug Delivery System Through Incorporation of a Passive Targeting Component. *Sci Rep*. 2014;4:5669. http://dx.doi.org/10.1038/srep05669.

91. Friedman AD, Claypool SE, Liu R. The Smart Targeting of Nanoparticles. *Curr Pharm Des*. 2013;19(35):6315-6329. http://www.ncbi.nlm.nih.gov/pmc/articles/PMC4016770/.

92. Perales JC, Grossmann GA, Molas M, et al. Biochemical and functional characterization of DNA complexes capable of targeting genes to hepatocytes via the asialoglycoprotein receptor. *J Biol Chem*. 1997;272(11):7398-7407. doi:10.1074/jbc.272.11.7398.

93. Hashida M, Takemura S, Nishikawa M, Takakura Y. Targeted delivery of plasmid DNA complexed with galactosylated poly(L- lysine). In: *Journal of Controlled Release*. Vol 53. ; 1998:301-310. doi:10.1016/S0168-3659(97)00263-0.

94. Huwyler J, Drewe J, Krähenbühl S. Tumor targeting using liposomal antineoplastic drugs. *Int J Nanomedicine*. 2008;3(1):21-29. http://www.ncbi.nlm.nih.gov/pmc/articles/PMC2526358/.

95. Kakudo T, Chaki S, Futaki S, et al. Transferrin-Modified Liposomes Equipped with a pH-Sensitive Fusogenic Peptide: An Artificial Viral-like Delivery System. *Biochemistry*. 2004;43(19):5618-5628. doi:10.1021/bi035802w.

96. Pathak A, Patnaik S, Gupta KC. Recent trends in non-viral vector-mediated gene delivery. *Biotechnol J*. 2009;4(11):1559-1572. doi:10.1002/biot.200900161.

97. Kirkham M, Parton RG. Clathrin-independent endocytosis: New insights into caveolae and non-caveolar lipid raft carriers. *Biochim Biophys Acta - Mol Cell Res*. 2005;1745(3):273-286. doi:10.1016/j.bbamcr.2005.06.002.

98. Gabrielson NP, Pack DW. Acetylation of polyethylenimine enhances gene delivery via weakened polymer/DNA interactions. *Biomacromolecules*. 2006;7(8):2427-2435. doi:10.1021/bm060300u.

99. Veron L, Ganée A, Ladavière C, Delair T. Hydrolyzable p(DMAPEMA) polymers for gene delivery. *Macromol Biosci*. 2006;6(7):540-554. doi:10.1002/mabi.200600071.

100. Dykxhoorn DM, Lieberman J. Knocking down Disease with siRNAs. *Cell*. 2006;126(2):231-235. doi:10.1016/j.cell.2006.07.007.

Chapter 2

Background

2.1 Rational and Design of EPPT1-Peptide Targeted, pH-Sensitive, Membrane-Destabilizing Nanoparticles for Selective and Enhanced Functional Delivery of siRNA into the Cytoplasm of Aggressive Breast Cancer Cells

2.1.1 "The inability of siRNA-based NP's to escape the endosomal/lysosomal trafficking pathway could result in poor transfection efficiency"

Endosomal entrapment is one of the major barriers, which limits the practical application of siRNA-based cancer therapy. In order to achieve effective gene silencing, several strategies have been developed to enhance the escape of nucleic acids from the endosomal/lysosomal trafficking pathway. Two mechanisms, namely "proton sponge" and membrane-destabilizing effect, have been extensively investigated to identify non-viral vector compositions that can escape the endosomal compartment[1].

2.1.1.1 Mechanism of endosomal escape

2.1.1.1.1 “Proton sponge” effect

The “proton sponge” effect was discovered in certain cationic polymers that comprise of a large number of ionizable groups (i.e, secondary and tertiary amine groups) with pKa values close to the endosomal/lysosomal pH (i.e., pH ranging from 5 to 7)[2]. Ionizable groups possess a charge that is dependent on the pH of the surrounding environment. In the endosome, these ionizable groups (i.e., pKa values between 5.4 and 7.6) present in siRNA-based polymers become protonated. In response to the protonation of amine groups, the ATPase proton pumps on the endosomal membrane facilitates an influx of protons from the cytosol into the endosome to maintain the acidic milieu. The influx of protons is accompanied by the inward movement of chloride counter ions and water molecules. The resultant endosmosis causes osmotic swelling and ultimately rupture of the endosomal membrane **(Figure 2.1)**[1, 2, 3, 4].

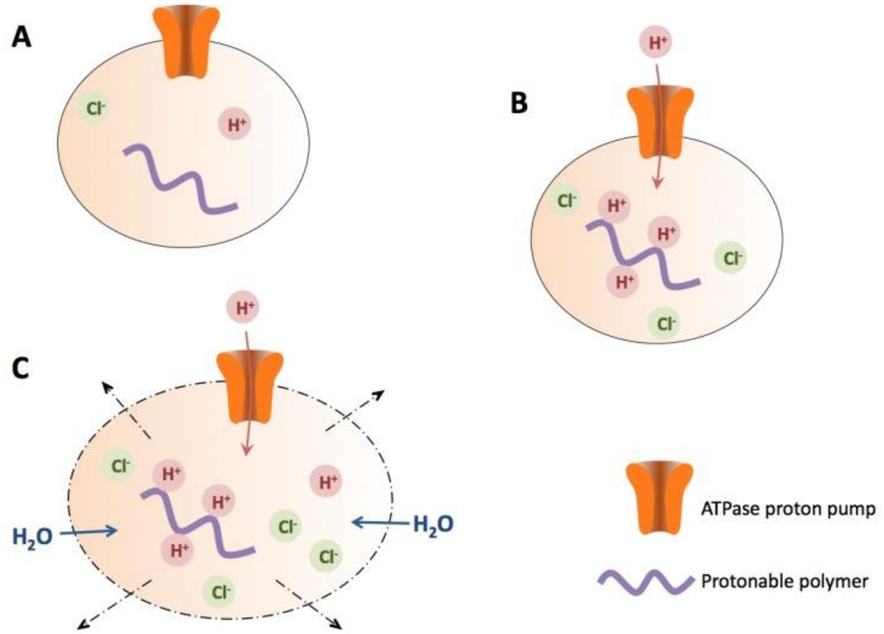

Figure 2.1: The ‘proton sponge’ hypotheses. (A) Polyplexes enter cell via endocytosis and are trapped in endosomes. (B) The membrane bound ATPase proton pumps actively translocate protons into endosomes. Polymers become protonated and resist the acidification of endosomes. More protons will be pumped into the endosomes continuously to lower the pH. (C) The proton pumping action is followed by passive chloride ions entry, increasing ionic concentration and hence water influx. High osmotic pressure causes the swelling and rupture of endosomes, releasing their contents to cytosol.

2.1.1.1.2 “Proton sponge” effect-based carriers

2.1.1.1.2.1 Polyethylenimine (PEI)

PEI is the most well-known cationic polymer which has been proved to be highly effective in gene delivery both *in vitro* and *in vivo*[3]. This can be attributed to the strong buffering capacity of PEI comprising of a high density of protonable amine groups resulting in rapid endosomal escape[5]. PEI vectors have been synthesized to exhibit different molecular weights and structural configurations (e.g., linear and branched) to be used as transfection agents[6] **(Figure 2.2)**. The clinical application of PEI is limited by its substantial toxicity. Earlier research showed that both the transfection efficiency and cytotoxicity of PEI-based vectors increase with increasing molecular weight (600 Da – 700 kDa)[7]. The observed toxicity is due to the aggregation of PEI complexes on the cell membrane resulting in significant necrosis[8]. In addition, higher-branched PEI showed stronger complexation with nucleic acids and better transfection efficiency than the lower branched polymers[9]. However, the resultant toxicity profile also increased with the degree of branching. Modified versions of PEI, such as low molecular weight PEI (LMW-PEI)[10] and low branching degree PEI, have been investigated to reduce the toxicity of the polymers without compromising their pH buffering capacity. In addition, the synthesis of various degradable PEI derivatives have resulted in lower toxicity profiles. For example, low MW PEI (2 kDa) cross-linked with reducible disulfide linkage and conjugated to hyaluronic acid (HA) to form (PEI-SS)-b-HA block copolymers encapsulated anti-vascular endothelial growth factor (VEGF) siRNA into serum-stable particles with negligible toxicity. These particles proved to efficiently suppress VEGF expression both *in vitro* and *in vivo,* as well as successfully suppress tumor growth following intratumoral injections[11]. The incorporation of negatively-charged succinic acid groups to the branched PEI (25 kDa) backbone also resulted in effective siRNA carriers with low toxicity[12]. Furthermore, the addition of PEG comprising Arg-Gly-Asp (RGD) peptide ligands to branched PEI (25 kDa) resulted in tumor-specific targeting and prolonged circulation *in vivo*[13].

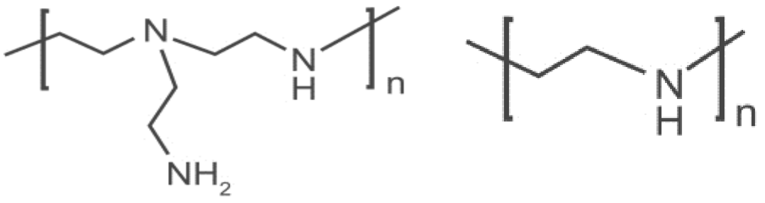

Figure 2.2: Chemical structure of branched and linear PEI

2.1.1.1.2.2 Poly (amidoamine) PAMAM dendrimers

PAMAM dendrimers are a family of water-soluble polymers that is characterized by a unique tree-like branching architecture with a large number of primary, secondary, and tertiary amine groups **(Figure 2.3)**[14, 15]. The high density of protonable amine groups enables rapid endosomal escape of PAMAM-based dendriplexes due to the "proton sponge" mechanism[16], but also leads to non-specific cytotoxicity. The toxicity of PAMAM dendrimers can be reduced by conjugation of hydrophilic polymers[17, 18] or by partial neutralization of the cationic amine groups[19]. However, their gene silencing capacity was also reduced due to the poor pH buffering capacity and subsequent endosomal escape[19]. The biocompatibility of dendrimers is related to their structure, molecular size, and surface charge[20]. Cytotoxicity and immunogenicity of dendrimers are related to its surface charge. Cationic polyamidoamine (PAMAM, amino-terminated surface) is more cytotoxic than anionic PAMAM (carboxylate-terminated surface) in Caco-2 cells. Similar to other nano-sized carriers, pegylation has been applied to improve the surface features of dendrimers[21].

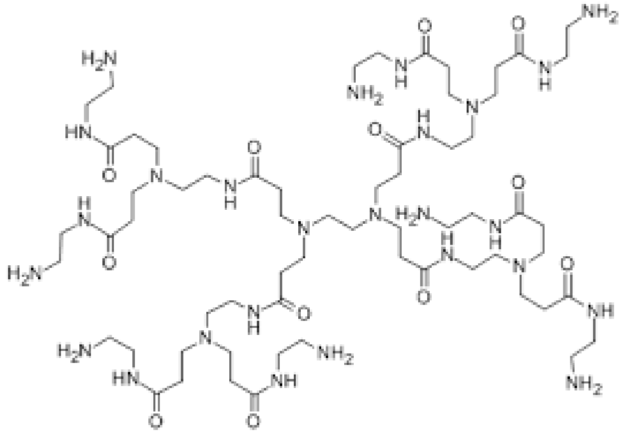

Figure 2.3: Chemical structure of PAMAM dendrimers (generation 1)

2.1.1.1.3 Membrane destabilization effect

Several viruses such as the influenza virus have evolved pH-responsive fusogenic proteins, hemagglutinin, that is responsible for the virus binding to the cell that is being infected. Hemagglutinin (HA) binds to monosaccharide sialic acid which is present on the surface of its target host cells **(Figure 2.4)**[22]. The cell membrane then engulfs the virus through endocytosis and forms endosome. When the pH within the endosome drops to 6.0, the HA molecule partially unfolds, releasing a very hydrophobic portion of its peptide chain that was previously hidden within the protein. This so-called "fusion peptide" acts like a molecular grappling hook by inserting itself into the endosomal membrane and locking on. Then, the rest of the HA molecule refolds into a new structure and pulls the endosomal membrane right up next to the virus particle's own membrane, causing the two to fuse together **(Figure 2.4)**[22]**.** Once this has happened, the viral RNA genome enters into the cell's cytoplasm. Several synthetic analogs of the pH responsive, membrane-destabilizing HA peptides have been developed to enhance cytoplasmic gene delivery. However, the clinical application of synthetic fusogenic peptides are limited by their potential immunogenicity, low stability, and high synthetic cost[22].

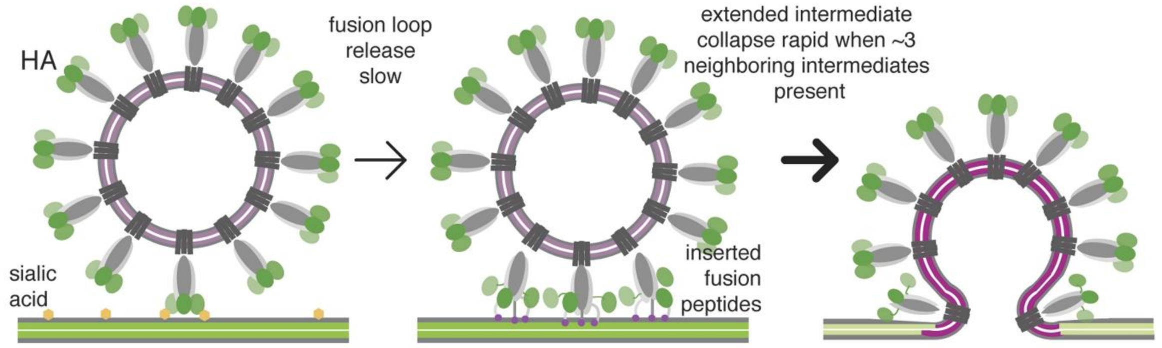

Figure 2.4: Model of the sequence of events in influenza hemagglutin-mediated fusion. A representative schematic cross-section is shown (an actual contact zone will include 100 or more trimers). Stochastic release of a sufficient minimum number of fusion peptides is rate limiting.

2.1.1.1.4 Amphiphilic membrane destabilizing carriers

To mimic the membrane-disruptive properties of viral fusogenic peptides, a family of pH-sensitive poly (alkylacrylic acid) polymers **(Figure 2.5)** has been synthesized to enhance the cytoplasmic delivery of therapeutic DNA/RNA molecules[23, 24].

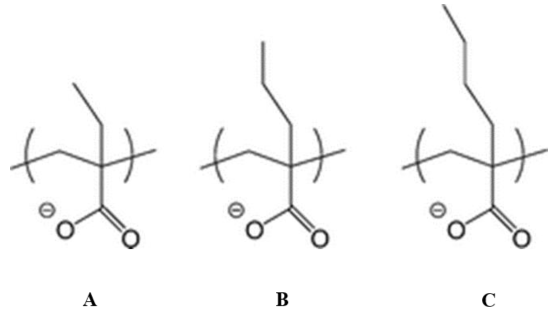

Figure 2.5: Chemical structure of pH-senstive amphiphilic polymers. **(A)** Poly (ethyl acrylic acid) (PEAA), **(B)** Poly (propyl acrylic acid), and **(C)** Poly (butyl acrylic acid) (PBAA)

The carboxyl groups on the amphiphilic polymers depicted in **Figure 2.5** possess the ability to sense a change in environmental pH and become protonated at acidic pH. These polymers bear pendant carboxylic acid groups and destabilize membrane bilayers by pH-triggered conformational changes[25]. They collapse from an expanded hydrophilic coil at physiological pH to a hydrophobic globule in an acidic environment[26, 27]**(Figure 2.6)**. Thus far, poly PEAA is the most extensively studied anionic carboxylated polymer for its membrane-destabilizing properties. PEAA is currently being investigated in liposomal delivery systems to induce pH-triggered release of liposome content[28–31]. It is also being evaluated as an endosomolytic agent[32,33]. At acidic pH and low concentrations, it can permeabilize cell membranes, whereas high polymer concentrations completely solubilize phospholipid bilayers[34]. Prior research illustrates that pH-responsive membrane destabilizing activity can be modulated by changing the number of alkyl groups in the polymer composition[23,24]. In addition, PPAA exhibited a pH-dependent membrane destabilization that is one order of magnitude higher than PEAA[25] and proved to enhance the transfection efficiency of cationic lipid/pDNA complexes both *in vitro*[25] and *in vivo*[35]. The modification of pH-responsive membrane-destabilizing polymer backbones to exhibit functionalized monomers like pyridyl disulphide acrylate (PDSA) via glutathione-sensitive disulphide linkages enabled coupling of negatively charged therapeutic macromolecules[24].

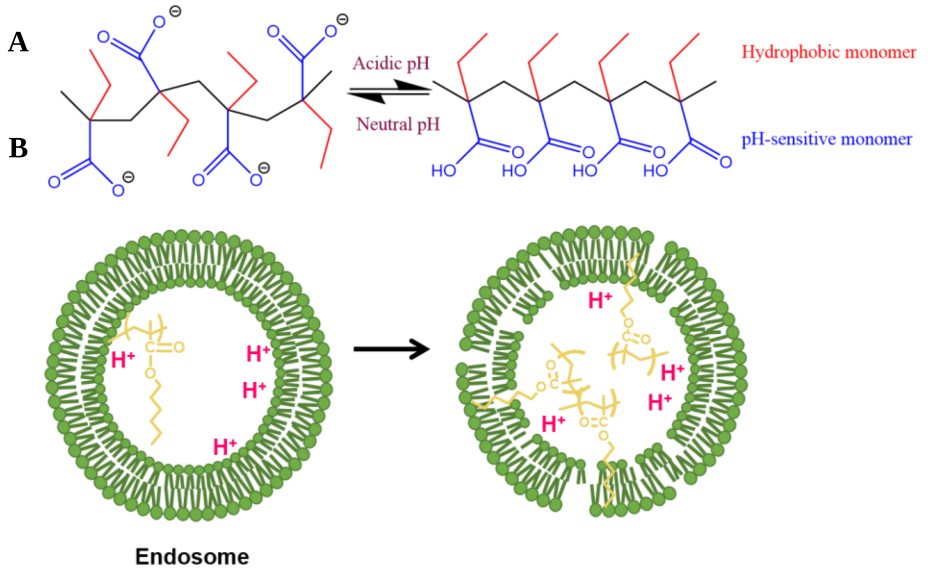

Figure 2.6: (A) Protonation of the pH-responsive carboxyl groups of PEAA at acidic pH induces **(B)** the hydrophobic alkyl groups to interact with the endosomal membrane, which results in the rupture of the membrane.

2.1.2 "Non-specific biodistribution of *in vivo*, systemic siRNA-based vectors can result in poor transfection efficiency"

The systemic administration of synthetic siRNA-based vectors often results in accumulation in the organs of the RES system, namely the liver, spleen, kidneys, and lungs. It is no coincidence that much of the successful siRNA delivery seen in the recent years has targeted diseases within these organs[36]. One major challenge in nanomedicine development is how to selectively deliver nanoparticles to diseased tissues. Nanoparticle delivery systems require targeting for specific delivery to pathogenic sites when enhanced permeability and retention effect

(EPR) is not suitable or is ineffective - this minimizes or avoids off-target effects of the active therapeutic agents on healthy tissues[2]. The conjugated targeting ligands are often specific to cell surface components that are unique, or upregulated in pathological tissues. The targeting ligands fall into several general classes: small molecules, polypeptide-based peptides, protein domains, antibodies, and nucleic acid-based aptamers[37]. At times, ligands from multiple classes (chimeras), or multiple ligands within the same class but with different targets (multi-valency and multi-specificity) have been implemented to enhance nanoparticle targeting. The coupling of ligands to nanoparticles requires precise chemistry that ensures ligand-directed coupling with correct orientation and desired surface density[37].

2.1.2.1 Advantages and disadvantages of general targeting strategies

2.1.2.1.1 Targeting with small molecules

This is the most prolific targeting strategy. The advantage of using small molecule as a targeting ligand is its stability, ease of conjugation with nanoparticles, and the potential low cost[38]. However, there is no systematic approach to develop such ligands, and most small molecule targeting ligands do not bind cell surface receptors with high specificity and affinity. Biotin, also known as vitamin H, has been widely used for facile conjugation with nanoparticles coated with (strept)avidin for *in vitro* applications[38]. This conjugation method exploits the extremely high affinity (10^{-14}–10^{-15} M) between biotin and (strept)avidin. Clinical applications of this conjugation system are limited, however, due to the bacterial origin of strept(avidin) and consequent immunogenicity[38].

2.1.2.1.2 Targeting with polypeptide-based homing peptide, protein domain, and antibody ligands

Polypetide-based targeting ligands, include homing peptides, protein domains, and antibodies, have advantages over other classes of targeting ligands in that they can be systemically developed and generated by using various biological selection and expression systems, respectively. Some major issues of these targeting ligands include immunogenicity, stability, and difficulty for site-specific conjugation with nanoparticles[38].

2.1.2.1.3 Targeting with aptamers

Since their introduction in 1990, aptamers have existed as a separate class of binding molecules[39]. Aptamers are short single-stranded nucleic acids (RNA or DNA) capable of displaying diverse structures with the potential of binding many biochemical targets, from small molecules to large proteins[40]. Aptamers are uniquely suited to nanoparticle targeting. Aptamers exhibit significant advantages relative to protein therapeutics in terms of size, synthetic accessibility and modification by medicinal chemistry. They are typically non-immunogenic[41], non-toxic[42], and modifiable for stability in circulation[42]. Despite these properties, aptamers have been slow to reach the marketplace, with only one aptamer-based drug receiving approval so far. As aptamers are subject to biological degradation by nucleases that poses a major barrier to *in vivo* aptamer-targeted nanoparticle applications.

2.1.3 Limitations of current siRNA carriers

Although both “proton sponge” and membrane destabilization effect proved efficient in enhancing cytoplasmic delivery of therapeutic nucleic acids – they have a number of limitations.

Cationic polymers with strong pH buffering capacity, such as PEI, usually deliver the desired dose of nucleic acid cargo into the cytoplasm of cells when a large amount of polymer is used. The use of a large amount of polymer results in non-specific cytotoxicity due to the excess positive charge destabilizing cell membranes. On the other hand, the membrane destabilizing activity of pH-sensitive amphiphilic polymers is based on a delicate balance between the hydrophilic and hydrophobic monomers. Excess positive charge abolishes their membrane destabilizing activity, while excess amount of hydrophobic groups reduces their solubility in aqueous solutions, thereby rendering them ineffective. In addition, PEI and the cohort of pH-responsive poly (alkylacrylic acid) polymers are non-biodegradable.

An ideal non-viral vector must be biodegradable, biocompatible, and non-immunogenic. In other words, the vector system should be hydrolyzed and degraded into small fragments (i.e., < 50 kDa) upon delivery of their therapeutic cargo. This ensures renal excretion of the vector fragments (the kidney typically excretes molecules less than 50 kDa in size) and eliminates accumulation and vector-associated toxicity. Moreover, the addition of targeting ligands to the afore-mentioned cationic polymers to improve target tissue accumulation of the non-viral vectors is not trivial and often affects the pH-buffering effect and the hydrophobic/hydrophilic balance. Finally, combination therapy – involving the co-delivery of therapeutic siRNA and small molecule anticancer drugs (e.g., chemotherapeutic agents) have shown to improve cancer treatment outcomes. Therefore, the development of polymeric carriers that can co-deliver both therapeutic DNA/RNA and anticancer drugs to the target cells has become the need of the hour.

2.1.4 Structural requirements of an "ideal" polymeric carrier for *in vivo* siRNA delivery

The design rational of an "ideal" polymeric carrier to overcome the limitations of existing polymeric-based siRNA carriers should include the following characteristic: (i) degradable, (ii) high drug loading, (iii) low toxicity, (iv) cell-specific, and (v) able to co-deliver other therapeutic drugs. To meet the requirements of an ideal carrier, we developed a library of degradable, pH-sensitive, membrane-destabilizing, star-shaped polymers as a platform technology that proved effective in complexing large doses of siRNA and functionally delivering therapeutic siRNA molecules into the cytoplasm of cancer cells *in vitro*. The carriers have a β-cyclodextrin (β-CD) core comprising of 7 glucose units linked by α-1,4-glycosidic bonds to form a cone-shaped structure. The β-CD core exhibits 7 hydroxyl (OH) groups on the primary face and 14 OH groups on the secondary face. The difference in the distribution of OH groups results in a difference in reactivity between the primary and secondary face, which facilitates the asymmetric conjugation of pH-sensitive/hydrophobic/cationic grafts on the secondary face and hydrophilic PEG grafts displaying targeting motifs on the primary face. The copolymer of pH-sensitive dimethyl aminoethyl methacrylate (DMAEMA), hydrophobic hexyl methacrylate (HMA) and cationic trimethyl aminoethyl methacrylate (TMAEMA) was grafted from the secondary face via acid-labile linkages **(Figure 2.7 B)**. Hydrazone linkages have been previously used to conjugate small molecular weight anticancer drugs (e.g., doxorubicin) to water-soluble hydroxypropyl methacrylate (HPMA) polymers and proved to hydrolyze and release the attached drug upon internalization into acidic intracellular vesicles[43]. Incorporation of the hydrazone linkages in these star-shaped polymers allows grafts with a large number of pH-sensitive/hydrophobic/cationic copolymers to achieve a high positive charge density that will allow the condensation of a large number of DNA/RNA molecules into the pH-sensitive particles with high therapeutic loading[44]. In addition, the acid-labile hydrazone linkages will be hydrolyzed in the endosome, which will result in the fragmentation of the carriers into multiple grafts that can be easily eliminated from the body without inducing significant toxicity. Besides the unique reactivity profile of β-CD molecules – they are water-soluble comprising of a hydrophobic cavity that facilitates the encapsulation of hydrophobic anticancer drugs inside and complexation of hydrophilic therapeutic DNA/RNA molecules outside[45]. The incorporation of PEG polymers on the primary face as a passive targeting moiety can help reduce the adhesive interactions associated with the peritoneal mucus membrane and facilitate an increased uptake into the blood circulation upon IP administration of the polymers. PEG has been shown to be safe for use with biological systems[46]; several PEGylated drugs have been approved by the FDA and others are being tested in clinical trials[47]. PEGylation presents an important tool for prolonging the blood circulation times[48–51] and by reducing the mononuclear phagocytic system (MPS) or reticuloendothelial system (RES) clearance as a result of minimizing the protein binding to the particle[52]. Finally, to address the non-specific distribution of siRNA-based delivery systems, we proposed the coupling of EPPT1-peptide as an active targeting moiety to the free ends of primary PEG brushes to facilitate target site accumulation of polymers. The synthetic peptide, designated EPPT1 (YCAREPPTRTFAYWG), is derived from the CDR3 V_h region of a monoclonal antibody (ASM2) raised against human epithelial cancer cells[53]. The EPPT1 synthetic peptide has significant affinity ($K_d = 20$ μM) for the uMUC-1-derived peptide, PDTRP, region. In a previous study, the EPPT1 peptide, labeled with ^{99m}Tc, was used to image breast carcinomas *in vivo*[54] .We chose a peptide-based targeting strategy as peptides are much smaller than antibodies but larger than small molecules. The design of a small molecule that fits into a usually shallow and hydrophobic binding pocket can be challenging. As a compromise between small molecules and large antibodies, short peptides fit in the pocket and have high specificity and affinity. Overall, these asymmetric, degradable, pH-sensitive, membrane destabilizing polymers possess are the features of an ideal non-viral vector for intracellular delivery of therapeutic macromolecule.

2.1.5 Objective and Hypothesis

The objective of this dissertation is to develop targeted "smart" particles to achieve enhanced cell specific cytoplasmic delivery of therapeutic anti-RhoC siRNA molecules to suppress metastatic RhoC protein expression in aggressive breast cancer cells with subsequent reduction of

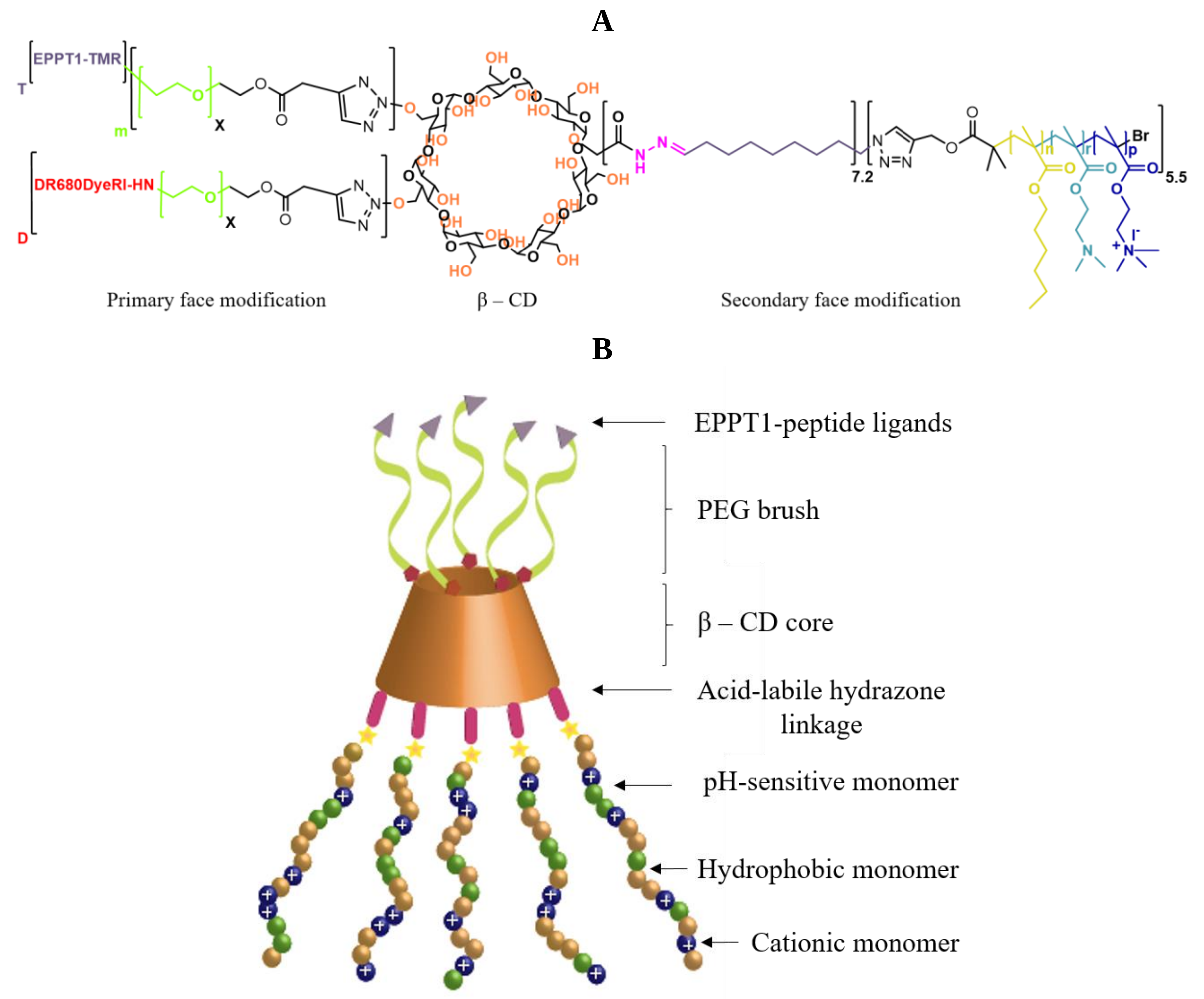

Figure 2.7: (A) Chemical representation of the proposed ideal polymeric star-shaped β-CD-P(HMA-co- DMAEMA-co-TMAEMA)n polymers. **(B)** Schematic drawing of the ideal β-CD-based polymers for cytoplasmic delivery of siRNA to the target site.

RhoC-associated cell invasion and migration *in vitro* and to determine our nanoparticle's biodistribution and therapeutic behavior *in vivo.* The pH-sensitive polymers can condense anti-RhoC siRNA molecules into "smart" particles that will be taken up by aggressive breast cancer cells via endocytosis. In the endosome, the particles will "sense" the drop in endosomal pH, which will trigger the degradation of the polymeric carrier into small membrane destabilizing fragments to destabilize the endosomal membrane and release the siRNA molecules into the cytoplasm *in vitro.* The addition of EPPT1-peptide ligands to the "smart" polymers can facilitate cell specific accumulation by binding to MUC1 receptors known to be overexpressed on aggressive breast cancer cells while minimizing uptake by healthy cells. The asymmetric, targeted "smart" nanoparticles were designed to maneuver through the systemic circulation without being recognized by blood components and to target the specific tumor tissue following extravasation out through the 'leaky' vasculature of the tumor *in vivo.*

We hypothesize that the EPPT1-peptide targeted "smart" nanoparticles complexing anti-RhoC siRNA molecules will demonstrate specificity and selectivity for uMUC1-receptor expressing breast cancer cells *in vitro* and *in vivo*. We hypothesize that the primary PEG grafts will shield the encapsulated siRNA from serum proteins and will reduce hemolysis of RBC's. The asymmetric targeted polymer can condense anti-RhoC siRNA into stable particles that will be internalized in cancer cells via receptor-mediated endocytosis. In the endosome, the particles will destabilize the endosomal membrane through both hydrophobic disruption and endosomal swelling mechanism, releasing siRNA cargo into the cytoplasm of breast cancer cells to suppress RhoC expression. We hypothesize the incorporation of EPPT1-peptide ligands and anti-RhoC siRNA on the same polymer system can synergistically reduce cell invasion and migration of aggressive breast cancer cell.

2.1.6 Specific aims

The specific aims of this dissertation are:

1. Investigate the feasibility of our “smart” nanoparticles’ amphiphilic copolymer graft composition to complex the desired dose of anti-RhoC siRNA molecules and to functionally deliver the therapeutic cargo past the endosome into the cytoplasm of aggressive breast cancer cells. Evaluate the effect of RhoC protein suppression on associated changes in cell invasion and migration in the aforementioned cell lines *in vitro.*

2. Design and synthesize EPPT1-peptide targeted, PEGylated “smart” polymers with improved biocompatibility against blood components and enhanced target cell specificity *in vitro*. We engineered asymmetric polymers with varying PEG graft lengths to evaluate the effect of PEG molecular weight on hemocompatibility and serum stability. Determine if the incorporation of EPPT1-peptides results in target cell specificity and enhanced functional delivery of therapeutic anti-RhoC siRNA into the cytoplasm of these cells.

3. Confirm the *in vivo* feasibility of our asymmetric “smart” nanoparticles. Evaluate the biodistribution of EPPT1-peptide targeted nanoparticles in SUM149 tumor-bearing mice compared to their non-targeted counterparts. Determine the dosing regimen of anti-RhoC siRNA complexing nanoparticles in suppressing RhoC protein expression following intra-tumoral administration.

References

1. Liang W, Lam JKW. Endosomal Escape Pathways for Non-Viral Nucleic Acid Delivery Systems. In: Rijeka: InTech; 2012:Ch. 0. doi:10.5772/46006.
2. Wong SY, Pelet JM, Putnam D. Polymer systems for gene delivery—Past, present, and future. *Prog Polym Sci*. 2007;32(8–9):799-837. doi:http://dx.doi.org/10.1016/j.progpolymsci.2007.05.007.
3. Boussif O, Lezoualc'h F, Zanta MA, et al. A versatile vector for gene and oligonucleotide transfer into cells in culture and in vivo: polyethylenimine. *Proc Natl Acad Sci U S A*. 1995;92(16):7297-7301. http://www.ncbi.nlm.nih.gov/pmc/articles/PMC41326/.
4. Morille M, Passirani C, Vonarbourg A, Clavreul A, Benoit J-P. Progress in developing cationic vectors for non-viral systemic gene therapy against cancer. *Biomaterials*. 2008;29(24–25):3477-3496. doi:http://dx.doi.org/10.1016/j.biomaterials.2008.04.036.
5. Boussif O, Zanta M a, Behr JP. Optimized galenics improve in vitro gene transfer with cationic molecules up to 1000-fold. *Gene Ther*. 1996;3(33):1074-1080.
6. Neu M, Fischer D, Kissel T. Recent advances in rational gene transfer vector design based on poly(ethylene imine) and its derivatives. *J Gene Med*. 2005;7(8):992-1009. doi:10.1002/jgm.773.
7. Godbey WT, Wu KK, Mikos AG. Poly(ethylenimine)-mediated gene delivery affects endothelial cell function and viability. *Biomaterials*. 2001;22(5):471-480. doi:10.1016/S0142-9612(00)00203-9.
8. Godbey WT, Wu KK, Mikos AG. Size matters: Molecular weight affects the efficiency of poly(ethylenimine) as a gene delivery vehicle. *J Biomed Mater Res*. 1999;45(3):268-275. doi:10.1002/(SICI)1097-4636(19990605)45:3<268::AID-JBM15>3.0.CO;2-Q.
9. Fischer D, Von Harpe A, Kunath K, Petersen H, Li Y, Kissel T. Copolymers of ethylene imine and N-(2-hydroxyethyl)-ethylene imine as tools to study effects of polymer structure on physicochemical and biological properties of DNA complexes. *Bioconjug Chem*. 2002;13(5):1124-1133. doi:10.1021/bc025550w.
10. Kunath K, Von Harpe A, Fischer D, et al. Low-molecular-weight polyethylenimine as a non-viral vector for DNA delivery: Comparison of physicochemical properties, transfection efficiency and in vivo distribution with high-molecular-weight polyethylenimine. *J Control Release*. 2003;89(1):113-125. doi:10.1016/S0168-3659(03)00076-2.
11. Park K, Lee M-Y, Kim KS, Hahn SK. Target specific tumor treatment by VEGF siRNA complexed with reducible polyethyleneimine–hyaluronic acid conjugate. *Biomaterials*. 2010;31(19):5258-5265. doi:http://dx.doi.org/10.1016/j.biomaterials.2010.03.018.
12. Zintchenko A, Philipp A, Dehshahri A, Wagner E. Simple Modifications of Branched PEI Lead to Highly Efficient siRNA Carriers with Low Toxicity. *Bioconjug Chem*. 2008;19(7):1448-1455. doi:10.1021/bc800065f.
13. Schiffelers RM, Ansari A, Xu J, et al. Cancer siRNA therapy by tumor selective delivery with ligand-targeted sterically stabilized nanoparticle. *Nucleic Acids Res*. 2004;32(19):e149. doi:10.1093/nar/gnh140.
14. Fréchet JMJ. Functional polymers and dendrimers. *Science (80-)*. 1994;263(5154):1710-1715.
15. Tomalia DA, Fréchet JMJ. Discovery of dendrimers and dendritic polymers: A brief historical perspective. *J Polym Sci Part A Polym Chem*. 2002;40(16):2719-2728.

doi:10.1002/pola.10301.

16. Sonawane ND, Szoka FC, Verkman AS. Chloride Accumulation and Swelling in Endosomes Enhances DNA Transfer by Polyamine-DNA Polyplexes. *J Biol Chem*. 2003;278(45):44826-44831. doi:10.1074/jbc.M308643200.
17. Kim T Il, Seo HJ, Choi JS, et al. PAMAM-PEG-PAMAM: Novel triblock copolymer as a biocompatible and efficient gene delivery carrier. *Biomacromolecules*. 2004;5(6):2487-2492. doi:10.1021/bm049563j.
18. Luo D, Haverstick K, Belcheva N, Han E, Saltzman WM. Poly(ethylene glycol)-conjugated PAMAM dendrimer for biocompatible, high-efficiency DNA delivery. *Macromolecules*. 2002;35(9):3456-3462. doi:10.1021/ma0106346.
19. Waite CL, Sparks SM, Uhrich KE, Roth CM. Acetylation of PAMAM dendrimers for cellular delivery of siRNA. *BMC Biotechnol*. 2009;9:38. doi:10.1186/1472-6750-9-38.
20. Svenson S. Dendrimers as versatile platform in drug delivery applications. *Eur J Pharm Biopharm*. 2009;71(3):445-462. doi:10.1016/j.ejpb.2008.09.023.
21. Tang MX, Redemann CT, Szoka FC. In vitro gene delivery by degraded polyamidoamine dendrimers. *Bioconjug Chem*. 1996;7(6):703-714. doi:10.1021/bc9600630.
22. Hensley SE, Das SR, Bailey AL, et al. Hemagglutinin Receptor Binding Avidity Drives Influenza A Virus Antigenic Drift. *Science (80-)*. 2009;326(5953):734-736. doi:10.1126/science.1178258.
23. Pack DW, Hoffman AS, Pun S, Stayton PS. Design and development of polymers for gene delivery. *Nat Rev Drug Discov*. 2005;4(7):581-593. http://dx.doi.org/10.1038/nrd1775.
24. El-Sayed MEH, Hoffman AS, Stayton PS. Rational design of composition and activity correlations for pH-responsive and glutathione-reactive polymer therapeutics. *J Control Release*. 2005;104(2):417-427. doi:10.1016/j.jconrel.2005.01.009.
25. Cheung CY, Murthy N, Stayton PS, Hoffman AS. A pH-sensitive polymer that enhances cationic lipid-mediated gene transfer. *Bioconjug Chem*. 2001;12(6):906-910. doi:10.1021/bc0100408.
26. Yessine M-A, Lafleur M, Meier C, Petereit H-U, Leroux J-C. Characterization of the membrane-destabilizing properties of different pH-sensitive methacrylic acid copolymers. *Biochim Biophys Acta - Biomembr*. 2003;1613(1–2):28-38. doi:http://dx.doi.org/10.1016/S0005-2736(03)00137-8.
27. Olea AF, Rosenbluth H, Thomas JK. Effect of the Molecular Weight on the Dynamics of the Conformational Transition of Poly(methacrylic acid). *Macromolecules*. 1999;32(24):8077-8083. doi:10.1021/ma990470h.
28. Mills JK, Eichenbaum G, Needham D. Effect of Bilayer Cholesterol and Surface Grafted Poly(Ethylene Glycol) on pH-Induced Release of Contents from Liposomes by Poly(2-Ethylacrylic Acid). *J Liposome Res*. 1999;9(2):275-290. doi:10.3109/08982109909024790.
29. Maeda M, Kumano A, Tirrell DA. H+-induced release of contents of phosphatidylcholine vesicles bearing surface-bound polyelectrolyte chains. *J Am Chem Soc*. 1988;110(22):7455-7459. doi:10.1021/ja00230a028.
30. Thomas JL, Tirrell DA. Polymer-induced leakage of cations from dioleoyl phosphatidylcholine and phosphatidylglycerol liposomes. *J Control Release*. 2000;67(2–3):203-209. doi:http://dx.doi.org/10.1016/S0168-3659(00)00209-1.
31. Chen T, Choi LS, Einstein S, Klippenstein MA, Scherrer P, Cuhis PR. Proton-Induced Permeability and Fusion of Large Unilamellar Vesicles by Covalently Conjugated Poly(2-

Ethylacrylic Acid). *J Liposome Res*. 1999;9(3):387-405. doi:10.3109/08982109909018658.

32. Mourad PD, Murthy N, Porter TM, et al. Focused Ultrasound and Poly(2-ethylacrylic acid) Act Synergistically To Disrupt Lipid Bilayers in Vitro. *Macromolecules*. 2001;34(8):2400-2401. doi:10.1021/ma000549i.
33. Murthy N, Robichaud JR, Tirrell DA, Stayton PS, Hoffman AS. The design and synthesis of polymers for eukaryotic membrane disruption. *J Control Release*. 1999;61(1–2):137-143. doi:http://dx.doi.org/10.1016/S0168-3659(99)00114-5.
34. Thomas JL, Tirrell DA. Polyelectrolyte-sensitized phospholipid vesicles. *Acc Chem Res*. 1992;25(8):336-342. doi:10.1021/ar00020a003.
35. Kyriakides TR, Cheung CY, Murthy N, Bornstein P, Stayton PS, Hoffman AS. pH-Sensitive polymers that enhance intracellular drug delivery in vivo. In: *Journal of Controlled Release*. Vol 78. ; 2002:295-303. doi:10.1016/S0168-3659(01)00504-1.
36. Whitehead K a, Langer R, Anderson DG. Knocking down barriers: advances in siRNA delivery. *Nat Rev Drug Discov*. 2009;8(2):129-138. doi:10.1038/nrd2742.
37. Liu R, Kay BK, Jiang S, Chen S. Nanoparticle delivery: targeting and nonspecific binding. *MRS Bull*. 2009;34(6):432-440.
38. Friedman AD, Claypool SE, Liu R. The Smart Targeting of Nanoparticles. *Curr Pharm Des*. 2013;19(35):6315-6329. http://www.ncbi.nlm.nih.gov/pmc/articles/PMC4016770/.
39. Wilson DS, Szostak JW. in Vitro Selection of Functional Nucleic Acids. *Annu Rev Biochem*. 1999;68(1):611-647. doi:10.1146/annurev.biochem.68.1.611.
40. Keefe AD, Pai S, Ellington A. Aptamers as therapeutics. *Nat Rev Drug Discov*. 2010;9(7):537-550. doi:10.1038/nrd3249.
41. de Campos WRL, Coopusamy D, Morris L, Mayosi BM, Khati M. Cytotoxicological Analysis of a gp120 Binding Aptamer with Cross-Clade Human Immunodeficiency Virus Type 1 Entry Inhibition Properties: Comparison to Conventional Antiretrovirals . *Antimicrob Agents Chemother*. 2009;53(7):3056-3064. doi:10.1128/AAC.01502-08.
42. Pagratis NC, Bell C, Chang Y-F, et al. Potent 2[prime]-amino-, and 2[prime]-fluoro-2[prime]- deoxyribonucleotide RNA inhibitors of keratinocyte growth factor. *Nat Biotech*. 1997;15(1):68-73. http://dx.doi.org/10.1038/nbt0197-68.
43. Studenovsky M, Pola R, Pechar M, et al. Polymer Carriers for Anticancer Drugs Targeted to EGF Receptor. *Macromol Biosci*. 2012;12(12):1714-1720. doi:10.1002/mabi.201200270.
44. Lin Y-L, Jiang G, Birrell LK, El-Sayed MEH. Degradable, pH-sensitive, membrane-destabilizing, comb-like polymers for intracellular delivery of nucleic acids. *Biomaterials*. 2010;31(27):7150-7166. doi:http://dx.doi.org/10.1016/j.biomaterials.2010.05.048.
45. Davis ME, Brewster ME. Cyclodextrin-based pharmaceutics: past, present and future. *Nat Rev Drug Discov*. 2004;3(12):1023-1035. http://dx.doi.org/10.1038/nrd1576.
46. Simpson CA, Salleng KJ, Cliffel DE, Feldheim DL. In vivo toxicity, biodistribution, and clearance of glutathione-coated gold nanoparticles. *Nanomedicine Nanotechnology, Biol Med*. 2013;9(2):257-263. doi:http://dx.doi.org/10.1016/j.nano.2012.06.002.
47. Ikeda Y, Nagasaki Y. PEGylation technology in nanomedicine. *Adv Polym Sci*. 2012;247(1):115-140. doi:10.1007/12_2011_154.
48. Lipka J, Semmler-Behnke M, Sperling RA, et al. Biodistribution of PEG-modified gold nanoparticles following intratracheal instillation and intravenous injection. *Biomaterials*. 2010;31(25):6574-6581. doi:10.1016/j.biomaterials.2010.05.009.

49. Owens DE, Peppas NA. Opsonization, biodistribution, and pharmacokinetics of polymeric nanoparticles. *Int J Pharm*. 2006;307(1):93-102. doi:10.1016/j.ijpharm.2005.10.010.
50. Woodle MC, Lasic DD. Sterically stabilized liposomes. *BBA - Rev Biomembr*. 1992;1113(2):171-199. doi:10.1016/0304-4157(92)90038-C.
51. Li S-D, Chen Y-C, Hackett MJ, Huang L. Tumor-targeted delivery of siRNA by self-assembled nanoparticles. *Mol Ther*. 2008;16(1):163-169. doi:10.1038/sj.mt.6300323.
52. Li SD, Huang L. Pharmacokinetics and biodistribution of nanoparticles. In: *Molecular Pharmaceutics*. Vol 5. ; 2008:496-504. doi:10.1021/mp800049w.
53. Hussain R, Courtenay-Luck NS, Siligardi G. Structure-function correlation and biostability of antibody CDR-derived peptides as tumour imaging agents. *Biomed Pept Proteins Nucleic Acids Struct Synth Biol Act*. 1996;2(3):67-70.
54. Sivolapenko GB, Douli V, Sirmalis G, et al. Breast cancer imaging with radiolabelled peptide from complementarity-determining region of antitumour antibody. *Lancet*. 1995;346(8991-8892):1662-1666. doi:10.1016/S0140-6736(95)92839-1.

Chapter 3

“Smart” Nanoparticles Enhance the Cytoplasmic Delivery of Anti-RhoC Silencing RNA and Inhibit the Migration and Invasion of Aggressive Breast Cancer Cells

3.1 Introduction

The American Cancer Society estimated that 232,670 women were diagnosed with invasive breast cancer in the U.S. in 2014[1]. Approximately, 20-30% of breast cancer patients develop distant metastases to the bone, brain, liver, and lungs, which results in 40,000 deaths from breast cancer[1, 2]. Metastasis of aggressive breast cancer cells is a complex process that involves cell detachment from the primary lesion, migration through the extracellular matrix, invasion through the basement membrane, entrance into lymphatic and blood vessels, evasion from the immune system in the lymphatic and systemic circulations, extravasation into the interstitial space of distant organs, colonization in secondary sites, and initiation of new tumor lesions[3, 4, 5]. Overexpression of the **R**as **ho**mology (**Rho**) family of low molecular weight (21-25 kDa) guanosine-5'-triphosphate (GTP)-binding proteins has been strongly implicated in the migration and invasion of aggressive breast cancer cells[6]. Specifically, the C-terminus of Rho proteins undergoes post-translational modification where isoprenoid lipids (e.g. farnesyl or geranylgeranyl lipids) are covalently attached to allow Rho proteins to anchor to the cell membrane[7]. This isoprenylation of Rho-GDPases is initiated by the transduction of extracellular signals through integrins and growth factor receptors to the cytoplasm in tightly regulated signaling pathways[6]. Upon insertion into the cell membrane, the GTPase domain of Rho proteins, which binds to guanosine-5'-diphosphate (GDP)[8] and GTP molecules, acts as a molecular on/off switch by cycling between inactive GDP-bound and active GTP-bound states[9]. The activated Rho-GTPase proteins are involved in all aspects of cellular motility and invasion including cell polarization, signal transduction, cytoskeletal reorganization, and formation of invasive cell membrane protrusions[10-12]. For example, RhoA and RhoC proteins play key roles in regulating the contractility of acto-myosin rings and cell motility[13]. In addition, the Rac1 protein stimulates the formation of lamellipodia (membrane ruffles)[13, 14] while the Cdc42 protein dictates the direction of cell migration by coordinating actin polymerization at the leading side of the cell[15].

Overexpression of RhoC GTPases has been linked to the metastasis of inflammatory breast cancer (IBC)[16, 17] and triple-negative breast cancer cells[18, 19] as well as low patient survival rates. The role of RhoC in promoting cell migration and invasion has been confirmed by multiple *in vitro and in vivo* studies[16, 19, 20]. In one such study, transfecting human mammary epithelial (HME) cells with the gene encoding for RhoC allowed the cells to grow in an anchorage-independent manner and become highly motile and invasive due to enhanced formation of actin and focal adhesion points *in vitro*[21]. Further, the RhoC-expressing HME cells were tumorigenic and produced angiogenic factors when orthotopically implanted into the mammary fat pads of athymic nude mice[21]. Another report described the role of RhoC GTPases in breast cancer metastasis by assessing the number of cancer lesions in the lungs of RhoC$^+$ and RhoC$^-$ tumor-bearing mice[19].

The detection of 37 ± 12 lesions in RhoC^+ mice ($n = 12$) compared to 5 ± 2 cancer lesions in RhoC^- mice ($n = 16$) confirmed the role of RhoC in promoting breast cancer metastasis[19]. Cytofectin-mediated transfection of anti-RhoC silencing RNA (siRNA) molecules into the cytoplasm of MDA-MB-231 cells has been shown to reduce RhoC expression at the mRNA and protein levels and result in 70% inhibition of cancer cell invasion *in vitro*[20]. In addition, direct injection of anti-RhoC siRNA into tumors formed by implanting MDA-MB-231 breast cancer cells in the flanks of *nu/nu* mice caused a 53% reduction in tumor growth[22]. These results collectively show the therapeutic benefit of suppressing the activity of RhoC proteins to inhibit the metastatic spread of aggressive breast cancer cells. However, using anti-RhoC siRNA as a therapeutic agent in a defined dosing regimen remains a significant challenge due to the lack of a biocompatible carrier that can efficiently protect and selectively deliver the RNA cargo into the cytoplasm of breast cancer cells in order to silence cancer cell migration, invasion, and metastasis without exhibiting non-specific toxicity to healthy cells[23]

We previously reported the synthesis of star-shaped, pH-sensitive, and membrane-destabilizing polymers that enhance the cytoplasmic delivery of siRNA molecules into epithelial cancer cells[24]. We utilized β-cyclodextrin (β-CD) as the core carrier to graft copolymers with equal molar ratios of the hydrophobic hexyl methacrylate (HMA) and the pH-sensitive 2-(dimethylamino)ethyl methacrylate (DMAEMA) monomers from the secondary face via acid-labile hydrazone linkages **(Figure 3.1)**[25]. Finally, 50% of the DMAEMA monomers in each graft copolymer were quarternized into cationic *N*, *N*, *N*-trimethylaminoethyl methacrylate (TMAEMA) monomers to facilitate efficient condensation of siRNA molecules via electrostatic interactions between the cationic amine (N) groups of the polymer and anionic phosphate (P) groups of the siRNA forming “smart” pH-sensitive and membrane-destabilizing particles **(Figure 3.2)**.

In this report, we investigate the ability of biodegradable, pH-sensitive, star-shaped polymers to complex anti-RhoC siRNA molecules at low N/P ratios forming “smart” nanoparticles and whether they achieve functional delivery of the loaded cargo into aggressive breast cancer cells. We hypothesize that “smart” anti-RhoC particles will be taken up by breast cancer cells via adsorptive endocytosis followed by fragmentation and release of the membrane-active P(HMA-*co*-DMAEMA-*co*-TMAEMA) grafts in response to acidic endosomal pH gradients, which will destabilize the endosomal membrane and release the loaded siRNA cargo into the cytoplasm **(Figure 3.2)**. In the cytoplasm, anti-RhoC siRNA molecules will selectively bind to the RhoC mRNA resulting in mRNA degradation and blocking the expression of RhoC protein. We investigated the effect of functional delivery of anti-RhoC siRNA into the cytoplasm of triple negative MDA-MB-231 and inflammatory SUM149 breast cancer cells on RhoC expression and the associated changes in cell invasion, migration, and motility *in vitro*.

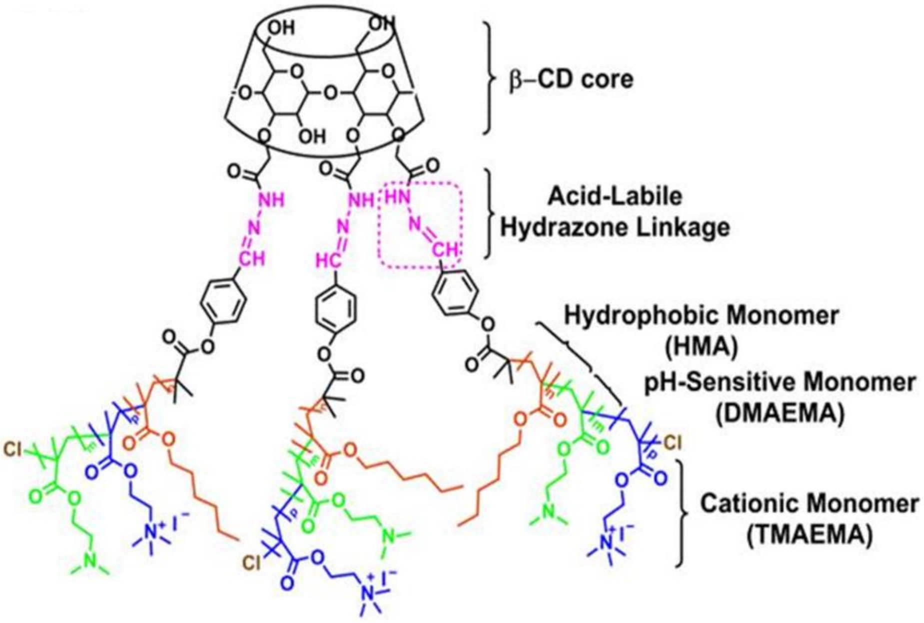

Figure 3.1: The chemical structure of the degradable, pH-sensitive, star-shaped β-CD-g-P(HMA$_{79}$-*co*-DMAEMA$_{33}$-*co*-TMAEMA$_{48}$)$_{4.8}$ polymer.

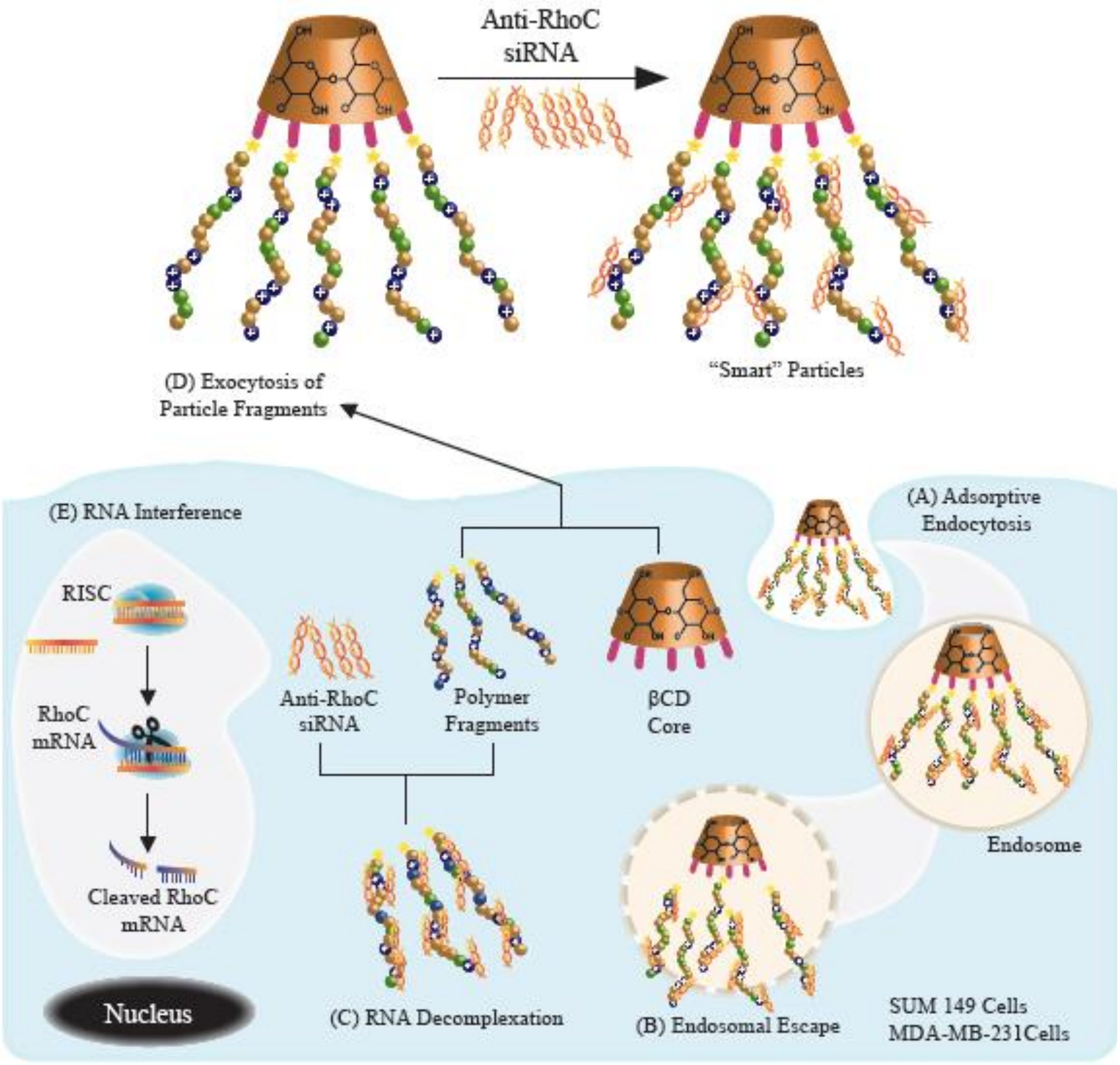

Figure 3.2: A schematic drawing showing condensation of anti-RhoC siRNA molecules by star-shaped pH-sensitive polymers forming "smart" particles, which are internalized by endocytosis. In the endosome, acid-labile hydrazone linkages are hydrolyzed by the acidic pH, which release the P(HMA-*co*-DMAEMA-*co*-TMAEMA) grafts that rupture the endosomal membrane and release the loaded siRNA cargo into the cytoplasm. In the cytoplasm, anti-RhoC siRNA binds to RhoC mRNA triggering its degradation while particle's debris are eliminated by exocytosis.

3.2 Materials and methods

3.2.1 Materials

Ham’s F12 medium, OPTI-MEM reduced serum medium, Rosewell Park Memorial Institute-1640 (RPMI) medium, fetal bovine serum (FBS), 0.05% trypsin/0.20% ethylenediaminetetraacetic acid (EDTA) solution, and phosphate buffered saline (PBS) solution were purchased from Invitrogen Corporation (Carlsbad, CA). The anti-RhoC (5'-GACCUGCCUCCUCAUCGUCTT-3') and scrambled (5'- CAGUCAGGAGGAUCCAAAGTG-3’) siRNA sequences were synthesized by Dharmacon Scientific (Lafayette, CO). The human anti-GAPDH siRNA, FAM-labeled GAPDH siRNA, scrambled siRNA, and siPORT-Amine transfection reagent were purchased from Ambion Inc. (Austin, TX). The RNeasy Mini kit and Omniscript reverse transcriptase kit were purchased from Qiagen (Valencia, CA). The SYBR green power master mix, forward and reverse RhoC, RhoA, and RPL19 primers were purchased from Applied Biosystems (Foster, CA). Anti-RhoC rabbit monoclonal antibody was purchased from Cell Signaling Technologies (Danvers, MA). The anti-RhoA mouse monoclonal antibody, anti-β-actin rabbit antibody, and goat anti-rabbit IgG-HRP antibodies were procured from Santa Cruz Biotechnology Inc. (Santa Cruz, CA). BD matrigel invasion assay and the motility assay kits were obtained from BD Biosciences (San Jose, CA) and Cellomics (Pittsburgh, PA), respectively. The Collagen I coated plates used in the motility assay were obtained from Life Technologies (Carlsbad, CA).

3.2.2 Formulation and characterization of “smart” particles

We synthesized our star-shaped β-CD-g-P(HMA$_{79}$-*co*-DMAEMA$_{33}$-*co*-TMAEMA$_{48}$)$_{4.8}$ polymers following established protocols[25]. The star-shaped particles were prepared by dissolving β-CD-g-P(HMA$_{79}$-*co*-DMAEMA$_{33}$-*co*-TMAEMA$_{48}$)$_{4.8}$ polymers in RNase-free water prior to the addition of 0.7μg of scrambled siRNA at varying nitrogen (N)/phosphate (P) (+/-) ratios. Each “smart” polymer-siRNA mixture was vortexed, centrifuged, and allowed to form particle complexes for 20min at room temperature. The lowest N/P ratio at which the β-CD-g-P(HMA$_{79}$-*co*-DMAEMA$_{33}$-*co*-TMAEMA$_{48}$)$_{4.8}$ polymer and scrambled siRNA molecules formed stable complexes was determined by loading each mixture onto a 1% w/v agarose gel containing ethidium bromide (EtBr). Prior to loading the samples into the individual wells, the agarose gel was soaked in Tris-acetate-EDTA (TAE) buffer, followed by running it at 120V for 30 min. The free and bound siRNA molecules were visualized on the gel under UV light. The size and electrophoretic mobility of our “smart” particles complexing 1.4μg of scrambled siRNA prepared at different N/P ratios were measured using 90Plus particle size analyzer with ZetaPALS capability (Brookhaven Instruments Corporation, Holtsville, NY). All experiments were performed in double distilled water at 25°C. The zeta potential was calculated from the electrophoretic mobility using the Smoluchowski equation. The results are expressed as mean values of five samples.

3.2.3 Cell culture

SUM149 and MDA-MB-231 breast cancer cells were generously provided by Dr. Sofia D. Merajver (University of Michigan, School of Medicine) and cultured following established protocols[27]. Briefly, SUM149 cells were cultured in Ham’s F12 medium supplemented with 5% fetal bovine serum (HyClone Laboratories, South Logan, UT), insulin, and hydrocortisone (Sigma-Aldrich, St. Louis, Mo). SUM149 cells were maintained at 37°C and 10% CO_2. MDA-MB-231 cells were cultured in RPMI-1640 medium supplemented with 10% fetal bovine serum, and incubated at 37°C and 5% CO_2.

3.2.4 Cellular uptake of “smart” particles

“Smart” β-CD particles were prepared at varying N/P (+/-) ratios (i.e., 1.5/1, 2.5/1, 4/1, 8/1, and 12/1) by dissolving our β-CD-g-P(HMA_{79}-*co*-$DMAEMA_{33}$-*co*-$TMAEMA_{48}$)$_{4.8}$ polymer in OPTI-MEM solution prior to the addition of 0.57μg FAM-labeled anti-GAPDH siRNA. Similarly, the siPORT Amine polymer was mixed with 0.57μg FAM-labeled anti-GAPDH siRNA following manufacturer’s instructions. All complexes were vortexed, centrifuged and allowed to stand at room temperature for 20 min. The “smart” particle complexes were incubated with SUM149 and MDA-MB-231 cancer cells seeded at a density of 40,000 cells per well in 24-well plates for 6h at 37°C. Cells were then harvested by washing them with PBS to remove unbound particle complexes, followed by detaching them with 0.05% Trypsin/EDTA for 5 min, and centrifuging them to form cell pellets and remove the supernatant with free particles. Cell pellets were collected, suspended in their respective culture medium, and analyzed using Biosciences FACSCalibur Flow Cytometer (Becton Dickinson, Franklin Lakes, NJ) to determine the % of live cells that are fluorescently labeled due to “smart” particle internalization. The results are expressed as mean average values + the standard error of the mean of four samples.

We visualized the uptake of β-CD-g-P(HMA_{79}-*co*-$DMAEMA_{33}$-*co*-$TMAEMA_{48}$)$_{4.8}$ polymers complexed with FITC-labeled siRNA into SUM149 and MDA-MB-231 breast cancer cells using a Nikon A1 confocal microscope (Nikon Instruments Inc., Melville, NY) equipped with diode-based lasers. Briefly, SUM149 and MDA-MB-231 cells were seeded in 4-well Lab-Tek II Chambered Glass Slides (Thermo Scientific, Waltham, MA) at a seeding density of 7,000 cells/well and allowed to adhere overnight. Both cell lines were incubated with free FITC-labeled siRNA and “smart” β-CD particles prepared by complexing β-CD-g-P(HMA_{79}-*co*-$DMAEMA_{33}$-*co*-$TMAEMA_{48}$)$_{4.8}$ polymers with FITC-labeled siRNA at a N/P ratio of 2.5/1 for 6 hours. The treated SUM149 and MDA-MB-231 cells were washed with PBS twice to remove the free “smart” particles in solution, and fixed with 4% paraformaldehyde for 30 min. The fixed cells were washed again with PBS prior to staining the cell cytoskeleton with Rhodamine Phalloidin for 15 min, and washed one more time with PBS before microscopic examination. We used (λ_{ex}) of 488 nm and (λ_{em}) of 530 nm to image FITC-labeled siRNA while using (λ_{ex}) of 512 nm and (λ_{em}) of 600 nm to image the Rhodamine-stained cytoskeleton. We used a Nikon Apo 10 /1.25na lens to capture planar images of the cells followed by image processing using Nikon NIS Confocal Software.

3.2.5 *In vitro* effect of "smart" anti-RhoC particles

The β-CD-g-P(HMA_{79}-*co*-$DMAEMA_{33}$-*co*-$TMAEMA_{48}$)$_{4.8}$ polymer dissolved in OPTI-MEM solution was allowed to complex with 0.57µg of anti-RhoC (+) or scrambled (-) siRNA at a N/P(+/-) ratio of 2.5/1 to prepare "smart" anti-RhoC (+) and scrambled (-) particles, respectively. SiPORT-Amine complexes loaded with 0.57µg of anti-RhoC (+) or scrambled (-) siRNA were prepared following manufacturer's instructions. SUM149 and MDA-MB-231 cells were seeded at 50,000 cells per well in 24-well plates and allowed to adhere for 18h before their incubation with different particles following established protocols[25]. The effect of different particles on RhoC expression in both cancer cell lines was quantified based on mRNA and protein levels. For the quantification of RhoC mRNA levels, the total RNA from each sample treatment condition of SUM149 and MDA-MB-231 cells was obtained using the RNeasy Mini Kit (Qiagen Inc., Valencia, CA) and quantified using Thermo Scientific NanoDrop™ 1000 Spectrophotometer. Equal amounts of total RNA (0.25µg) from each treatment condition were reverse transcribed using Omniscript reverse transcriptase kit (Qiagen Inc., Valencia, CA) following manufacturer's protocols. Quantitative PCR was performed with an Applied Biosystems PCR System at a final volume of 20µl, containing1.25µL of cDNA (corresponding to 250ng of total RNA for RhoA, RhoC and RPL19 rRNA amplification), 0.1µL of each forward and reverse primer (corresponding to 0.01µg/µL of RhoA, RhoC and RPL19 primer sets), and 10µL of SYBR green qPCR Master Mix. The sequences of the forward and reverse primers for RhoC are 5'-CATCCTGGTGGGGAATAAGA-3' and 5'-GCACTCAAGGTAGCCAAAGG-3', respectively. The sequences of the forward and reverse primers for RhoA are 5'-ACCCGCCTTCGTCTCCGAGT-3' and 5'-TGTGGGCACACACCTCTGGG-3', respectively. The sequences of the forward and reverse primers for RPL19 are 5'-GCTGCTCAGAAGATACCGTCA-3' and 5'-TTGTCTGCCTTCAGCTTGTG-3', respectively (Applied Biosystems, Foster, CA). The RPL19 primer was used as an internal control. The mean fold difference ($2^{-\Delta\Delta CT}$) in RhoA and RhoC mRNA expression in response to different particles was calculated following published protocols and normalized to untreated cells used as a negative control[28].

The change in the amount of RhoA and RhoC protein expression in treated SUM149 and MDA-MB-231 cells was quantified using western blotting techniques following established protocols[29]. Briefly, after the 48 h transfection cycle, the cells were washed in cold PBS and incubated with RIPA lysis buffer on ice for 5 min. The lysed cells were centrifuged at 14,000 rpm for 15 min to isolate the supernatant containing the protein fraction. The total protein concentration was measured using the *b*icinchoninic acid *assay* (Pierce Biotechnology, Rockford, IL) following manufacturer's protocol. Equal amounts of protein extracts (10 µg) obtained from different particle treatments were resolved by 12% sodium dodecyl sulfate-polyacrylamide gel electrophoresis (SDS-PAGE) before transferring to a polyvinylidene fluoride (PVDF) membrane using a semidry apparatus (Bio-Rad, Hercules, CA). Membranes were probed overnight at 4 °C with anti-β-actin rabbit antibody (Santa Cruz, CA) at a 1:1000 dilution and primary anti-RhoC rabbit monoclonal antibody (Cell Signaling Technologies, MA) or anti-RhoA mouse antibody (Santa Cruz, CA) at a 1:500 dilution. Bound primary antibodies were visualized using enhanced chemiluminescence (Pierce, Rockford, IL) after incubating with secondary horseradish peroxidase-coupled anti-rabbit or anti-mouse antibody (Santa Cruz, CA) at a 1:1000 dilution for 1 h at room temperature. The knockdown of RhoA and RhoC proteins in response to different particles was quantified using the ImageJ software (NIH, Bethesda, MD) and normalized to the endogenous β-actin control and untreated SUM149 and MDA-MB-231 cells. Five replicates were used for each condition in each experiment and the results show the average + the standard error of the mean (SEM).

3.2.6 Boyden chamber invasion assay

We used BD matrigel invasion assay chambers (BD Biosciences, Bedford, MA) to quantify cell invasion in both SUM149 and MDA-MB-231 cells as per manufacturer's instructions. Briefly, SUM149 and MDA-MB-231 cell lines were plated in 6-well plates at a seeding density of 300,000 cells per well and allowed to adhere for 18 h. The adhered cells were then treated with "smart" anti-RhoC (+) and scrambled (-) particles prepared by complexing β-CD-g-P(HMA$_{79}$-*co*-DMAEMA$_{33}$-*co*-TMAEMA$_{48}$)$_{4.8}$ polymer with 2.28μg of anti-RhoC (+) and scrambled (-) siRNA molecules at a N/P ratio of 2.5/1 for 6 h in serum-free OPTI-MEM, followed by the addition of 1mL of fresh culture medium to each well. After a total of 12 h, the culture medium was aspirated, replaced with serum-free OPTI-MEM containing the same particle mixtures for a second transfection cycle. After a total of 24 h, cells were washed with PBS, trypsinized using 0.05% Trypin/EDTA, and centrifuged to collect the cell pellets before suspending them in serum-free culture medium at a density of 50,000 cells per mL. The matrigel-coated inserts were rehydrated in serum-free media before adding 0.5 mL of the cell suspension to each insert. Wells in the culture dish were filled with 0.75 mL serum-containing medium before placing the inserts with the seeded cells in each well and incubating for 24 h at 37°C. Adherent cells in the upper chamber that did not invade through the matrigel layer were gently removed using cotton swabs, while the adherent cells on the lower surface of each insert were stained with 1% crystal violent in 20% methanol for 1 h followed by rinsing with water to remove excess dye. The stained cells were dissolved in 10% acetic acid and their absorbance was measured at 560 nm. Results were normalized to the untreated SUM149 and MDA-MB-231 cells and reported as the average of three independent experiments + SEM.

3.2.7 Random motility assay

Random cell motility was determined by using a motility assay kit following manufacturer's specifications (Cellomics, Pittsburg, PA). The β-CD-g-P(HMA$_{79}$-*co*-DMAEMA$_{33}$-*co*-TMAEMA$_{48}$)$_{4.8}$ polymer was mixed with 2.28 µg of anti-RhoC (+) or scrambled (-) siRNA at a N/P ratio of 2.5/1 to prepare "smart" anti-RhoC (+) and scrambled (-) particles, respectively. SUM149 and MDA-MB-231 cells were transfected with "smart" anti-RhoC siRNA (+) and scrambled siRNA (-) particles, respectively, following the same protocol used in the Boyden chamber invasion assay. The treated cells were harvested in regular culture medium, and plated at a seeding density of 1,000 cells per well on the top of microscopic fluorescent beads evenly distributed in 96-well plates coated with collagen I (Life technologies, Carlsbad, CA). After incubation for 24 h at 37°C, the cells were fixed in formaldehyde and were stained with rhodamine-conjugated phalloidin. Track and cell areas were quantified using the ImageJ software (NIH, Bethesda, MD). Cell motility for each treatment condition was calculated by dividing the track area by the cell area. The average track area per cell for particle-treated cells was normalized to the average track area observed with untreated cells. Results are the average + SEM of five independent replicates.

3.2.8 Scratch assay

We evaluated the effect of “smart” anti-RhoC (+) particles prepared at N/P ratio of 2.5/1 on the migratory activity of SUM149 and MDA-MB-231 cells compared to scrambled (-) particles using the wound healing assay. SUM149 and MDA-MB-231 cells were plated in 24-well plates at a seeding density of 50,000 cells/ well and allowed to grow under normal culture conditions to 95% confluence. The cell monolayer was scratched with a sterile 200μL pipette tip to create a “wound” across the center of each well. Each well was washed with PBS to remove the detached cells, and the wound was imaged (t = 0 h) at a 10X magnification using a Nikon Eclipse Ti inverted microscope equipped with a camera to capture phase contrast images of the wound. Subsequently, the SUM149 and MDA-MB-231 cell monolayers were treated with “smart” anti-RhoC (+) or scrambled (-) particles prepared at an N/P ratio of 2.5/1 following the same protocol used in the Boyden chamber invasion assay. After 36 h, the wounds were imaged at a 10X magnification using the same microscope setup. The acquired images were processed using Green’s theorem to calculate the wound area at t = 0 h and 36 h. The wound area after 36 h was normalized to the initial area (t = 0 h) to quantify the change in cell migration in response to different particles.

3.2.9 Statistical analysis

Results are presented as the mean ± standard error of the mean (SEM). Comparisons of various “smart” particle parameters (i.e., size, zeta potential, and cell uptake) at varying N/P ratios were done using one-way ANOVA with Tukey’s post hoc analysis. Statistical difference between group population means (i.e., varying N/P ratios) was significant at the 0.05 level. Statistical difference between particles encapsulating anti-RhoC (+) and scrambled (-) siRNA sequence was evaluated using paired *t* test where the population means were statistically significant at $p \leq 0.05$. Similarly, the difference between particles encapsulating scrambled (-) siRNA sequence and untreated controls in both cell lines was evaluated using paired *t* test where the population means were statistically significant at $p \leq 0.05$.

3.3 Results and Discussion

3.3.1 Formulation and characterization of "smart" particles

We successfully utilized the asymmetric distribution of seven primary (C-6) and fourteen secondary (C-2 and C-3) hydroxyl (OH) groups on opposite sides of the β-CD core to graft the amphiphilic P(HMA$_{79}$-*co*-DMAEMA$_{81}$) polymers from the secondary face via acid-labile linkers technique following our published methods[25]. We grafted ~ five 25kDa polymer chains with an average 50/50 molar ratio of hydrophobic HMA and pH-sensitive DMAEMA monomers followed by 50% quaternization of DMAEMA monomers into TMAEMA to prepare star-shaped β-CD-g-P(HMA$_{79}$-*co*-DMAEMA$_{33}$-*co*-TMAEMA$_{48}$)$_{4.8}$ polymers. The polymer composition used in our study previously showed fragmentation in response to the acidic pH of the endosome (pH 5.8) within 6 h[25]. The membrane active P(HMA$_{79}$-*co*-DMAEMA$_{33}$-*co*-TMAEMA$_{48}$) grafts released from the β-CD core were successful in destabilizing the endosomal membrane and proved most effective in delivering their siRNA cargo into the cytoplasm of multiple epithelial cancer cells[25, 30].

We evaluated the ability of our "smart" β-CD-g-P(HMA$_{79}$-*co*-DMAEMA$_{33}$-*co*-TMAEMA$_{48}$)$_{4.8}$ particles complexing scrambled siRNA at different N/P (+/-) ratios using the standard gel retardation assay. The results show complete condensation of our β-CD-g-P(HMA$_{79}$-*co*-DMAEMA$_{33}$-*co*-TMAEMA$_{48}$)$_{4.8}$ polymers with the loaded siRNA molecules to form stable particles that were retained in the loading wells at N/P ratios as low as 1.5/1 **(Figure 3.3 A)**. This complexation ratio (i.e., 1.5/1) is relevant as it much lower than the N/P ratios > 10/1[31, 32] of commonly used transfection reagents like polyethylenimine (PEI) and cationic PAMAM dendrimers. Therefore, resulting in a significant improvement over existing carriers as it warrants the use of small amounts of β-CD polymer for the condensation and delivery of a high dose of siRNA molecules, thereby, reducing the associated side effects[33].

Results show that β-CD particles prepared at a N/P ratio of 1.5/1 had an average size of 154 ± 1.4 nm, which dropped to 112 ± 1.9 nm and 104 ± 2.0 nm upon increasing the N/P ratio to 2.5/1 and 4/1, respectively **(Figure 3.3 B)**. This is not surprising given that the increase in N/P ratio increases the number of cationic TMAEMA monomers available to complex the anionic phosphate groups, which results in better condensation and tighter packing of the siRNA cargo indicated by the smaller particle size. The drop in the particle size at different N/P ratios was compared using one-way ANOVA (Tukey's post hoc) analysis and showed no statistical difference. Increasing the N/P ratio to 8/1 and 12/1 increased particle's size to 180 ± 1.7 nm and 151 ± 1.3 nm, which may be a result of the loose association of excess polymer with the particle's surface. However, as the molecular size cut off for tumor vasculature is between 400 and 600 nm[34, 35], "smart" particles prepared at all N/P ratios are suited for delivery of therapeutic siRNA cargo into solid tumors[34]. Results show that particles' zeta potential increased from 37 ± 1.21 mV for the those prepared at a N/P ratio of 1.5/1 to 50 ± 1.18 mV for the particles prepared at N/P ratio of

12/1 **(Figure 3.3 B)**. The observed increase in zeta potential as a function of increasing N/P ratios was not significantly different. The positive zeta potential confirms the cationic nature of "smart" particles' surface, which will mediate their efficient internalization by epithelial cancer cells via adsorptive endocytosis[24, 36, 37].

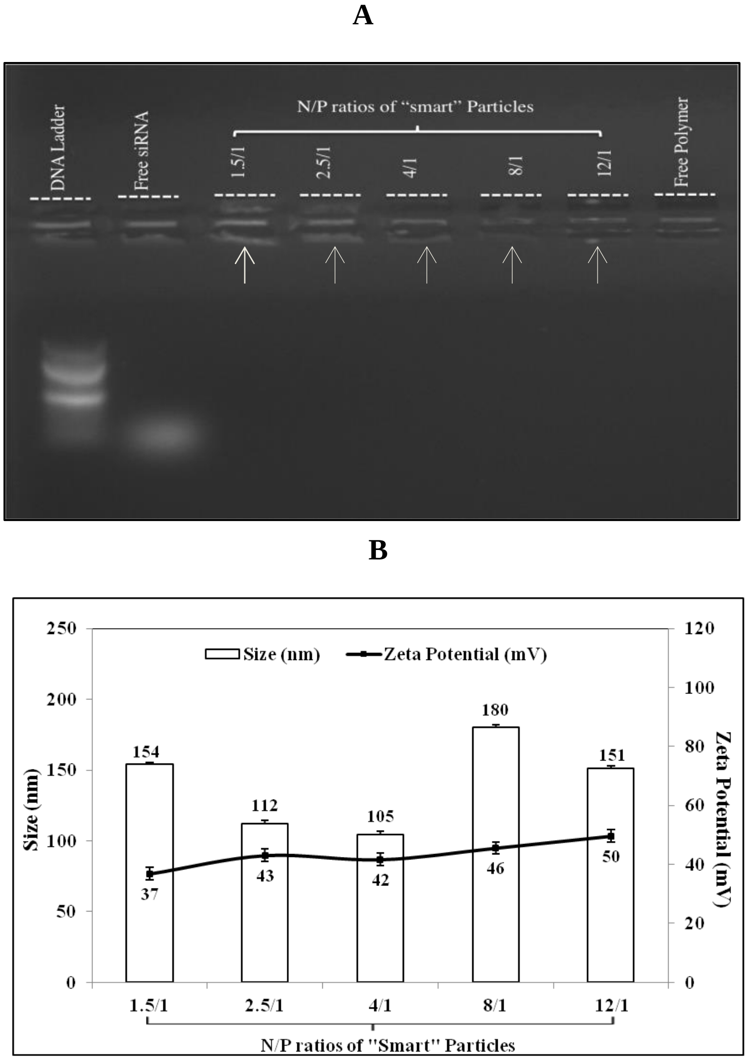

Figure 3.3: (A) Image of 1% w/v agarose gel containing ethidium bromide showing the electrophoretic mobility of free siRNA and "smart" particles prepared by the complexation of β-CD-g-P(HMA$_{79}$-*co*-DMAEMA$_{33}$-*co*-TMAEMA$_{48}$)$_{4.8}$ polymer with anti-GAPDH siRNA (0.71 µg) at different N/P (+/-) ratios. **(B)** Size (white bars) and zeta potential (solid squares) of "smart" particles prepared by complexation of β-CD-g-P(HMA$_{79}$-*co*-DMAEMA$_{33}$-*co*-TMAEMA$_{48}$)$_{4.8}$ polymer with anti-GAPDH siRNA (1.4 µg) at different N/P (+/-) ratios. Results are the average ± SEM.

3.3.2 Cellular uptake of "smart" particles

We prepared fluorescently-labeled particles by complexating β-CD-g-P(HMA$_{79}$-*co*-DMAEMA$_{33}$-*co*-TMAEMA$_{48}$)$_{4.8}$ polymers with FAM-labeled anti-GAPDH siRNA at different N/P ratios and evaluated their uptake into both cell lines compared to free siRNA and siPORT amine-based complexes using flow cytometry. Results show insignificant uptake of free siRNA indicated by the low fraction of fluorescently-labeled SUM149 (0.4 ± 0.1%) and MDA-MB-231 (15.2 ± 1.8%) cells **(Figure 3.4, Panel A)**. "Smart" particles prepared at 1.5/1, 2.5/1, and 4/1 N/P ratios exhibited similar and efficient uptake by SUM149 and MDA-MB-231 cells indicated by fluorescence labeling of 98% - 100% of the treated cells. Incubating the cells with "smart" particles prepared an 8/1 and 12/1 N/P ratios reduced the fraction of fluorescently-labeled SUM149 and MDA-MB-231 cells to 90% and 83%-85%, respectively **(Figure 3.4, Panel A)**. Uptake of "smart" particles prepared at all N/P ratios was statistically higher than free siRNA ($p \leq 0.005$) but there was no statistical difference between all particles. The drop in the number of fluorescent cells can be attributed to higher positive surface charge density on particles' surface due to the excess of cationic β-CD-based polymer used for siRNA complexation, which may result in cell death similar to other cationic particles[38, 39]. Therefore, we limited our studies to "smart" particles prepared at a N/P ratio of 2.5/1 and investigated their ability to deliver anti-RhoC siRNA into the cytoplasm of SUM149 and MDA-MB-231 breast cancer cells by quantifying the knockdown in RhoC expression at the mRNA and protein levels.

We also visualized the uptake of "smart" β-CD particles encapsulating FITC-labeled siRNA (P + siRNA) and free FITC-labeled siRNA (free siRNA) in SUM149 and MDA-MB-231 cells using confocal laser scanning microscopy. Confocal microscopy images of SUM149 **(Figure 3.4, Panel B)** and MDA-MB-231 **(Figure 3.4, Panel C)** cells incubated with "smart" β-CD particles loaded with FITC-labeled siRNA show a strong and uniform distribution of green fluorescence in the cytoplasm indicating efficient particle internalization by endocytosis. In comparison, images of the cell treated with free FITC-labeled siRNA shows no green fluorescence of the cytoplasm indicating poor RNA internalization **(Figure 3, Panel B and C)**. Confocal microscopy images provide visual evidence of particles internalization by both cancer cell lines.

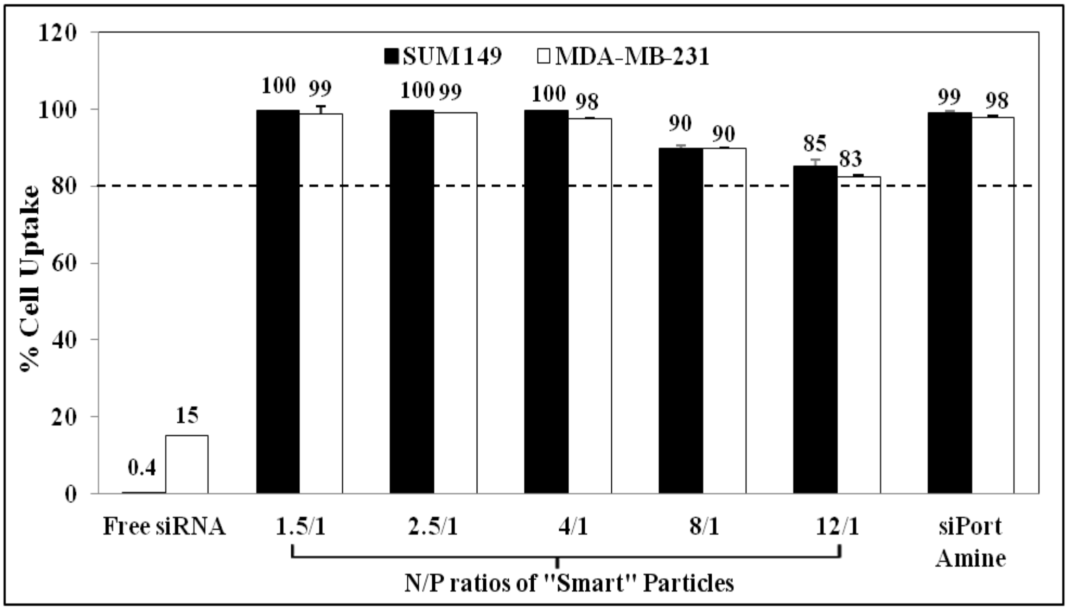

Figure 3.4 (A): Percentage of fluorescently-labeled SUM149 and MDA-MB-231 breast cancer cells after incubating for 6 h in a serum-free culture medium with free siRNA, siPORT amine-based complexes, and “smart” particles prepared by complexation of β-CD-g-$P(HMA_{79}\text{-}co\text{-}DMAEMA_{33}\text{-}co\text{-}TMAEMA_{48})_{4.8}$ polymer with FAM–labeled anti-GAPDH siRNA (1.14µg) at different N/P ratios. Results are the average + SEM

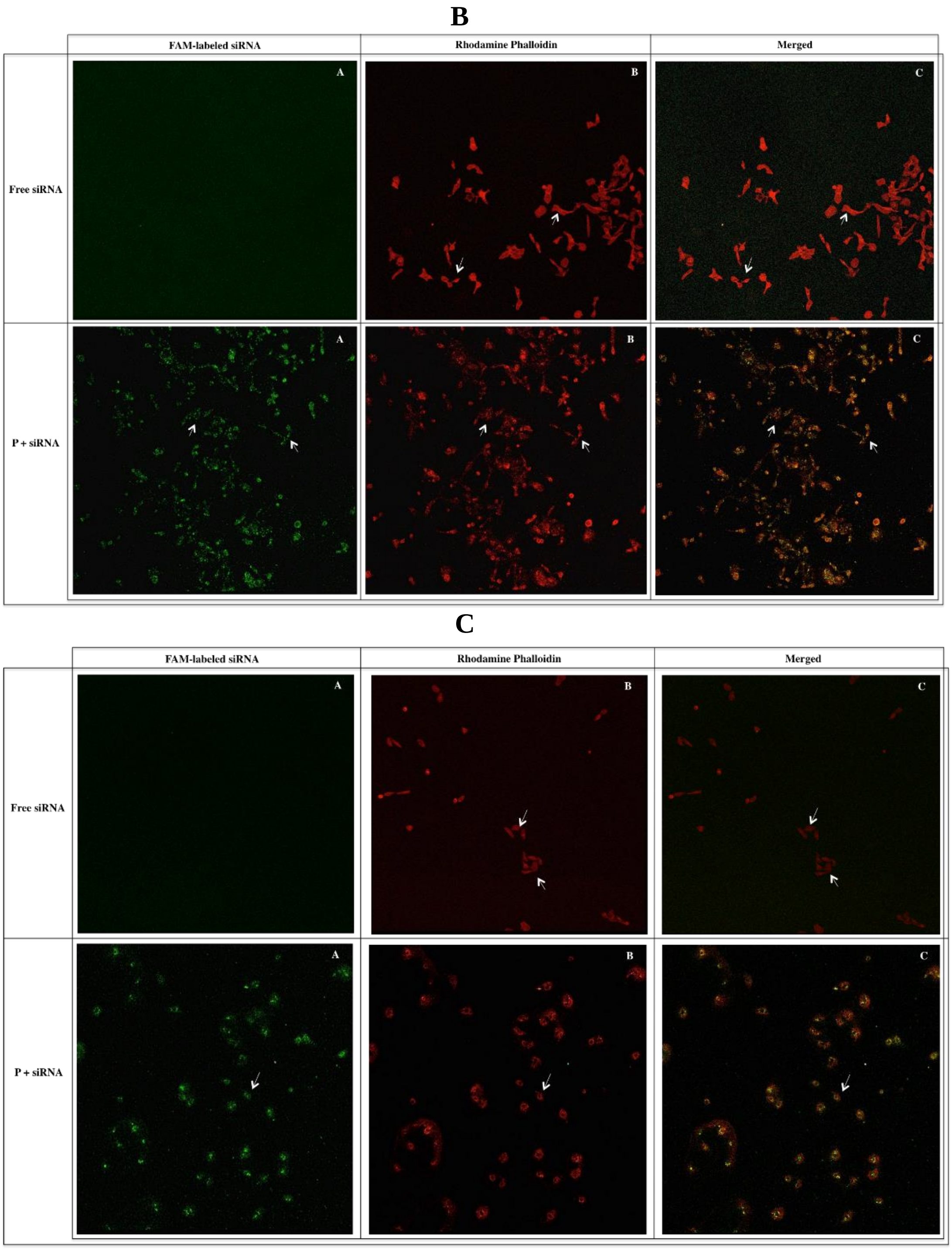

Figure 3.4: Fluorescence images of SUM149 **(B)** and MDA-MB-231 **(C)** cells after incubating with free FITC-labeled siRNA and "smart" βCD particles encapsulating FITC-labeled siRNA at an N/P ratio of 2.5/1 for 6 hours. Cell cytoskeleton was stained with Rhodamine-Phalloidin dye (λ_{ex} = 540 nm; λ_{em} = 565 nm) while the intracellular distribution of FITC-labeled siRNA was visualized at λ_{ex} of 494 nm and λ_{em} of 520 nm.

3.3.3 Silencing RhoC expression in SUM149 and MDA-MB-231 cells

We investigated the ability of "smart" particles prepared at an N/P ratio of 2.5/1 to functionally deliver anti-RhoC siRNA molecules into the cytoplasm of SUM149 and MDA-MB-231 cells by evaluating their ability to selectively knockdown RhoC gene expression at both the mRNA and protein levels compared to scrambled siRNA particles. Results show that our "smart" anti-RhoC siRNA particles (+) knockdown RhoC mRNA expression by 87 ± 1.1% in SUM149 cells compared to scrambled siRNA particles (-) ($p \leq 0.001$) **(Figure 3.5 A)**. Similarly, "smart" anti-RhoC particles (+) knockdown RhoC mRNA level by 70 ± 11.4% in MDA-MB-231 cells compared to their scrambled counterparts (-) ($p \leq 0.01$) **(Figure 3.5 A)**.

Anti-RhoC particles (+) prepared using siPORT-Amine transfection agent reduced RhoC mRNA level by 86 ± 1.9% ($p \leq 0.001$) and 80% ± 11.7% ($p \leq 0.05$) compared to scrambled siRNA particles (-) in SUM149 and MDA-MB-231 cell lines, respectively. "Smart" particles encapsulating the scrambled siRNA sequence (-) caused no statistical difference in RhoC mRNA levels compared to that observed in untreated SUM149 and MDA-MB-231 cells, which indicates the biocompatibility of the β-CD-g-P(HMA$_{79}$-*co*-DMAEMA$_{33}$-*co*-TMAEMA$_{48}$)$_{4.8}$ carrier **(Figure 3.5 A)**.

We quantified the change in RhoC protein expression in SUM149 and MDA-MB-231 when transfected with "smart" anti-RhoC particles (+) prepared at N/P ratio of 2.5/1 and loaded with 100nM of the RNA cargo compared to particles loaded with the scrambled siRNA sequence (-). Results show 100% reduction in RhoC protein level in SUM149 cells treated with the anti-RhoC (+) particles compared to those treated with scrambled one (-) **(Figure 3.5 B)**. Similarly, "smart" anti-RhoC (+) particles reduced RhoC protein expression by 90% in MDA-MB-231 cells compared to particles loaded with the scrambled siRNA sequence (-) **(Figure 3.5 C)**. In comparison, anti-RhoC particles prepared using the commercial siPORT-Amine carrier reduced RhoC protein expression by only 34% and 28% in SUM149 and MDA-MB-231 cells, respectively. The limited effect of anti-RhoC siPORT-Amine particles on RhoC protein levels in SUM149 **(Figure 3.5 B)** and MDA-MB-231 cells **(Figure 3.5 C)** compared to their more pronounced effect on RhoC mRNA levels **(Figure 3.5 A)** can be attributed to several factors including slow and incomplete dissociation of the siRNA from the cationic carrier observed with PEI-based complexes[40] and higher degradation of the released siRNA molecules[41]. These results clearly show the ability of the β-CD-g-P(HMA$_{79}$-*co*-DMAEMA$_{33}$-*co*-TMAEMA$_{48}$)$_{4.8}$ polymer to condense the desired dose (100nM) of anti-RhoC siRNA at a low N/P ratio forming "smart" particles that successfully delivered their cargo into the cytoplasm of SUM149 and MDA-MB-231 knocking down RhoC expression at the mRNA and protein levels **(Figure 3.5)**.

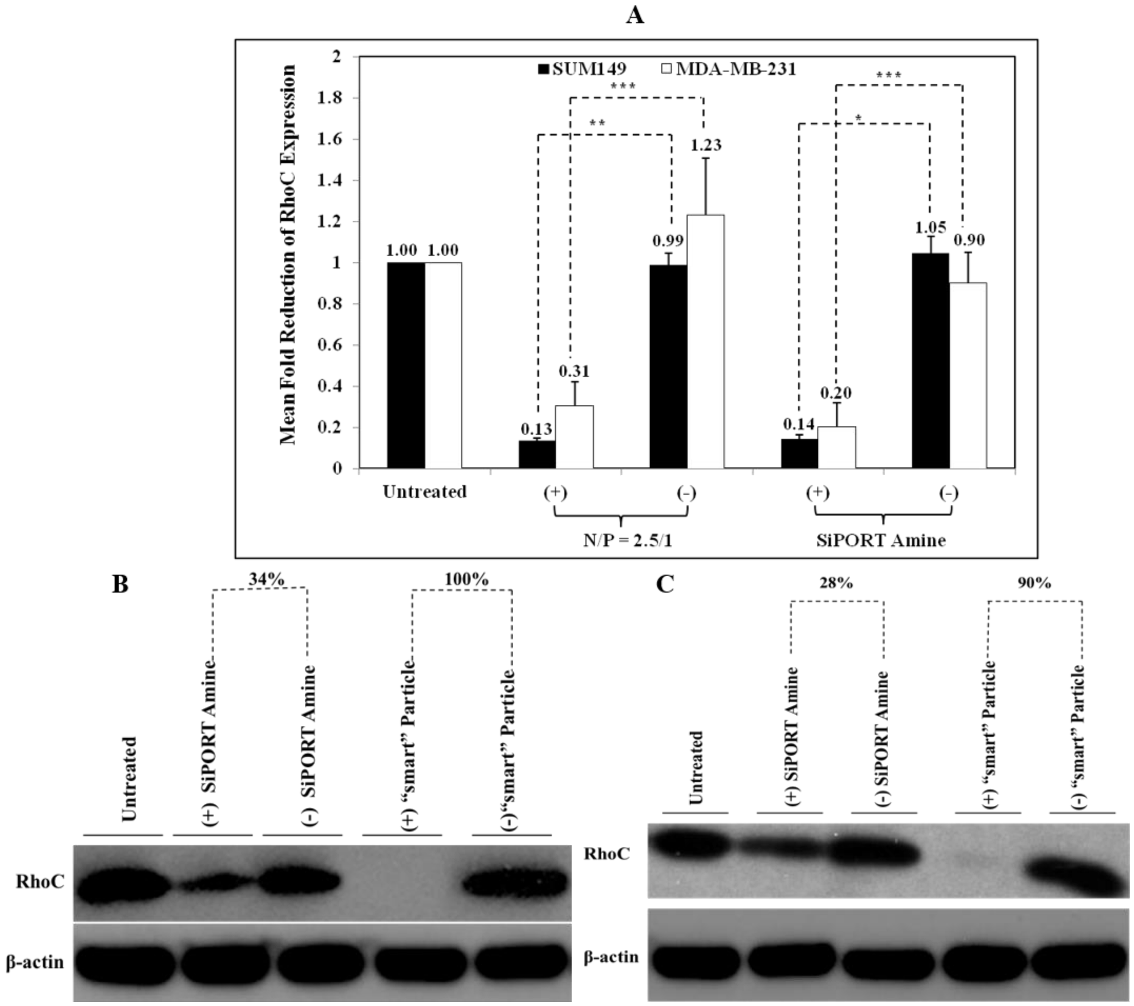

Figure 3.5: Effect of siPORT amine-based complexes and "smart" particles prepared by complexing β-CD-g-P(HMA_{79}-*co*-$DMAEMA_{33}$-*co*-$TMAEMA_{48}$)$_{4.8}$ polymer with 1.14µg of anti-RhoC (+) or scrambled (-) siRNA at N/P ratio of 2.5/1 on **(A)** RhoC mRNA and protein levels in **(B)** SUM149 and **(C)** MDA-MB-231 cells. Results are the average + the standard error of the mean of five replicates. Statistical difference between particles encapsulating anti-RhoC (+) and scrambled (-) siRNA sequence was evaluated using paired *t* test where * denotes $p \leq 0.05$, ** denotes $p \leq 0.01$ and, *** denotes $p \leq 0.005$.

Given that the protein sequences of RhoA and RhoC are approximately 90% homologous[27], we investigated the change in RhoA mRNA and protein levels in SUM149 cells upon treatment with "smart" anti-RhoC particles. ANOVA tests show no statistical significance in RhoA mRNA **(Figure 3.6 A)** and protein **(Figure 3.6 B)** expression levels between SUM149 cells treated with "smart" anti-RhoC particles (+) and the scrambled control (-). These results show the specificity of "smart" anti-RhoC particles and confirm that the observed changes in cell invasion, migration, and motility are a direct result of RhoC knockdown. Further, this is an additional indication of the biocompatibility of the β-CD-g-P(HMA$_{79}$-*co*-DMAEMA$_{33}$-*co*-TMAEMA$_{48}$)$_{4.8}$ polymer.

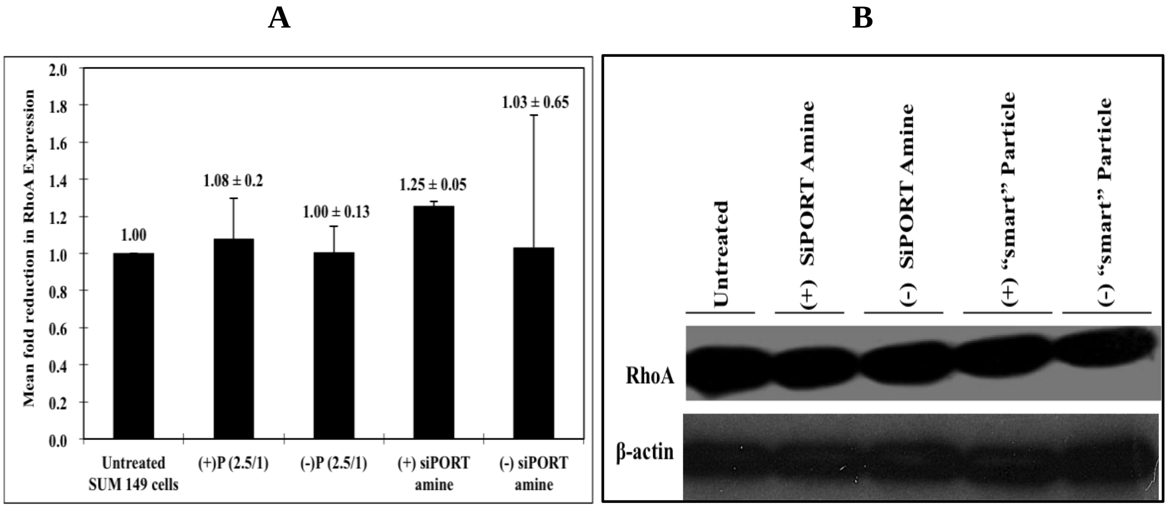

Figure 3.6: Effect of siPORT amine-based complexes and "smart" particles prepared by complexing the respective polymers with anti-RhoC siRNA (+) or scrambled siRNA (-) on **(A)** RhoA mRNA and **(B)** protein level in SUM149 cells after 48 h. Results are the average + the standard error of the mean of five replicates. Statistical difference between particles encapsulating anti-RhoC siRNA (+) and scrambled siRNA sequence (-) was evaluated using paired *t* test where * denotes $p \leq 0.05$, ** denotes $p \leq 0.01$ and, *** denotes $p \leq 0.005$.

3.3.4 Effect of RhoC knockdown on cell invasion

We evaluated the effect of RhoC knockdown using "smart" anti-RhoC particles (+) on the invasion of SUM149 and MDA-MB-231 cells through matrigel basement membrane using the Boyden chamber invasion assay **(Figure 3.7 A)**. Results show statistically significant ($p \leq 0.01$) reduction in the invasion of SUM149 cells transfected with "smart" anti-RhoC particles loaded with 100nM of siRNA by 40 ± 0.4% compared to their scrambled controls (-) **(Figure 3.7 B)**. Similarly, invasion of MDA-MB-231 cells transfected with "smart" anti-RhoC particles loaded with 100nM of siRNA is reduced by 47 ± 0.2% compared to scramble particles (-) **(Figure 3.7 B)**.

Treatment of SUM149 and MDA-MB-231 cells with "smart" particles loaded with the scrambled siRNA sequence (-) did not cause a statistically significant change in cell invasion through the matrigel matrix compared to untreated cells (control group) **(Figure 3.7 B)**. These results are in agreement with previous reports showing that double transfection of MDA-MB-231 cells with anti-RhoC siRNA using cytofectin as a carrier suppressed cell invasion by 70%[20].

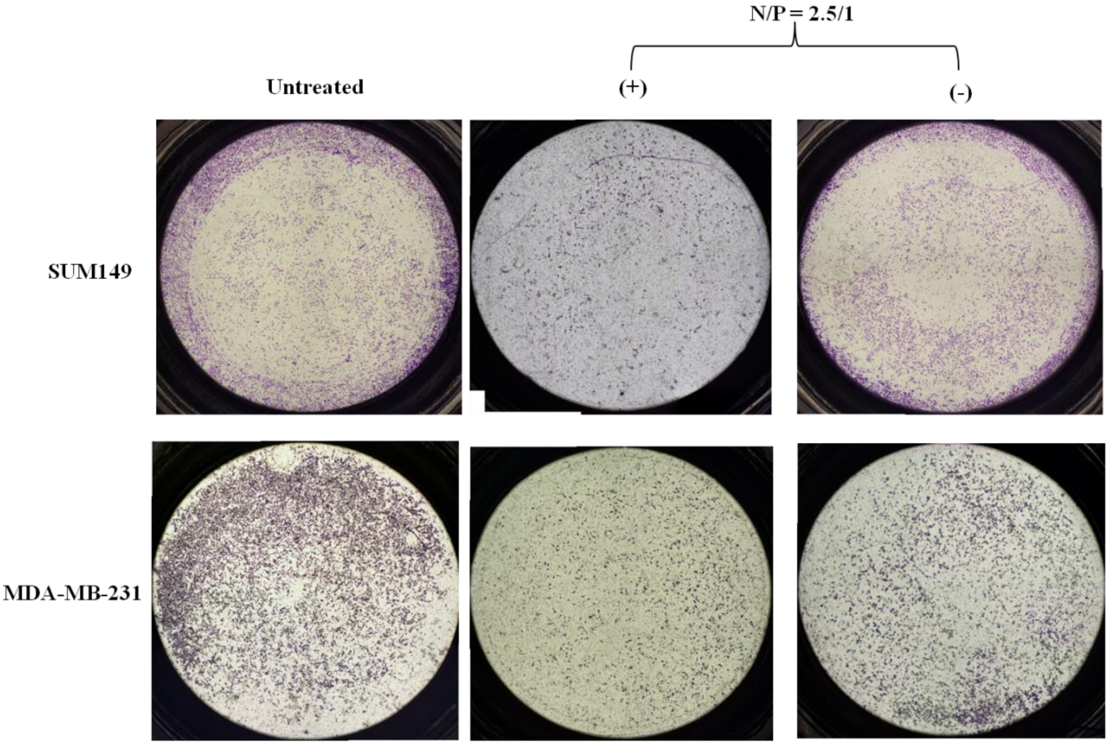

Figure 3.7 (A): SUM149 and MDA-MB-231 cells were plated on Matrigel invasion chambers and treated with "smart" particles prepared by complexing β-CD-g-P(HMA_{79}-co-$DMAEMA_{33}$-co-$TMAEMA_{48}$)$_{4.8}$ polymer with 1.14μg of anti-RhoC siRNA (+) or scrambled siRNA (-). Representative images of the invaded SUM149 and MDA-MB-231 cells on the lower membrane.

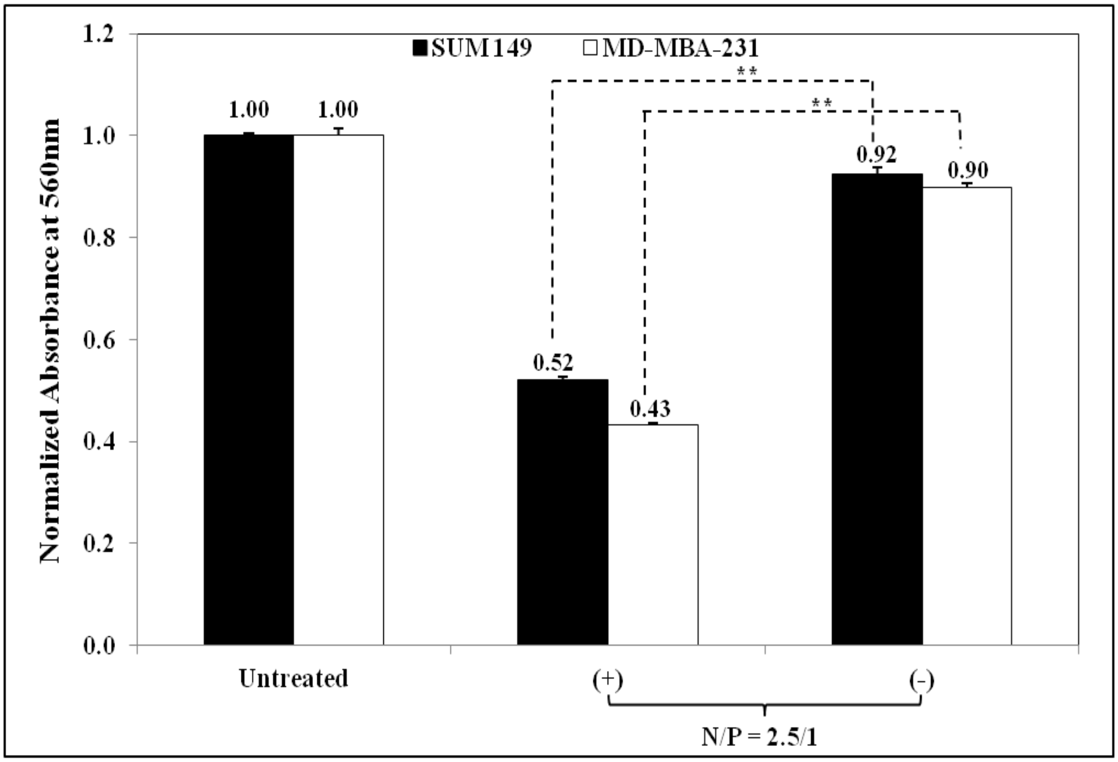

Figure 3.7 (B): The 1% crystal violet used to stain the invaded SUM149 and MDA-MB-231 cells on the lower membrane was dissolved in 10% acetic acid and its absorbance was measured at 560 nm. Absorbance of cells treated with "smart" anti-RhoC (+) and the scrambled (-) particles was normalized to that of untreated cells (control group). Plotted results are the average + the standard error of the mean of five replicates. Statistical difference between "smart" anti-RhoC (+) and scrambled (-) particles was evaluated using paired *t* test where * denotes $p \leq 0.05$, ** denotes $p \leq 0.01$ and, *** denotes $p \leq 0.005$.

3.3.5 Effect of RhoC knockdown on cell motility

We started by quantifying the effect of RhoC knockdown on the phagokinetic motility of SUM149 and MDA-MB-231 cells using Cellomics Random Motility Assay Kit where we measured the area of the phagokinetic tracks of each migrating cell using ImageJ software (NIH, Bethesda, MD).

We normalized the area of the phagokinetic tracks of cells treated with “smart” anti-RhoC particles (+) and those loaded with the scrambled siRNA sequence (-) to the area of the phagokinetic tracks of untreated cells (control group) to calculate the % reduction in cell motility. Results show 60 ± 8.7% inhibition in the migration of SUM149 cells treated with “smart” anti-RhoC particles (+) compared to those treated with the scramble particles (-) **(Figure 3.8)**. Similarly, migration of MDA-MB-231 cells treated with “smart” anti-RhoC particles (+) was reduced by 57 ± 1.1% compared to the cells treated with the negative scramble control (-) **(Figure 3.8)**. These results show a statistically significant ($p \leq 0.001$) reduction in the migration of SUM149 and MDA-MB-231 cells treated with “smart” anti-RhoC particles compared to the cells transfected with the scrambled siRNA sequence (-). In addition, there was no change in the migration of SUM149 and MDA-MB-231 cells transfected with the scrambled siRNA sequence (-) compared to untreated cells (control group) indicating the lack of non-specific effect of the polymeric carrier on cell survival or migration **(Figure 3.8)**.

We also used the wound-healing assay to investigate the change in cell migration in response to different treatments following established protocols[42, 43]. Images show that SUM149 **(Figure 3. 9 A)** and MDA-MB-231 cells **(Figure 3.9 B)** treated with “smart” particles loaded with the scrambled siRNA sequence retained their migration capacity indicated by complete “healing” of the scratch after 36 h similar to untreated cells (control group). In comparison, SUM149 and MDA-MB-231 cells treated with “smart” anti-RhoC particles (+) exhibited reduced migration indicated by the incomplete healing of the scratched area. Using Green’s theorem to calculate the unoccupied area of the scratch after 36 h and normalizing it to the initially scratched surface (at $t = 0$ h), results show coverage of only 33 ± 5.4% of the scratched surface by SUM149 cells treated with “smart” anti-RhoC particles, which is statistically ($p \leq 0.01$) less than the 94.2 ± 4.4% wound coverage observed for the cells transfected with the scrambled siRNA sequence (-) **(Figure 3.9 C)**. Similarly, MDA-MB-231 cells treated with "smart" anti-RhoC particles (+) occupied only 33.1 ± 20.4% of the wound area, which is statistically ($p \leq 0.05$) less than the 106.1 ± 24.4% wound coverage observed for the cells transfected with the scrambled siRNA sequence (-) **(Figure 3.9 C)**. These results clearly show that knockdown of RhoC expression inhibits the migration of SUM149 and MDA-MB-231 cells by 61.5% and 73%, respectively.

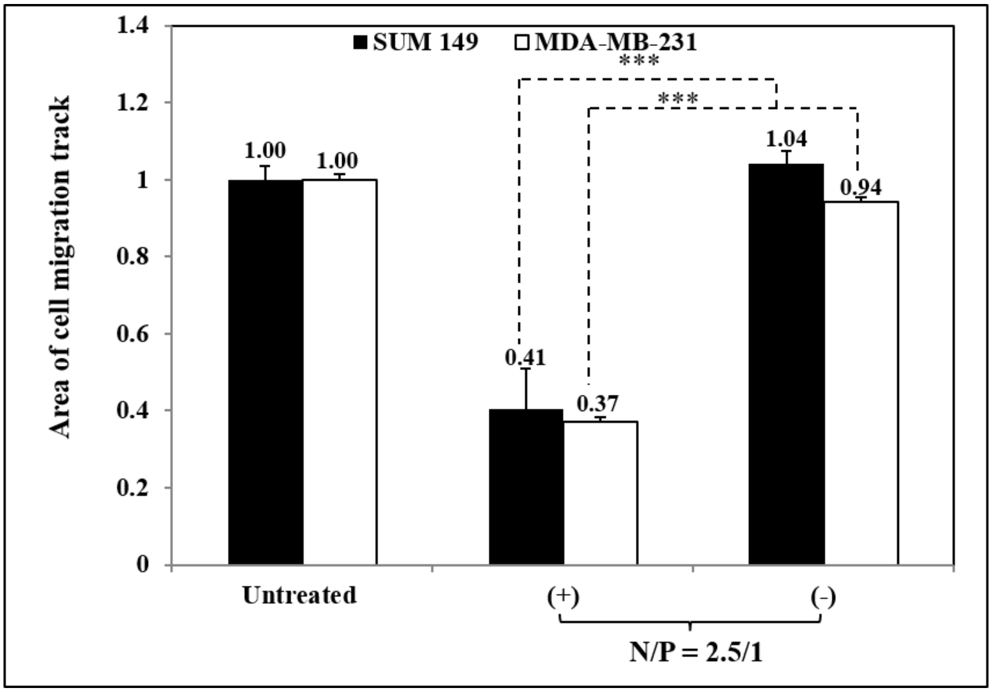

Figure 3.8: Effect of "smart" anti-RhoC (+) and the scrambled (-) particles on the phagokinetic motility of SUM149 and MDA-MB-231 cells. The phagokinetic cell tracks were quantified using ImageJ software and the average track area per cell transfected with "smart" anti-RhoC (+) and the scrambled (-) particles were normalized to that of untreated cells. Statistical difference between "smart" anti-RhoC (+) and scrambled (-) particles was evaluated using paired *t* test where * denotes $p \leq 0.05$, ** denotes $p \leq 0.01$ and, *** denotes $p \leq 0.005$.

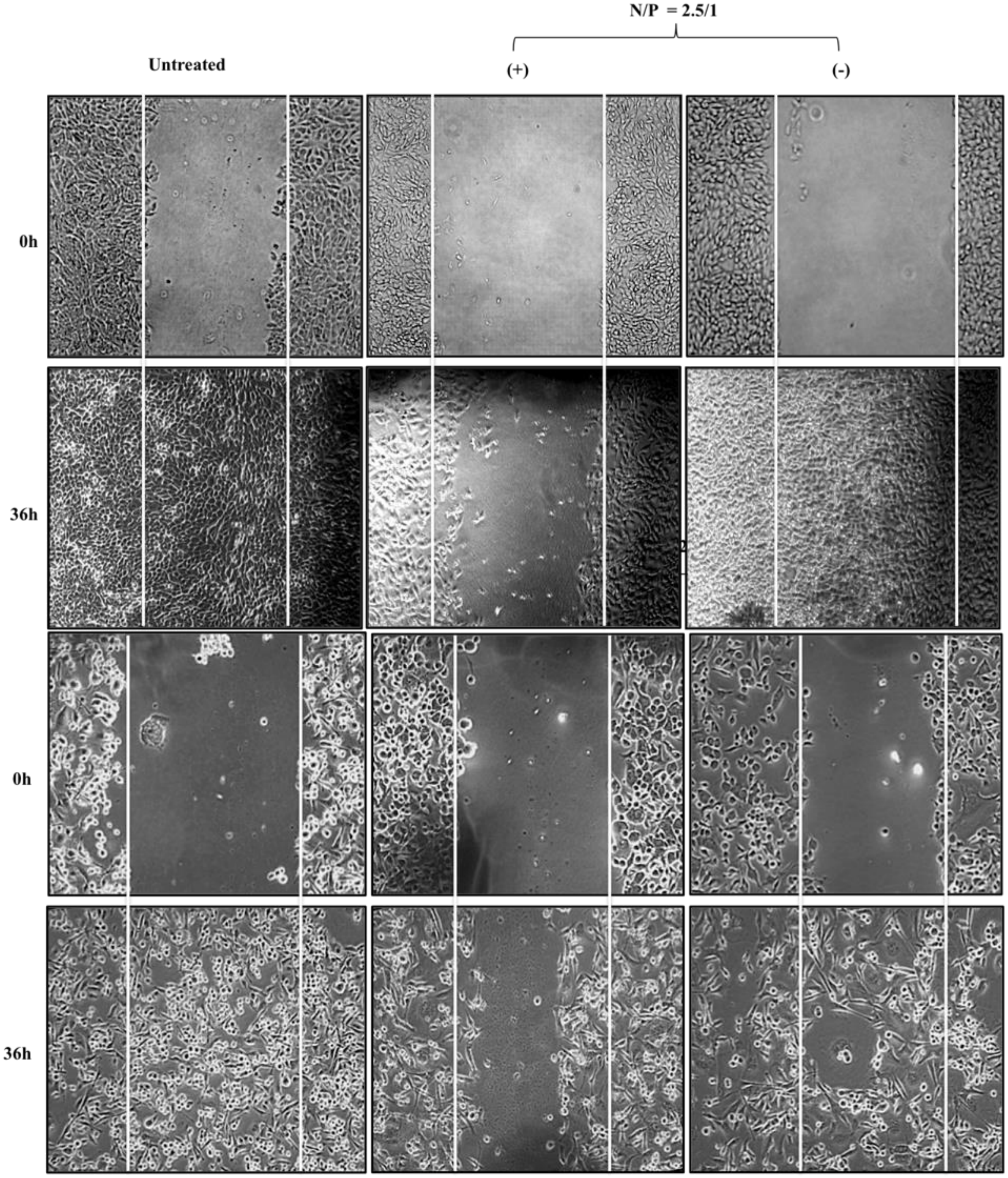

Figure 3.9: Representative images (10X magnification) showing the effect of "smart" anti-RhoC (+) and scrambled (-) particles on the migration of **(A)** SUM149 and **(B)** MDA-MB-231 cells.

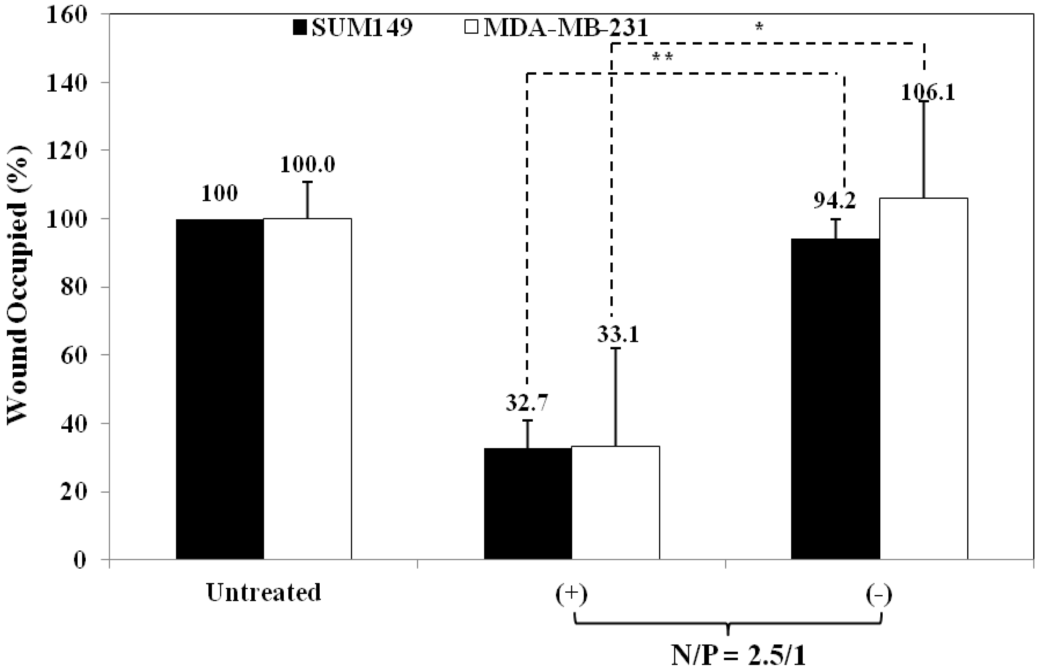

Figure 3.9 (C): The percentage of wound coverage by SUM149 and MDA-MB-231 cells 36 hours after treatment with “smart” anti-RhoC (+) and scrambled (-) particles normalized to the initial wound (t = 0 h). Plotted results are the average + the standard error of the mean of three replicates. Statistical difference between “smart” anti-RhoC (+) and scrambled (-) particles was evaluated using paired *t* test where * denotes $p \leq 0.05$, ** denotes $p \leq 0.01$ and, *** denotes $p \leq 0.005$.

References

1. *Metastatic Cancer Fact Sheet*; *J. Natl. Cancer Inst.: 2013.*

2. *Breast Cancer: Facts & Figures 2013-2014*; *Cancer News:* 2014.

3. Bacac, M.; Stamenkovic, I. Metastatic Cancer Cell. *Annu. Rev. Pathol.: Mech. Dis.* **2008,** *3*, 221-47.

4. Eger, A.; Mikulits, W. Models of epithelial–mesenchymal transition. *Drug Discovery Today: Dis. Models* **2005,** *2*, 57-63.

5. Steeg, P.S.; Hartsough, M.T.; Clare, S.E. Nm23, breast differentiation, cancer metastasis. *Contemp. Cancer Res.* ***1*998**, (267-283).

6. Sahai, E.; Marshall, C.J. RHO–GTPases and cancer. *Nat. Rev. Cancer* **2002,** *2*, 133-142.

7. Roberts, P. J.; Mitin, N.; Keller, P. J.; Chenette, E. J.; Madigan, J. P.; Currin, R. O.; Cox, A. D.; Wilson, O.; Kirschmeier, P.; Der, C. J. Rho Family GTPase Modification and Dependence on CAAX Motif-signaled Posttranslational Modification. *J. Biol. Chem.* **2008,** *283(37)*, 25150-25163.

8. Etienne-Manneville, S.; Hall, A. Rho GTPases in cell biology. *Nature* **2002,** *420(6916)*, (629-635).

9. Wagner, A. C. C.; Williams, J. A. Low molecular weight GTP-binding proteins: molecular switches regulating diverse cellular functions. *Am. J. Physiol.* **1994,** *266*, G1-G14.

10. Hall, A. Small GTP-binding proteins and the regulation of the actin cytoskeleton. *Annu. Rev. Cell Biol.* **1994,** *10*, 31-54.

11. Hall, A. Rho GTPases and the actin cytoskeleton. *Science* **1998,** *279*, (5350), 509-514.

12. Nobes, C. D.; Hall, A. Rho, Rac, and CDC42 GTPases regulate the assembly of multimolecular focal complexes associated with actin stress fibers, lamellipodia, and filopodia. *Cell* **1995,** *81*, (1), 53-62.

13. Parri, M.; Chiarugi, P. Rac and Rho GTPases in cancer cell motility control. *Cell Commun. Signaling* **2010,** *8*, (1), 1-14.

14. Ridley, A. J.; Hall, A. The small GTP-binding protein Rho regulates the assembly of focal adhesions and stress fibers in response to growth factors. *Cell* **1992,** *70*, 389-399.

15. Ridley, A. J.; Schwartz, M. A.; Burridge, K.; Firtel, R. A.; Ginsberg, M. H.; Borisy, G.; Parsons, J. T.; Horwitz, A. R. Cell Migration: Integrating Signals from Front to Back. *Science* **2003,** *302*, (5651), 1704-1709.

16. Rosenthal, D.T.; Zhang, J.; Bao, L.; Zhu, L.; Wu, Z.; Toy, K.; Kleer, C.G.; Merajver, S. D. RhoC Impacts the Metastatic Potential and Abundance of Breast Cancer Stem Cells. *Plos One* **2012,** *7*, (7).

17. Van Golen, K.; Wu, Z.; Qiao, X.; Bao, L.; Merajver, S.D. RhoC GTPase, a novel transforming oncogene for human mammary epithelial cells that partially recapitulates the inflammatory breast cancer phenotype. *Cancer Res.* **2000,** *60*, (20), 5832 - 5838.

18. Liu, A. X.; Rane, N.; Liu, J. P.; Prendergast, G. C. RhoB is dispensable for mouse development, but it modifies susceptibility to tumor formation as well as cell adhesion and growth factor signaling in transformed cells. *Mol Cell Biol.* **2001,** *21*, 6906–6912.

19. Hakem, A.; Sanchez-Sweatman, O.; You-Ten, A.; Duncan, G.; Wakeham, A.; Khokha, R.; Mak, T. W. RhoC is dispensable for embryogenesis and tumor initiation but essential for metastasis. *Genes Dev.* **2005,** *19*, 1974-1979.

20. Pillé J.Y.; Denoyelle, C.; Varet, J.; Bertrand, J.R.; Soria, J.; Opolon, P.; Lu, H.; Pritchard L.L.; Vannier, J.P.; Malvy, C.; Soria, C.; Li, H. Anti-RhoA and anti-RhoC siRNAs inhibit the

proliferation and invasiveness of MDA-MB-231 breast cancer cells in vitro and in vivo. *Mol Ther.* **2005**, 267-74.

21. Wu, M.; Wu, Z.; Kumar-Sinha, C.; Chinnaiyan, A.; Merajver, S. RhoC Induces Differential Expression of Genes Involved in Invasion and Metastasis in MCF10A Breast Cells. *Breast Cancer Res. Treat.* **2004,** *84*, (1), 3-12.

22. van Golen, K.L.; Wu, Z.; Qiao, Z.T.; Bao, L.; Merajver, S. D. RhoC GTPase, a Novel Transforming Oncogene for Human Mammary Epithelial Cells That Partially Recapitulates the Inflammatory Breast Cancer Phenotype. *Cancer Res.* **2000,** *60*, 5832.

23. Fernandes, C.J.; Qiu, Z.; Winnik, F.M.; Benderdour, M.; Zhang, X.; Dai, K.; Sh, Q. Linear polyethylenimine produced by partial acid hydrolysis of poly(2-ethyl-2-oxazoline) for DNA and siRNA delivery in vitro. *Int. J. Nanomed.* **2013,** *8*, 4091-4102.

24. Lin, Y. L.; Birrell, L. K.; El-Sayed, M.E. Degradable, pH-sensitive, membrane-destabilizing, comb-like polymers for intracellular delivery of nucleic acids. *Biomaterials* **2010**, 7150-66.

25. Durmaz, Y. Y.; Lin, Y.L.; ElSayed, M. E. H. Development of Degradable, pH-Sensitive Star Vectors for Enhancing the Cytoplasmic Delivery of Nucleic Acids. *Adv. Funct. Mater.* **2013,** *23*, (31), 3885-3895.

26. Haddleton, D.M.; Waterson, C. Phenolic Ester based Initiators for Transition Metal Mediated Living Polymerisation. *Macromolecules* **1999,** *32*, 8732-8739.

27. Wu, M.; Wu, Z.; Rosenthal, D.T.; Rhee, E.M.; Merajver, S.D. Characterization of the roles of RHOC and RHOA GTPases in invasion, motility, and matrix adhesion in inflammatory and aggressive breast cancers. *Cancer* **2010,** *116*, (S11), 2768-2782.

28. Livak, K.J.; Schmittgen, T.D. Analysis of Relative Gene Expression Data Using Real-Time Quantitative PCR and the $2^{-\Delta\Delta CT}$ Method. *Methods* **2001,** *25*, (4), 402-408.

29. Wu, M.; Wu, Z.; Rosenthal D.T.; Rhee, E.M.; Merajver, S.D. Characterization of the roles of RHOC and RHOA GTPases in invasion, motility, and matrix adhesion in inflammatory and aggressive breast cancers. *Cancer* **2010**, :2768-82.

30. Lin, Y.L.; Durmaz, Y. Y.; Nör, J.E.; ElSayed, M. E. H. Synergistic Combination of Small Molecule Inhibitor and RNA Interference against Antiapoptotic Bcl-2 Protein in Head and Neck Cancer Cells. *Mol. Pharmaceutics* **2013**, 2730-2738.

31. Zhao, Q. Q.; Chen, J. L.; Lv, T. F.; He, C. X.; Tang, G. P.; Liang, W. Q.; Tabata, Y.; Gao, J. Q. N/P Ratio Significantly Influences the Transfection Efficiency and Cytotoxicity of a Polyethylenimine/Chitosan/DNA Complex. *Biol. Pharm. Bull.* **2009,** *32*, (4), 706-710.

32. Park, M. R.; Han, K. O.; Han, I. K.; Cho, M. H.; Nah, J. W.; Choi, Y. J.; Cho, C. S. Degradable polyethylenimine-alt-poly(ethylene glycol) copolymers as novel gene carriers. *J. Controlled Release* **2005,** *105*, (3), 367-380.

33. Liang, G. F.; Zhu, Y. L.; Sun, B.; Hu, F.H.; Tian, T.; Li, S. C.; Xiao, Z. D. PLGA-based gene delivering nanoparticle enhance suppression effect of miRNA in HePG2 cells. *Nanoscale Res. Lett.* **2011,** *1*, (6), 447.

34. Yuan, F.; Dellian, M.; Fukumura, D.; Leunig, M.; Berk, D.A.; Torchilin, V.P.; Jain, R.K. Vascular permeability in a human tumor xenograft: molecular size dependence and cutoff size. *Cancer Res.* **1995,** *55*, (17), 3752-6.

35. Jang, S.; Wientjes, M. G.; Lu, D.; Au, J. S. Drug Delivery and Transport to Solid Tumors. *Pharmaceutical Research* **2003,** *20*, (9), 1337-1350.

36. Goula, D.; Becker, N.; Lemkine, G.F.; Normandie, P.; Rodrigues, J.; Mantero, S.; Levi, G.; Demeneix B.A. Rapid crossing of the pulmonary endothelial barrier by polyethylenimine/DNA complexes. *Gene Ther.* **2000,** *6*, (7), 499-504.
37. Neu, M.; Fischer, D.; Kissel, T. Recent advances in rational gene transfer vector design based on poly(ethylene imine) and its derivatives. *J. Gene Med.* **2005,** *7*, (8), 992-1009.
38. Oskuee, R. K.; Dehshahri, A.; Shier, W. T.; Ramezani, M. Alkylcarboxylate grafting to polyethylenimine: a simple approach to producing a DNA nanocarrier with low toxicity. *The J. Gene Med.* **2009,** *11*, (10), 921-932.
39. Wen, Y.; Pan, S.; Luo, X.; Zhang, X.; Zhang, W.; Feng, M. A Biodegradable Low Molecular Weight Polyethylenimine Derivative as Low Toxicity and Efficient Gene Vector. *Bioconjug. Chem.* **2009,** *20* (2), 322-332.
40. Yadava, P.; Roura, D.; Hughes, J.A. Evaluation of two cationic delivery systems for siRNA. *Oligonucleotides* **2007,** *17*(2), 213-22.
41. Hwang, H. S.; Kang, H.C.; Bae, Y.H. Bioreducible polymers as a determining factor for polyplex decomplexation rate and transfection. *Biomacromolecules* **2013,** *14(2)*, 548-556.
42. Hoffmeyer, M.R.; Wall, K. M.; Dharmawardhane SF. In vitro analysis of the invasive phenotype of SUM149, an inflammatory breast cancer cell line. *Cancer Cell Int.* **2005**, *5(1)*, 11
43. Liang, C.C.; Park, A. Y.; Guan J.L. In vitro scratch assay: a convenient and inexpensive method for analysis of cell migration in vitro. *Nat Protoc* **2007**, *2(2)*, 329-33.

Chapter 4

Presentation of EPPT1 Peptide for Binding of Underglycosylated MUC1 and Cytoplasmic Delivery of Anti-RhoC Silencing RNA by "Smart" Particles Synergistically Inhibit the Migration and Invasion of Aggressive Breast Cancer Cells

4.1 Introduction

The American Cancer Society estimated that 231,840 women were diagnosed with invasive breast cancer in 2015 in the United States of America [1] and ~25% of these cases would succumb to their disease due to the progression and development of distant metastases in the bone, brain, liver, and lungs [1, 2]. Metastasis of aggressive breast cancer cells require a well-orchestrated sequence of cellular events that include the disruption of cell-cell and cell-matrix adhesion, loss of cell polarity, acquisition of invasive and migratory phenotype(s), cell extravasation into the systemic and lymphatic circulations, and dissemination to secondary sites [3, 4, 5]. The increase in cancer cell motility and invasion has been closely linked to the onset of cancer metastasis, poor patient prognosis, and increased patient mortality [6]; therefore, motivating the search for potential therapeutic targets to suppress the metastatic spread of aggressive cancer cells.

RhoC protein belongs to the Ras superfamily of small guanosine triphosphatases (GTPases)[7], which has been implicated in the progression of metastasis in several cancers [8]. Unlike other Ras family proteins[9], RhoC expression has been shown to progressively increase as primary tumors become aggressively metastatic[10, 11]. Overexpression of RhoC GTPases is observed in most metastatic breast cancers and 90% of inflammatory breast cancers (IBC)[12]. Down-regulation of RhoC expression using silencing RNA (siRNA) has greatly inhibited stress fiber formation and subsequently reduced the invasive spread of metastatic breast cancer cells *in vitro* [13] as well as significantly decreased the formation of metastatic lung foci *in vivo* [14]. These results collectively indicate the potential of pursuing RhoC as a therapeutic target to suppress metastases of aggressive breast cancer cells. Therefore, we reported the use of degradable, pH-sensitive, membrane-destabilizing polymers composed of a β-cyclodextrin (β-CD) core with amphiphilic polymers grafted from the secondary face via acid-labile hydrazone linkers to complex anti-RhoC siRNA into "smart" nanoparticles[15]. The "smart" nanoparticles proved effective in shuttling anti-RhoC siRNA cargo past the endosomal membrane and into the cytoplasm of MDA-MB-231 and SUM149 breast cancer cells resulting in the knockdown of RhoC expression at the mRNA and protein levels by 90% and 100%, respectively [15]. The knockdown in RhoC expression; however, resulted in a 50% and 70% suppression of invasion and migration in both aggressive MDA-MB-231 and SUM149 breast cancer cells, respectively [15]. This partial reduction in invasive and migratory phenotypes, despite the complete knockdown of RhoC protein expression, suggests the contribution of other potential molecular players in facilitating the invasion and migration pathways.

Mucins belong to a family of large, heavily glycosylated transmembrane proteins, that constitute the protective mucous layer of epithelial surfaces and play an important role in signal transduction [16]. Mucin-1 (MUC1), a membrane-tethered mucin, has been extensively studied due to its widespread implication in cancer progression through increased cell invasion, growth, and metastasis [17, 18]. MUC1 comprises of a characteristic extracellular domain (ECD) with up to 120 tandem peptide repeats (TR) and a short preserved cytoplasmic tail [19]. In normal epithelial cells, the TR region of the ECD remains protected via extensively glycosylated oligosaccharide chains [20]. However, in greater than 90% of human breast carcinomas, the once heavily glycosylated and protected peptide backbone becomes exposed due to the underglycosylation of MUC1 (uMUC1) with fewer and shorter glycans [21] **(Figure 4.1)**. Furthermore, underglycosylation of the peptide core has been linked with poor prognosis and an increased risk for breast cancer metastasis [22]. Earlier studies using uMUC1 knockout mice showed a delay in tumor growth and a reduction in the number of metastatic foci formed compared to transgenic mice overexpressing uMUC1 antigens [23]; therefore, linking uMUC1 overexpression to the development of invasive breast cancer. Prior work showed that uMUC1 receptors recruit β-catenin to the cytoplasmic domain upon binding to galectin-3 (a galactoside-binding protein) [24]. This interaction disrupts β-catenin-mediated adheren junction formation that results in the loss of cell-cell adhesion and enables cancer cell invasion of the surrounding tissue [24, 25]. Furthermore, uMUC1 has the ability to firmly adhere to ICAM-1 present on the vascular endothelium that results in the downstream activation of non-receptor kinase Src [26]. Src activation has been implicated in the promotion of metastasis of cancer cells through downstream interaction with focal adhesion kinase (FAK) and the subsequent activation of the CrkL signaling pathways [27]. CrkL, a known activator of Rho GTPases like Cdc42 and Rac1, plays a key part in actin cytoskeletal reorganization and migration; thereby, making uMUC1 receptors a potential molecular target to further suppress cancer cell invasion and migration[27].

Moreover, the exposed ECD peptides of uMUC1 antigens have been previously exploited for the development of targeted immunotherapeutic vaccines such as anti-mucin-1 antibodies as well as for targeted tumor imaging[28–30]. To date, while most anti-MUC1 monoclonal antibodies (mAbs) successfully target the exposed TR domains – their long plasma half-life and poor pharmacokinetic properties often elicits detrimental immunogenic responses – halting their clinical development[31 ,32]. To address the limitations of mAbs, researchers developed a shorter synthetic peptide sequence namely EPPT1 (YCAREPPTRTFAYWG) derived from the third heavy-chain complementarity-determining region (CDR-3V_H) of the antitumor ASM2 mAb[33]. The EPPT1 peptide selectively binds uMUC1 receptors with a high binding affinity (K_d = 20 μM)[30, 34, 35]. This prompted its use as a targeting ligand to achieve selective homing of super magnetic iron oxide nanoparticles to uMUC1-expressing breast cancer cells *in vivo* [35]. Further, the EPPT1 peptide allowed selective binding and uptake of cationic polyacrylamide nanoparticles into uMUC1 expressing malignant colorectal cancer cells[34]. We, therefore predict that the binding of EPPT1–targeted nanoparticles to uMUC1 receptors could potentially exhibit dual functionality of uMUC1–specific targeting for selective intracellular delivery of therapeutic targets via receptor-mediated internalization as well as prevent downstream signal transduction and the subsequent inactivation of molecular targets involved in cell invasion and migration pathways.

In this study, we expand on our previous work by asymmetrically functionalizing the β-CD core to display a “brush” of hydrophilic polyethylene glycol (PEG) chains on the primary face and amphiphilic cationic/hydrophobic grafts on the secondary face, which complex the siRNA cargo forming “smart” pH-sensitive nanoparticles. The free tips of the PEG chains are functionalized to display the EPPT1 targeting ligands to achieve selective recognition and internalization of the nanoparticles by uMUC1 receptors present on the surface of aggressive breast cancer cells **(Figure 4.1)**. We investigate the effects of nanoparticle PEGylation by evaluating their ability to complex siRNA molecules as well as their interaction with red blood cells (RBCs) and serum proteins (e.g., FBS). We then evaluate the ability of EPPT1-targeted nanoparticles to achieve functional delivery of anti-RhoC siRNA into both MDA-MB-231 and SUM149 cancer cells compared to their non-targeted counterparts based on the associated suppression of RhoC protein expression. Finally, we explore if combining EPPT1 peptides and anti-RhoC siRNA molecules on the same nanoparticle can elicit a synergistic reduction in cell invasion and migration. We evaluate the synergistic effect by quantifying the suppression of cell invasion and migration achieved by: i) the cytoplasmic delivery of anti-RhoC siRNA, ii) the presentation of EPPT1 targeting ligands, and iii) the combination of cytoplasmic delivery of anti-RhoC siRNA and EPPT1 presentation of "smart" nanoparticles.

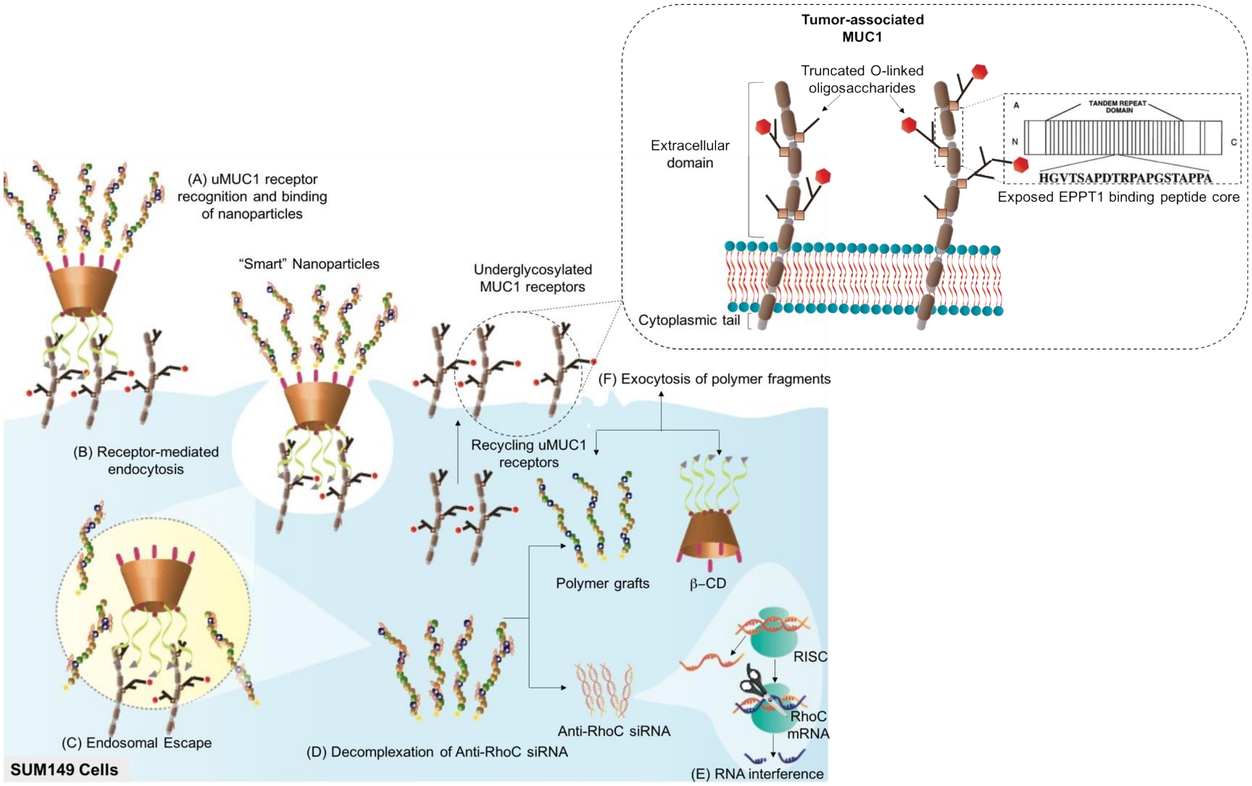

Figure 4.1: The illustration represents the hypothesized mode of action of $(EPPT1)_6$ – $(5kDa\text{-}PEG)_{6.5}$ – β – CD – $P(HMA\text{-}co\text{-}DMAEMA\text{-}co\text{-}TMAEMA)_{5.9}$ polymers complexing therapeutic anti-RhoC siRNA in aggressive breast cancer cells. We propose that the preferential binding of EPPT1 peptides to the EC domain of uMUC1 receptors expressed on the surface of inflammatory breast cancer cells would result in selective receptor-mediated endocytosis of our targeted "smart" nanoparticles. Once inside the endosome, the acidic microenvironment will facilitate hydrolysis of the acid-labile hydrazone linkers to release the P(HMA-co-DMAEMA-co-TMAEMA) grafts. The hydrophobic (HMA) and pH-sensitive (DMAEMA) monomers of the P(HMA-co-DMAEMA-co-TMAEMA) graft will further trigger the rupture of the endosomal membrane and release the loaded anti-RhoC siRNA cargo into the cytoplasm

4.2 Materials and methods

4.2.1. Materials

Poly (ethylene glycol) methyl ether with M_n 2 kDa and 5 KDa (Sigma-Aldrich, St. Louis, MO, US), α-NHS-ω-Alkyne PEG with M_n 5000 Da (Rapp polymere, Tübingen, Germany) were purchased and used as delivered. Iodine (I_2), 1-ethyl-3-(3-dimethylaminopropyl) carbodiimide HCl (EDC.HCl), hydroxybenzotriazole (HOBt), 4-pentynoic acid, 4-dimethylaminopyridine (DMAP), anisole anhydrous, iodomethane, *p*-toluenesulfonyl hydrazide, propargyl alcohol, oxalyl chloride were procured from Sigma-Aldrich (St. Louis, MO, US, > 98% purity). 2-bromoisobutyryl bromide (Fluka, >97%), triphenylphosphine ($P(Ph)_3$, Acros chemicals, NJ, US), sodium azide (NaN_3, Acros chemicals, NJ, US), *N*, *N*-diisopropylethylamine (DIPEA, Alfa Aesar, Haverhill, MA, US), *N*, *N'*-dicyclohexylcarbodiimide (DCC, TCI chemicals, Portland, OR, US), 8-bromo-1-octanol (Alfa Aesar, Haverhill, MA, US, 95%). EPPT1-NH_2 (YCAREPPTRTFAYWG, proteomics & peptide synthesis core facility, University of Michigan, Ann Arbor, MI, US) was used as received. All chemicals used for the secondary face modification of the β-CD core were obtained as previously reported[36]. All solvents were procured from Sigma Aldrich (St. Louis, MO, US, > 97% purity). All reagents involved in the sub-culturing of both SUM149 and MDA-MB-231 breast cancer cells were obtained and cultured as previously described [15]. DMEM/F12 medium, horse serum, epidermal growth factor (EGF), hydrocortisone, cholera toxin, and insulin were obtained from Invitrogen (Carlsbad, CA, US). All experimental reagents used to characterize and validate the efficacy of our β-CD nanoparticles were procured as previously outlined[15]. All anti-rabbit mAb were purchased from Cell Signaling Technologies (Danvers, MA, US). The anti-β-actin rabbit antibody and goat anti-rabbit IgG-HRP antibodies were procured from Santa Cruz Biotechnology Inc. (Santa Cruz, CA, US). The Pico Green assay was purchased from Molecular probes (Eugene, OR, US).

4.2.2. Synthesis of asymmetric, PEGylated, and EPPT1-targeted pH-sensitive β-CD carriers

We previously reported selective grafting of the amphiphilic P(HMA$_{79}$-*co*-DMAEMA$_{33}$-*co*-TMAEMA$_{48}$)$_{4.8}$ polymers from the hydroxyl (OH) groups of the secondary face of the β-CD core via acid-labile hydrazine linkages forming (OH)$_7$-β-CD-g-P(HMA$_{79}$-*co*-DMAEMA$_{33}$-*co*-TMAEMA$_{48}$)$_{4.8}$ as the first star-shaped pH-sensitive carrier[36]. We report grafting of P(HMA-*co*-DMAEMA) polymers onto the secondary face of the β-CD core via "click" coupling while maintaining the hydrazine linkages and the associated sensitivity to acidic pH values **(Figure 4.2)**. We capitalized on the difference in reactivity between the primary and secondary OH groups to covalently attach 2 kDa or 5 kDa PEG chains to the primary face of the β-CD core to prepare (2 kDa-PEG)$_7$-β-CD-P(HMA-*co*-DMAEMA-*co*-TMAEMA)$_{6.1}$ and (5 kDa-PEG)$_7$-β-CD-P(HMA-*co*-DMAEMA-*co*-TMAEMA)$_{6.4}$ carriers, respectively **(Figure 4.3)**. The free ends of the 5 kDa PEG brushes were further modified to present the EPPT1 peptides forming the (EPPT1)$_6$-(5 kDa-PEG)$_{6.5}$-β-CD-P(HMA-*co*-DMAEMA-*co*-TMAEMA)$_{5.9}$ carriers **(Figure 4.4)**. The following sections summarize the details of the synthesis process.

4.2.2.1. Synthesis of (OH)$_7$ - β-CD-P(HMA-co-DMAEMA-co-TMAEMA)$_{4.8}$ polymers

Synthesis of amphiphilic β-CD-based carriers started with protecting the primary OH groups of the β-CD core (1) by reacting it with *tert*-butyldimethylsilyl chloride (TBDMSCl) in pyridine to obtain (TBDMS)$_7$-β-CD (2) **(Figure 4.2)**. Protecting the highly reactive primary OH groups was imperative to facilitate the selective modification of secondary OH groups in subsequent reactions. Compound 2 was then reacted with phenyl bromoacetate in the presence of NaH in DMF to obtain (TBDMS)$_7$-β-CD-(phenylacetate)$_{8.4}$ (3). The acid-labile hydrazone linkers were introduced by reacting compound 3 with (*E*)-N'-(8-azidooctylidene)-4-methyl-benzenesulfonohydrazide (compound A) in the presence of NaH in DMF to obtain (TBDMS)$_7$-β-CD-O-(*E*)-N'-[(8-azidooctylidene) acetohydrazide]$_{8.4}$ (4). Synthesis of compound A is described in the supplementary data **(Scheme S5)**. The alkyne-P(HMA-*co*-DMAEMA) copolymers (B) were synthesized using atom transfer radical polymerization (ATRP) techniques following published protocols [36]. Compound 4 and alkyne-P(HMA-*co*-DMAEMA) copolymers (B) were reacted together in the presence of Cu(I)Br and PMDETA in DMF to obtain (TBDMS)$_7$-β-CD-P(HMA-*co*-DMAEMA)$_5$ polymers (5). The primary OH groups were deprotected by treating compound 5 with TBAF in THF to yield (OH)$_7$-β-CD-P(HMA-*co*-DMAEMA)$_{4.8}$ (6) before quaternizing 50% of DMAEMA monomers in the grafts into TMAEMA using methyl iodide, which yielded (OH)$_7$-β-CD-P(HMA-*co*-DMAEMA-*co*-TMAEMA)$_{4.8}$ (7).

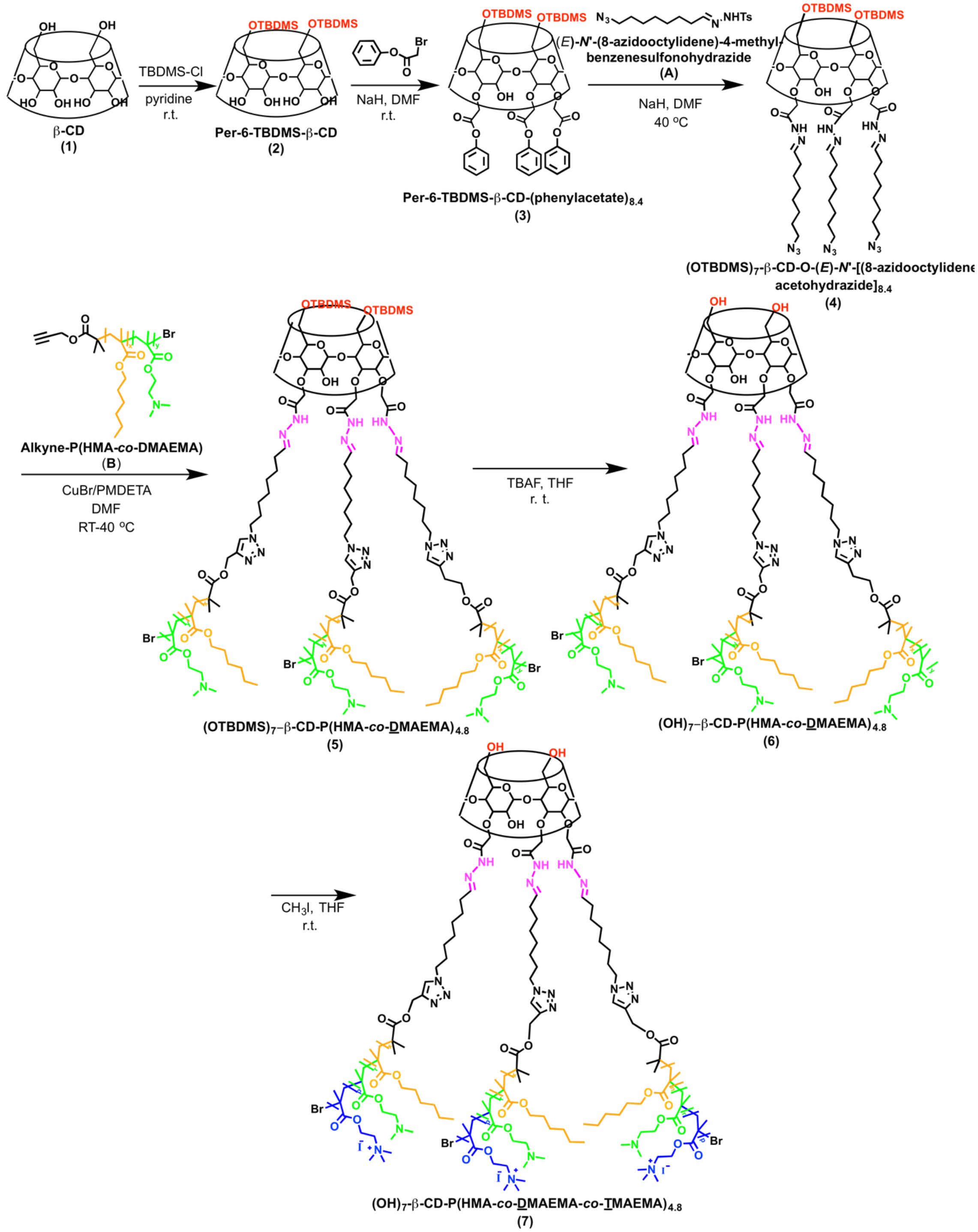

Figure 4.2: Chemical illustration representing the synthesis of (OH)$_7$–β–CD–P(HMA-*co*-DMAEMA-*co*-TMAEMA)$_5$ polymer

4.2.2.2. Synthesis of $(PEG)_7$-β-CD-P(HMA-co-DMAEMA-co-TMAEMA)$_n$ polymer

We capitalized on the high reactivity of primary OH groups to transform them into iodo groups by reacting the β-CD core (1) with I_2 and $P(Ph)_3$ to obtain (6-Iodo)$_7$-β–CD (8) **(Figure 4.3)**. Compound 8 was reacted with NaN_3 in DMF at high temperature to obtain (6-Azido)$_7$-β-CD (9), which will allow "click" coupling with PEG-alkyne. Subsequently, we focused on modifying the secondary OH groups of compound 9 by reacting with phenyl bromoacetate to obtain (6-Azido)$_7$-β-CD-(phenylacetate)$_{8.3}$ (10). To prepare non-targeted carriers, we "clicked" alkyne-PEG-OMe (2 kDa or 5 kDa; C or D) polymers to the primary face of compound 10 in presence of CuBr and PMDETA in DMF to obtain (2 kDa-PEG)$_7$-β-CD-(Phenylacetate)$_{8.3}$ (11) or (5 kDa-PEG)$_7$-β-CD-(Phenylacetate)$_{8.3}$ (12), respectively. Following PEGylation of the primary face, compounds 11 and 12 were reacted with (*E*)-N'-(8-azidooctylidene)-4-methylbenzenesulfonohydrazide (A) to produce compound 13 and 14, respectively. The alkyne-P(HMA-*co*-DMAEMA) copolymers were grafted to the secondary face of compounds 13 and 14 via "click" coupling in the presence of Cu(I)Br and PMDETA in DMF to obtain (2 kDa-PEG)$_7$-β-CD-P(HMA-*co*-DMAEMA)$_{6.1}$ (15) and (5 kDa-PEG)$_7$-β-CD-P(HMA-*co*-DMAEMA)$_{6.4}$ (16), respectively. Approximately 50% of DMAEMA monomers in polymers 15 and 16 were quaternized to obtain (2 kDa-PEG)$_7$-β-CD-P(HMA-*co*-$\underline{D}$MAEMA-*co*-$\underline{T}$MAEMA)$_{6.1}$ (17) and (5 kDa-PEG)$_7$-β-CD-P(HMA-*co*-$\underline{D}$MAEMA-*co*-$\underline{T}$MAEMA)$_{6.4}$ (18), respectively.

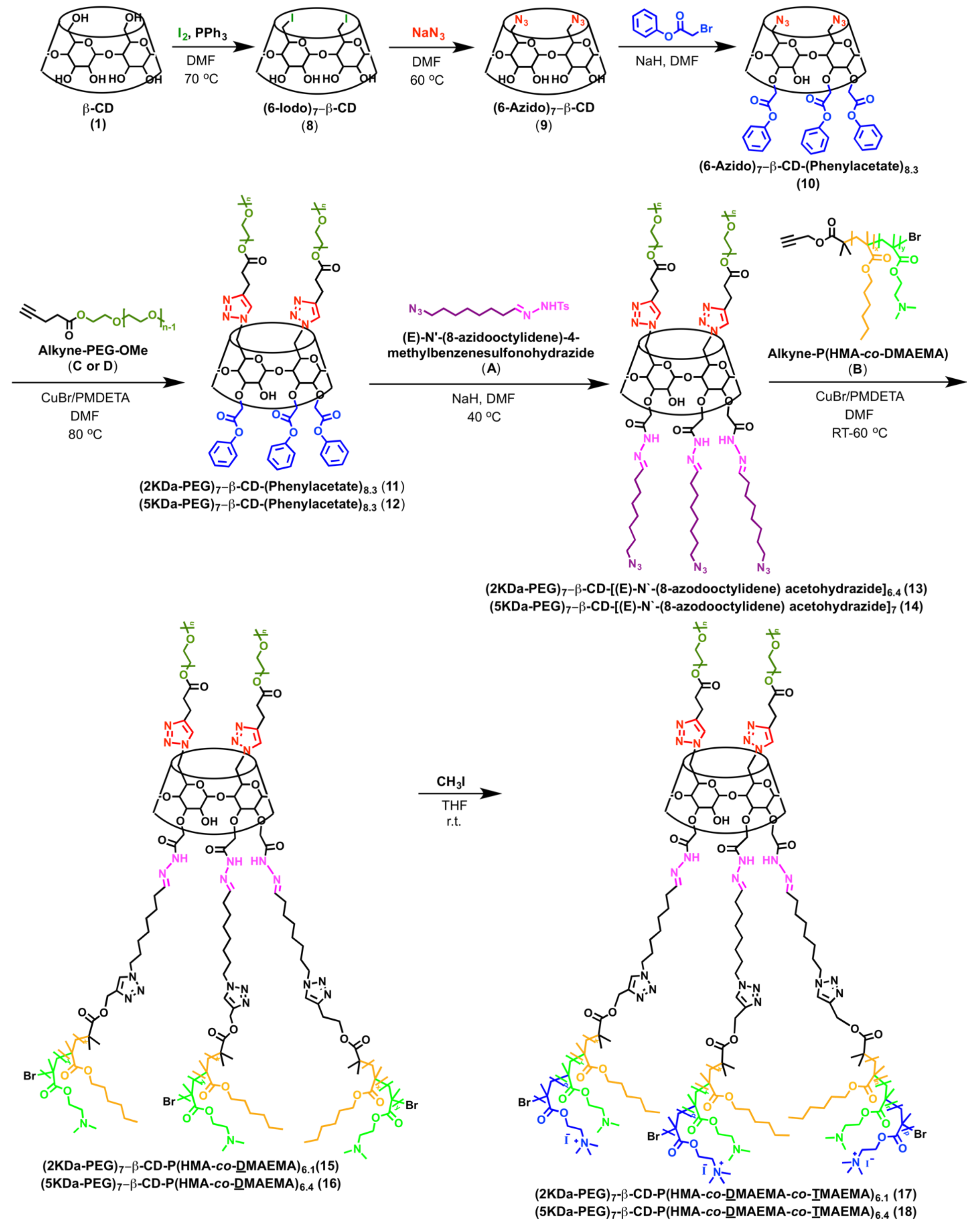

Figure 4.3: Chemical illustration representing the synthesis of $(PEG)_7$–β–CD–P(HMA-*co*-DMAEMA-*co*-TMAEMA)$_n$ polymers of varying PEG lengths (i.e., 2 kDa, and 5 kDa), respectively

4.2.2.3. Synthesis of $(EPPT1)_6$-$(5kDa\text{-}PEG)_{6.5}$-β-CD-$P(HMA\text{-}co\text{-}DMAEMA\text{-}co\text{-}TMAEMA)_{5.9}$ polymer

We followed the synthesis scheme outlined in **Figure 4.3** to obtain (6-Azido)$_7$-β-CD-(phenylacetate)$_{8.3}$ (10). Subsequently, compound 10 was reacted with alkyne-PEG-NHS (M_W 5 kDa, E) in the presence of Cu(I)Br and PMDETA in DMF to obtain (NHS-PEG)$_{6.5}$-β-CD-(Phenylacetate)$_{8.3}$ (19) **(Figure 4.4)**. The phenyl bromoacetate of compound 19 was reacted with (*E*)-N'-(8-azidooctylidene)-4-methyl-benzenesulfonohydrazide (A) in presence of NaH in DMF to obtain (NHS-PEG)$_{6.5}$-β-CD-[(*E*)-N`-(8-azodooctylidene)-acetohydrazide]$_{7.2}$ (20). Compound 20 was then reacted with EPPT1-$NH_2$ in the presence of EDC, HOBt, DIPEA in DMF to obtain (EPPT1)$_6$-(PEG)$_{6.5}$-β-CD-[(*E*)-N`-(8-azodooctylidene) acetohydrazide]$_{7.2}$ (21). Finally, compound 21 was "clicked" to alkyne-P(HMA-*co*-DMAEMA-*co*-TMAEMA) (F) in presence of Cu(I)Br and PMDETA in DMF at 40°C to obtain the final product (EPPT1)$_6$-(PEG)$_{6.5}$-β-CD-P(HMA-*co*-DMAEMA-*co*-TMAEMA)$_{5.9}$ (22). It is important to note that the identity, purity, and exact composition of all the synthesized compounds, reagents, intermediates, and polymers were monitored using ^{1}H-NMR and MALDI-TOF analyses.

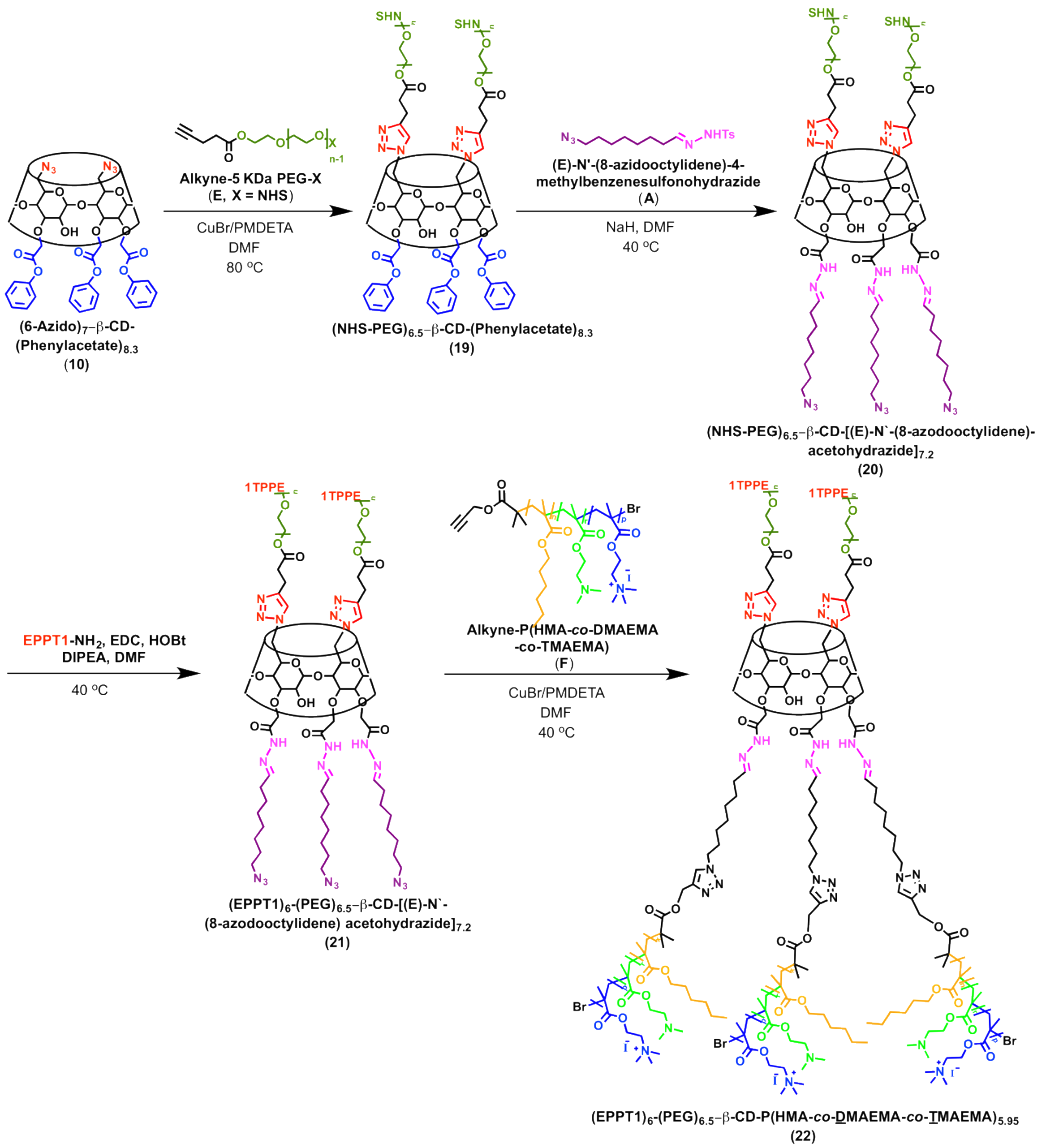

Figure 4.4: Chemical illustration representing the synthesis of (EPPT1)$_6$–(5kDa-PEG)$_{6.5}$–β–CD–P(HMA-*co*-DMAEMA-*co*-TMAEMA)$_{5.9}$ polymer

4.2.3. Formulation and characterization of "smart" anti-RhoC particles

Stock polymer solution was prepared by dissolving 1 mg of the lyophilized (OH)$_7$-β-CD-P(HMA-*co*-DMAEMA-*co*-TMAEMA)$_{4.8}$ polymer in 5% DMSO in PBS (pH 7.4) whereas

PEGylated β-CD carriers were dissolved in 0.2% DMSO in PBS (pH 7.4). We evaluated the ability of all polymer compositions to complex FAM-labeled scrambled siRNA molecules (0.75 μg) after simple mixing and allowing the solution mixture to stand at room temperature for 20 min before loading onto a 1% w/v agarose gel containing 0.5 μg/ml ethidium bromide (EtBr) dye. The ability of PEGylated and non-PEGylated β-CD polymers to complex siRNA molecules was investigated at different nitrogen/phosphate (N/P, +/-) ratios of 1.5/1, 2.5/1 and 4/1. Free FAM-labeled siRNA (0.75 μg) and free polymer solutions were loaded onto the agarose gel as positive and negative controls, respectively. The gels were immersed in Tris-Acetate-EDTA (TAE) buffer and exposed to 60V for 60 min before visualizing the gels under UV light. We used ImageJ software (NIH, Bethesda, MD) to quantify the amount of free siRNA observed with different polymers at different N/P ratios and normalized the observed fluorescence to that of the free siRNA loaded on the gel as a positive control to determine the optimum N/P ratio for full complexation of the loaded siRNA cargo. We prepared four anti-RhoC particles by complexing 1.42 μg (2 μl of a 50 μM stock solution) of anti-GAPDH siRNA with $(OH)_7$-β-CD-P(HMA-*co*-DMAEMA-*co*-TMAEMA)$_{4.8}$, (2 kDa-PEG)$_7$-β-CD-P(HMA-*co*-DMAEMA-*co*-TMAEMA)$_{6.1}$, (5 kDa-PEG)$_7$-β-CD-P(HMA-*co*-DMAEMA-*co*-TMAEMA)$_{6.4}$, and (EPPT1)$_6$-(5 kDa-PEG)$_{6.5}$-β-CD-P(HMA-*co*-DMAEMA-*co*-TMAEMA)$_{5.9}$ polymers as a function of varying N/P ratios of 1.5/1, 2.5/1, and 4/1 to obtain P0, P1, P2, and P3, respectively. We measured the size and zeta potential of P0-P3 particles prepared at different N/P (+/-) ratios using 90Plus particle size analyzer with ZetaPALS capability (Brookhaven Instruments Corporation, Holtsville, NY).

4.2.4. Assessment of hemolytic activity

We assessed the effect of PEGylation as well as the length of PEG chains (2 kDa vs. 5 kDa) on the hemo-compatibility of P1 and P2 compared to non-PEGylated P0 as a function of polymer concentration following established protocols [36]. Briefly, whole human blood was collected from volunteers following an approved IRB protocol in accordance with the University of Michigan and NIH guidelines. The collected blood was centrifuged at 13,500 × g for 5 min to separate the red blood cells (RBCs) fraction, which was washed three times with 0.15 M saline solution before diluting it 10-fold (1:10 v/v) with 0.1 M phosphate buffer solution (PBS) at pH 7.4 to obtain a final RBC concentration of 10^8 RBC's per 200 µl solution. Stock solutions of P0, P1, and P2 "smart" anti-RhoC particles were prepared in PBS (pH 7.4) as previously described. The appropriate volume of each stock solution was mixed with 800 µl of PBS (pH 7.4) and 200 µl of diluted RBC's to reach the desired polymer concentration (i.e., 0.5, 1, 1.5, 2, 2.5, 5 µg/ml) followed by gentle mixing and incubating the solution at 37°C for 60 min. RBC's were mixed with PBS (pH 7.4) and water as negative and positive controls, respectively. At the end of the incubation period, the RBC solutions were centrifuged at 13,500 × g for 5 min to pellet the intact RBC's followed by measuring hemoglobin absorbance in the supernatant at its characteristic wavelength (λ = 541 nm). We measured % hemolysis of RBC's in response to different concentrations of P0-P2 using the following equation.

$$\% \text{ Hemolysis} = \frac{\text{Sample Absorbance} - \text{Absorbance of RBC}'\text{s incubated with PBS}}{\text{Average Absorbance of RBC}'\text{sincubated with distilled water}}$$

4.2.5. Nanoparticles stability in serum

We investigated the ability of P0-P3 anti-RhoC particles to retain their siRNA cargo upon incubating with different concentrations of FBS to determine the ability of PEG to shield the siRNA cargo. Briefly, P0-P3 nanoparticles were prepared by mixing the appropriate β-CD polymer with 1.42 μg (2 μl of a 50 μM stock solution) of anti-GAPDH siRNA in PBS (pH 7.4) at N/P ratio of 2.5/1. Particle solutions were mixed with different volumes of FBS to adjust FBS content to 0%, 10% or 25% (v/v) before incubating at 37°C for 6 h. We added the Pico Green dye to different particle solutions to allow complexation of released siRNA molecules, which would result in a detectable increase in solution fluorescence (λ_{ex} = 485 nm & λ_{em} = 518 nm) measured using a Fluoroskan microplate reader (Thermo Fisher Scientific Inc., Waltham, MA). We normalized the fluorescence signal of each solution to that observed upon mixing the Pico Green dye with 1.42 μg anti-GAPDH siRNA incubated with FBS (0%, 10%, 25% v/v) under the same conditions to determine the fraction of siRNA cargo released from each particle upon incubation with serum.

4.2.6. Cell culture

SUM149, MDA-MB-231, and MCF10A breast cancer cells were generously provided by Dr. Sofia D. Merajver (University of Michigan, School of Medicine). While SUM149 and MDA-MB-231 cells were cultured following established protocols as previously described[15]. MCF10A cells were cultured in DMEM/F12 medium supplemented with 5% horse serum, EGF (20 ng/ml), hydrocortisone (0.5 mg/ml), cholera toxin (100 ng/ml), and insulin (10 μg/ml). MCF10A cells were incubated at 37°C and 5% CO_2.

4.2.7. Cellular uptake of “smart” particles

We investigated the ability of EPPT1-targeted (P3) and non-targeted (P2) particles to discriminate between SUM149, MDA-MB-231, and MCF10A cells expressing varying levels of underglycosylated MUC1 (uMUC1) surface receptors based on particle's uptake into each cell line. Briefly, cells were seeded at a density of 50,000 cells per well in 24-well plates and allowed to adhere for 16 h at 37°C before incubating with different concentrations of P2 and P3 particles loaded with FAM-labeled scrambled siRNA prepared at a N/P ratio of 2.5/1 as previously described. After 6 h of incubation, the cells were washed with PBS, treated with 0.05% Trypsin/EDTA for 5 min, harvested, pelleted, and re-suspended in the appropriate culture medium before being analyzed using Biosciences FACSCalibur Flow Cytometer (Becton Dickinson, Franklin Lakes, NJ) to determine the % of fluorescently-labeled cells. All cells were gated by forward/side scatter and 10,000 gated events were collected per sample to discriminate between live and dead cells to account only for live cells.

4.2.8. "Smart" particles effect on RhoC expression

We investigated the ability of EPPT1-targeted (P3) and non-targeted (P2) particles to achieve functional delivery of the anti-RhoC siRNA cargo into the cytoplasm of SUM149 and MDA-MB-231 breast cancer cells by quantifying the changes in expression of RhoC protein following published protocols [15]. Briefly, SUM149 and MDA-MB-231 cells were seeded at a density of 2.5×10^5 cells per well in 6-well plates and allowed to adhere for 18 h. "Smart" P2 and P3 particles loaded with anti-RhoC (+) or scrambled siRNA (-) molecules were prepared in OPTI-MEM solution at a N/P ratio of 2.5/1. P2 and P3 particles were incubated with SUM149 and MDA-MB-231 cells at a final siRNA concentration of 25 or 50 nM for 6 h before adding fresh culture medium (1 ml) and incubating for a total of 48 or 72 h. We investigated the effect of double transfection (i.e. incubating the cells with a given treatment at t = 0 and 24 h) on RhoC expression as a function of siRNA concentration (25 and 50 nM) while keeping total incubation time at 48 h or 72 h.

At the end of the transfection cycle, we washed the cells twice with cold PBS, incubated them with RIPA lysis buffer for 5 min on ice, and centrifuged the solution at 14,000 rpm for 15 min to isolate the supernatant containing the protein fraction. We measured the total protein concentration in isolated cell lysates using the BCA kit (Pierce Biotechnology, Rockford, IL) following manufacturer's protocol. Equal amount of protein (10 μg/ml) isolated from different treatments were resolved on 12.5% Criterion Tris-HCl gels (Bio-Rad, Hercules, CA) and transferred onto a polyvinylidene fluoride (PVDF) membrane using a semidry apparatus (Bio-Rad, Hercules, CA). Membranes were blocked with 5% milk solution for 1 h and probed overnight at 4°C with either anti-β-actin rabbit antibody (Santa Cruz, CA) and primary anti-RhoC rabbit mAb (Cell Signaling Technologies, MA) at a 1:1000 dilution. Bound primary antibodies were visualized using enhanced chemiluminescence (Pierce, Rockford, IL) after incubating with secondary horseradish peroxidase-coupled anti-rabbit antibody (Santa Cruz, CA) at a 1:5000 dilution for 1 h at room temperature. The knockdown of RhoC proteins in response to different particles and treatment conditions was quantified using the ImageJ image analysis software (NIH, Bethesda, MD) and normalized to the endogenous β-actin control and untreated SUM149 and MDA-MB-231 cells.

4.2.9. Boyden chamber invasion assay

We evaluated the ability of our EPPT1–targeted (P3) and non-targeted (P2) particles to suppress RhoC-associated cell invasion in aggressive breast cancer cells. BD matrigel invasion assay chambers (BD Biosciences, Bedford, MA) were used to quantify cell invasion in both SUM149 and MDA-MB-231 cells as per manufacturer's instructions. Briefly, SUM149 and MDA-MB-231 cell lines were plated in 6-well plates at a seeding density of 2.5×10^5 cells per well and allowed to adhere for 18 h, respectively. The adhered cells were then treated with "smart" P2 and P3 particles loaded with anti-RhoC (+) or scrambled siRNA (-) molecules at a final concentration of 25 or 50 nM for 6 h in serum-free OPTI-MEM, followed by the addition of respective growth media and incubated for a total of 72 h. At 24 h, the treated MDA-MB-231 cells were subjected to dual particle transfection for a total incubation period of 72 h. After 72 h, both cell lines were washed with PBS, trypsinized using 0.05% Trypin/EDTA, and centrifuged to collect the cell pellets before suspending them in serum-free culture medium at a density of 50,000 cells per ml. The cells were added to the upper chamber and allowed to invade the matrigel membrane for 20 h at 37°C in a CO_2 incubator. The lower chamber contained growth media with varying serum concentrations (i.e., 5 or 10% v/v). Non migrating cells were removed from the upper chamber with a cotton swab. The remaining cells on the lower surface of each insert were fixed, stained with staining buffer (1% (w/v) crystal violent in 20% (v/v) methanol) for 1 h at room temperature, and measured at 595 nm after extraction with 10% acetic acid for 10 min. Results were normalized to the untreated SUM149 and MDA-MB-231 cells and reported as the average of three independent experiments + SEM.

4.2.10. Scratch assay

We evaluated the effect of "smart" P2 and P3 anti-RhoC siRNA (+) particles prepared at a N/P ratio of 2.5/1 on the migratory activity of SUM149 and MDA-MB-231 cells compared to their scrambled siRNA (-) counterpart using scratch assay. SUM149 and MDA-MB-231 cells were plated in 24-well plates at a seeding density of 50,000 cells per well and allowed to grow under normal culture conditions to 95% confluence. The cell monolayer was scratched with a sterile 200 μl pipette tip to create a "wound" across the center of each well. Each well was washed with PBS to remove the detached cells and the wound was imaged (t = 0 h) at a 10X magnification using a Nikon Eclipse Ti inverted microscope equipped with a camera to capture phase contrast images of the wound. Subsequently, the SUM149 and MDA-MB-231 cell monolayers were treated with "smart" P2 and P3 anti-RhoC siRNA (+) or scrambled siRNA (-) particles prepared at an N/P ratio of 2.5/1 following the same treatment conditions as described in the Boyden chamber invasion assay. After 72 h, the wounds were imaged using the same microscope setup. The acquired images were processed using ImageJ image analysis software to calculate the wound area at t = 0 h and 72 h. The wound area after 72 h was normalized to the initial area (t = 0 h) to quantify the change in cell migration in response to different particle compositions.

4.2.11. Coefficient of drug interaction

The coefficient of drug interaction (CDI) was used to analyze the synergistic effect of EPPT1–targeting peptides and anti-RhoC siRNA on the suppression of cancer cell invasion and migration. CDI was calculated as follows: CDI=AB/(A×B). AB is the ratio of the 2-treatment combination group (i.e., (+) P3) to the control group, and A or B is the ratio of the single treatment group (i.e., (-) P3 or (+) P2) to the control group. In the Boyden chamber invasion assay, the CDI values were calculated as a function of the number of cells invading the matrigel following different treatment conditions to the untreated controls of the respective cell lines. While in the scratch assay, the ratio was evaluated as a function of the unoccupied wound area after different treatment conditions to the untreated controls, respectively. Furthermore, CDI <1 indicates synergism, CDI <0.7 indicates a significantly synergistic effect, CDI =1 indicates an additive effect, and CDI >1 indicates antagonism.

4.2.12. Effect of targeted $(\text{EPPT1})_6$-(5 kDa-PEG)$_{6.5}$-β-CD-P(HMA-co-DMAEMA-co-TMAEMA)$_{5.9}$ polymers on phosphorylated Src and FAK protein expression

Activated P-Src (Y419) and P-FAK (Y576/577) protein expression levels in SUM149 cells upon treatment with different particle compositions were quantified using previously described western blot techniques. Briefly, SUM149 cells were plated in 6 well plates at a seeding density of 2.5 x 10^5 cells/well. The cells were allowed to adhere overnight and treated with either “smart” non-targeted P2 and EPPT1–targeted P3 particles complexing scrambled siRNA (-) at a N/P ratio of 2.5/1 at a final siRNA concentration of 50 nM for a total incubation time of 48 or 72 h, respectively. The treated cells were harvested and total protein lysates of respective treatments collected and quantified using BCA protein assay. Equal amounts of total protein extracts (60 μg/μl) obtained from different particle treatments and incubation time points were resolved on 4-15% Criterion Tris-HCl gel (Bio-Rad, Hercules, CA) and transferred onto polyvinylidene fluoride (PVDF) membranes using the iBlot apparatus (Thermo Scientific, Waltham, MA). Membranes were blocked with 5% milk solution for 1 h and probed overnight at 4°C with β-actin goat antibody (Santa Cruz, CA), Phospho-Src (Tyr419) rabbit mAb, Phospho-Fak (Tyr567/577) rabbit mAb, Src (Tyr419) rabbit mAb, and Fak (Tyr567/577) rabbit mAb (Cell Signaling Technologies, MA) at a 1:1000 dilution. Bound primary antibodies were visualized using enhanced chemiluminescence (Pierce, Rockford, IL) after incubating with secondary horseradish peroxidase-coupled anti-rabbit antibody (Santa Cruz, CA) at a 1:5000 dilution for 1 h at room temperature. The activated P-Src (Y419) and P-FAK (Y576/577) protein levels in response to different particle formulations and treatment conditions were quantified using ImageJ software (NIH, Bethesda, MD) and normalized to the endogenous β-actin control as well as their respective total Src and total Fak protein expression levels, respectively. Four replicates were used for each condition and particle formulation and the results show the average + the standard error of the mean (SEM).

4.2.13. Statistical analysis

Results are presented as the mean ± standard error of the mean (SEM). Comparisons of various "smart" particle parameters in all experiments were analyzed using one-way ANOVA with Tukey's post hoc analysis.

4.3. Results and Discussion

4.3.1. Synthesis of $(OH)_7$ - β-CD-P(HMA-co-DMAEMA-co-TMAEMA)$_{4.8}$ polymers

The highly reactive primary OH groups of the β-CD core were successfully protected with TBDMS groups **(Figure 4.2,** compound **2)**, followed by the successful modification of the secondary OH's with phenylacetate groups **(Figure 4.2,** compound **3)**. The identity and purity of compound **(2)** and **(3)** were determined by ^{1}H NMR spectra, respectively. The ^{1}H NMR spectra showed successful capping of all 7 primary OH groups with TBDMS groups, while approximately 8.4 units of secondary OH groups were modified with phenylacetate determined by quantifying the aromatic protons observed between 6.66 – 7.35ppm compared to sugar protons. The incomplete conversion of secondary OH groups can be attributed to the steric hindrance of the bulky phenylacetate groups. However, the incorporation of 8.4 phenylactetate units on the secondary face is in accordance with our previously reported scheme for the synthesis of amphiphilic “smart” nanoparticles[36]. Compound **4** in **Figure 4.2** showed a 100% conversion of secondary face aromatic groups into acid labile hydrozone aliphatic linkers. The identity and purity of compound **4** was verified by ^{1}H NMR spectrum that confirmed the successful coupling of 8.4 aliphatic chains on the secondary face based on the aliphatic protons observed between 0.90 – 1.85ppm relative to sugar protons. We modified our previously reported synthesis strategy[36] by using compound **A (Figure 4.2)** to form acid-labile hydrozone linkages at the secondary face due their ability to facilitate kinetically favorable forward reactions between their self-eliminating tosyl group and phenylacetate in the presence of a base. Moreover, the 8 carbon atom aliphatic chain terminating in an azide (N_3) group of compound **8** allowed “click” coupling of bulky polymeric grafts **(Figure 4.2,** compound **B)** with minimum steric hindrance and maximum coupling efficiency. Compound **B** was synthesized using atom transfer radical polymerization reactions (ATRP) to control the molecular weight (25 kDa) and the molar feed ratio of HMA and DMAEMA (50/50) monomers per graft. The graft composition and purity was characterized using ^{1}H NMR techniques. Using the ^{1}H NMR spectra, the number of HMA/DMAEMA monomers present per graft was determined by quantifying the ratio of HMA protons (3.92ppm) relative to DMAEMA protons (2.26, 2.54, and 4.04ppm). Further, the “click” coupling reaction between the alkyne group of compound **B** and the terminal N_3 of compound **4** resulted in the successful grafting of 4.8 copolymers from the secondary face as seen in compound 5 **(Figure 4.2)**. The identity and purity of compound **5** was determined by ^{1}H NMR spectra. The number of polymeric grafts attached to the secondary face was quantified by comparing the ratios between the sugar and HMA/DMAEMA protons. Prior to the partial conversion of DMAEMA monomers into cationic TMAEMA units, the primary OH groups were successfully deprotected **(Figure 4.2,** compound **6)** and characterized via ^{1}H NMR techniques. Compound **7 (Figure 4.2)** revealed that 54% of

DMAEMA monomers were converted into TMAEMA units and confirmed via ^{1}H NMR. The final $(OH)_7$ - β-CD-P(HMA-co-DMAEMA-co-TMAEMA)$_{4.8}$ **(P0)** polymer (compound **7**) exhibited approximately 4.8 polymer grafts coupled to the secondary face (comprising of 86 units of HMA, 39 units of DMAEMA, and 47 units of TMAEMA per graft) with a molecular weight of 155597.6 g/mol, and a yield of 580 mg. Every step involved in the synthesis of compound **7** was further characterized by ^{13}C NMR and MADLI-TOF techniques. The presence of N_3 groups was confirmed using FT-IR techniques.

4.3.2. Synthesis of $(PEG)_7$-β-CD-P(HMA-co-DMAEMA-co-TMAEMA)$_n$ polymer

The highly reactive primary OH groups were successfully substituted with I_2 groups **(Figure 4.3,** compound **8)**, followed by the nucleophilic substitution of all seven primary I_2 with N_3 groups **(Figure 4.3,** compound **9)**. The identity and purity of compounds **8** and **9** were determined using standard ^{1}H NMR techniques. Furthermore, the successful nucleophilic substitution of the primary face with N_3 groups was confirmed by the characteristic FT-IR peak observed at 2113.6 and MALDI-TOF that suggested a 100% conversion from I_2 (MW_{calc} 1926.7 g/mol) to N_3 groups (MW_{calc} 1332.4 g/mol). The primary OH was modified prior to secondary face modifications due to their ease of accessibility as well as higher susceptibility to nucleophilic substitution reactions. Following primary face nucleophilic substitution reactions, the secondary face OH’s were modified and characterized to exhibit approximately 8.3 phenylacetate groups as described in the section 4.3.1. The primary N_3 groups on compound **10 (Figure 4.3)** were “click” coupled with either compound **C** or **D** to produce compound **11** and **12 (Figure 4.3)**, respectively. The identity and purity of compound **11** and **12** were determined using ^{1}H NMR spectra, respectively. The 100% “click” coupling efficiency was quantified by calculating the number of protons appearing between 2.70-3.80 ppm as well as validated via MALDI-TOF techniques. Following the primary face modification with either 2 or 5 kDa PEG molecules, the secondary face phenylacetate groups were successfully reacted with compound **A** to exhibit acid labile hydrazone linkers, namely compound **13** & **14**, respectively. The ^{1}H NMR spectra of compounds **13** & **14** revealed the coupling of approximately 6.4 and 7 units of hydrazone linkers on the secondary face. The “click” coupling of compound **B** to the secondary face resulted in approximately 6.1 & 6.4 amphiphilic grafts per β-CD core of compounds **15** & **16 (Figure 4.2)**, respectively. The number of amphiphilic grafts were quantified using ^{1}H NMR spectrum to compare the ratios between sugar and HMA/DMAEMA protons. The higher polymer graft coupling efficiency observed in compounds **15** & **16** compared to compound **5** can be attributed to improved solubility in DMF due to the presence of primary PEG brushes. Finally, ^{1}H NMR was used to calculate the % of DMAEMA quaternization into TMAEMA monomers in compounds **17** & **18 (Figure 4.3)**, respectively. The ratios between the number of methyl protons of DMAEMA monomers at 2.26 ppm and TMAEMA methyl protons at 3.16 ppm indicated 54% and 47% degree of quaternization in compounds **17** & **18**, respectively. (2 kDa-PEG)$_7$-β-CD-P(HMA-co-DMAEMA-co-TMAEMA)$_{6.1}$ **(P1)** polymers exhibited an amphiphilic graft polymer composition of 75 units of HMA, 34 units of DMAEMA, and 38 units of TMAEMA monomers with a molecular weight of 201387 g/mol and a yield of 32 mg. The (5 kDa-PEG)$_7$-β-CD-P(HMA-co-DMAEMA-co-TMAEMA)$_{6.4}$ **(P2)** comprised of an amphiphilic graft composition of 77 units of HMA, 41 units of DMAEMA, and 36 units of TMAEMA with a molecular weight of 221539 g/mol and a yield of 21 mg. All steps involved in the synthesis of compounds **17** & **18** was further characterized by ^{13}C NMR and MADLI-TOF techniques. The presence of N_3 groups were confirmed using FT-IR techniques.

4.3.3. Synthesis of $(EPPT1)_6$-(5 kDa-PEG)$_{6.5}$-β-CD-P(HMA-co-DMAEMA-co-TMAEMA)$_{5.9}$ polymer

The primary N_3 groups of compound **10 (Figure 4.3)** were "click" coupled to compound **E (Figure 4.4)** to obtain compound **19 (Figure 4.4)**. The successful coupling of all 7 primary N_3 groups with compound **E** was confirmed using ^{1}H NMR by quantifying the number of CH_2 protons on compound **E** relative to the number of sugar protons. The secondary face phenylacetate groups of compound **19** were modified and characterized as previously reported in section 4.3.1. Approximately 6.5 units of EPPT1 targeting peptide was successfully attached in situ to the NHS groups present on compound **E** to obtain compound **21**. The EPPT1 peptide density per β-CD molecule (i.e., 6.5 units/β-CD) was chosen based on previously published work [37] that showed significant homing of nanoparticles that exhibited nearly 7.8 EPPT1-targeting peptides into uMUC1 expressing tumors. Unlike the above synthesis schemes **(Figure 4.2 and 4.3)**, the amphiphilic polymer grafts **(Figure 4.4, compound F)** were partially quaternized prior to "click" coupling to the secondary face N_3 groups of compound **21**. ^{1}H NMR spectrum indicated the coupling of approximately 5.9 amphiphilic grafts per β-CD molecule. The reason for partially quaternizing the amphiphilic grafts prior to coupling was to prevent an undesired quaternization of amine groups present in the amino acid residues of EPPT1 peptides. The final $(EPPT1)_6$-(5 kDa-PEG)$_{6.5}$-β-CD-P(HMA-co-DMAEMA-co-TMAEMA)$_{5.9}$ polymer **(P3)** comprised of an amphiphilic graft composition of 76 units of HMA, 43 units of DMAEMA, and 34 units of TMAEMA with a molecular weight of 228416 g/mol and a yield of 118 mg (92% yield). All steps involved in the synthesis of compounds **17** & **18** were further characterized by ^{13}C NMR and MADLI-TOF techniques.

4.3.4. Formulation and characterization of "smart" anti-RhoC particles

Polymer P0 was soluble in physiological media containing 5% DMSO, while the PEGylated polymer series (P1-3) showed improved solubility by dissolving in physiological media containing 0.2% DMSO. The incorporation of amphiphilic PEG molecules (either 2 or 5 kDa) on the primary face of the β-CD core further improved their solubility profile in physiological media at room temperature compared to their non-PEGylated counterparts. All polymers (P0-3) showed complete complexation of 0.75 μg of FAM-labeled scrambled siRNA molecules at all N/P ratios (i.e., 1.5/1, 2.5/1, and 4/1) compared to free siRNA molecules as seen in **Figure 4.5 A** & **B**. Therefore, suggesting that both 2 or 5 kDa PEG molecules present on the non-targeted particles P1-2 and EPPT1-targeted particles P3 do not interfere with siRNA complexation. The incorporation of PEG molecules with increasing molecular weight resulted in a modest increase in size distribution for all "smart" particles (P1-3) prepared at N/P ratios of 1.5/1, 2.5/1, and 4/1 **(Figure 4.5 C)**. With the average "smart" particle size at the desired N/P ratio of 2.5/1 increasing from 104 ± 1.4 nm for P1 and 110 ± 5.6% for P2 to 191 ± 8.2% for P3. However, all nanoparticles were within the acceptable 200 nm tumor size cut-off range. All "smart" particle compositions (P1-3) exhibited a net positive zeta potential at all N/P ratios (+/-) (**Figure 4.5 D**). At the desired N/P ratio of 2.5/1, "smart" particle P1 exhibited a positive charge density of 32 ± 0.6%, while P2 showed a lower charge of 19.4 ± 0.1% suggesting that the 5 kDa PEG molecules of P2 demonstrated significantly better cationic shielding capability compared to P1's 2 kDa PEG molecules. On the other hand, P3 particles had a charge of 28 ± 0.6% that could be attributed to the net +2 charge/EPPT1 peptide molecule present on the primary face of nanoparticles.

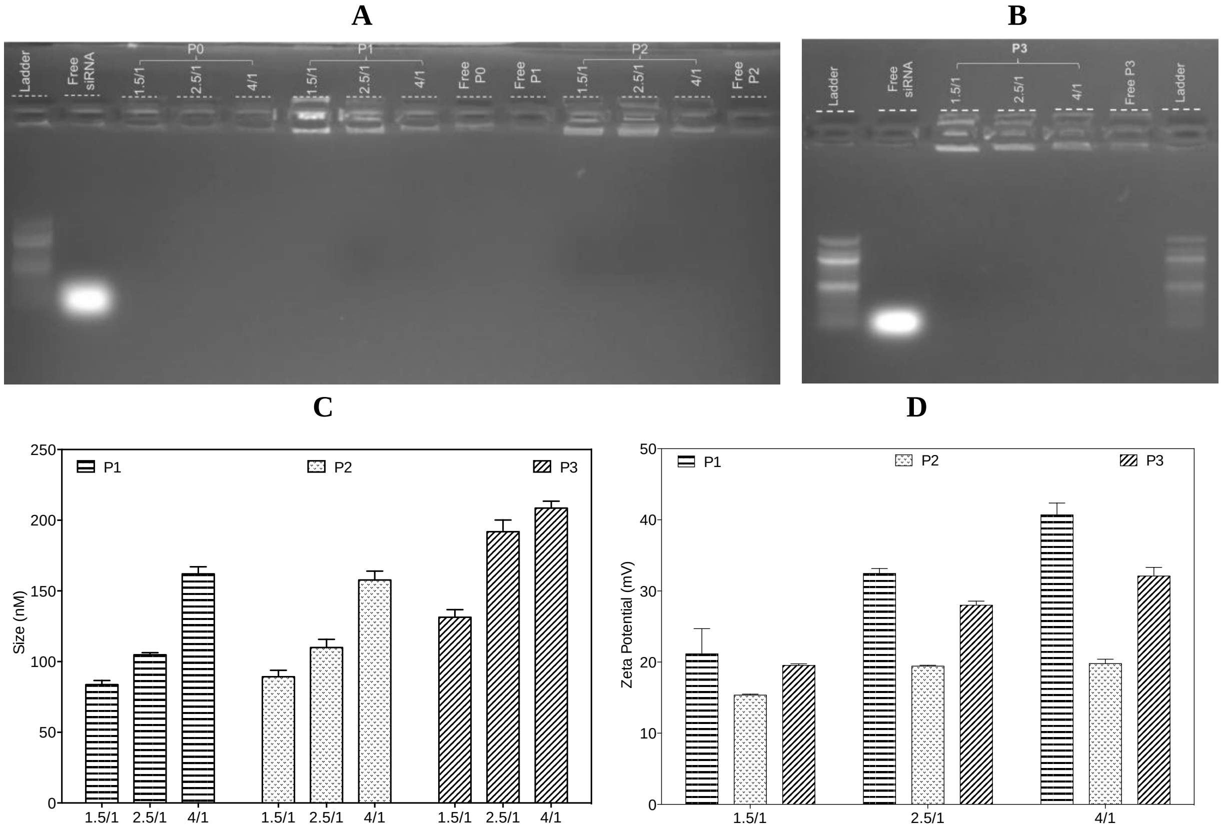

Figure 4.5: Characterization of asymmetric "smart" nanoparticles. The degree of siRNA complexation achieved by our "smart" polymers as a function of different N/P (+/-) ratios (i.e., 1.5/1, 2.5/1, and 4/1) was determined using a 1% w/v agarose gel and quantified using ImageJ software (NIH, Bethesda) relative to free siRNA molecules. **(A)** Illustrates the ability of (OH)$_7$–β–CD–P(HMA-*co*-DMAEMA-*co*-TMAEMA)$_5$ (P0), (2kDa-PEG)$_7$–β–CD–P(HMA-*co*-DMAEMA-*co*-TMAEMA)$_{6.1}$ (P1), (5KDa-PEG)$_7$–β–CD–P(HMA-*co*-DMAEMA-*co*-TMAEMA)$_{5.9}$ (P2), and (EPPT1)$_6$ - (5kDa-PEG)$_{6.5}$–β–CD–P(HMA-co-DMAEMA-co-TMAEMA)$_{5.9}$ polymer (P3) **(B)** to complex siRNA molecules as a function of varying N/P (+/-) ratios. The size **(C)** and zeta potential **(D)** of particles P0-3 prepared by complexation of "smart" polymers (P0-3) with 0.57 µg of anti-GAPDH siRNA were determined as a function of different N/P (+/-) ratios of 1.5/1, 2.5/, and 4/1, respectively. The plotted results are the average + the standard error of the mean of two independent experiments each carried out in triplicates.

4.3.5. Biocompatibility study of our "smart" particles

The effect of PEG length on the systemic biocompatibility of our asymmetric β-CD polymers were evaluated *in vitro* based on their stability in varying serum concentrations and their hemocompatibility profiles in RBC solutions under physiological conditions.

4.3.5.1. Hemolytic activity of “smart” particles

The determination of hemolytic properties is one of the most common preclinical tests performed to understand nanoparticle interaction with blood components namely RBC’s. The β-CD polymers (P0-2) effect on RBC’s were determined by measuring the amount of hemoglobin pigment present in the supernatant using spectrophotometry (λ = 541 nm) after 1 h and normalized to the positive water control. The % RBC hemolysis observed by β-CD polymers (P0-2) was plotted in **Figure 4.6** as a function of varying polymer and siRNA concentration. From the results, we observe that polymers P0 and P1 exhibit relatively high hemolysis profiles (20 – 50%) at low polymer concentrations of 0.5, 1, 1.5 μg/ml compared to P2 (< 15%). We can, therefore infer that while the 2 kDa PEG molecules (P1) are not significantly better in preventing hemolysis compared to non-PEGylated P0 particles - the 5 kDa PEG brushes show statistically significant improvement in minimizing RBC disruption compared to P0 and P1. At polymer concentrations of 2 – 2.5 μg/ml (i.e., polymer concentrations used in the subsequent study), P2 continued to show significantly low hemolysis profiles (i.e., < 20%), while both P0 and P1 showed a significantly higher degree of RBC hemolysis. We can thus conclude that 5 kDa PEG molecules present of polymer P2 significantly improved the biocompatibility profile of our β-CD polymers by reducing RBC hemolysis compared to their 2 kDa counterparts; therefore, were used to conjugate EPPT1 targeting peptides onto their free ends as seen in polymer P3.

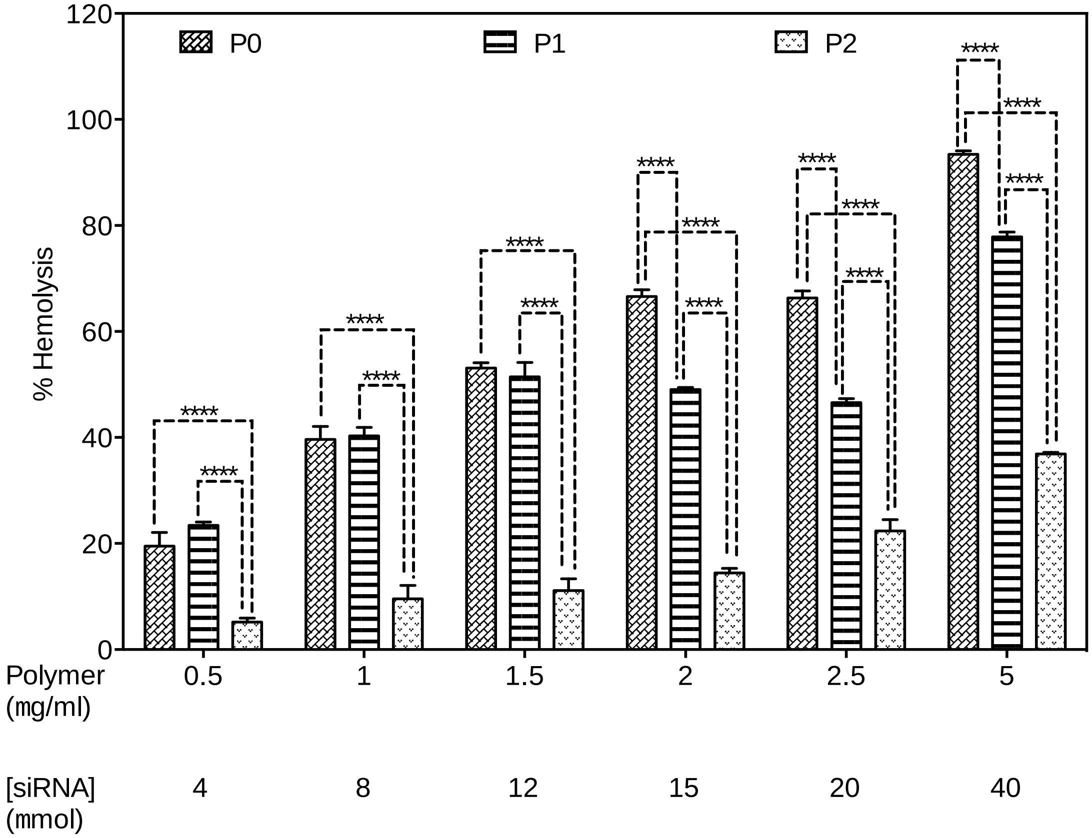

Figure 4.6: The biocompatibility profile of our "smart" nanoparticles (P0-2) was determined by evaluating their effect on eliciting RBC membrane hemolysis at physiological pH as a function of varying polymer concentrations. The observed hemolytic activity for each polymer formulation was normalized to that of the positive control (DI water). Results are the average + the standard error of the mean of three independent experiments each carried out in triplicates. Statistical difference between "smart" nanoparticle (P0-2) means at a given polymer concentration were evaluated using one-way ANOVA test with Tukey's post hoc. Statistical difference between group population means was significant at the 0.05 level where * denotes $p \leq 0.05$, ** denotes $p \leq 0.01$, *** denotes $p \leq 0.005$, and **** denotes $p \leq 0.001$

4.3.5.2. Nanoparticles stability in serum

The % of siRNA released from each particle composition (P0-3) was determined by normalizing the PicoGreen dye signal obtained from each particle condition to the free siRNA signal using a Fluoroskan microplate reader at λ_{ex} = 485 nm and λ_{em} = 518 nm. The results plotted in **Figure 4.7** represent the % of unshielded siRNA observed as a function of varying nanoparticle composition and serum concentrations. Results show that "smart" particles (P0 – 3) retained 90 – 92% of the loaded siRNA cargo in serum-free medium after 6 h. The incubation of nanoparticles (P0 – 2) with 10 – 25% of FBS resulted in partial siRNA decomplexation with a modest reduction in the amount of shielded siRNA molecules to nearly 75% of the loaded sample. This siRNA decomplexation pattern was observed across β-CD polymer compositions (P0-2) irrespective of their PEG lengths suggesting that neither 2 kDa nor 5 kDa PEG MW brushes significantly altered the serum stability of our nanoparticles. Thereby, suggesting that neither 2 kDa nor 5 kDa PEG brushes are sufficiently long enough to completely shield the cationic amphiphilic grafts complexing siRNA molecules on the secondary face. Moreover, prior studies have shown no considerable decrease in serum adsorption by PEG MW brushes > 5 kDa [38]. Despite the partial release of 25% of the loaded siRNA molecules, these particles retained and shielded the bulk of the loaded siRNA dose at a low N/P ratio (i.e., 2.5/1) and over a relatively long incubation time (6 h). On the other hand, particle P3 displayed a partially improved siRNA shielding capacity of 80 – 90% at all serum concentrations **(Figure 4.7)**. The serum stability of polymeric nanoparticles plays a critical role upon introduction into systemic circulation as the dilution effect often experienced results in nanoparticle disassembly and drug unloading [39].

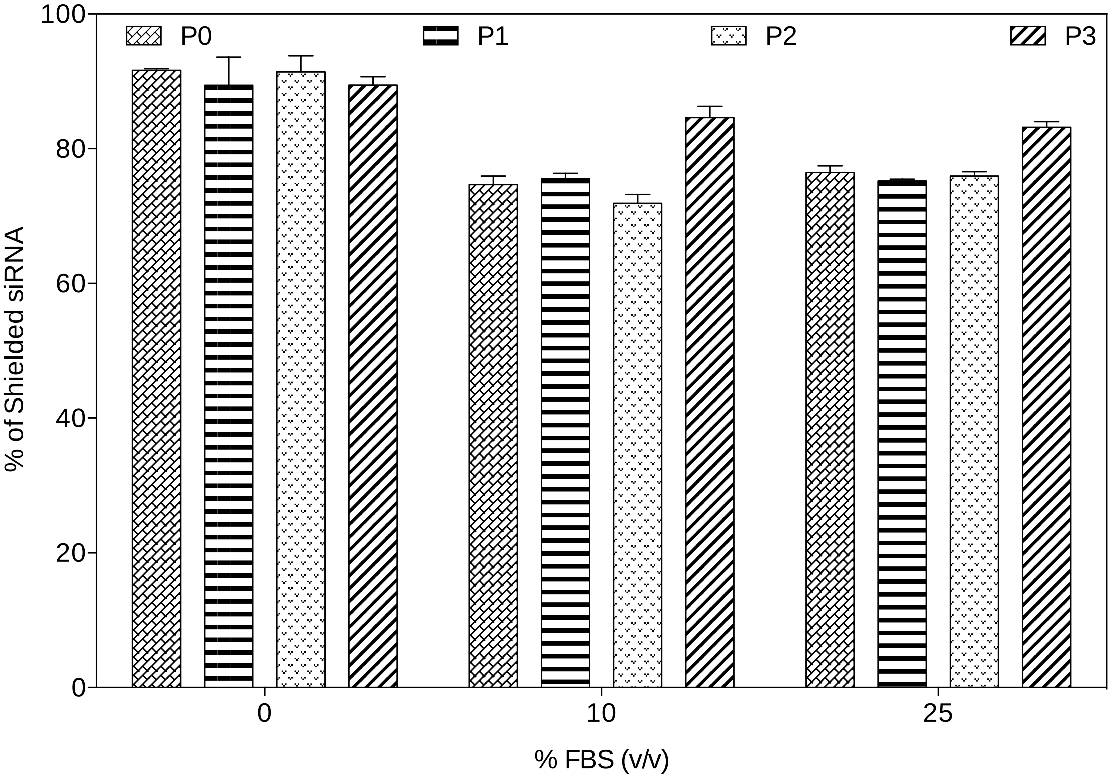

Figure 4.7: Percentage of siRNA molecules shielded by "smart" polymers complexing anti-GAPDH siRNA (i.e., P0, P1, P2, and P3) upon incubation with varying concentrations of FBS (i.e., 10% and 25% v/v) for 6 h at 37°C compared to "smart" nanoparticles incubated in serum-free medium (0% v/v). PicoGreen dye was used to determine the amount of unshielded siRNA molecules present in solution that were released from each particle formulation incubated in different FBS concentrations. The RFU values obtained for each particle formulation were normalized to RFU values obtained for the total encapsulated siRNA dose (0.75 μg) to determine % of shielded siRNA in each particle under different conditions. All particles were prepared at N/P ratio of 2.5/1. The plotted results are the average + the standard error of the mean of a single experiment carried out in triplicates.

4.3.6. Nanoparticles uptake into breast cancer cells

We evaluated if our EPPT1 targeted approach for the selective recognition of dysregulated uMUC1 target biomarkers showed significantly improved cellular internalization compared to our non-targeted β-CD particles. We used three different cell lines exhibiting varying degrees of uMUC1 receptor expression, namely a normal mammary epithelial cell line MCF10A (devoid of uMUC1 receptors), a TNBC cell line MDA-MB-231 (basal uMUC1 expression, +), and IBC cell line SUM149 cells (high uMUC1 expression, +++). The % cell uptake was determined by measuring the relative fluorescence intensity of each cell line incubated for 6 h with either non-targeted P2 or EPPT1-targeted P3 particles complexing FAM-labeled siRNA molecules (N/P of 2.5/1) at varying siRNA concentrations using flow cytometry. In **Figure 4.8, panel A, B, and C** we observe that non-targeted particle P2 showed no significant labeling of all three cell lines at lower siRNA concentration (i.e., 5, 7.5, 10, 15 nM) compared to their respective untreated cells. While at higher siRNA concentration (50 nM), particle P2 showed a 64.8 ± 1.7% uptake into MCF10A cells, and a significantly higher uptake of 89.5 ± 0.2% and 95.7 ± 0.8% into MDA-MB-231 and SUM149 cells, respectively. These findings indicate that there is no selective internalization of particle P2 into the three cell lines at all siRNA concentrations suggesting that at lower siRNA concentrations (i.e., < 15 nM) the 5 kDa PEG molecules on the primary face hinder cell uptake, while at higher siRNA concentrations the higher uptake profiles can be contributed to absorptive endocytosis due to an increase in the number of polymeric amphiphilic grafts present in solution. On the other hand, EPPT1-labeled P3 particles showed a significantly higher uptake of 55.2 ± 5.0% in SUM149 **(Figure 4.8 C)** cells compared to 1.8 ± 0.2% and 7.5 ± 1.7% in MCF10A **(Figure 4.8 A)** and MDA-MB-231 **(Figure 4.8 B)** cells, respectively at the lowest siRNA concentration of 5 nM. At 15 nM siRNA concentration, P3 particles showed maximum uptake of 92.4 ± 0.5% in SUM149 cells and significantly higher uptake of 81.7 ± 0.2% in MDA-MB-231 cells compared to a 4.5 ± 0.3% uptake in MCF10A cells. The results indicate that the significantly higher uptake (> 90%) of EPPT1-peptide coupled particles (P3) in uMUC1 expressing SUM149 cells at siRNA concentrations ≤ 25nM compared to non-targeted particle P2 that showed < 25% uptake is due to improved particle selectivity and receptor-mediated endocytosis. The significant difference in P3 uptake profiles at a given concentration in the three cell lines can be attributed to varying uMUC1 receptor expression levels, thus further corroborating the ability of our EPPT1-coupled particles to distinguish between the normal and cancer epithelial cells and reduce particle-associated cytotoxicity. Furthermore, our P3 particles exhibit increased cell specificity and higher uMUC1 sensitivity at lower polymer concentrations compared to non-targeted P2 particles.

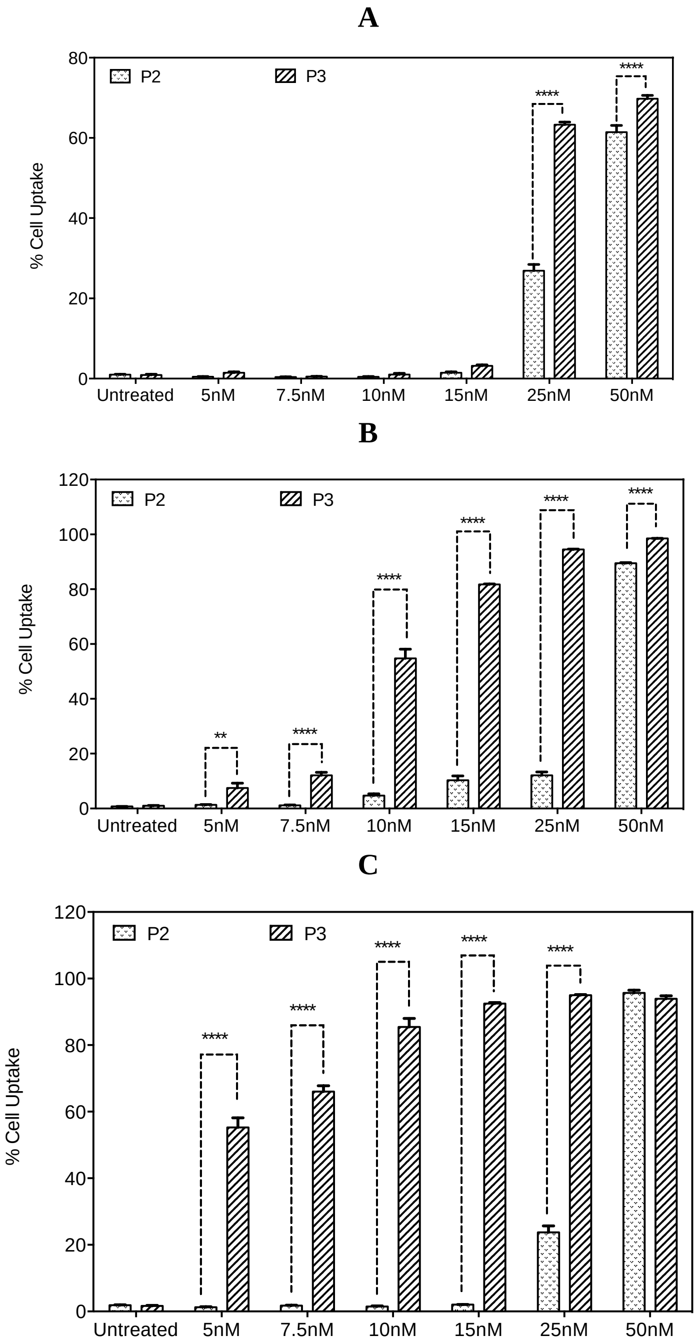

Figure 4.8: The plot represents the % of fluorescently-labeled **(A**) MCF10A, **(B**) MDA-MB-231, and **(C)** SUM149 cells after incubating for 6 h in a serum-free culture medium with "smart" nanoparticles (P2-3) prepared by complexing these "smart" polymers with 1.14 µg of FAM–labeled anti-GAPDH siRNA at N/P ratio of 2.5/1 as a function of different siRNA molecule concentrations (i.e., 5, 7.5, 10, 25, 50 nM). Cells treated with free siRNA were used as a negative control. Statistical difference between the nanoparticles' means were evaluated using one-way ANOVA test with Tukey's post hoc. Statistical difference between group population means was significant at the 0.05 level where * denotes $p \leq 0.05$, ** denotes $p \leq 0.01$, and *** denotes $p \leq 0.005$.

4.3.7. Effect of “smart” particles on RhoC expression

We evaluated the ability of our “smart” particles, P2 and P3, to functionally deliver anti-RhoC siRNA molecules (+) at a N/P ratio of 2.5/1 into the cytoplasm of MDA-MB-231 and SUM149 cells by quantifying their ability to suppress RhoC protein expression using western blots compared to their scrambled siRNA (-) counterparts, respectively. The results illustrated in **Figure 4.9** represent % RhoC protein suppression in both cell lines as a function of varying particle composition (i.e., P2 or P3 in **panel A**), siRNA concentration (i.e., 25 nM and 50 nM in **panel B, C**), and particle incubation time (i.e., 48 and 72 h in **panel B, C**) and frequency (i.e., 1x and 2x in **panel B**). The % knockdown of RhoC proteins in response to different treatment conditions were quantified using ImageJ software and normalized to the endogenous β-actin control and untreated SUM149 and MDA-MB-231 cells, respectively.

Figure 4.9 (A) compares the transfection efficacy of particle P2 and P3 complexing anti-RhoC siRNA molecules (+) (50nM) in both cell lines after a single transfection for 48 h. The results indicate that the (+) P2 particles showed no suppression and 56 ± 3.5% knockdown of RhoC protein expression in MDA-MB-231 and SUM149 cells, respectively compared to their scrambled control (-) P2. While (+) P3 showed 47 ± 3.5% and 66 ± 1.4% RhoC protein expression in MDA-MB-231 and SUM149 cells, respectively. In both cell lines, (+) P2 showed a significantly lower RhoC protein reduction compared to (+) P3 that could be attributed to their 5 kDa PEG brushes affecting endosomal escape and therefore, the subsequent release of anti-RhoC siRNA molecules. Also, the significantly higher RhoC protein knockdown using (+) P3 in SUM149 cells compared to MDA-MB-231 cells could be due to improved particle internalization as a result of higher uMUC1 receptor expression in SUM149 cells.

Figure 4.9 (B) outlines the RhoC protein expression levels in MDA-MB-231 cells treated with P3 encapsulating varying concentrations of anti-RhoC siRNA molecules (i.e., 25 or 50 nM) following either a single or double transfection cycles for different incubation lengths (i.e., 48 or 72 h). The results suggest that the double transfection cycle (i.e., at t = 0 h, and t = 24 h) shows significantly higher RhoC protein knockdown in MDA-MB-231 cells compared to single transfection at all anti-RhoC siRNA concentrations and incubation times. These observations are in compliance with the findings reported by Pille et. al. demonstrating significant improvement in RhoC knockdown upon the second and third transfection cycles. Furthermore, the results also suggest that on increasing the P3 complexed anti-RhoC siRNA concentration from 25 nM to 50 nM, the RhoC protein knockdown significantly increased from 59 ± 0.13% to 88 ± 2.2% in MDA-MB-231 cells upon double transfection for a 48 h incubation period suggesting a dose-dependent effect. Increasing particle incubation periods from 48 h to 72 h, however, did not significantly reduce RhoC protein expression, thereby suggesting a sustained RhoC suppression effect over time.

Figure 4.9 (C) exhibits the ability of P3 encapsulating different concentrations of anti-RhoC siRNA molecules (i.e., 25 or 50 nM) on suppressing RhoC protein expression in SUM149 cells following single transfection for different incubation times (i.e., 48 h or 72 h). The results indicate a time-dependent increase in RhoC protein knockdown at both anti-RhoC siRNA concentrations. The highest RhoC knockdown in SUM149 cells was observed (91 ± 2.4%) after a 72 h incubation with P3 encapsulating 50 nM anti-RhoC siRNA molecules. At all treatment conditions, we observed no particle associated cytotoxicity.

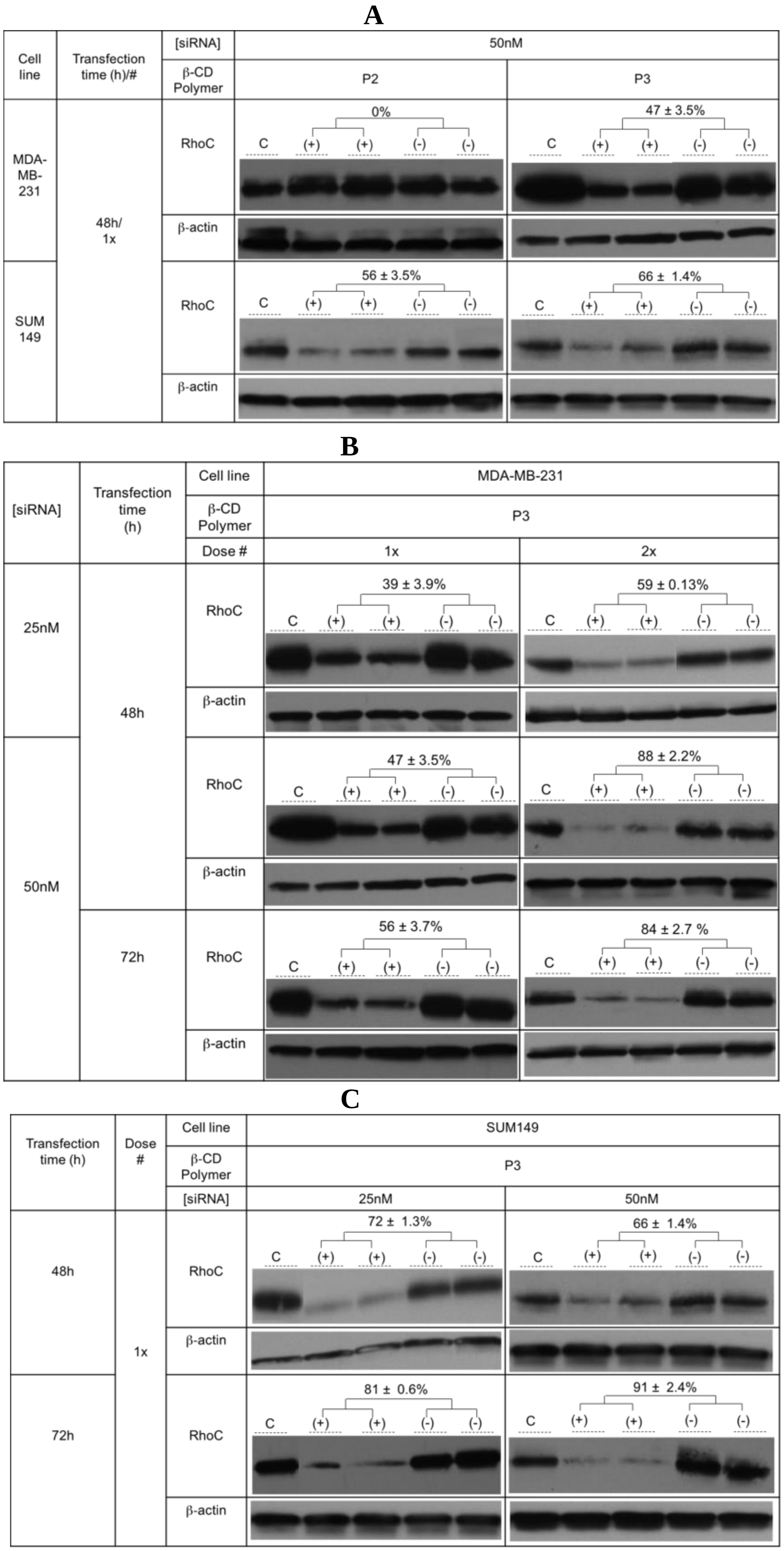

Figure 4.9: Effect of “smart” β-CD polymers complexing anti-RhoC siRNA (+) or scrambled siRNA (-) at an N/P ratio of 2.5/1 on RhoC protein levels in SUM149 and MDA-MB-231 cells were evaluated using western blot experiments. The RhoC protein expression levels **(A), (B), (C)** using both particles P2 and P3 were evaluated as a function of varying siRNA concentrations (i.e., 25, and 50 nM), varying transfection frequency (i.e., 1x, and 2x), and varying transfection duration (i.e., 48, and 72h). RhoC protein levels at each condition was quantified using ImageJ software (NIH, Bethesda, MD) and normalized to the levels of β-actin at similar time points. Results are the average + the SEM of five replicates.

4.3.8 Boyden chamber invasion assay

We evaluated both the individual and combinatorial effect of reducing RhoC expression via anti-RhoC siRNA and inhibiting uMUC1 receptor activity via the EPPT1 binding on suppressing the invasive phenotypes of both breast cancer cells using the Boyden invasion chamber. The results of both individual and combinatorial treatment effects in both cell lines have been shown in **Figure 4.10, panel A-G**. The individual contribution of anti–RhoC siRNA molecules and EPPT1-targeted peptides in suppressing cell invasion illustrated in **Figure 4.10 (G)** was determined by quantifying the number of invading cancer cells upon treatment with either (+) P2 and (-) P3 complexing 50 nM siRNA, respectively. In **Figure 4.10 (G)**, we observe a 44 ± 1.0% and 43% ± 6.4% significant reduction in the number of invading MDA-MB-231 cells, while a 37 ± 4.1% and 41 ± 6.0% statistical reduction in invading SUM149 cells compared to the untreated control upon treatment with (+) P2 and (-) P3 particles, respectively. The combinatorial effect of anti-RhoC siRNA molecules and EPPT1-targeted peptides on cell invasion shown in **Figure 4.10 (G)** treated with (+) P3 complexing 50 nM siRNA concentration demonstrated a significant reduction of 86 ± 4.6% and 75 ± 1.4% in invading MDA-MB-231 and SUM149 cells, respectively. The negative scrambled control (-) P2 showed no particle associated cytotoxicity compared to the untreated controls in both cell lines. The combinatorial interaction of both therapeutic components determined using CDI analysis suggested a synergistic inhibition (CDI < 1) of invasive phenotypes in both cell line. We previously reported a ~50% reduction in invasive phenotypes in SUM149 and MDA-MB-231 cells on silencing RhoC expression using our non-PEGylated “smart” nanoparticle complexing anti-RhoC siRNA molecules. Using (+) P2 nanoparticles, we demonstrated similar reduction in invasive phenotypes (~44%) upon knocking down RhoC expression in the above mentioned cell types. These results suggest that RhoC expression is responsible for only a portion of the invasive machinery of metastatic breast cancer cells and further lead us to investigate the effect of uMUC1 inhibition on suppressing cell invasion. The ~40% reduction in invasive phenotypes observed in both cell lines upon treatment with (-) P3 compared to negative control (-) P2 and untreated controls, respectively indicates the potential role of EPPT1-peptides binding in inhibiting uMUC1 activity. We hypothesize that the observed results could be due to the high binding affinity of EPPT1 peptides for the PDTR region of the ECD uMUC1 receptors that prevents the binding of other factors like galectin-3 to these sites may inhibit the uMUC1 cytoplasmic signal transduction by preventing β-catenin recruitment through the activation of non-receptor kinase src, thereby suppressing adheren junction disruption and reduction of loss of cell adhesion.

Now on combining the individual therapeutic agents (i.e., anti-RhoC siRNA and EPPT1 peptides) into the same “smart” nanoparticle (i.e., (+) P3), we observed a synergistic reduction in invasion (~80%) in both SUM149 and MDA-MB-231 cells. We believe that this synergistic inhibition observed maybe due to the suppression of the Rho-GTPase subfamily, namely RhoC, Cdc42 and Rac1 proteins in both cell lines that have been implicated in the reorganization of actin cytoskeleton and the assembly of focal adhesion points involved in cell invasion. By preventing the activity of non-receptor kinase scr through EPPT1-uMUC binding could suppress activation of downstream signaling pathways like FAK and CrkL that are known regulators of Rho-GTPases like Cdc42 and Rac1. It is important to note that all experiments were performed as per pre-optimized treatment conditions identified during the western blot experiments. We observed a similar reduction in the number of cells invading the matrigel on treatment with P3 complexing a reduced dose of siRNA concentration (i.e., from 50 nM to 25 nM) in both cell lines.

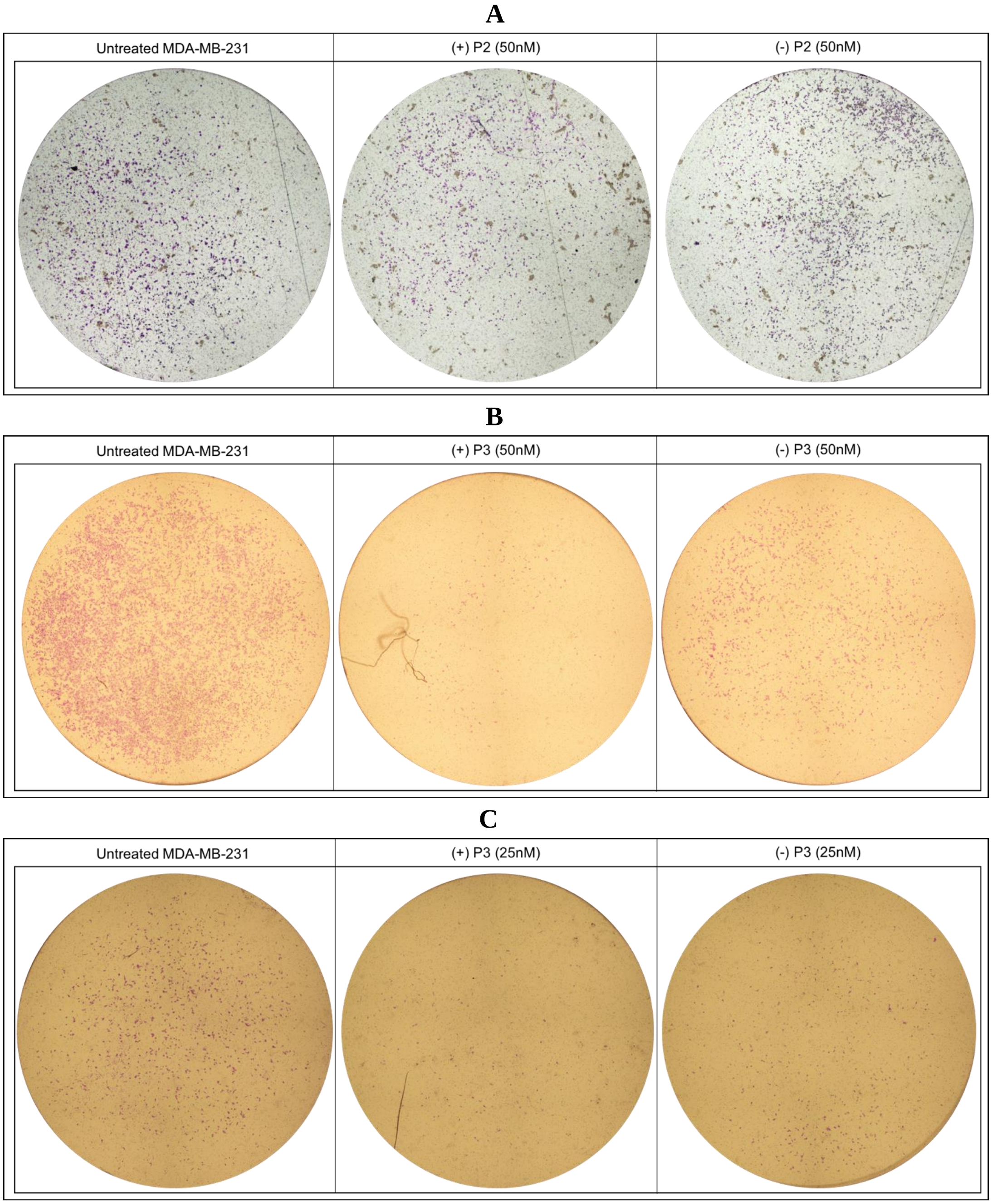

Figure 4.10: SUM149 and MDA-MB-231 cells were plated on Matrigel invasion chambers and treated with “smart” β-CD polymers P2 and P3 complexing 1.14μg of anti-RhoC siRNA (+) or scrambled siRNA (-). **(A), (B),** and **(C)** represent images of MDA-MB-231 cells invading the lower matrigel membrane as a function of varying siRNA concentrations (i.e., 25, and 50nM).

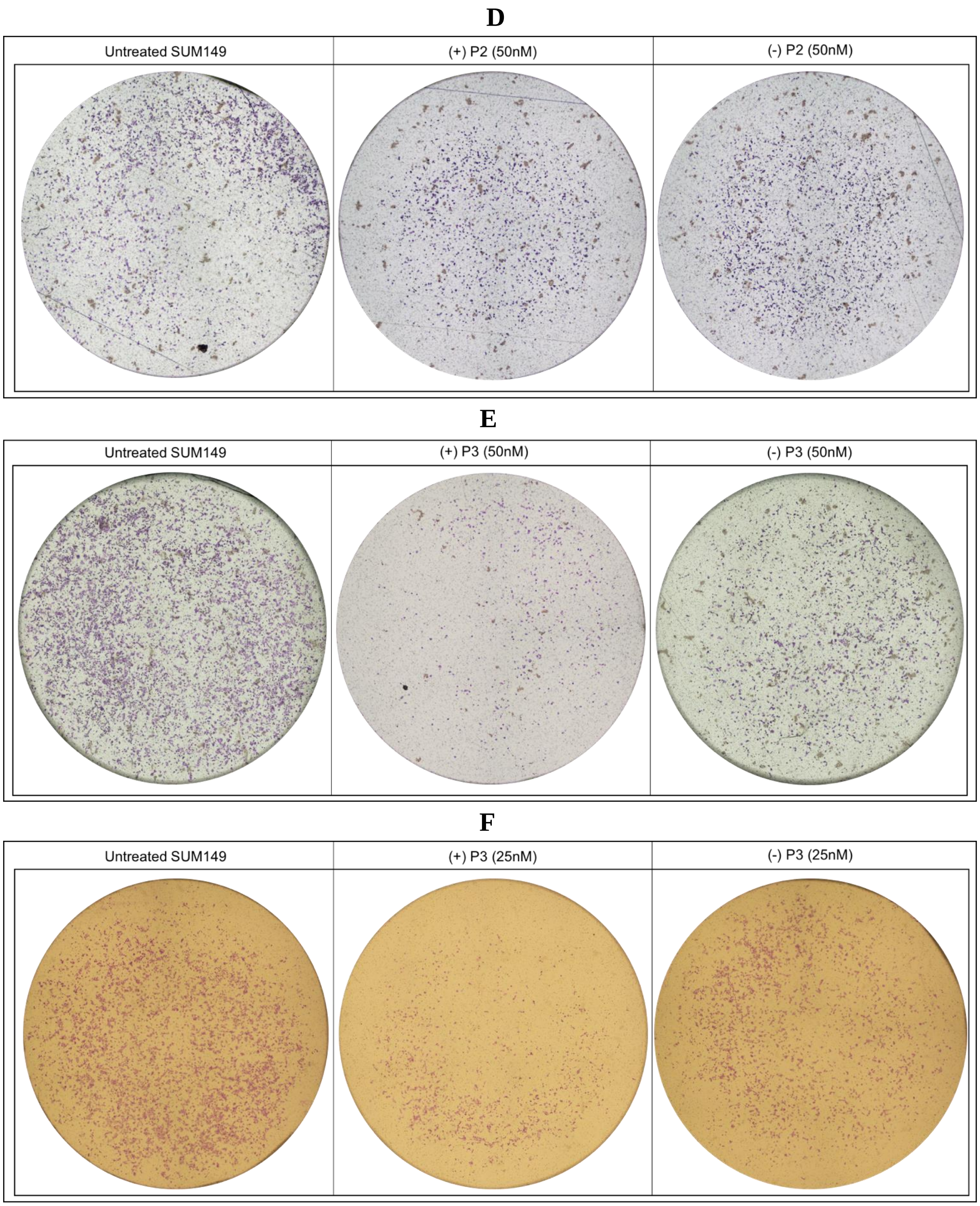

Figure 4.10: SUM149 and MDA-MB-231 cells were plated on Matrigel invasion chambers and treated with “smart” β-CD polymers P2 and P3 complexing 1.14μg of anti-RhoC siRNA (+) or scrambled siRNA (-). **(D), (E),** and **(F)** represent images of SUM149 cells invading the lower matrigel membrane as a function of varying siRNA concentrations (i.e., 25, and 50nM).

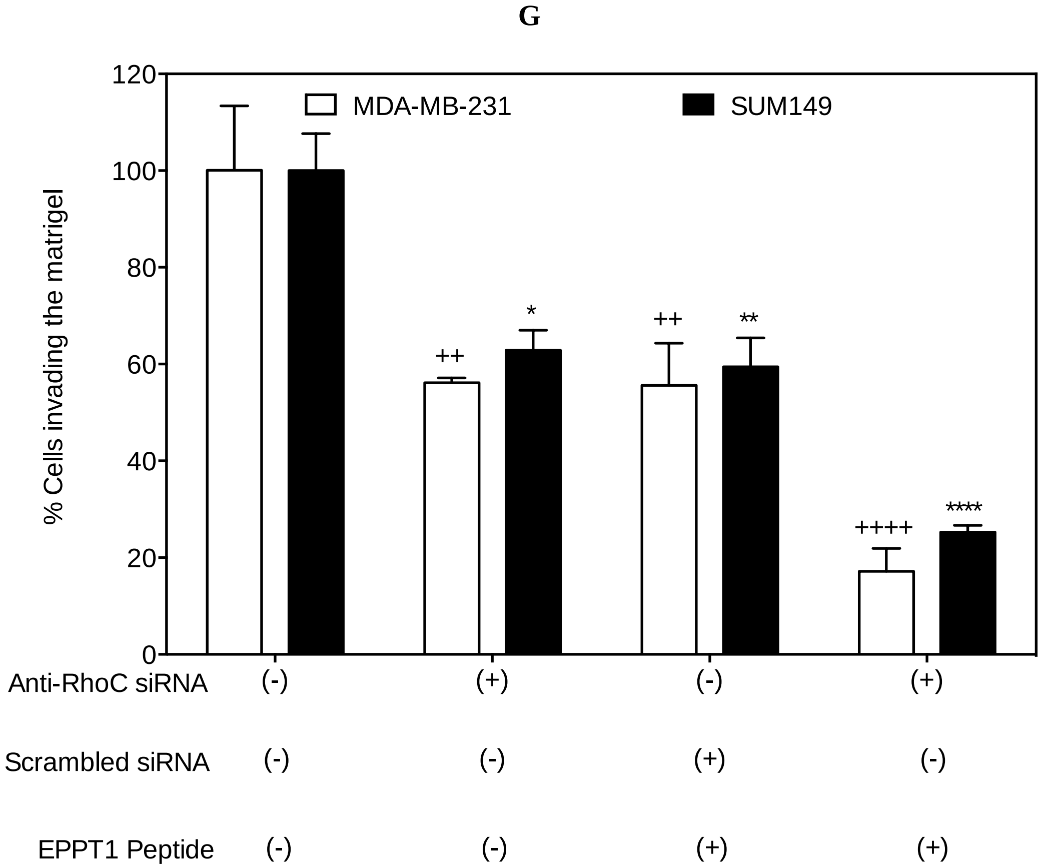

Figure 4.10: The % of MDA-MB-231 and SUM149 cells invading the lower matrigel following their treatment with different polymer compositions after 72 h. **G** represents the % of cells treated with "smart" polymer (P2) complexing 50 nM anti-RhoC siRNA (+) and EPPT1-targeted polymer (P3) complexing 50 nM anti-RhoC siRNA (+) or scrambled siRNA (-). Plotted results are the average + the SEM of five replicates. Statistical difference between the nanoparticles' means were evaluated using one-way ANOVA test with Tukey's post hoc. Statistical difference between group population means was significant at the 0.05 level where * denotes $p \leq 0.05$, ** denotes $p \leq 0.01$, and *** denotes $p \leq 0.005$.

4.3.9 Scratch assay

The effect of anti-RhoC siRNA molecules and EPPT1-targeted peptides on suppressing cancer cell migration was evaluated using standard wound healing assay. The results obtained are shown in **Figure 4.11, panel A-C**. As described in the previous section, the individual contribution of each therapeutic entity on suppressing cell migration was evaluated by treating each cell line with either (+) P2 to determine the migratory effect of knocking down RhoC expression and (-) P3 to evaluate the effect of uMUC1 inhibition. **Figure 4.11 (C)** shows a 0% and 39% ± 2.5% reduction in migration in MDA-MB-231 cells, while a 62 ± 2.2% and 31 ± 2.5% suppression in migration in SUM149 cells compared to the untreated controls upon treatment with (+) P2 and (-) P3 particles, respectively. The combinatorial effect of anti−RhoC siRNA molecules and EPPT1−targeted peptides on cell migration (**Figure 4.11 C)** was evaluated with (+) P3 complexing 50 nM siRNA concentration that demonstrated a significant reduction in migration by 72 ± 6.5% and 80 ± 2.4% in MDA-MB-231 and SUM149 cells, respectively. The negative scrambled control (-) P2 showed no particle associated cytotoxicity compared to the untreated controls in both cell lines. The combinatorial interaction of both therapeutic components determined using CDI analysis suggested a synergistic inhibition (CDI < 1) of migratory phenotypes in both cell line. Prior work has demonstrated MUC1 and β-catenin co-localization with the actin-bundling protein fascin in membrane protrusions of migrating cells - suggesting this complex plays a role in cell migration. The role of fascin in membrane reorganization involves tight packing of actin filaments into membrane protrusions such as lamellipodia, microspikes, and membrane ruffles resulting in invasion and migration. We believe that the EPPT1-peptide binding to uMUC1 inhibits the co-localization of proteins and subsequently results in a synergistic decrease in cancer cell migration.

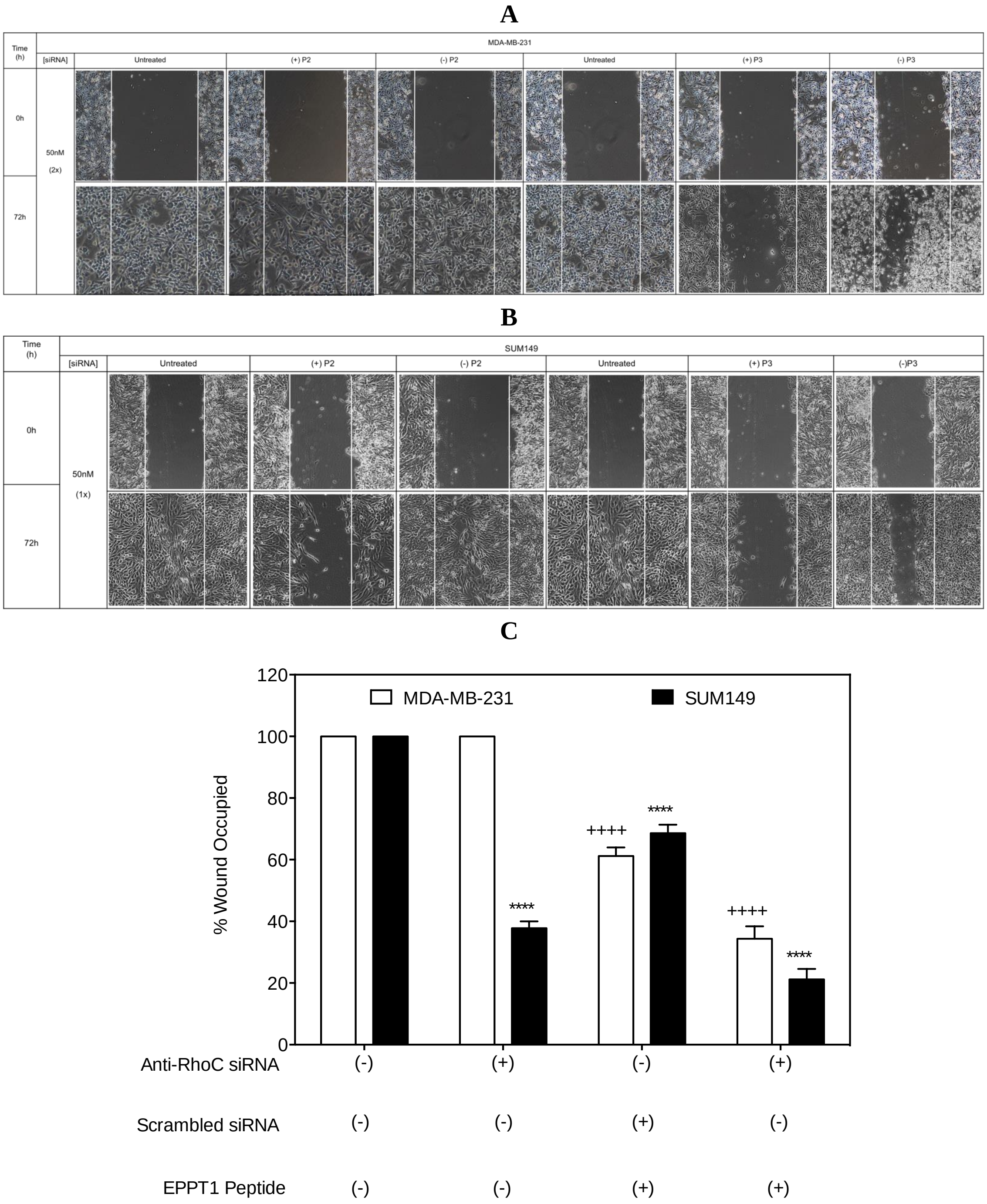

Figure 4.11: Representative images (10X magnification) showing the effect of "smart" anti-RhoC (+) and scrambled (-) particles P2 and P3 on the migration of **(A)** SUM149 and **(B)** MDA-MB-231 cells. **(C)** The percentage of wound coverage by SUM149 and MDA-MB-231 cells (48 h) after treatment with "smart" anti-RhoC (+) and scrambled (-) particles normalized to the initial wound (t = 0 h). Statistical difference between "smart" anti-RhoC (+) and scrambled (-) particles was evaluated using paired *t* test where * denotes $p \leq 0.05$, ** denotes $p \leq 0.01$ and, *** denotes $p \leq 0.005$

4.3.10 Effect of targeted $(EPPT1)_6$-(5 kDa-PEG)$_{6.5}$-β-CD-P(HMA-co-DMAEMA-co-TMAEMA)$_{5.9}$ polymers on phosphorylated Src and FAK protein expression

We further investigated the potential drivers of the observed synergistic reduction in both invasive and migratory phenotypes in SUM149 breast cancer cells treated with EPPT1-targeted (P3) particles encapsulating anti-RhoC siRNA molecules (i.e., 50 nM) at a N/P ratio of 2.5/1. We determined the downstream effect of EPPT1 peptide binding to uMUC1 receptors by evaluating the activation of P-Src (Y419) and P-FAK (Y576/577) protein expression in SUM149 cells following treatment with EPPT1-targeted (P3) and non-targeted (P2) particles complexing scrambled siRNA (-) for 48 and 72 h. The amount of activated P-Src (Y419) and P-FAK (Y576/577) protein expressed in SUM149 cells were quantified as a function of total Src and FAK protein expression under different treatment conditions and time points (i.e., 48 and 72 h) in **Figure 4.12**. The results show a 25% and 35% reduction in activated P-Src (Y419), while a 26% and 21% reduction in P-FAK (Y576/577) expression levels after a 48 h treatment with (-) P2 and (-) P3 particles compared to the untreated control, respectively. However, a significant reduction of 75% in P-Src (Y419) and 87% in P-FAK (Y576/577) was observed after a 72 h treatment of SUM149 cells with (-) P3 compared to the untreated controls. The P-Src (Y419) and P-FAK (Y576/577) levels of SUM149 cells treated with (-) P2 particles remained unchanged after the 72 h treatment. The results, therefore suggest that the binding of EPPT1 peptides to uMUC1 receptors affect the downstream activation of Src and FAK proteins. Previous studies have shown that the activation of uMUC1 receptors plays a significant role in the activation and phosphorylation of several SH2 domain containing proteins including c-Src and activation of SH_2 domain containing proteins like c-Src [27]. Following activation by c-Src via phosphorylation at the active site, the activated Src directly phosphorylates its downstream effector molecule FAK resulting in increased metastasis and invasion **(Figure 4.13)**. These findings suggest a temporal overlap in activity of both the EPPT1 targeting peptides and the anti-RhoC siRNA molecules delivered into the cytoplasm of SUM149 cells following a 72 h treatment; thereby, resulting in a synergistic reduction of cell invasion and migration.

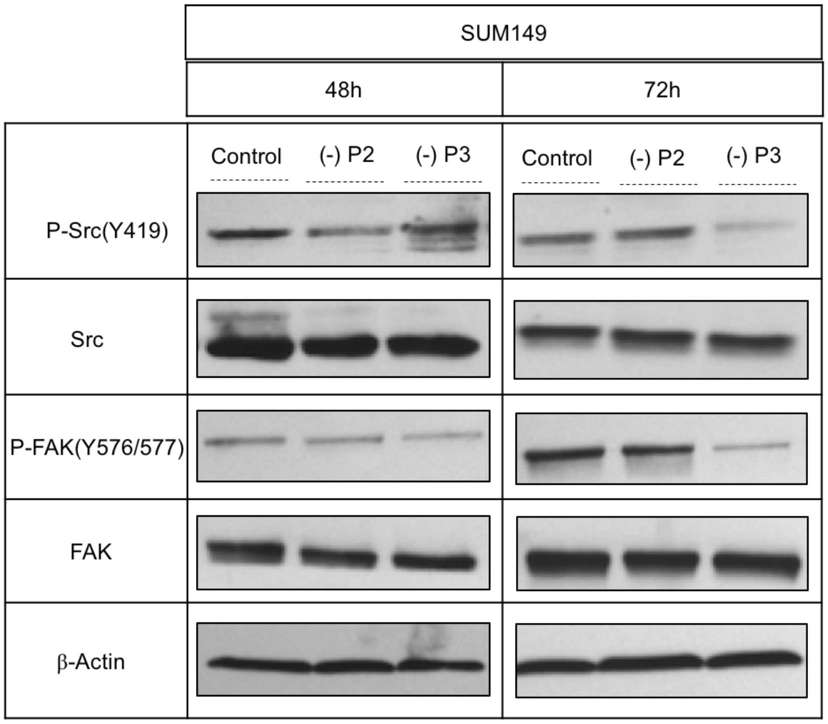

Figure 4.12: Determine the downstream effect elicited by EPPT1 - targeting peptides upon binding to uMUC1 receptors overexpressed on the surface of SUM149 cells after 48 h and 72 h. SUM149 cells were treated with (-) P2 and (-) P3 particles encapsulating 50nM scrambled siRNA, respectively. The western blot illustrates the effect of (-) P3 particles on the activation of Src and FAK compared to their negative controls suggesting that the synergistic reduction in invasion and migration can be attributed to the inactivation of P-Src(Y419) and P-FAK(Y576/577) upon EPPT1 binding to uMUC1 receptors. Statistical difference (-) P2 and (-) P3 particles was evaluated using paired *t* test where * denotes $p \leq 0.05$, ** denotes $p \leq 0.01$ and, *** denotes $p \leq 0.005$.

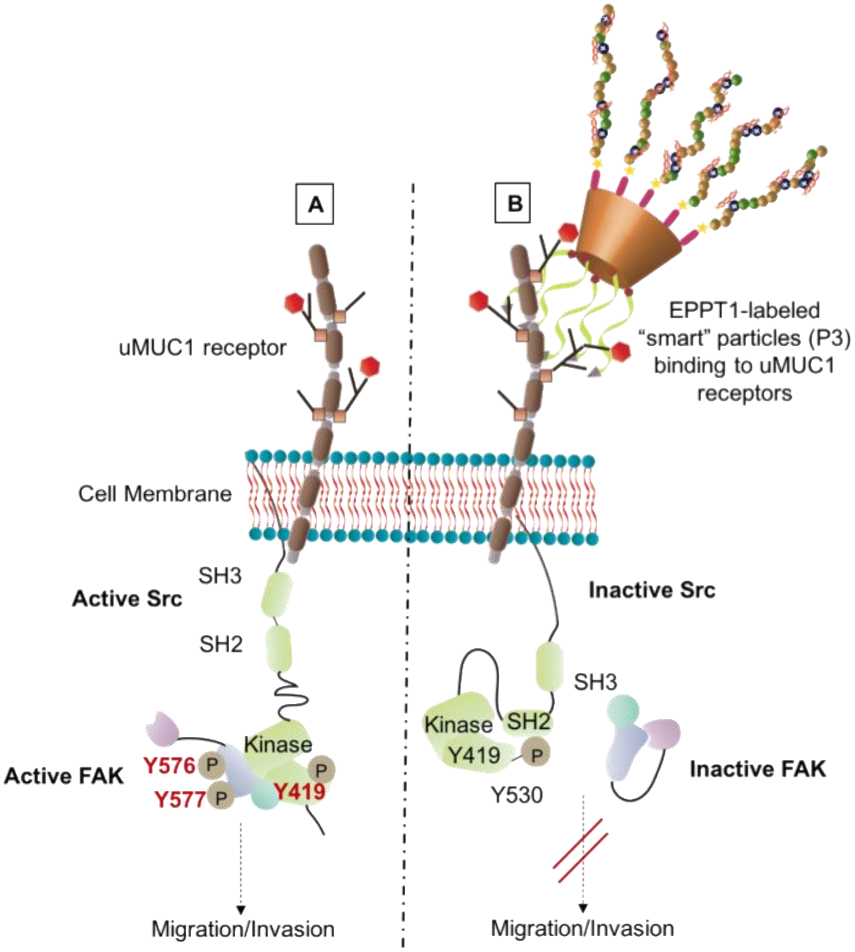

Figure 4.13: Illustrates the suggested mechanism of action following the binding of EPPT1 peptides displayed on P3 particles to uMUC1 receptors **(panel B)**. **Panel A** represents the signal transduction pathway upregulated following the binding of specific growth factors to uMUC1 antigens.

References

[1] A. Jemal, F. Bray, M. M. Center, J. Ferlay, E. Ward, and D. Forman, “Global cancer statistics,” *CA. Cancer J. Clin.*, vol. 61, no. 2, pp. 69–90, Apr. 2011.

[2] US Preventive Services Task Force, “Screening for breast cancer: U.S. Preventive Services Task Force recommendation statement,” *Ann. Intern. Med.*, vol. 151, no. 10, pp. 716–726, W–236, Nov. 2009.

[3] B. Weigelt, J. L. Peterse, and L. J. van’t Veer, “Breast cancer metastasis: markers and models,” *Nat. Rev. Cancer*, vol. 5, no. 8, pp. 591–602, Aug. 2005.

[4] C. D. Nobes and A. Hall, “Rho, Rac, and Cdc42 GTPases regulate the assembly of multimolecular focal complexes associated with actin stress fibers, lamellipodia, and filopodia,” *Cell*, vol. 81, no. 1, pp. 53–62, Apr. 1995.

[5] A. F. Chambers, A. C. Groom, and I. C. MacDonald, “Dissemination and growth of cancer cells in metastatic sites,” *Nat. Rev. Cancer*, vol. 2, no. 8, pp. 563–572, Aug. 2002.

[6] F. van Zijl, G. Krupitza, and W. Mikulits, “Initial steps of metastasis: Cell invasion and endothelial transmigration,” *Mutat. Res. Mutat. Res.*, vol. 728, no. 1–2, pp. 23–34, Jul. 2011.

[7] K. Kimura, M. Ito, M. Amano, K. Chihara, Y. Fukata, M. Nakafuku, B. Yamamori, J. Feng, T. Nakano, K. Okawa, A. Iwamatsu, and K. Kaibuchi, “Regulation of myosin phosphatase by Rho and Rho-associated kinase (Rho-kinase),” *Science*, vol. 273, no. 5272, pp. 245–248, Jul. 1996.

[8] C. G. Kleer, K. A. Griffith, M. S. Sabel, G. Gallagher, K. L. van Golen, Z.-F. Wu, and S. D. Merajver, “RhoC-GTPase is a novel tissue biomarker associated with biologically aggressive carcinomas of the breast,” *Breast Cancer Res. Treat.*, vol. 93, no. 2, pp. 101–110, Sep. 2005.

[9] I. A. Prior, P. D. Lewis, and C. Mattos, “A comprehensive survey of Ras mutations in cancer,” *Cancer Res.*, vol. 72, no. 10, pp. 2457–2467, May 2012.

[10] A. J. Ridley, “Rho Proteins and Cancer,” *Breast Cancer Res. Treat.*, vol. 84, no. 1, pp. 13–19, Mar. 2004.

[11] M. Wu, Z.-F. Wu, C. Kumar-Sinha, A. Chinnaiyan, and S. D. Merajver, “RhoC induces differential expression of genes involved in invasion and metastasis in MCF10A breast cells,” *Breast Cancer Res. Treat.*, vol. 84, no. 1, pp. 3–12, Mar. 2004.

[12] D. T. Rosenthal, J. Zhang, L. Bao, L. Zhu, Z. Wu, K. Toy, C. G. Kleer, and S. D. Merajver, “RhoC Impacts the Metastatic Potential and Abundance of Breast Cancer Stem Cells,” *PLoS ONE*, vol. 7, no. 7, p. e40979, Jul. 2012.

[13] M. Wu, Z.-F. Wu, D. T. Rosenthal, E. M. Rhee, and S. D. Merajver, “Characterization of the roles of RHOC and RHOA GTPases in invasion, motility, and matrix adhesion in inflammatory and aggressive breast cancers,” *Cancer*, vol. 116, no. 11 Suppl, pp. 2768–2782, Jun. 2010.

[14] K. L. van Golen, Z. F. Wu, X. T. Qiao, L. W. Bao, and S. D. Merajver, “RhoC GTPase, a novel transforming oncogene for human mammary epithelial cells that partially recapitulates the inflammatory breast cancer phenotype,” *Cancer Res.*, vol. 60, no. 20, pp. 5832–5838, Oct. 2000.

[15] N. Kaushal, Y. Y. Durmaz, L. Bao, S. D. Merajver, and M. E. H. ElSayed, “‘Smart’ Nanoparticles Enhance the Cytoplasmic Delivery of Anti-RhoC Silencing RNA and Inhibit the Migration and Invasion of Aggressive Breast Cancer Cells,” *Mol. Pharm.*, vol. 12, no. 7, pp. 2406–2417, Jul. 2015.

[16] C. L. Hattrup and S. J. Gendler, “Structure and Function of the Cell Surface (Tethered) Mucins,” *Annu. Rev. Physiol.*, vol. 70, no. 1, pp. 431–457, 2008.

[17] H. Tsutsumida, B. J. Swanson, P. K. Singh, T. C. Caffrey, S. Kitajima, M. Goto, S. Yonezawa, and M. A. Hollingsworth, “RNA interference suppression of MUC1 reduces the growth rate and metastatic phenotype of human pancreatic cancer cells,” *Clin. Cancer Res. Off. J. Am. Assoc. Cancer Res.*, vol. 12, no. 10, pp. 2976–2987, May 2006.

[18] Y. Li, D. Liu, D. Chen, S. Kharbanda, and D. Kufe, “Human DF3/MUC1 carcinoma-associated protein functions as an oncogene,” *Oncogene*, vol. 22, no. 38, pp. 6107–6110, Sep. 2003.

[19] S. J. Gendler, C. A. Lancaster, J. Taylor-Papadimitriou, T. Duhig, N. Peat, J. Burchell, L. Pemberton, E. N. Lalani, and D. Wilson, “Molecular cloning and expression of human tumor-associated polymorphic epithelial mucin,” *J. Biol. Chem.*, vol. 265, no. 25, pp. 15286–15293, Sep. 1990.

[20] J. M. Burchell, A. Mungul, and J. Taylor-Papadimitriou, “O-linked glycosylation in the mammary gland: changes that occur during malignancy,” *J. Mammary Gland Biol. Neoplasia*, vol. 6, no. 3, pp. 355–364, Jul. 2001.

[21] I. Brockhausen, J. M. Yang, J. Burchell, C. Whitehouse, and J. Taylor-Papadimitriou, “Mechanisms underlying aberrant glycosylation of MUC1 mucin in breast cancer cells,” *Eur. J. Biochem. FEBS*, vol. 233, no. 2, pp. 607–617, Oct. 1995.

[22] J. J. Rahn, L. Dabbagh, M. Pasdar, and J. C. Hugh, “The importance of MUC1 cellular localization in patients with breast carcinoma: an immunohistologic study of 71 patients and review of the literature,” *Cancer*, vol. 91, no. 11, pp. 1973–1982, Jun. 2001.

[23] J. A. Schroeder, M. C. Thompson, M. M. Gardner, and S. J. Gendler, “Transgenic MUC1 Interacts with Epidermal Growth Factor Receptor and Correlates with Mitogen-activated Protein Kinase Activation in the Mouse Mammary Gland,” *J. Biol. Chem.*, vol. 276, no. 16, pp. 13057–13064, Apr. 2001.

[24] S. Tanida, Y. Mori, A. Ishida, K. Akita, and H. Nakada, “Galectin-3 binds to MUC1-N-terminal domain and triggers recruitment of β-catenin in MUC1-expressing mouse 3T3 cells,” *Biochim. Biophys. Acta*, vol. 1840, no. 6, pp. 1790–1797, Jun. 2014.

[25] J. A. Schroeder, M. C. Adriance, M. C. Thompson, T. D. Camenisch, and S. J. Gendler, “MUC1 alters β-catenin-dependent tumor formation and promotes cellular invasion,” *Oncogene*, vol. 22, no. 9, pp. 1324–1332, 2003.

[26] A. J. Bernier, J. Zhang, E. Lillehoj, A. R. Shaw, N. Gunasekara, and J. C. Hugh, “Non-cysteine linked MUC1 cytoplasmic dimers are required for Src recruitment and ICAM-1 binding induced cell invasion,” *Mol. Cancer*, vol. 10, p. 93, Jul. 2011.

[27] Q. Shen, J. J. Rahn, J. Zhang, N. Gunasekera, X. Sun, A. R. E. Shaw, M. J. Hendzel, P. Hoffman, A. Bernier, and J. C. Hugh, “MUC1 initiates Src-CrkL-Rac1/Cdc42-mediated actin cytoskeletal protrusive motility after ligating intercellular adhesion molecule-1,” *Mol. Cancer Res. MCR*, vol. 6, no. 4, pp. 555–567, Apr. 2008.

[28] E. Pichinuk, I. Benhar, O. Jacobi, M. Chalik, L. Weiss, R. Ziv, C. Sympson, A. Karwa, N. I. Smorodinsky, D. B. Rubinstein, and D. H. Wreschner, “Antibody targeting of cell-bound MUC1 SEA domain kills tumor cells,” *Cancer Res.*, vol. 72, no. 13, pp. 3324–3336, Jul. 2012.

[29] H. M. Prinssen, C. F. Molthoff, R. H. Verheijen, T. J. Broadhead, P. Kenemans, J. C. Roos, Q. Davies, A. C. van Hof, M. Frier, W. den Hollander, A. J. Wilhelm, T. S. Baker, M. Sopwith, E. M. Symonds, and A. C. Perkins, “Biodistribution of 111In-labelled engineered

human antibody CTM01 (hCTM01) in ovarian cancer patients: influence of prior administration of unlabelled hCTM01," *Cancer Immunol. Immunother. CII*, vol. 47, no. 1, pp. 39–46, Sep. 1998.

[30] M. Kumar, M. Yigit, G. Dai, A. Moore, and Z. Medarova, "Image-Guided Breast Tumor Therapy Using a Small Interfering RNA Nanodrug," *Cancer Res.*, vol. 70, no. 19, pp. 7553–7561, Oct. 2010.

[31] J. S. de Bono, S. Y. Rha, J. Stephenson, B. C. Schultes, P. Monroe, G. S. Eckhardt, L. A. Hammond, T. L. Whiteside, C. F. Nicodemus, J. M. Cermak, E. K. Rowinsky, and A. W. Tolcher, "Phase I trial of a murine antibody to MUC1 in patients with metastatic cancer: evidence for the activation of humoral and cellular antitumor immunity," *Ann. Oncol.*, vol. 15, no. 12, pp. 1825–1833, Dec. 2004.

[32] M. D. Pegram, V. F. Borges, N. Ibrahim, J. Fuloria, C. Shapiro, S. Perez, K. Wang, F. S. Stark, and N. C. Luck, "Phase I dose escalation pharmacokinetic assessment of intravenous humanized anti-MUC1 antibody AS1402 in patients with advanced breast cancer," *Breast Cancer Res.*, vol. 11, no. 5, p. R73, Oct. 2009.

[33] R. Hussain, N. S. Courtenay-Luck, and G. Siligardi, "Structure-function correlation and biostability of antibody CDR-derived peptides as tumour imaging agents," *Biomed. Pept. Proteins Nucleic Acids Struct. Synth. Biol. Act.*, vol. 2, no. 3, pp. 67–70, 1997 1996.

[34] M. Bloch, Y. Kam, E. Yavin, D. Moradov, A. Nissan, I. Ariel, and A. Rubinstein, "The relative roles of charge and a recognition peptide in luminal targeting of colorectal cancer by fluorescent polyacrylamide," *Eur. J. Pharm. Sci. Off. J. Eur. Fed. Pharm. Sci.*, vol. 47, no. 5, pp. 904–913, Dec. 2012.

[35] M. Kumar, M. Yigit, G. Dai, A. Moore, and Z. Medarova, "Image-Guided Breast Tumor Therapy Using a Small Interfering RNA Nanodrug," *Cancer Res.*, vol. 70, no. 19, pp. 7553–7561, Oct. 2010.

[36] Z. Medarova, L. Rashkovetsky, P. Pantazopoulos, and A. Moore, "Multiparametric Monitoring of Tumor Response to Chemotherapy by Noninvasive Imaging," *Cancer Res.*, vol. 69, no. 3, pp. 1182–1189, Jan. 2009.

[37] Y. Y. Durmaz, Y.-L. Lin, and M. E. H. ElSayed, "Development of Degradable, pH-Sensitive Star Vectors for Enhancing the Cytoplasmic Delivery of Nucleic Acids," *Adv. Funct. Material*, vol. 23, no. 31, pp. 3885–3895, Aug. 2013.

[38] N. Kaushal, Y. Y. Durmaz, L. Bao, S. D. Merajver, and M. E. H. ElSayed, "'Smart' Nanoparticles Enhance the Cytoplasmic Delivery of Anti-RhoC Silencing RNA and Inhibit the Migration and Invasion of Aggressive Breast Cancer Cells," *Mol. Pharm.*, vol. 12, no. 7, pp. 2406–2417, Jul. 2015.

[39] Z. Medarova, W. Pham, Y. Kim, G. Dai, and A. Moore, "In vivo imaging of tumor response to therapy using a dual-modality imaging strategy," *Int. J. Cancer*, vol. 118, no. 11, pp. 2796–2802, Jun. 2006.

[40] R. Gref, M. Lück, P. Quellec, M. Marchand, E. Dellacherie, S. Harnisch, T. Blunk, and R. H. Müller, "'Stealth' corona-core nanoparticles surface modified by polyethylene glycol (PEG): influences of the corona (PEG chain length and surface density) and of the core composition on phagocytic uptake and plasma protein adsorption," *Colloids Surf. B Biointerfaces*, vol. 18, no. 3–4, pp. 301–313, Oct. 2000.

[41] B. M. D. C. Godinho, "PEGylated cyclodextrins as novel siRNA nanosystems: Correlations between polyethylene glycol length and nanoparticle stability," *Int. J. Pharm.*, vol. 473, no. 1–2, pp. 105–112, Oct. 2014.

Chapter 5

In vivo evaluation of active and passive targeted nanoparticle strategies for the enhanced delivery of therapeutic siRNA to breast cancer tumors

5.1 Introduction

Since the discovery of endogenous RNA interference (RNAi) in mammalian cells[1], there has been a drive toward developing this pathway for the treatment of several diseases[2, 3]. However, RNAi-based drugs, like silencing RNA (siRNA), often suffer from poor tissue penetration and low serum stability *in vivo* that results in reduced therapeutic efficacy. To achieve the clinical potential of RNAi-based drugs, delivery vechicles that incorporate siRNA are required to efficiently transport the therapeutic payload into the cytoplasm of target cells[4]. In general, these delivery vechicles are designed to facilitate efficient uptake into the target tissue of interest and when used for systemic delivery, protect siRNA payloads and inhibit non-specific distribution[5].

To design efficient siRNA-based delivery systems for systemic applications, we previously reported the development of a series of biocompatible, pH-sensitive, membrane-destabilizing β-cyclodextrin (β-CD) polymers[6, A]. These β-CD-based polymers can successfully complex a large dose of therapeutic anti-RhoC siRNA at low N/P ratios (e.g., 2.5/1) to form stable nanoparticles and can functionally deliver their therapeutic cargo into the cytoplasm of aggressive breast cancer cell lines, namely SUM149 and MDA-MB-231 cells[7, A]. This was done by utilizing the varying reactivity of the primary and secondary hydroxyl (OH) groups exhibited by the β-CD core. The secondary OH groups were coupled to cationic amphiphilic copolymers coupled via acid-labile hydrazone linkages, while the primary OH groups were attached to hydrophilic PEG grafts comprising peptide-based targeting ligands (e.g. EPPT1 peptide sequence)[A] to produce asymmetric polymer configurations.

In the simplified *in vitro* setting, the positive charge of the secondary face amphiphilic copolymer graft facilitates both formation of stable nanocomplexes with polyanionic anti-RhoC siRNA molecules and promotes cell uptake by associating with the negatively charged cellular membrane[8]. In complex *in vivo* models, however, the positively charged nanocomplexes tend to bind the negatively charged serum proteins in the bloodstream, thereby, making them ineffective[9]. To mitigate this problem, we coupled seven PEG molecules to the primary face of the β-CD core via click chemistry. In addition, by varying the lengths of the primary face PEG chains (e.g., MW = 2 kDa & 5 kDa), we were able to modulate the hemolytic and serum stability profile of the β-CD-based nanoparticles *in vitro*[A]. We identified that the 5 kDa PEG chains exhibit negligible hemolytic degradation as a function of increasing nanoparticle concentration compared to 2 kDa PEG chains[A]. The β-CD-based polymer design can be further optimized by building upon the 5 kDa PEG graft composition through the incorporation of active-targeting ligands for tissue specific distribution[11].

We addressed the issue of non-specific tissue distribution of siRNA-based delivery systems to the organs of the RES system, namely the liver, lungs, spleen, and kidneys, by conjugating EPPT1-peptide ligands to the free ends of the seven primary face 5 kDa PEG chains. The EPPT1-peptide has a significant affinity (K_d = 20 μM) for underglycosylated mucin-1 (uMUC1) receptors[10]. The reduced glycosylation of MUC-1 antigens is an early hallmark of tumorigenesis and is overexpressed and underglycosylated on almost all human epithelial cell adenocarcinomas (e.g., in > 90% breast carcinomas)[10]. To determine the tumor specificity and biodistribution profile of the asymmetric β-CD nanoparticles, we conjugated a near-infrared dye, IRDye 680RD (λ_{ex} = 675nm, λ_{em} = 720nm), to a single 5 kDa PEG molecule of both non-targeted **(IRDye 680RD-P2)** and EPPT1-targeted **(IRDye 680RD-P3)** polymers, respectively. Following the intraperitoneal (IP) injection of both the IRDye 680RD-labeled β-CD nanoparticles in immune-suppressant SUM149 tumor-bearing female mice, we were able to determine their distribution and accumulation profiles in uMUC-1 expressing SUM149 tumors as well as in the organs of the RES system.

Most synthetic RNAi-based delivery systems demonstrate effective gene silencing *in vitro*, but this effect often does not translate into the desired therapeutic effect *in vivo*[11]. We previously demonstrated that our non-targeted **(P2)** and EPPT1-targeted **(P3)** β-CD polymers complexing anti-RhoC siRNA at an N/P ratio of 2.5/1 suppressed RhoC protein expression in SUM149 cells by approximately 90% after 72 h, respectively[A]. We extended our study to identify the dosing regimen of our anti-RhoC siRNA β-CD polymers, namely (+) P2 and (+) P3, that would exhibit a comparable RhoC protein suppression following their intratumoral administration in SUM149 tumor-bearing female mice.

The objective of our study is twofold, one: to evaluate if our EPPT1-targeted, degradable β-CD nanoparticle strategy can facilitate improved tumor-specific accumulation in SUM149 tumor-bearing mice compared to their non-targeted counterparts upon IP administration. And two: to evaluate the therapeutic efficacy of our nanoparticles in suppressing RhoC expression in SUM149 cells upon direct administration into the tumor site. This will provide us with the necessary information regarding the siRNA dose and dosing frequency of our anti-RhoC siRNA nanoparticles to obtain the desired knockdown of RhoC protein expression.

5.2 Materials and methods

5.2.1 Materials

β-Cyclodextrin (β-CD, Aldrich, 98%) was freeze-dried before using. 2-(dimethylamino)ethyl methacrylate (DMAEMA, Aldrich, 98%), and hexyl methacrylate (HMA, Aldrich, 98%) were purified in a basic alumina column to remove the inhibitor. 1,1,4,7,10,10-Hexamethyltriethylenetetramine (HMTETA, Aldrich, 97%), *N*,*N*,*N′*,*N′*,*N′′*-pentamethyl-diethylenetriamine (PMDETA, Aldrich, 99%) were distilled before use. Sodium hydride (NaH, Aldrich, 60% dispersion in mineral oil, washed with hexane, dried before use). Poly(ethylene glycol) methyl ether (M_n 5000 from Fluka); α-NHS-ω-Alkyne PEG (M_n 5000 from Rapp polymere, Germany). Copper (I) bromide (CuBr, Aldrich, 99.9%), bromophenyl acetate (Aldrich, 98%), iodine (I_2, Aldrich), triphenylphosphine (Pph_3, Acros chemicals), sodium azide (NaN_3, Acros chemicals), 1-ethyl-3-(3-dimethylaminopropyl)carbodiimide HCl (EDC.HCl, Aldrich), hydroxybenzotriazole (HOBt, Aldrich), *N*,*N*-diisopropylethylamine (DIPEA, Alfa Aesar), 4-dimethylaminopyridine (DMAP, Aldrich, 99%), triethylamine (TEA, Aldrich), 2-bromoisobutyryl bromide (Fluka, >97%), iodomethane (Aldrich, 99%), 8-bromo-1-octanol (Alfa Aesar, 95%), Oxalyl chloride (Aldrich, 99%), *p*-Toluenesulfonyl hydrazide (Aldrich, 97%), propargyl alcohol (Aldrich, 99%), tetrahydrofuran anhydrous (THF, Aldrich, >99.9 %), dichloromethane anhydrous (DCM, Aldrich, >99.9 %), N-N-dimethylformamide anhydrous (DMF, Aldrich, >99.9 %), IRDye 680 NHS ester (LI-COR biosciences), EPPT1-NH_2 (Proteomics & peptide synthesis core facility, University of Michigan) were used as received. All cell lines and reagents used in cell culture work were procured and used as previously described.

5.2.2 Synthesis of near-infrared labeled polymers

We previously reported the synthesis of asymmetric, degradable, pH-sensitive β-CD-based polymers where we modified the primary face of the β-CD core to exhibit either active EPPT1-targeted peptides attached to the free ends of PEG brushes (P3) or passive non-targeted PEG brushes (P2). We previously optimized the EPPT1-peptide density (approximately 6.5 peptides/β-CD) and PEG molecular weight (i.e., 2 kDa or 5 kDa) to identify nanoparticle compositions that exhibited selective accumulation in uMUC1-receptor overexpressing aggressive breast cancer cells, while improving overall nanoparticle biocompatibility *in vitro*. The secondary face of both asymmetric polymer compositions displayed similar modifications. Briefly, amphiphilic P(HMA-*co*-**D**MAEMA-*co*-**T**MAEMA) copolymer grafts were characterized to exhibit a molecular weight of 25 kDa, a 50/50 molar feed ratio of HMA/DMAEMA monomers, and 50% quaternization of DMAEMA monomers to cationic TMAEMA monomers[6]. The amphiphilic graft composition was based on previously reported *in vitro* results that demonstrated effective functional delivery of the therapeutic cargo into the cytoplasm of target cells[7]. In this study, we synthesized two near-infrared (NIR)-labeled, degradable, pH-sensitive, asymmetric β-CD-based polymers that exhibited the same primary and secondary face modifications as polymers P2 and P3, with the exception of a single IRDye-680RD dye coupled to the free end of a primary face PEG molecule. Detailed description of the experimental procedures for the synthesis and characterization of these polymers along with the supporting spectra are provided in the attached **Supplementary information**

5.2.3 Characterization of near-infrared labeled polymers

The near-infrared labeled polymer compositions, namely IRDye 680RD-P2 and IRDye 680RD-P3, were formulated in aqueous PBS (1X, pH 7.4) and 1% (v/v) dimethyl sulfoxide (DMSO) solution for both *in vitro* and *in vivo* experiments. Briefly, for *in vitro* experiments – a stock solution of either near-infrared labeled nanopolymer was prepared by dissolving 1 mg of the respective nanopolymers in 0.5 ml of aqueous PBS (1X, pH 7.4) and 1% DMSO solution for gel retardation and size and zeta potential experiments, while the same amount of the respective polymers were dissolved in 3 ml of Opti-MEM and 1% DMSO for cell uptake studies. The *in vivo* stock formulation involves dissolving 1 mg of the respective nanopolymers in 100 µl of aqueous PBS (1X, pH 7.4) and 1% DMSO solution. **Gel retardation assay.** We evaluated the ability of our near-infrared labeled polymer compositions to complex FAM-labeled scrambled siRNA molecules (0.75 μg) was investigated at different nitrogen/phosphate (N/P, +/-) ratios of 1.5/1, 2.5/1 and 4/1 and compared to free siRNA (0.75 μg) and free polymer solutions. Following the simple mixing, the solution mixture was allowed to stand at room temperature for 20 min before loading onto a 1% w/v agarose gel containing 0.5 μg/ml ethidium bromide (EtBr) dye. The gels were immersed in Tris-Acetate-EDTA (TAE) buffer and exposed to 60 V for 60 min before visualizing the gels under UV light. We used ImageJ software (NIH, Bethesda, MD) to quantify the amount of free siRNA observed with different polymers at different N/P ratios and normalized the observed fluorescence to that of the free siRNA loaded on the gel as a positive control to determine the optimum N/P ratio for full complexation of the loaded siRNA cargo. **Size and zeta potential.** We prepared our near-infrared labeled nanoparticles, IRDye 680RD-P2 and IRDye 680RD-P3, by complexing the respective polymer compositions with 1.42 μg (2 μl of a 50 μM stock solution) of anti-GAPDH siRNA at an N/P ratios of 2.5/1 to obtain the respective nanoparticles. We measured the size and zeta potential the near-infrared labeled nanoparticles using 90Plus particle size analyzer with ZetaPALS capability (Brookhaven Instruments Corporation, Holtsville, NY).

5.2.4 Cell culture

SUM149, an inflammatory breast cancer cell line, was generously provided by the Merajver lab (University of Michigan, Ann Arbor, MI). SUM149 was grown in Ham's F-12 medium (Gibco, Carlsbad, CA, USA) supplemented with 5% fetal bovine serum (FBS, Hyclone, South Logan, Utah, USA), insulin (5µg/ml), and hydrocortisone (HC, 1µg/ml) (Sigma-Aldrich, St. Louis, MO). The cell line was maintained in a humidified incubator with 10% CO_2 atmosphere at 37ºC. HepG2 cells was acquired from the American Type Culture Collection (ATCC, Manassas, VA, USA). HepG2 cells was cultured in MEM medium (Gibco, Carlsbad, CA, USA) supplemented with 10% FBS, and 1% penicillin/streptomycin/amphotericin, sodium pyruvate, and non-essential amino acids. HepG2 cells were incubated at 37ºC**,** 5% CO_2 and 95% relative humidity.

5.2.5 Cell uptake study

We investigated the ability of our near-infrared labeled nanoparticles, IRDye 680RD-P2 and IRDye 680RD-P3, to be taken up by SUM149 cells as a function of varying siRNA concentration (i.e., 15 nM, 25 nM, and 50nM). Briefly, cells were seeded at a density of 50,000 cells per well in 24-well plates and allowed to adhere for 16 h at 37°C before incubating with different polymer compositions, namely IRDye 680RD-P2 and IRDye 680RD-P3, loaded with different concentrations of FAM-labeled scrambled siRNA prepared at a N/P ratio of 2.5/1 as previously described. After 6 h of incubation, the cells were washed with PBS, treated with 0.05% Trypsin/EDTA for 5 min, harvested, pelleted, and re-suspended in the appropriate culture medium and analyzed using Biosciences FACSCalibur Flow Cytometer (Becton Dickinson, Franklin Lakes, NJ) to determine the % of fluorescently-labeled cells. All cells were gated by forward/side scatter and 10,000 gated events were collected per sample to discriminate between live and dead cells to account only for live cells.

5.2.6 Tumor model

All animal housing and experimental conditions were in compliance with the protocol approved by the Institutional Animal Care and Use Committee at the University of Michigan. SUM149 and HepG2 cells were suspended in HBSS solution and diluted 1:1 with Matrigel (BD Biosciences). Orthotopic SUM149 tumors were established in female NOD/SCID/gamma (NSG) mice (8-10 weeks old, 20 – 25g). Briefly, the animals were anesthetized, the mammary fat pad was exposed, and the mice were injected with 100µl of 1 x 10^5 SUM149 cells directly into the fourth mammary gland. HepG2 tumors were prepared by inoculating a suspension of 1 x 10^6 HepG2 cells into the subcutaneous dorsa of in male NSG mice (8-10 weeks old, 25 – 30g). Tumors were monitored weekly and tumor volume(s) measured using calipers. The tumor size was calculated as $a \times b^2/2$, where a is the largest and b is the smallest diameter. All experiments were initiated when the tumors measured approximately 100 mm^3. The mice were euthanized once tumor volume approached 2 cm^3 or mice showed signs of morbidity.

5.2.7 Whole-body *in vivo* biodistribution

To evaluate the biodistribution of EPPT1-targeted and non-targeted β-CD nanoparticles in tumor-bearing mice, both β-CD nanoparticles were labeled with IRDye 680RD (Licor Biosciences, Lincoln, NE), a near-infrared fluorophore. SUM149 tumor-bearing mice were randomized into four groups (n=4) once the tumors were palpable. Each group was given either IRDye 680RD-labeled EPPT1-targeted or IRDye 680RD-labeled non-targeted β-CD nanoparticles complexing either 2.5 mg/kg or 5 mg/kg scrambled siRNA molecules at an N/P (+/-) ratio of 2.5/1 via the intraperitoneal (IP) route of administration, respectively. The volume of administration was 0.15 ml/mouse. All groups were subjected to non-invasive fluorescent imaging performed at various time points (e.g., 10min, 4h, 24h, and 48h) up to 2 days after injection using the IVIS Spectrum (PerkinElmer). The mice were sedated and imaged for 1-2 s at a λ_{ex} = 675 nm and λ_{em} = 720 nm. The data was analyzed with the IVIS software (Living Image Program (v.4.0)). HepG2 tumor-bearing mice (n=4) were given a single IP injection of IRDye 680RD-labeled EPPT1-targeted β-CD nanoparticles complexing 5 mg/kg of scrambled siRNA molecules at the above mentioned volume and N/P (+/-) ratio. The animals were imaged and the data analyzed via IVIS Spectrum as previously described.

5.2.8 *Ex vivo* biodistribution

To evaluate the tissue-specific distribution of the various IRDye 680RD-labeled β-CD nanoparticle compositions in tumor-bearing mice after 48 h, NSG mice in all groups were euthanized and organs (liver, lungs, kidney, spleen, heart, and stomach) and tumors were harvested. The organs and tumors were washed with 1X PBS prior to near-infrared fluorescence imaging and analysis using IVIS Spectrum (PerkinElmer) as previously outlined. The fluorescence signal obtained from each organ and tumor for all groups was measured as a function of radiant efficiency.

5.2.9 *In vivo* effect of anti-RhoC siRNA nanoparticles

The ability of anti-RhoC siRNA complexing β-CD nanoparticles to efficaciously deliver the therapeutic cargo in SUM149 tumor-bearing mice was evaluated by quantifying RhoC expression levels in the tumor mass using western blot techniques. Female NSG mice inoculated with SUM149 cells were randomized into various treatment groups (n=3) upon exhibiting tumors that measured approximately 100 mm^3 in size. Briefly, non-targeted **(P2)** and EPPT1-targeted **(P3)** β-CD nanoparticles were prepared by dissolving the respective polymers in 1X PBS solution containing 2.5 mg/kg of either anti-RhoC siRNA (+) or scrambled siRNA (-) molecules at an N/P ratio of 2.5/1. The volume of administration was 0.15 ml/mouse. The control group received 1X PBS solution, and the treatment groups received (+) P2, (-) P2, (+) P3, or (-) P3 solutions, respectively. Mice were treated everyday by intratumoral injections, for up to 3 days. The animals were euthanized on day 4 and their tumors excised to determine RhoC expression levels. Briefly, the excised tumors from all groups were homogenized in tissue lysis buffer and the total protein lysate collected following centrifugation at the maximum speed for 30 min at 4ºC. Total protein concentration was quantified using BCA assay. 60 µg/ml of protein was loaded and separated on a 12.5% Tris-HCl gel (Bio-Rad, Hercules, CA) and transferred onto NC membrane using a dry blotting system (Thermo Scientific, Waltham, MA). Membranes were blocked for 1 h in 5% milk solution and hybridized in 5% BSA solution containing 1X TBS and 0.1% Tween-20 with RhoC mAb (1:1000, CST) and β-actin (1:5000, Santa Cruz) at 4°C with gentle shaking, overnight. Membranes were subjected to secondary detection using 1:5000 dilution of HRP-conjugated anti-rabbit or anti-goat antibody (Santa Cruz). The membranes were stained with a chemiluminescence substrate and the RhoC and β-actin proteins were quantified using ImageJ software (NIH, Bethesda, MD).

5.3 Results

5.3.1 Synthesis of near-infrared labeled polymers

We utilized the asymmetric distribution and reactivity of primary and secondary OH groups to exhibit seven PEG brushes on the primary face and approximately six amphiphilic poly(hexyl methacrylate-*co*-(2-(dimethylamino)ethyl methacrylate) (P(HMA-*co*-DMAEMA) copolymer grafts via click coupling onto the secondary face. Here, we used previously reported strategies to successfully synthesize NIR-labeled non-targeted β-CD (IRDye 680RD-P2) and EPPT1-targeted β-CD polymers (IRDye 680RD-P3).

5.3.1.1 Synthesis of EPPT1-targeted IRDye 680RD-P3 polymers

The synthesis of EPPT1-targeted IRDye 680RD-P3 polymers is outlined **Figure 5.1**

5.3.1.1.1 Primary face modification

Briefly, alkyne-PEG-NHLicor (**2**) and alkyne-PEG-NHS (**3**) were allowed to react with the primary azide groups on compound **1 (Figure 5.1)** in the presence of Cu(I)Br and PMDETA in DMF to obtain $(\text{NHS-PEG})_{5.5}$-$(\text{PEG-Licor})_{1}$-β-CD-$(\text{Phenylacetate})_{8.3}$ (**4**). All compounds were characterized using ^{1}H NMR spectrum.

5.3.1.1.2 Secondary face modification

Compound **4** on reacting with compound **A** in the presence of NaH resulted in (NHS-PEG)$_{5.5}$-(PEG-Licor)$_1$-β-CD-[(*E*)-N`-(8-azodooctylidene)-acetohydrazide]$_{7.2}$ (**5**). Compound **A** was synthesized as previously reported.[R] Compound **5** was then reacted with EPPT1-$NH_2$ in the presence of EDC, HOBt, DIPEA in DMF to give (EPPT1-PEG)$_{5.5}$-(PEG-Licor)$_1$-β-CD-[(*E*)-N`-(8-azodooctylidene) acetohydrazide]$_{7.2}$ (**6**). We used ^{1}H NMR to analyze the number of EPPT1 peptides attached by comparing PEG protons to aromatic protons of the EPPT1 peptide. Alkyne-P(HMA-*co*-DMAEMA-*co*-TMAEMA) (**C**) grafts were click coupled to compound **6** in the presence of Cu(I)Br and PMDETA in DMF at 40^{o}C to give the final polymer product (EPPT1-PEG)$_{5.5}$-(PEG-Licor)$_1$-β-CD-P(HMA-*co*-DMAEMA-*co*-TMAEMA)$_{5.5}$ (**7**). We used ^{1}H NMR to quantify the number of amphiphilic grafts coupled to the secondary face of the β-CD by comparing the ratios between PEG and HMA protons in the polymer grafts. Finally, the grafts were quaternized by reacting alkyne-P(HMA-co-DMAEMA) (compound **B**) with methyl iodide in THF **(Supplementary information)**. The methyl protons of DMAEMA monomers at 2.24 ppm and the TMAEMA monomers at 3.61 ppm were used to calculate the % of DMAEMA quaternized **(Supporting information)**.

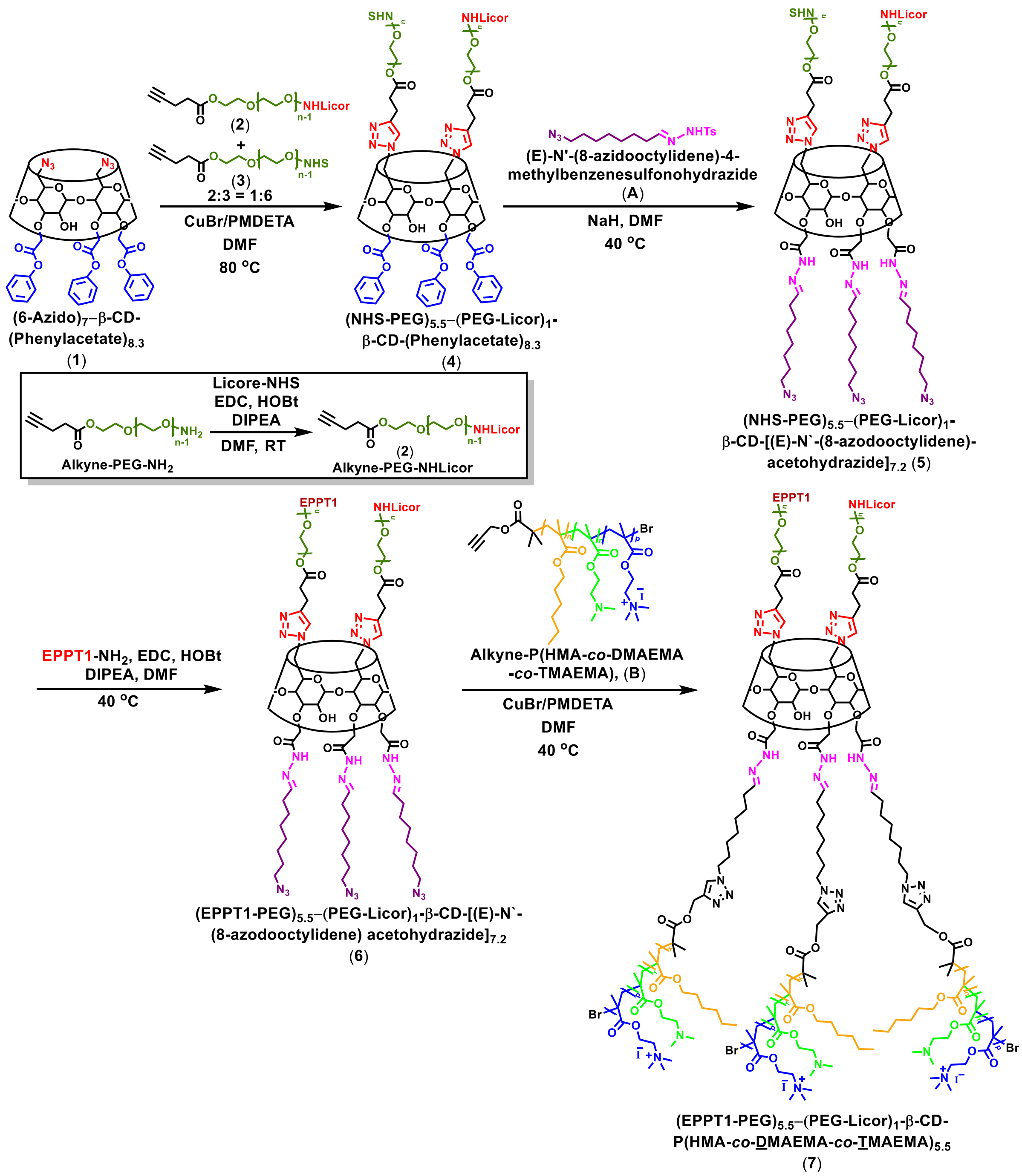

Figure 5.1: Schematic of (EPPT1-PEG)$_{5.5}$-(Licor-PEG)$_{1}$-β-CD-[(hydrazone)-*p*(HMA-*co*-DMAEMA-*co*-TMAEMA)$_{5.5}$ targeted star polymer **(IRDye 680RD-P3)**

5.3.1.2 Synthesis of non-targeted IRDye 680RD-P2 polymers

The synthesis of non-targeted IRDye 680RD-P2 polymers is outlined **Figure 5.2**

5.3.1.2.1 Primary face modification

Briefly, alkyne-PEG-NHLicor (**2**) and alkyne-PEG-OMe (**8**) were allowed to react with the primary azide groups on compound **1** in the presence of Cu(I)Br and PMDETA in DMF to obtain (OMe-PEG)$_{5.5}$-(PEG-Licor)$_{1}$-β-CD-(Phenylacetate)$_{8.3}$ (**9**). **(Figure 5.2).** Compound **8** was synthesized as previously described[R].

5.3.1.2.2. Secondary face modification

Compound **9** was then reacted with compound **A** in the presence of NaH to produce (OMe-PEG)$_{5.5}$-(PEG-Licor)$_{1}$-β-CD-[(*E*)-N`-(8-azodooctylidene)-acetohydrazide]$_{7.2}$ (**10**). The click coupling between compound **10** and compound **B** in the presence of Cu(I)Br and PMDETA in DMF resulted in (OMe-PEG)$_{5.5}$-(PEG-Licor)$_{1}$- β -CD-P(HMA-co-DMAEMA)$_{5.5}$ (**11**). We quantified the number of amphiphilic grafts coupled to the secondary face by ^{1}H NMR spectrum. By comparing the ratios between sugar and HMA/DMAEMA protons (**supporting information**). Alkyne-P(HMA-co-DMAEMA) (**B**) was synthesized using ATRP polymerization in the presence of Cu(I)Br, HMTETA in THF[A]. We partially quaternized the DMAEMA monomers into TMAEMA monomers using methyl iodide to obtain the final polymer (OMe-PEG)$_{5.5}$-(PEG-Licor)$_{1}$-β-CD-P(HMA-co-DMAEMA-co-TMAEMA)$_{5.5}$ (**12**). We used ^{1}H NMR spectrum to calculate the % of DMAEMA quaternized as previously described.

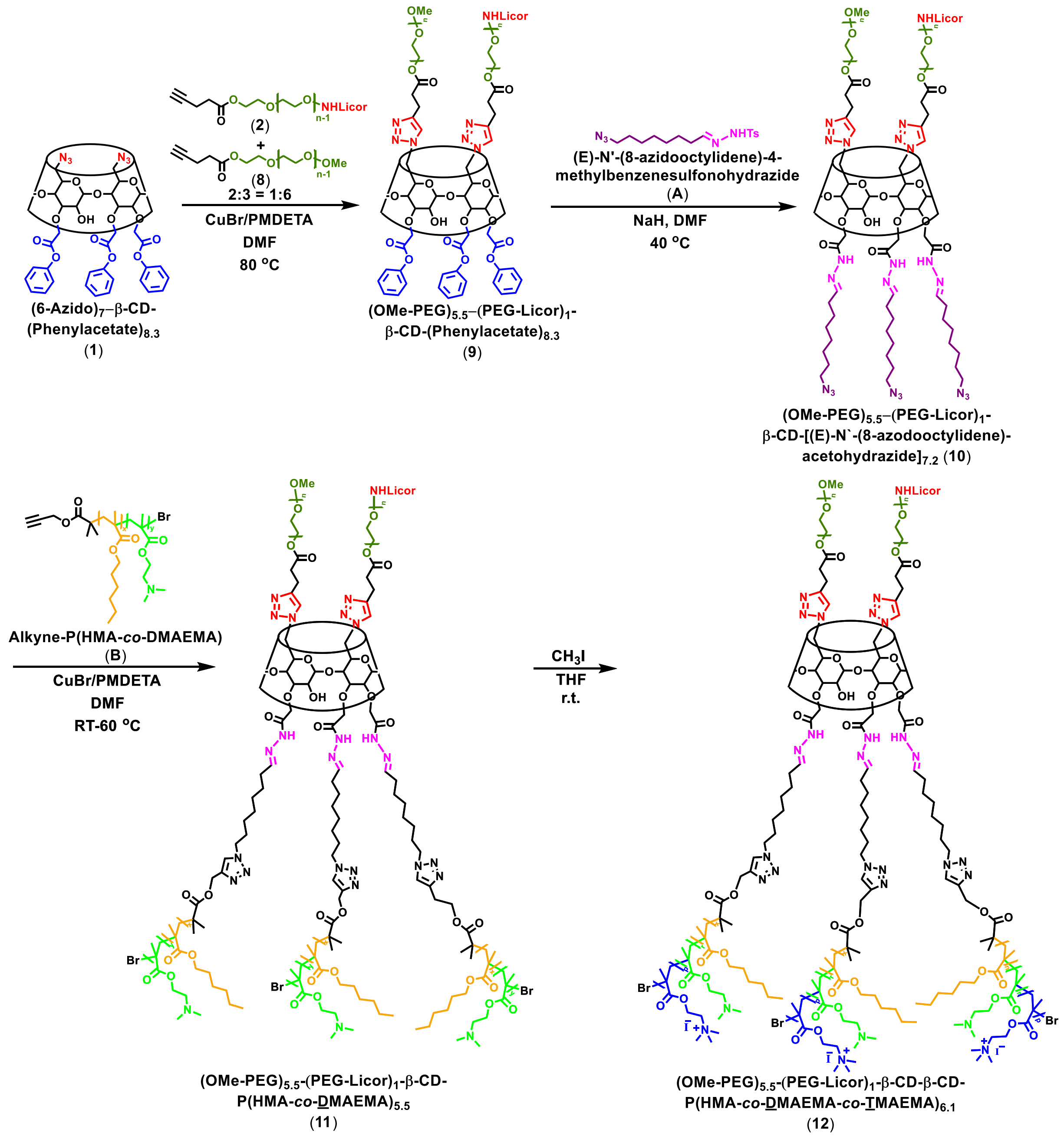

Figure 5.2: (OMe-PEG)$_{5.5}$-(Licor-PEG)$_1$-β-CD-[(hydrazone)-*p*(HMA-*co*-DMAEMA-*co*-TMAEMA)$_{5.5}$ polymer

5.3.2 Characterization of near-infrared labeled polymers

All polymer compositions were completely soluble in aqueous PBS (1X, pH 7.4) and 1% DMSO solution. **Figure 5.3 (A)** shows the degree of complexation between different polymer compositions and FAM-labeled scrambled siRNA molecules as a function of varying N/P (+/-) ratios. The gel indicates that both near-infrared (NIR) polymer compositions can completely complex siRNA molecules at all N/P ratios (i.e., 1.5/1, 2.5/1, and 4/1) when compared to the positive control (free siRNA). **Table 5.1** contains the information regarding the nanoparticle composition loaded in each well of the 1% (w/v) agarose gel**. Figure 5.3 (B)** represents the plot of the size (in nm) of the respective near-infrared labeled nanoparticle compositions at an N/P ratio of 2.5/1. The non-targeted IRDye 680RD-P2 particles were 213 ± 4.7 nm and EPPT1-targeted IRDye 680RD-P3 particles were 189 ± 5.4 nm in size. The incorporation of a single, hydrophobic NIR unit to polymer P2 and P3 did not significantly alter their size profile or result in particle aggregation compared to the parent polymer P2 and P3 at the same N/P ratio. The zeta potential measurements of both nanoparticles, namely IRDye 680RD-P2 and IRDye 680RD-P3, exhibited a net positive charge.

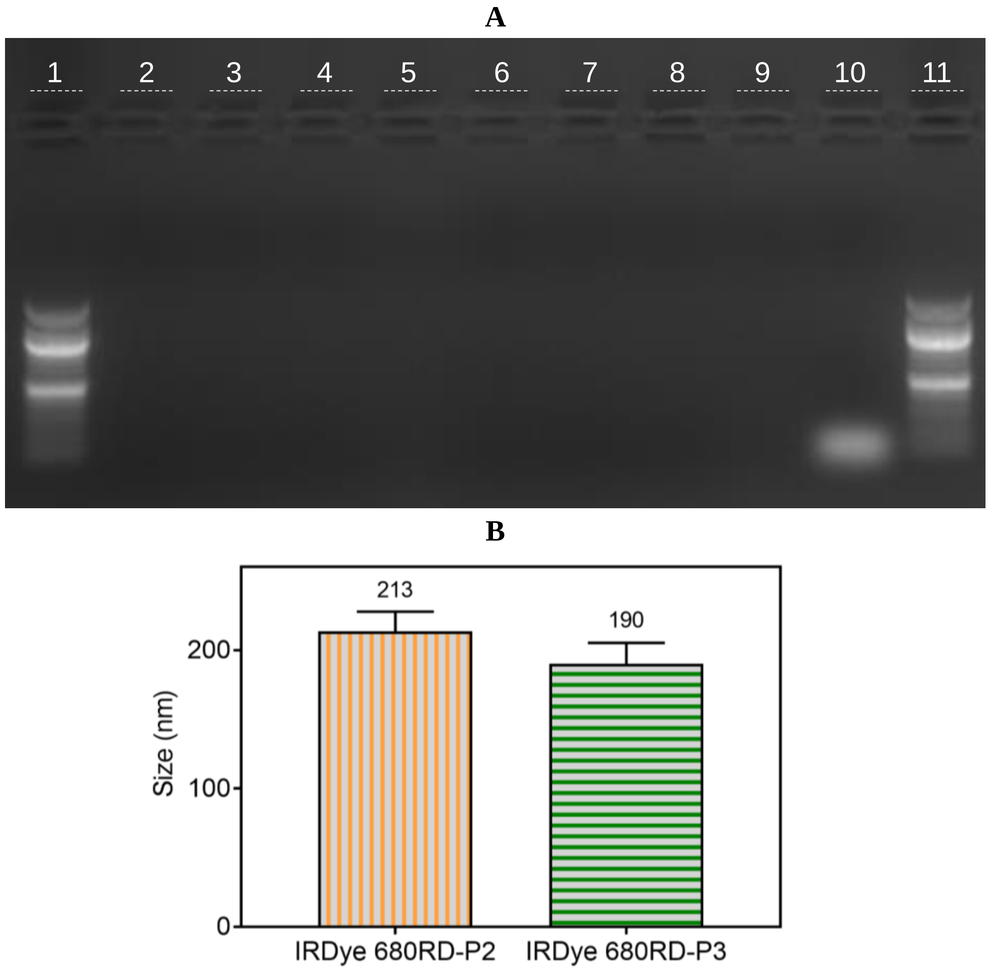

Figure 5.3: (A) The image indicates the degree of complexation of NIR-labeled polymers complexing FAM-labeled scrambled siRNA molecules at varying N/P ratios (i.e., 1.5/1, 2.5/1, and 4/1). The different polymer compositions were loaded on a 1% (w/v) agarose gel stained with 0.5 μg/ml EtBr and subjected to electrolysis at 60 V for 1 h. The degree of complexation at each condition was compared to the free siRNA (0.71 μg) molecules loaded in lane 10. **(B)** Represents the size data of NIR-labeled polymers complexing scrambled siRNA at an N/P ratio of 2.5/1

Lane no.	Sample information	
1	DNA ladder (100 kbp)	
2	IRDye 680RD-P2	1.5/1
3		2.5/1
4		4/1
5		Free polymer
6	IRDye 680RD-P3	1.5/1
7		2.5/1
8		4/1
9		Free polymer
10	Free siRNA (0.71 µg)	
11	DNA ladder (100 kbp)	

Table 5.1: Represents the sample composition loaded in each lane of the 1% (w/v) agarose gel illustrated in **Figure 5.3 (A)**

5.3.3 Cell uptake study

We evaluated the *in vitro* uptake of non-targeted IRDye 680RD-P2 and EPPT1-targeted IRDye 680RD-P3 polymers complexing FAM-labeled scrambled siRNA at an N/P ratio of 2.5/1 by uMUC1 receptor expressing SUM149 cells. **Figure 5.4** represents the % labeled SUM149 cells by the respective FAM-labeled siRNA complexing nanoparticles as a function of varying siRNA concentrations (i.e., 15 nM, 25 nM, and 50 nM). At the siRNA concentration, namely 25 nM and 50 nM, previously reported to exhibit therapeutic suppression of RhoC protein expression in SUM149 cells using anti-RhoC siRNA complexing P2 and P3 nanoparticles, we observed > 85% labeling of SUM149 cells compared to the untreated control and free siRNA molecules (not shown in **Figure 5.4**). At 25 nM siRNA concentration, IRDye 680RD-P2 nanoparticles labeled cells by 87 ± 0.7%, while IRDye 680RD-P3 nanoparticles labeled 93 ± 0.2% cells. At 50 nM siRNA concentration, IRDye 680RD-P2 nanoparticles labeled 93 ± 0.8% cells, while IRDye 680RD-P3 nanoparticles labeled 94 ± 1.1% cells. At 25 nM siRNA concentration, the EPPT1 targeted IRDye 680RD-P3 nanoparticles showed significant labeling of SUM149 cells compared to their non-targeted counterparts. However, at 50 nM siRNA concentration there was no statistical difference in the % SUM149 cells labeled by the respective NIR-labeled nanoparticles. The % labeling of SUM149 cells by NIR-labeled nanoparticles at the above reported siRNA concentrations were comparable to the results previously reported for nanoparticles P2 and P3 complexing FAM-labeled scrambled siRNA molecules.

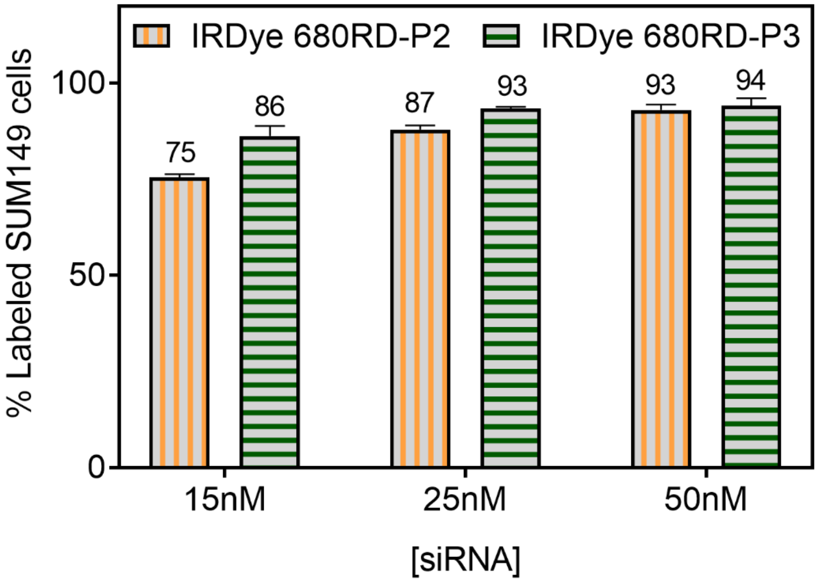

Figure 5.4: The plot represents the % labeled SUM149 cells after incubating for 6 h in a serum-free culture medium with NIR-labeled nanoparticles complexing varying concentrations of FAM-labeled scrambled siRNA at an N/P ratio of 2.5/1. The experiment was performed in triplicates and the results represent the mean + SEM.

5.3.4 Whole body *in vivo* biodistribution

We evaluated the biodistribution of EPPT1-targeted IRDye 680RD-P3 nanoparticles in SUM149 tumor-bearing female NSG mice compared to their non-targeted counterparts. Briefly, we initiated the IP administration of the NIR-labeled nanoparticles on the SUM149 tumors raised in the mammary fat pads of female NSG mice attaining approximately 100 mm^3 in size. The SUM149 tumor-bearing mice were grouped at random into three treatment groups (n = 4). Each group received either IRDye 680RD-P3 polymers complexing 2.5 mg/kg or 5mg/kg of scrambled siRNA molecules or IRDye 680RD-P2 polymers complexing 5 mg/kg of scrambled siRNA, respectively. The treated groups were then imaged using IVIS Spectrum (λ_{ex} = 675nm, λ_{em} = 720nm) at different time points (i.e., t = 10 min, 24 h, and 48 h). **Figure 5.5 (A)** represents the biodistribution profile (measured in radiant efficiency) of EPPT1-targeted IRDye 680RD-P3 nanoparticles in SUM149 tumor bearing mice as function of time and siRNA concentration**.** In **Figure 5.5 (A),** the **upper panel** represents the ventral side, while the **lower panel** indicates the dorsal side of SUM149 tumor-bearing mice administered with varying concentrations of EPPT1-targeted IRDye 680RD-P3 nanoparticles. The observed biodistribution profile for IRDye 680RD-P3 nanoparticles shows a strong signal in the intraperitoneal space at all time points and siRNA concentrations. The dorsal images of SUM149 tumor-bearing mice in **Figure 5.5 (A)** shows two distinct regions of high signal intensity labeled **A** and **B** contributed by the NIR dye coupled to EPPT1-targeted P3 nanoparticles. Region A in **Figure 5.5 (A)** represent the stomach and gastrointestinal (GI) region of the animal. Thereby, suggesting that the IRDye 680RD-P3 nanoparticles predominately distribute and is potentially cleared out by the GI tract. The second region of interest (B) in **Figure 5.5 (A)** represents the mammary fat pad tumors suggesting the potential accumulation of EPPT1-targeted nanoparticles (IRDye 680RD-P3) in SUM149 tumors. IRDye 680RD-P3 nanoparticles appear to accumulate in region B at the ealiest time point (i.e., t = 10 min) when administered at 5 mg/kg siRNA concentration and the signal persists over the 48 h time period. While a distinct signal is observed in region B only at t = 48 h for the IRDye 680RD-

P3 polymers complexing 2.5 mg/kg suggesting a dose-dependent accumulation of EPPT1-targeted nanoparticles in region B. **Figure 5.5 (B)** represents the biodistribution profile measured in radiant efficiency of non-targeted IRDye 680RD-P2 polymers complexing 5 mg/kg scrambled siRNA in SUM149 tumor-bearing mice as function of time**.** Similar biodistribution profiles were observed for IRDye 680RD-P2 nanoparticles in SUM149 tumor-bearing mice. However, the dorsal side in **Figure 5.5 (B)** indicates a strong signal in region A, while no signal was observed in the previously defined (in **Figure 5.5 (A)**) region B. Therefore, suggesting that the non-targeted IRDye 680RD-P2 nanoparticles predominantly distribute to the stomach and gut of the animal with little or no distribution to the SUM149 tumors.

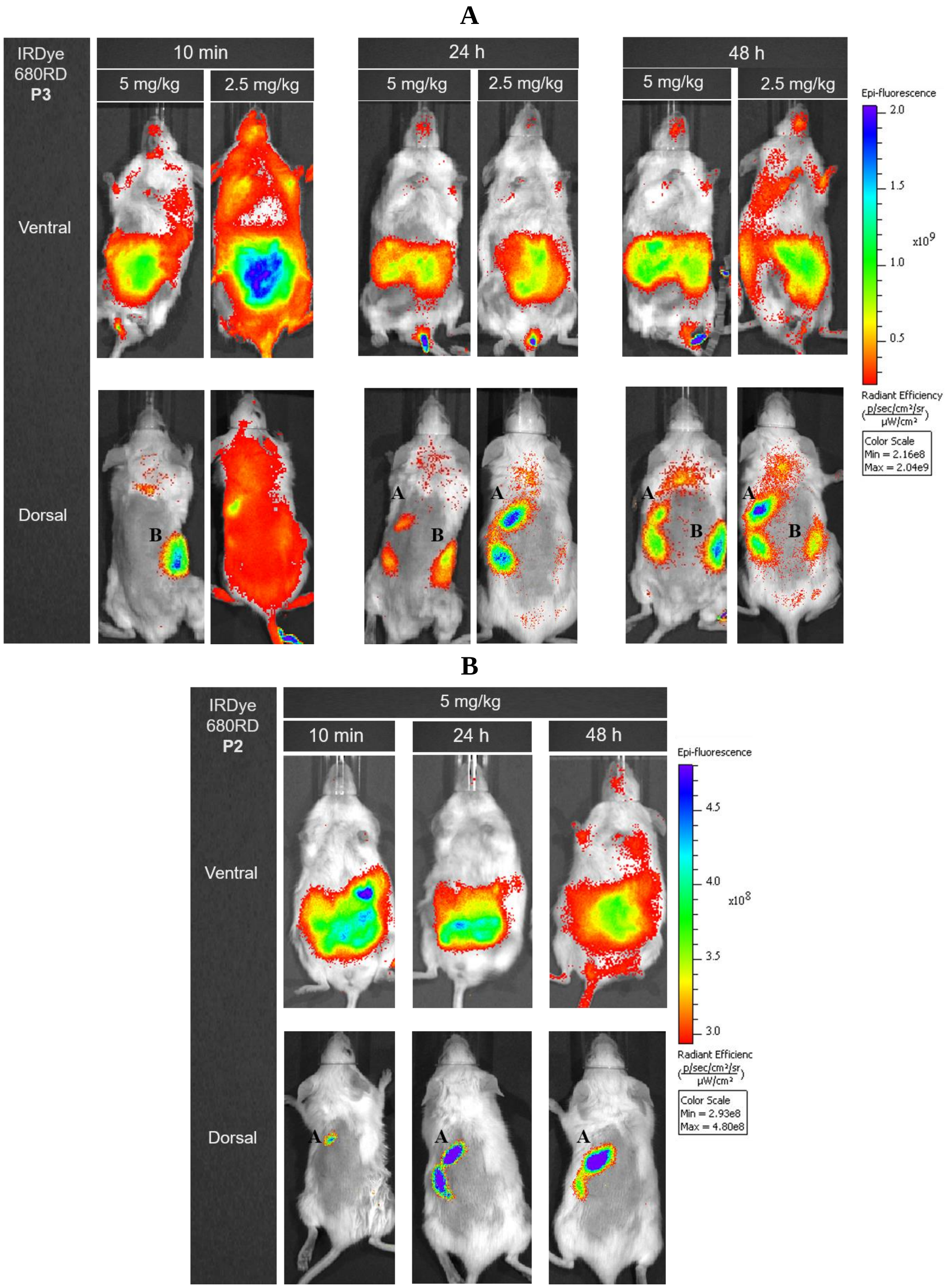

Figure 5.5: Represents the biodistribution profile of NIR-labeled nanoparticles, namely IRDye 680RD-P3 **(A)** and IRDye 680RD-P2 **(B)** upon IP administration into SUM149 tumor –bearing mice measured at different time-points (i.e., t = 10 min, 24 h, 48 h). The SUM149 tumor-bearing mice were imaged using IVIS Spectrum (λ_{ex} = 675nm, λ_{em} = 720nm) and the signal intensity measured in units of radiant efficiency. The dosal sections of **Figure 5.5 (A)** & **(B)** indicate two distinct regions of high signal intensity, namely **A** and **B**, respectively

5.3.5 *Ex-vivo* biodistribution

We harvested the organs of the RES system and the tumors of all the animals in every treatment group after 48 h. The excised organs and tumors were imaged using the IVIS Spectrum (λ_{ex} = 675nm, λ_{em} = 720nm) as illustrated in **Figure 5.6 (A), (B),** and **(C)**. **Figure 5.6 (A)** and **(B)** represents the distribution profile of IRDye 680RD-P3 polymers complexing either 2.5 mg/kg or 5 mg/kg of scrambled siRNA at an N/P ratio of 2.5/1 in different organs and tumors, respectively. **Figure 5.6 (C)** represents the organ-distribution profile of IRDye 680RD-P2 polymers complexing 5 mg/kg of scrambled siRNA at an N/P ratio of 2.5/1. The total NIR dye signal was measured in units of radiant efficiency ((p/s)/(μW/cm^2)). **Figure 5.6 (D)** depicts a plot of the total radiant efficiency measured in the RES organs and SUM149 tumors following treatment with IRDye 680RD-P3 nanoparticles as a function of varying siRNA concentration**. Figure 5.6 (E)** illustrates the total radiant efficiency measured in the RES organs and SUM149 tumors following treatment with IRDye 680RD-P2 polymers complexing 2.5 mg/kg of scrambled siRNA molecules. The results obtained from ex-vivo organ imaging experiments suggests that IRDye 680RD-P3 nanoparticles show a dose-dependent accumulation of EPPT1-targeted nanoparticles in SUM149 tumors after 48 h. **Figure 5.6 (D)** indicates a significantly higher labeling of SUM149 tumors when subjected to 5 mg/kg siRNA nanoparticle concentration ($4.4 \times 10^8 \pm 1.2 \times 10^8$ (p/s)/(μW/cm^2)) compared to 2.5 mg/kg siRNA nanoparticle concentration ($1.4 \times 10^8 \pm 6.8 \times 10^7$ (p/s)/(μW/cm^2)). There was no significant accumulation in the liver at either 5 mg/kg siRNA nanoparticle concentration ($6.1 \times 10^7 \pm 3.4 \times 10^7$ (p/s)/(μW/cm^2)) or 2.5 mg/kg siRNA nanoparticle concentration ($6.7 \times 10^7 \pm 4.6 \times 10^7$ (p/s)/(μW/cm^2)) as seen in **Figure 5.6 (D)**. After 48 h, a significantly higher signal (approximately 10^{10} (p/s)/(μW/cm^2)) was detected in the stomach and GI tract of all animals in either treatment groups. This strong signal detected in the stomach and

GI tract correlates with the biodistribution profile previously observed at both 5 mg/kg siRNA and 2.5 mg/kg siRNA IRDye 680RD-P3 polymer concentrations during whole-body imaging of the animals. The higher tumor accumulation of EPPT1-targeted IRDye 680RD-P3 nanoparticles at 5 mg/kg prompted us explore the biodistribution profile of non-targeted IRDye 680RD-P2 nanoparticles at this concentration **Figure 5.6 (E).** The plot indicates negligible accumulation in SUM149 tumors and the organs of the RES system (in the order of 10^7 (p/s)/(μW/cm^2)). The large error bars can be attributed to the lack of a signal detected in all tissues of three out of the four mice. While a significantly strong signal was detected in the stomach and GI tract of mice subjected to IRDye 680RD-P2 nanoparticles. HepG2 subcutaneous tumors raised in male NSG mice (n = 4) were subjected to IP administration of IRDye 680RD-P3 polymers complexing 5 mg/kg scrambled siRNA at an N/P ratio of 2.5/1. The RES organs and tumors harvested after 48 h showed no signal, while a strong signal was detected in the stomach and GI tract of the all animals as previously observed **(Supplementary information)**

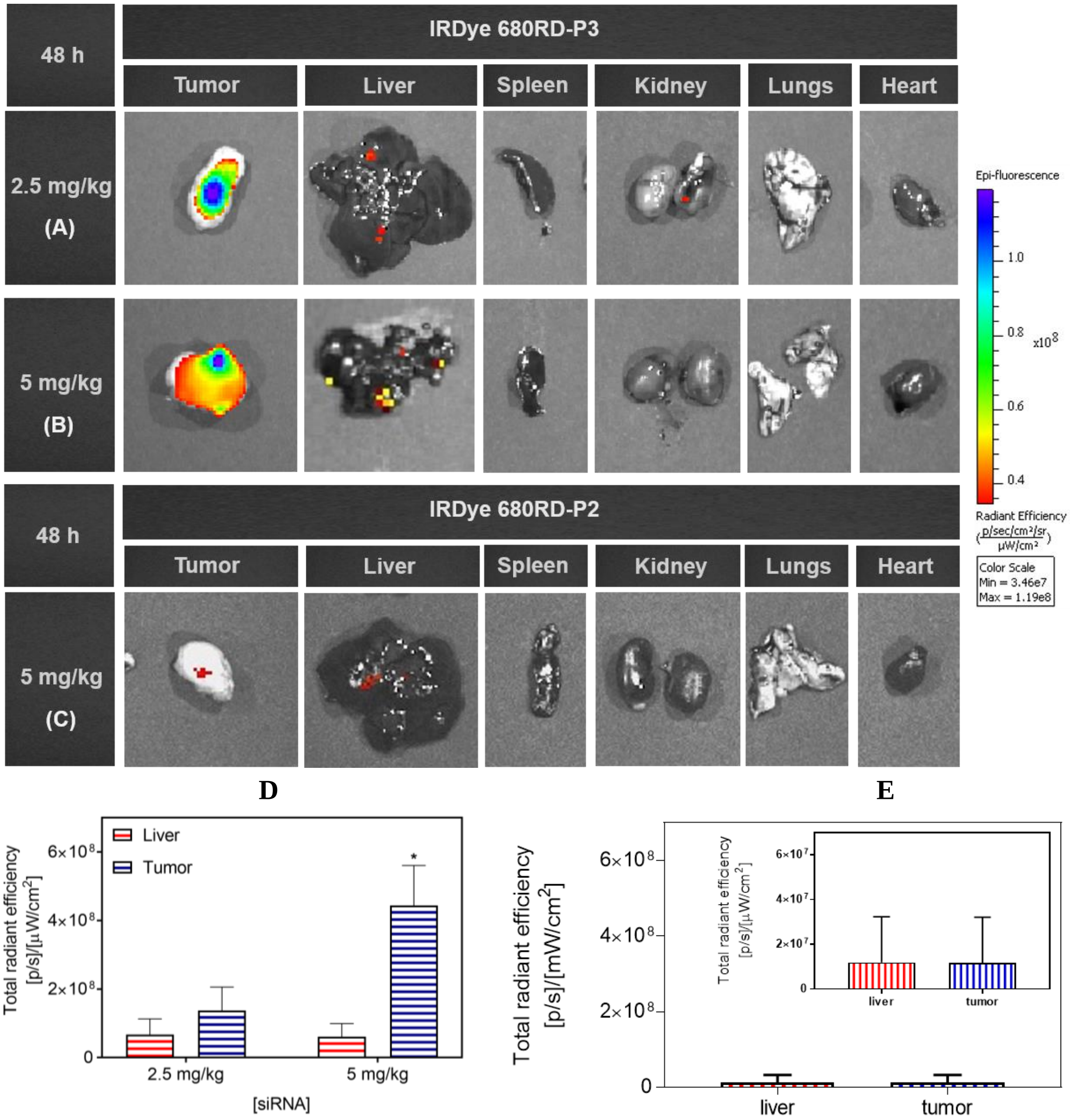

Figure 5.6: *Ex-vivo* distribution of NIR-labeled nanoparticles upon IP administration. The images represent the biodistribution profile of EPPT1-targeted IRDye 680RD-P3 polymers complexing 2.5 mg/kg **(A)** and 5 mg/kg **(B)** of scrambled siRNA molecules at an N/P ratio of 2.5/1. **(C)** represents the biodistribution profile of non-targeted IRDye 680RD-P2 polymers complexing 5 mg/kg of scrambled siRNA molecules at an N/P ratio of 2.5/1. **Figure 5.6 (D)** and **(E)** represents the NIR signal measured in total radiant efficiency ((p/s)/(µW/cm^2)) from SUM149 tumors and the RES organs excised from SUM149 tumor-bearing mice treated with EPPT1-targeted IRDye 680RD-P3 nanoparticles and non-targeted IRDye 680RD-P2 nanoparticles, respectively.

5.3.6 *In vivo* effect of anti-RhoC siRNA nanoparticles

We evaluated the ability of our non-targeted P2 and EPPT1-targeted P3 polymers complexing 2.5 mg/kg of therapeutic anti-RhoC siRNA molecules at an N/P ratio of 2.5/1 to suppress RhoC protein expression in SUM149 tumor-bearing mice upon intratumoral administration. When the SUM149 tumors raised in the fourth mammary fat pad of female NSG mice attained approximately 100 mm^3 in size, the mice were randomly divided into five treatment groups (n = 3). The negative control group received 100 µl of saline solution once every day for three days (i.e., t = 0 h, 24 h, 48 h) intratumorally. The remaining four treatment groups received 100 µl of one of the following polymer compositions: non-targeted P2 polymers complexing either 2.5 mg/kg of anti-RhoC siRNA **(+ P2)** or scrambled sequence siRNA **(- P2)** or EPPT1-targeted P3 polymers complexing either 2.5 mg/kg of anti-RhoC siRNA **(+ P3)** or scrambled sequence siRNA **(- P3)**. Each polymer composition was administered once daily for three days. After 72 h, animals in all groups were euthanized and their tumors harvested to quantify RhoC protein expression for different treatment conditions using western blot. The 72 h treatment regimen was chosen based on previously reported *in vitro* results that showed a 91 ± 2.4% reduction in RhoC protein expression in SUM149 cells following treatment with anti-RhoC siRNA complexing P3 nanoparticles (at 50 nM siRNA concentration). **Figure 5.7** shows the % reduction in RhoC protein expression in the excised SUM149 tumor mass as a function of different treatment conditions. The groups subjected to (+) P2 and (+) P3 nanoparticle treatment conditions exhibited 87.7 ± 5.8% and 84.6 ± 1.7% reduction in RhoC protein expression compared to their scrambled counterparts, respectively. The groups treated with scrambled siRNA (-) complexing P2 and P3 nanoparticles showed comparable RhoC protein expression compared to the negative saline control groups, respectively. The endogenous β-actin control showed unaltered expression levels in all treatment groups.

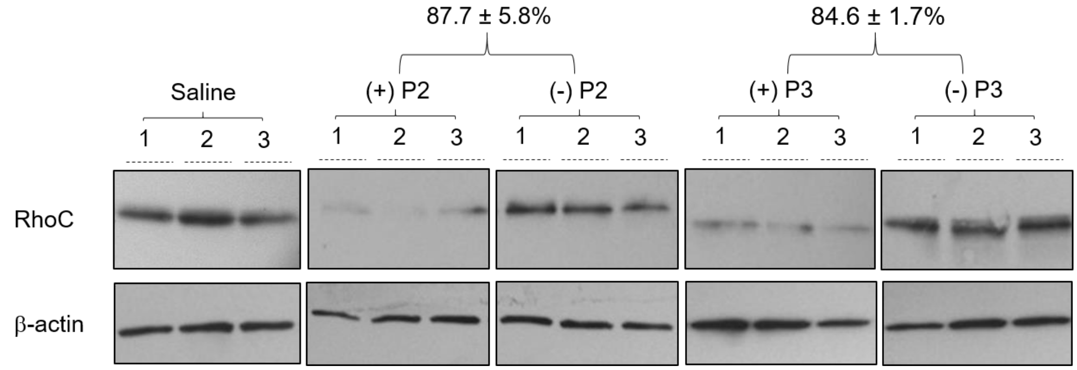

Figure 5.7: *In vivo* therapeutic effect of non-targeted P2 and EPPT1-targeted P3 polymers complexing 2.5 mg/kg of anti-RhoC siRNA (+) at an N/P ratio of 2.5/1 in suppressing RhoC protein expression compared to their scrambled siRNA complexing counterparts. RhoC protein levels at each condition was quantified using ImageJ software (NIH, Bethesda, MD) and normalized to the endogenous β-actin. Results are the average + SEM.

5.4 Discussions

The key criterion for the development of effective nanotherapeutics include (i) overcoming biological barriers, (ii) specific accumulation of the therapeutic at the target site (i.e, targeting), and (iii) preventing rapid clearance from the body. To achieve the characteristics of an “ideal” nanoparticle, we previously reported the use of versatile β-cyclodextrin (β-CD) as the core molecule to develop assymetric, biocompatible β-CD-based polymers that can successfully complex and can functionally deliver a therapeutic dose of anti-RhoC siRNA molecules into the cytoplasm of aggressive breast cancer cells *in vitro*. Briefly, we incorporated seven PEG brushes (MW = 5 kDa) containing EPPT1-peptide targeting moieties on to the primary face to ensure improved circulation time and prevent rapid clearance from the body as well as achieve selective accumulation in uMUC1-overexpressing SUM149 cells. While the secondary face was modified to exhibit six cationic amphiphilic copolymer grafts attached via acid-labile hydrazone linkages. The cationic amphiphilic grafts facilitated the electrostatic complexation of the desired dose of therapeutic siRNA molecules, while the pH-sensitive DMAEMA and hydrophobic HMA monomers enabled endosomal escape of particle fragments upon hydrolysis of the acid-labile hydrazone linkages in acidic endosomal pH. In order to translate these β-CD based polymers into suitable *in vivo* nanotherapeutics, it is crucial to primarily understand the pharmacokinetics and tissue distribution profile of nanoparticles as they have been shown to profoundly dictate the therapeutic effect and potential toxicity profiles[11, 12] . Based on this fact, the goal of our study was to investigate the pharmacokinetics of our targeted drug delivery system and explore the effects of active targeting compared to passive targeting strategies on nanoparticle biodistribution. To this end, we succefully developed and characterized near-infrared labeled active EPPT-1 peptide targeted nanoparticles (IRDye 680RD-P3) and passive targeted nanoparticles (IRDye 680RD-P2) using previously optimized synthesis schemes.

Previous studies have demonstrated that nanoparticle size, surface charge, and mode of administration has a tremendous consequence on nanoparticle behavior *in vivo*[13]. Size dependent organ distribution has been previously investigated and nanoparticles with a hydrodynamic diameter less than 5.5 nm are known to be cleared through the kidneys. Nanoparticles between 50 and 100 nm primarily accumulated in the liver and spleen[13]. Both our active EPPT1-targeted IRDye 680RD-P3 and passive targeted IRDye 680RD-P2 nanoparticles measured 189 ± 5.4 nm and 213 ± 4.7 nm in size. Therefore, the lack of a signal in the RES organs, namely liver, kidney, spleen, **(Figure 5.5 A, B, C)** for both the NIR-labeled nanoparticles following imaging by IVIS Spectrum (λ_{ex} = 675nm, λ_{em} = 720nm) can be attributed to their relatively large size profiles (> 100 nm). Moreover, both NIR-labeled nanoparticles exhibit a net positive charge due to the presence of cationic TMAEMA monomers in the amphiphilic graft composition and the complexation of a higher molar ratio of positively-charged polymer amine groups to the negatively charged siRNA phosphate groups (i.e., N/P =2.5/1) used to form serum stable nanoparticles. Hirano et al. described that the charge of the liposomes is a predictive factor for the retention time[14]. For instance, when the liposomes have a negative charge they were rapidly absorbed from the peritoneal cavity, while positively charged liposomes had a slower absorption rate. This might be attributed to the electrostatic interaction between the positively charged liposomes and the negative surface of the peritoneal mesothelium, in combination with a low uptake of positive liposomes by peritoneal macrophages[15]. This explanation potentially holds true for both our NIR-labeled nanoparticles as we observed a strong signal in the peritoneal cavity 48 h after IP administration of our nanoparticles, thereby suggesting that the net positive charge on our particles increases their retention time in the peritoneal space.

Following IP injection, the nanoconjugate must cross the peritoneal barrier that protects the abdominal cavity before entering into the blood stream or accumulating in organs. The peritoneal membrane is a semi-permeable membrane composed of the parietal peritoneum that lines the abdominal wall and the visceral peritoneum that lines the abdominal viscera and internal organs[16]. Moreover, the peritoneal membranes are comprised of mucus secreting cells, which we hypothesized is a reason for low bioavailability and nanoconjugate accumulation at these sites following IP administration. Mucus is a complex, viscous biological material that typically serves as a lining, a protective barrier, as well as a lubricant[17]. The Hanes group demonstrated the use of low molecular weight PEG molecules to penetrate mucus[17]. We, therefore employed PEG in our nanoparticle design as a passive targeting moiety to reduce the adhesive interactions associated with the mucus in the peritoneum and to facilitate an improved uptake into the blood circulation.

Our active targeted EPPT1-peptide nanoparticles (IRDye 680RD-P3) demonstrated a dose-dependent accumulation of NIR-labeled nanoparticles in uMUC1-expressing SUM149 tumors as seen in **Figure 5.6 A and B**. However, our passively targeted strategy (IRDye 680RD-P2) failed to capitalize on the hyperpermeability of the “leaky” tumor vasculature and showed negligible accumulation at the tumor site **(Figure 5.6 C)**. Both targeting strategies showed rapid clearance (i.e., t = 4 h) via the GI tract and accumulation in the stomach. Finally, we briefly looked into the therapeutic dosing strategy of both our active EPPT1-targeted nanopolymers (P3) and passive targeted nanopolymers (P3) encapsulating either therapeutic anti-RhoC siRNA (+) or scrambled sequence siRNA (-). Both nanotherapeutics showed comparable reduction in RhoC protein expression (> 80%) upon intratumoral administration.

In summary, the active targeting strategy proved significantly more effective in accumulating at the tumor site compared to our passively targeted nanoparticles. While both nanoparticle strategies were rapidly cleared out by the GI tract, neither particles showed accumulation in the RES organ system. The therapeutic efficacy observed by both our nanoparticles in suppressing RhoC expression *in vitro* was carried over into our *in vivo* model.

References

1. Fire A, Xu S, Montgomery MK, Kostas SA, Driver SE, Mello CC. Potent and specific genetic interference by double-stranded RNA in Caenorhabditis elegans. *Nature*. 1998;391(6669):806-811. http://dx.doi.org/10.1038/35888.
2. Morrissey D V, Lockridge JA, Shaw L, et al. Potent and persistent in vivo anti-HBV activity of chemically modified siRNAs. *Nat Biotechnol*. 2005;23(8):1002-1007. doi:10.1038/nbt1122.
3. Ptasznik A, Nakata Y, Kalota A, Emerson SG, Gewirtz AM. Short interfering RNA (siRNA) targeting the Lyn kinase induces apoptosis in primary, and drug-resistant, BCR-ABL1(+) leukemia cells. *Nat Med*. 2004;10(11):1187-1189. doi:10.1038/nm1127.
4. Wang J, Lu Z, Wientjes MG, Au JL-S. Delivery of siRNA therapeutics: barriers and carriers. *AAPS J*. 2010;12(4):492-503. doi:10.1208/s12248-010-9210-4.
5. Whitehead K a, Langer R, Anderson DG. Knocking down barriers: advances in siRNA delivery. *Nat Rev Drug Discov*. 2009;8(2):129-138. doi:10.1038/nrd2742.
6. Durmaz YY, Lin Y-L, ElSayed MEH. Development of Degradable, pH-Sensitive Star Vectors for Enhancing the Cytoplasmic Delivery of Nucleic Acids. *Adv Funct Mater*. 2013;23(31):3885-3895. doi:10.1002/adfm.201203762.
7. Kaushal N, Durmaz YY, Bao L, Merajver SD, ElSayed MEH. “Smart” Nanoparticles Enhance the Cytoplasmic Delivery of Anti-RhoC Silencing RNA and Inhibit the Migration and Invasion of Aggressive Breast Cancer Cells. *Mol Pharm*. 2015;12(7):2406-2417. doi:10.1021/acs.molpharmaceut.5b00114.
8. Torchilin V, Levchenko T, Rammohan R, Volodina N, Papahadjopoulos-Sternberg B, D'Souza G. Cell transfection in vitro and in vivo with nontoxic TAT peptide-liposome-DNA complexes. *Proc Natl Acad Sci U S A*. 2003;100(4):1972-1977. doi:10.1073/pnas.0435906100435906100 [pii].
9. Li L, ten Hagen TLM, Schipper D, et al. Triggered content release from optimized stealth thermosensitive liposomes using mild hyperthermia. *J Control Release*. 2010;143(2):274-279. doi:10.1016/j.jconrel.2010.01.006.
10. Hattrup CL, Gendler SJ. Structure and Function of the Cell Surface (Tethered) Mucins. *Annu Rev Physiol*. 2008;70(1):431-457. doi:10.1146/annurev.physiol.70.113006.100659.
11. Friedman AD, Claypool SE, Liu R. The Smart Targeting of Nanoparticles. *Curr Pharm Des*. 2013;19(35):6315-6329. http://www.ncbi.nlm.nih.gov/pmc/articles/PMC4016770/.
12. Li SD, Huang L. Pharmacokinetics and biodistribution of nanoparticles. In: *Molecular Pharmaceutics*. Vol 5. ; 2008:496-504. doi:10.1021/mp800049w.
13. Simpson CA, Huffman BJ, Gerdon AE, Cliffel DE. Unexpected toxicity of monolayer protected gold clusters eliminated by PEG-thiol place exchange reactions. *Chem Res Toxicol*. 2010;23(10):1608-1616. doi:10.1021/tx100209t.
14. Choi HS, Liu W, Liu F, et al. Design considerations for tumour-targeted nanoparticles. *Nat Nano*. 2010;5(1):42-47. http://dx.doi.org/10.1038/nnano.2009.314.
15. Hirano K, Hunt CA, Strubbe A, MacGregor RD. Lymphatic Transport of Liposome-Encapsulated Drugs Following Intraperitoneal Administration – Effect of Lipid Composition. *Pharm Res*. 1985;2(6):271-278. doi:10.1023/A:1016337500364.
16. Dadashzadeh S, Mirahmadi N, Babaei MH, Vali AM. Peritoneal retention of liposomes: Effects of lipid composition, PEG coating and liposome charge. *J Control Release*. 2010;148(2):177-186. doi:http://dx.doi.org/10.1016/j.jconrel.2010.08.026.

17. Williams PL, Bannister LH, Berry MM, et al. Gray's anatomy. *Soames, RW*. 1995;p:612. doi:10.1002/bjs.1800761258.
18. Lai SK, Wang Y-Y, Wirtz D, Hanes J. Micro- and macrorheology of mucus. *Adv Drug Deliv Rev*. 2009;61(2):86-100. doi:http://dx.doi.org/10.1016/j.addr.2008.09.012.

A. Kaushal N, Tiruchinapally T, Bao LD, Gilani R, Merajver SD, ElSayed MEH. Presentation of EPPT1 Peptide for Binding of Underglycosylated MUC1 and Cytoplasmic Delivery of Anti-RhoC Silencing RNA by "Smart" Particles Synergistically Inhibit the Migration and Invasion of Aggressive Breast Cancer Cells. *J Control Release.* 2017, Under revision

Chapter 6

Conclusion and Future Direction

6.1 Conclusion

6.1.1 "Smart" nanoparticles enhance the cytoplasmic delivery of anti-RhoC silencing RNA and inhibit the migration and invasion of aggressive breast cancer cells

Degradable, pH-sensitive, star-shaped β-CD-g-P(HMA$_{79}$-*co*-DMAEMA$_{33}$-*co*-TMAEMA$_{48}$)$_{4.8}$ polymers were developed as a siRNA-based delivery platform to complex and efficaciously delivery the therapeutic payload into the cytoplasm of target cells. Briefly, the star polymers utilized β-CD, a cone-shaped oligosaccharide composed of seven glucose units, as the core for the development of the "smart" vectors. The seven primary OH groups on the primary face of the β-CD core and the fourteen secondary OH groups on the secondary face have different chemical reactivity; therefore, allowing us to graft amphiphilic membrane-destabilizing polymers from the secondary face of the β-CD core via acid-labile hydarzone linkages while leaving the primary face for further modification.

The “ideal” graft composition of the amphiphilic membrane-destabilizing polymer was previously identified from a library of star-shaped polymers that exhibited different graft compositions (i.e, varying molecular weight of 25 kDa and 40 kDa, hydrophobic/hydrophilic ratio of 50/50 and 75/25, and degree of quaternization of 50% and 100%)[1]. The star-shaped polymers that exhibited secondary face amphiphilic grafts with a polymer composition of 25 kDa and molar hydrophobic/hydrophilic feed ratio of 50/50 with partial (50%) conversion of the hydrophilic pH-sensitive methacrylate monomers to cationic methacrylate monomers exhibited the most desirable physicochemical properties as well as the highest suppression of specific mRNA in target cells. To validate the therapeutic efficacy of this amphiphilic graft composition in aggressive breast cancer cells, we were interested in complexing the star-shaped β-CD-g-P(HMA$_{79}$-*co*-DMAEMA$_{33}$-*co*-TMAEMA$_{48}$)$_{4.8}$ polymers with a therapeutic dose of anti-RhoC siRNA at low N/P ratios (i.e., 2.5/1) and evaluate the functional delivery of their cargo past the endosomal membrane and into the cytoplasm of SUM149 and MDA-MB-231 cells, respectively.

We chose RhoC-GTPase protein as our molecular target of interest as they are known to be overexpressed and linked to the metastatic progression observed in inflammatory breast cancer (IBC) and triple-negative breast cancer (TNBC). The role of RhoC in promoting cancer cell migration and invasion has been confirmed by multiple *in vitro and in vivo* studies. In our study, we demonstrated that our “smart” anti-RhoC siRNA particles could successfully knockdown RhoC protein expression by 90-100% in both SUM149 and MDA-MB-231 cells, respectively. We, further demonstrated that this suppression of RhoC protein expression translated into a significant reduction in cell invasion, motility, and migration of both SUM149 and MDA-MB-231 cells by approximately 50%. In conclusion, the results from this study suggested that our “smart” anti-RhoC nanoparticle composition was effective in suppressing the metastatic spread of aggressive breast cancer cells. Therefore, validating the efficacy of our star-polymers' amphiphilic graft composition to functionally deliver therapeutic anti-RhoC siRNA into the cytoplasm of aggressive breast cancer cells.

6.1.2 Presentation of EPPT1 Peptide for Binding of Underglycosylated MUC1 and Cytoplasmic Delivery of Anti-RhoC Silencing RNA by "Smart" Particles Synergistically Inhibit the Migration and Invasion of Aggressive Breast Cancer Cells

In our previous study, we demonstrated that our star-shaped β-CD-based polymers exhibiting the "ideal" secondary face amphiphilic copolymer graft composition demonstrated effective suppression of target RhoC expression in aggressive breast cancer cells with no particle-associated cytotoxicity *in vitro*. Here, we were interested in developing *in vivo* based delivery solutions by utilizing the seven primary face OH groups of our star-shaped β-CD polymers to conjugate either passive-targeted PEG moieties or active-targeted EPPT1-peptides. We successfully designed and synthesized a series of asymmetric multimodal PEGylated and EPPT1-targeted β-CD polymers that can complex the desired dose of anti-RhoC siRNA to form stable "smart" particles. We showed that 5 kDa PEG particles exhibited significantly improved biocompatibility profiles *in vitro* compared to their 2 kDa PEG counterparts; therefore, prompting their future use in developing our *in vivo* nanoparticle strategy. We, therefore developed our EPPT1-targeting strategy using 5 kDa PEG particles that specifically targeted uMUC1 expressing breast cancer cells (like SUM149 cells) and showed efficient internalization via receptor-mediated endocytosis. We demonstrated significantly higher uptake of EPPT1-targeted particles into SUM149 and MDA-MB-231 cells at low siRNA concentrations (i.e., 15 nM) compared to their non-targeted counterparts. Upon receptor-mediated internalization, the EPPT1-targeted-β-CD particles showed a sustained release of anti-RhoC siRNA molecules and a subsequent knockdown of RhoC protein expression in SUM149 and MDA-MB-231 cells after 72 h compared to the previously reported 48 h study using non-targeted-β-CD nanoparticles. The successful incorporation of EPPT1-targeted peptides and encapsulation of anti-RhoC siRNA molecules on the same nanoparticle also exhibited a synergistic suppression in cell invasion and migration in aggressive breast cancer cells. Further investigation of the effect of EPPT1-targeted particles in suppressing breast cancer cell invasion and migration showed that the EPPT1-peptide binding to uMUC1 receptors resulted in the downstream inactivation of p-Src and p-FAK proteins that are known to play a vital role in cell invasion and migration. The successful characterization of our *in vivo* based nanoparticles *in vitro* warranted their evaluation in SUM149 tumor-bearing animal models.

6.1.3 *In vivo* evaluation of active and passive-targeted nanoparticle strategies for the efficient delivery of therapeutic siRNA for treatment of aggressive breast cancer

Nanoparticles show their promise for improving the efficacy of drugs with a narrow therapeutic window or low bioavailability, such as anticancer and nucleic acid-based drugs. The pharmacokinetics (PK) and tissue distribution of nanoparticles largely define their therapeutic effect and toxicity. Chemical and physical properties of the nanoparticles, including size, surface charge, and surface chemistry, are important factors that determine their PK and biodistribution. In this study, we evaluated the *in vivo* behavior of our asymmetric active EPPT1-peptide targeted and passive PEG-targeted β-CD nanoparticles upon administration in SUM149 tumor-bearing mice. Briefly, we synthesized near-infrared labeled EPPT1-peptide targeted and non-targeted

PEGylated β-CD polymers based on similar strategies outlined in **supplementary information** of Chapter 4. The labeling of nanoparticles with a near-infrared dye (IRDye 680RD, λ_{ex} = 675 nm and λ_{em} = 720 nm) enables real-time imaging (using IVIS Spectrum, PerkinElmer Inc.) of the animals at pre-defined time-points (i.e, 10 min, 24 h, 48 h) and mitigates the issue of tissue auto fluorescence. The whole-body and ex-vivo imaging of the mice demonstrated that both active EPPTI-targeted and passive PEG targeted nanoparticles were rapidly cleared from the body through the GI tract upon IP administration potentially due to their net positive charge. Moreover, the size of the nanoparticles (approximately 200 nm) hindered their accumulation or clearance by the organs of the RES system, namely liver, kidney, and spleen. While the passive PEG targeted nanoparticles failed to harness the enhanced retention and permeability (EPR) effect of the tumor vasculature to accumulate at the tumor site, the active EPPT1-targeted nanoparticles demonstrated a dose-dependent accumulation in the tumor mass upon ex-vivo tumor imaging at 48 h. Therefore, suggesting that our active EPPT1-targeted nanoparticles have improved tumor specificity compared to their passively targeted counterparts. We, also demonstrated the ability of both our polymer strategies complexing anti-RhoC siRNA to functionally deliver their therapeutic cargo into SUM149 tumors upon intratumoral administration. This study showed comparable therapeutic efficiency in suppressing RhoC protein expression (by 80%) on using either nanoparticle formulation. In conclusion, the results from the *in vivo* evaluation of our nanoparticles suggests that if deliver approximately 2.5 mg/kg of anti-RhoC siRNA at the tumor site upon IP administration of anti-RhoC siRNA complexing EPPT1-peptide targeted nanoparticles, we can potentially achieve therapeutic suppression of RhoC expression and subsequently inhibit tumor metastasis.

6.2 Future direction

6.2.1 Understanding the mechanism of nanoparticle internalization and fate of EPPT1-bound uMUC1 receptors

MUC1, aberrantly overexpressed in various cancer cells, is known to serve as a physical barrier from the extracellular environment and as a receptor for various extracellular molecules[10]. The goal of this study is to understand the fate of MUC1 during and after the interaction with our EPPT1-peptide targeted β-CD nanoparticles. In order to better understand the cellular trafficking of MUC1 antigens upon binding to EPPT1-peptides displayed on the primary face of β-CD polymers, we have synthesized of a series of β-CD polymers (positive control) that display EPPT1-peptides on the primary face of the core molecule, but are void of any secondary face amphiphilic graft modifications **(Figure 6.1)**. This is essential to delineate the effect attributed solely by the EPPT1-peptides binding to the MUC1 receptors and the potential interaction that may be elicited by the cationic amphiphilic grafts coupled to our EPPT1-peptide targeted β-CD nanoparticles on MUC1 binding. We are interested in understanding the mechanism of internalization of our EPPT1-targeted asymmetric nanoparticles into SUM149 and other MUC1 expressing cell lines like MCF7, Panc-1, and HEK293 cells[10]. The internalization of a membrane protein has been shown to be mediated by the clathrin-dependent, raft/caveolin-dependent, or clathrin- and raft/caveolin-independent mechanism. Macropinocytosis, is another endocytotic mechanisms involving a raft/caveolin-dependent pathway to internalize extracellular fluid[11], mycobacteria[12], peptide[13], as well as ligand receptor complexes[14].

In our proposed strategy to test the mechanism of entry, we intend on pretreating the respective MUC1-recepetor expressing cells with chlorpromazine, a clathrin-dependent endocytosis inhibitor[15], methyl-β-cyclodextrin which inhibits a raft/caveolae-dependent endocytosis[16], or amiloride and ethylisopropyl amiloride (EIPA), that selectively inhibit macropinosome formation compared with other endocytosis pathway[17], respectively **(Figure 6.2)**. This is followed by a time-dependent co-incubation of these pre-treated cells with the respective inhibitor and our near-infrared labeled EPPT1-targeted β-CD nanoparticles and positive control nanoparticles, respectively. The near-infrared fluorescence signal from each treatment group can be visualized by confocal laser microscopy to determine our nanoparticles' mechanism of entry. Furthermore, we can use GFP-labeled MUC1 receptors to track the internalization and trafficking mechanism of these receptors upon binding to our EPPT1-nanoparticles. Finally, we can examine whether the internalization of MUC1 is dependent on the presence of MUC1 on cell surface. By using MUC1-receptor variants with deleted MUC1-cytoplasmic tails. Previous studies showed that MUC1 internalization failed upon deletion of MUC1-cytoplasmic tail, but not by mutations at Y20, Y35, Y46, and Y60 of MUC1-cytoplasmic tail in transfected HEK cells[10] which have been shown to be important for cellular signaling and/or trafficking[18, 19].

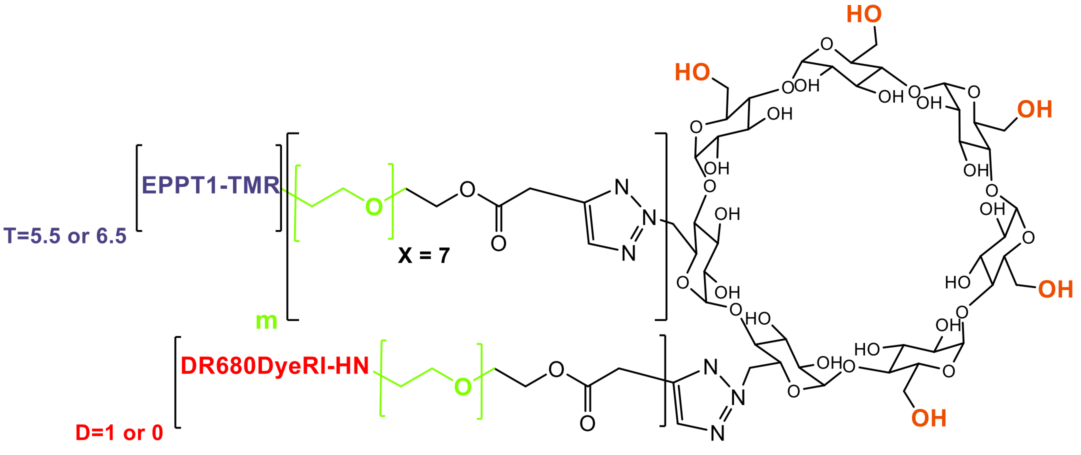

Figure 6.1: (EPPT1)$_T$-(NH-IRDye680RD)$_D$-(PEG-5 kDa)$_X$-β-CD polymer (positive control polymers)

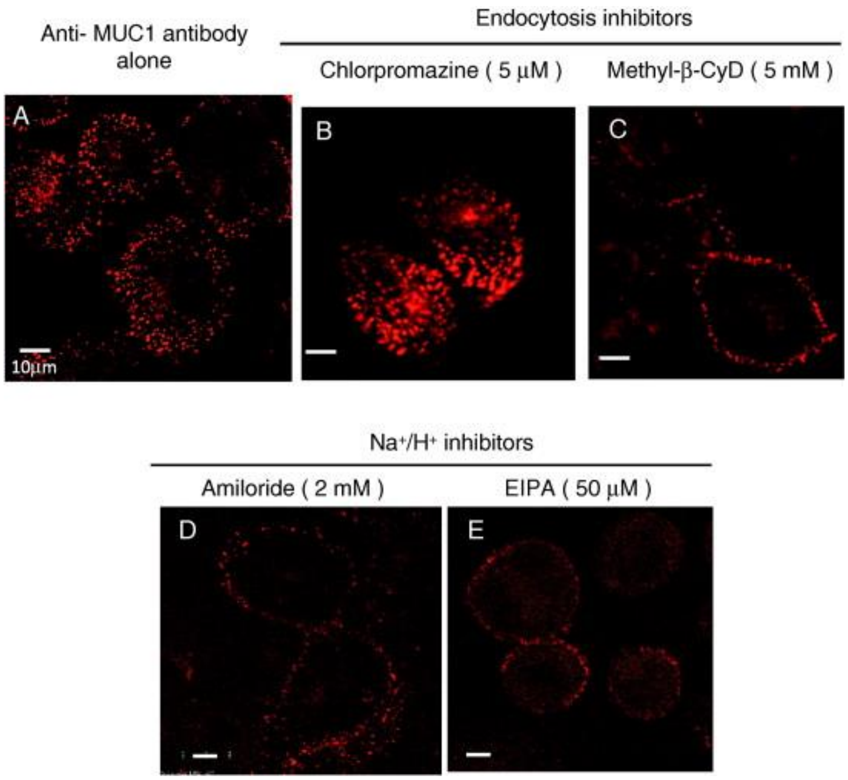

Figure 6.2: Antibody-induced internalization of MUC1 was mediated through macropinocytotic pathway. Panc-1 cells were pretreated without (A) or with chlorpromazine (5 µM, B), methyl-β-CyD (5 mM, C), amiloride (2 mM, D), EIPA (50 µM, E) for 30 min, followed by co-treatment with anti-MUC1 antibody and inhibitors at 37 °C for 1 h. After staining with TRITC-conjugated secondary antibody, fluorescence signals were visualized by confocal laser microscopy.

6.2.2 *In vivo* evaluation of our asymmetric active and passive-targeted nanoparticles

The preliminary *in vivo* testing of the behavior of our nanoparticle strategies in SUM149 tumor-bearing mice (outlined in Chapter 5) set the stage for a more detailed and methodical evaluation of a) the effect of route of administration on nanoparticle biodistribution profiles in SUM149 tumor bearing mice, b) evaluating nanoparticle-associated toxicity profiles via MTD studies in both healthy and tumor-bearing mice, c) Determining the dosing regimen and therapeutic effect of anti-RhoC siRNA complexing nanoparticles upon IP or IV administration in SUM149 tumor-bearing mice, and d) Establishing metastatic tumor models in mice and evaluating the effect of our anti-RhoC siRNA complexing nanoparticles on suppressing the metastatic spread of the disease. Evaluation of the therapeutic and toxicity effects of our nanoparticles in pre-clinical animal models can give us a better understanding of the potential steps required to translate this technology into a clinically-viable siRNA vector system.

6.2.3 Synthesis of a library of MUC1-targeted nanoparticle therapies

In many tumor types, MUC1 expression correlates with aggressive, metastatic disease, poor response to therapy and overall survival. While MUC1 expression is limited to the apical surface of most ductal epithelium, in metastatic disease, MUC1 is overexpressed and becomes localized throughout the cell[2]. This phenomenon has been most intensively studied in breast cancer, in which MUC1 expression has been evaluated clinically at the level of immunohistochemistry,[3, 4] RNA,[5] shed MUC1 in sera, expression on circulating tumor cells and biochemically[6], and has correlated with poor disease-free and overall survival, as well as axillary node metastases. Therefore, the role of MUC1 in both transformation and metastatic progression has led to extensive focus on this protein for the development of targeted therapies to treat metastatic disease **(Figure 6.3)**. A number of groups have developed vaccine-like therapies to target MUC1 and is listed in **Table 6.1**

The incorporation of these MUC1 targeted peptides or antibodies (outlined in **Table 6.1**) on the primary face of our asymmetric β-CD polymers can be developed to generate an arsenal of actively-targeted platform strategies. The advantage of these targeted strategies is twofold: one, it can potentially facilitate improved tumor accumulation of our MUC1 targeted nanoparticles, thereby improving the therapeutic efficiency and functional delivery of their siRNA cargo into the tumor space, and two, the MUC1 targeted moieties upon binding to the intended region of the MUC1 antigen can facilitate inhibition of MUC1 associated cell invasion and migration[7, 8, 9]. In addition to the MUC1-targeting therapeutic strategy, these "smart" nanoparticles will be equipped to deliver a plethora of siRNA-based drugs to the target site (as described previously); thereby, establishing a platform delivery system that can elicit dual therapy through MUC1 targeted moieties and target-specific siRNA delivery that can alter the associated gene expression.

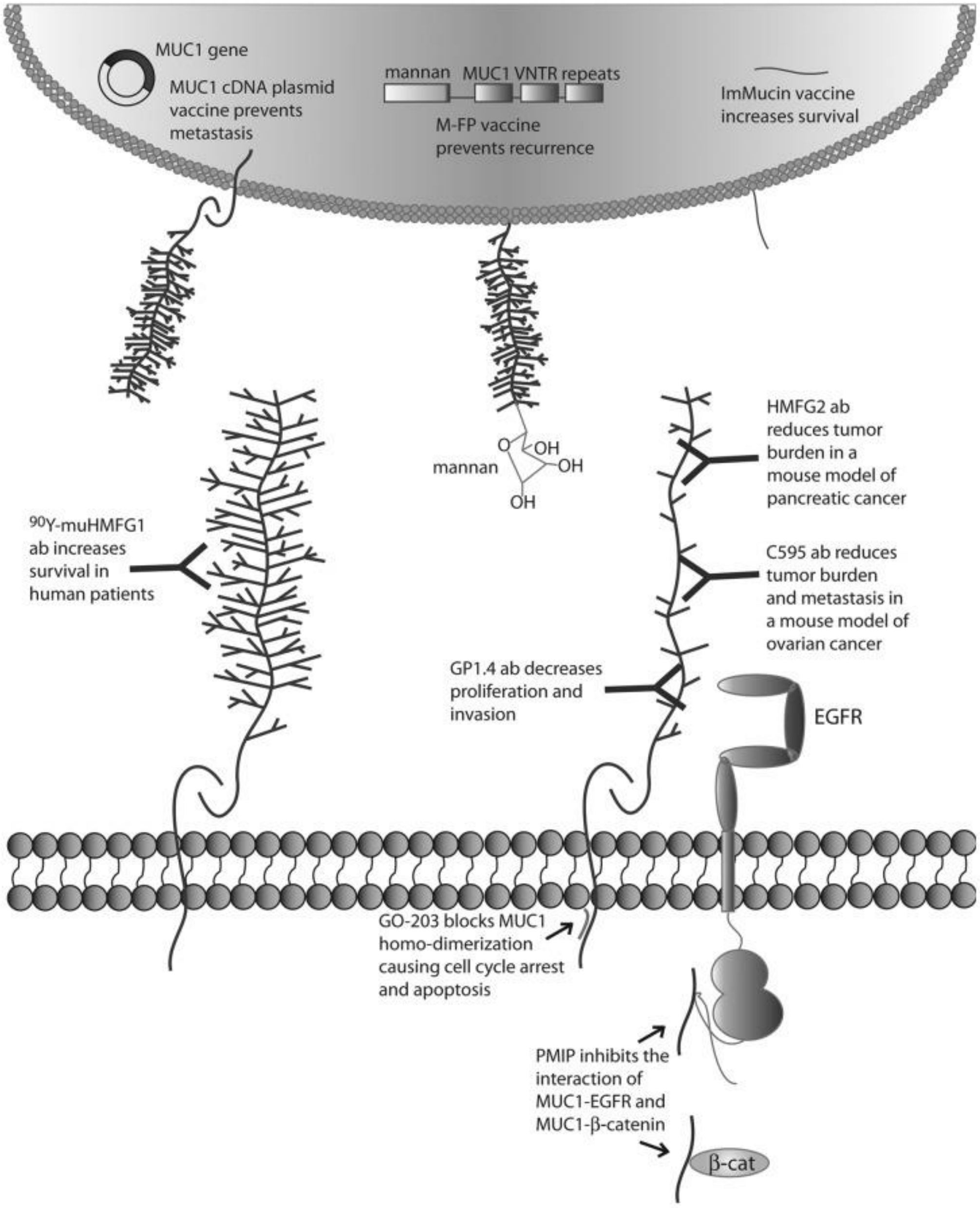

Figure 6.3: Targeted therapies directed against MUC1. MUC1 cDNA vaccine, M-FP vaccine and ImMucin vaccine induce immune response to MUC1 tumor antigen. ^{90}Y-muHMGF1 antibody binds glycosylated extracellular MUC1 and increases survival in human patients. HMFG2 and C595 antibodies bind the protein core of underglycosylated MUC1 and reduce tumor burden in mouse models of cancer. GP1.4 binds to MUC1 protein and decreases proliferation and invasion. GO-203 peptide binds to the juxtamembrane domain of MUC1 and blocks MUC1 homodimerization, preventing MUC1 activity and causing cell cycle arrest and apoptosis. PMIP decoy peptide inhibits MUC1-EGFR interaction and MUC1-β-catenin interaction, decreasing EGFR activity and inhibiting proliferation and invasion and inhibiting tumor growth and metastasis in mouse models of cancer.

Therapy	Mechanism	Pre clinical/clinical cancer tested	Stage of development
Antibody			
C595	extracellular; targets MUC1 core	ovarian	Pre-clinical
GP1.4	extracellular; binds MUC1 and leads to EGFR internalization	pancreatic	Pre-clinical
HMFG1	extracellular; binds cancer cells and kills with a conjugated yttrium moiety	ovarian	Phase 3
Peptides			
PMIP	intracellular; blocks MUC1/EGFR, MUC1/p120catenin, and MUC1/βcatenin protein interactions	Breast, lung	Pre-clinical
Vaccines			
MUC1 cDNA	vaccine; MUC1 expression on cells activates immune system	melanoma	Pre-clinical
M-FP	vaccine; oxidized mannan conjugated to MUC1GST fusion protein binds mannose receptor on macrophage	breast	Phase 3

Table 6.1: MUC1-dependent metastasis inhibitors

References

1. Durmaz YY, Lin Y-L, ElSayed MEH. Development of Degradable, pH-Sensitive Star Vectors for Enhancing the Cytoplasmic Delivery of Nucleic Acids. *Adv Funct Mater*. 2013;23(31):3885-3895. doi:10.1002/adfm.201203762.
2. Rahn JJ, Dabbagh L, Pasdar M, Hugh JC. The importance of MUC1 cellular localization in patients with breast carcinoma: an immunohistologic study of 71 patients and review of the literature. *Cancer*. 2001;91(11):1973-1982.
3. Lavrsen K, Madsen CB, Rasch MG, et al. Aberrantly glycosylated MUC1 is expressed on the surface of breast cancer cells and a target for antibody-dependent cell-mediated cytotoxicity. *Glycoconj J*. 2013;30(3):227-236. doi:10.1007/s10719-012-9437-7.
4. Brockhausen I, Yang JM, Burchell J, Whitehouse C, Taylor-Papadimitriou J. Mechanisms underlying aberrant glycosylation of MUC1 mucin in breast cancer cells. *Eur J Biochem*. 1995;233(2):607-617.
5. Greenberg R, Schwartz I, Skornick Y, Kaplan O. Detection of hepatocyte growth factor/scatter factor receptor (c-Met) in axillary drainage after operations for breast cancer using reverse transcriptase–polymerase chain reaction. *Breast Cancer Res*. 2003;5(3):R71. doi:10.1186/bcr588.
6. Schroeder JA, Adriance MC, Thompson MC, Camenisch TD, Gendler SJ. MUC1 alters β-catenin-dependent tumor formation and promotes cellular invasion. *Oncogene*. 2003;22(9):1324-1332. doi:10.1038/sj.onc.1206291.
7. Bitter BG, Menzl I, Huerta CL, et al. Intracellular MUC1 peptides inhibit cancer progression. *Clin Cancer Res*. 2009;15(1):100-109. doi:10.1158/1078-0432.CCR-08-1745.
8. Bitler BG, Schroeder J a. Anti-cancer therapies that utilize cell penetrating peptides. *Recent Pat Anticancer Drug Discov*. 2010;5(2):99-108. doi:10.2174/157489210790936252.
9. Kharbanda A, Rajabi H, Jin C, et al. Targeting the oncogenic MUC1-C protein inhibits mutant EGFR-mediated signaling and survival in non-small cell lung cancer cells. *Clin Cancer Res*. 2014;20(21):5423-5434. doi:10.1158/1078-0432.CCR-13-3168.
10. Hisatsune A, Kawasaki M, Nakayama H, et al. Internalization of MUC1 by anti-MUC1 antibody from cell membrane through the macropinocytotic pathway. *Biochem Biophys Res Commun*. 2009;388(4):677-682. doi:http://dx.doi.org/10.1016/j.bbrc.2009.08.059.
11. Kirkham M, Parton RG. Clathrin-independent endocytosis: New insights into caveolae and non-caveolar lipid raft carriers. *Biochim Biophys Acta - Mol Cell Res*. 2005;1745(3):273-286. doi:10.1016/j.bbamcr.2005.06.002.
12. García-Pérez BE, Hernández-González JC, García-Nieto S, Luna-Herrera J. Internalization of a non-pathogenic mycobacteria by macropinocytosis in human alveolar epithelial A549 cells. *Microb Pathog*. 2008;45(1):1-6. doi:10.1016/j.micpath.2008.01.009.
13. Nishimura S, Takahashi S, Kamikatahira H, et al. Combinatorial targeting of the macropinocytotic pathway in leukemia and lymphoma cells. *J Biol Chem*. 2008;283(17):11752-11762. doi:10.1074/jbc.M708849200.
14. Bryant DM, Kerr MC, Hammond L a, et al. EGF induces macropinocytosis and SNX1-modulated recycling of E-cadherin. *J Cell Sci*. 2007;120:1818-1828.

doi:10.1242/jcs.000653.

15. Wang LH, Rothberg KG, Anderson RG. Mis-assembly of clathrin lattices on endosomes reveals a regulatory switch for coated pit formation. *J Cell Biol*. 1993;123(5):1107 LP-1117. http://jcb.rupress.org/content/123/5/1107.abstract.
16. Nichols B. Caveosomes and endocytosis of lipid rafts. *J Cell Sci*. 2003;116(Pt 23):4707-4714. doi:10.1242/jcs.00840.
17. West MA, Bretscher MS, Watts C. Distinct endocytotic pathways in epidermal growth factor-stimulated human carcinoma A431 cells. *J Cell Biol*. 1989;109(6 I):2731-2739. doi:10.1083/jcb.109.6.2731.
18. Kinlough CL, Poland PA, Bruns JB, Harkleroad KL, Hughey RP. MUC1 membrane trafficking is modulated by multiple interactions. *J Biol Chem*. 2004;279(51):53071-53077. doi:10.1074/jbc.M409360200.
19. Singh PK, Hollingsworth MA. Cell surface-associated mucins in signal transduction. *Trends Cell Biol*. 2006;16(9):467-476. doi:10.1016/j.tcb.2006.07.006.